

Quantifying Turbidity Current Interactions with Topography

by

Kyle M. Straub

B.S., Geosciences, The Pennsylvania State University

Submitted to the Department of Earth, Atmospheric and Planetary Science, in partial fulfillment of the requirements for the degree of

Doctor of Philosophy

at the

MASSACHUSETTS INSTITUTE OF TECHNOLOGY

June 2007

© Massachusetts Institute of Technology, 2007. All rights reserved.

Author
Geology, Department of Earth, Atmospheric and Planetary Sciences
May 25, 2007

Certified by
David Mohrig
Associate Professor of Geology
Thesis Supervisor

Accepted by
Maria T. Zuber
E.A. Griswold Professor of Geophysics
Head of the Department of Earth, Atmospheric and Planetary Sciences

Quantifying Turbidity Current Interactions with Topography

by

Kyle M. Straub

Submitted to the Department of Earth, Atmospheric and Planetary Sciences on April 20th, 2007, in partial fulfillment of the requirements for the degree of

Doctor of Philosophy

Abstract

This thesis advances our understanding of how transport properties of turbidity currents are mediated by interactions with seafloor topography, specifically channelized surfaces. Turbidity currents are responsible for crafting the morphology of continental margins. Unfortunately, very few direct observations exist defining turbidity current interactions with submarine channels and canyons because infrequent occurrence, great water depths, and high current velocities make measurements difficult to obtain. To overcome this problem, I utilize reduced scale laboratory experiments, remote sensing of the seafloor and subsurface deposits, and numerical analysis of transport processes. I focus on resolving the topography and composition of the evolving water-sediment interface with additional measurements that characterize the sediment transport and flow fields. I begin by quantifying interactions between turbidity currents and channel-bounding levees. Levees are the primary elements of self-formed channels and act to confine flows within channels, thereby increasing transport efficiency. I quantify the morphology and growth of levees in a submarine channel network offshore Borneo. Levee deposit trends are interpreted using laboratory observations and a morphodynamic model describing levee growth. Channel and levee deposits resulting from interactions between turbidity currents and sinuous submarine channels are then studied using reduced-scale laboratory experiments. Measurements of current super-elevation in channel bends are used to illustrate the importance of current runup onto the outer banks of channel bends. This runup resulted in focused overbank flow and production of thick, coarse, steep levees at these sites. Additional laboratory experiments illustrate the importance of current-channel bend interactions to the runout length of turbidity currents. I observed enhanced mixing in channel bends that reduced proximal deposition rates in sinuous channels compared to straight channels. I hypothesize that a wholesale vertical mixing of suspended sediment within turbidity currents at channel bends is a necessary condition for the construction of submarine channels greater than 100 km in length. Finally, I document the deepening of submarine canyons under net depositional conditions using an industry-grade seismic volume from the continental slope offshore Borneo. Interpretation of seismic horizons suggests deposition resulted from sheet-like turbidity currents, highlighting the importance of unconfined currents to the evolution of seascapes.

Thesis Supervisor: Dr. David Mohrig
Title: Associate Professor

Acknowledgements

I have received support and guidance from numerous individuals during my five years at M.I.T. The following paragraphs represent an attempt to formally repay this support and guidance through many statements of thank you. Unfortunately, due to the large number of stimulating and caring people who helped in the completion of this degree, it is possible that I forget to recognize someone. I apologize to anyone whose name does not appear here explicitly but please know that my thanks include you.

My interest in the geosciences began at an early age, but remained largely unfocused prior to interactions with Peter Flemings. During my sophomore year at Penn State, I knocked on Peter's door, asking to help out in any way I could with his group's research. Over the following two years he took me under his wing and helped focus my research interest in addition to teaching me the importance of a strong work ethic.

The research presented in this thesis would not have been completed without the immense guidance provided by David Mohrig. Over the last five years I have benefited from David's immeasurable scientific knowledge, unquenchable enthusiasm for studying interesting problems, valuable guidance during my patches of self-doubt, and above all his friendship. I could not have asked for a better advisor. Thank you very much.

Several chapters in this thesis incorporate data obtained from laboratory experiments. The quantity and quality of data collected in these experiments was greatly increased through my interactions with Jim Buttles. Working with Jim was always fun, even when the Radio-Factor with Bill O'Reilly was on in the background.

I owe a huge debt of gratitude to various support staff in the building. Thanks to Vicki McKenna and Carol Sprague in the Education Office for all their help over the years. Thank you to Jacqui Taylor and Roberta Allard on the 9th floor for help with all kinds of logistics and good chats. And a massive thank you goes to Roberta Bennett-Calorio who runs the 8th floor with grace and style. You have been my mother-in-Cambridge, feeding me, encouraging me, and offering a helpful hand whenever you could.

During my years in Cambridge I have gained many friends both inside and outside the confines of M.I.T. Will Ouimet was both a technical and personal resource. The long hours I spent on the 8th floor would not have been as fun without him. Doug Jerolmack's

work ethic was inspirational, while his singing voice was not inspirational. Bill Lyons was a supportive elder graduate student and good friend who was often willing to join me at the Muddy for a Sox game. Emmanuel Vassilaki was a trusted friend, so much so that I jumped out of a plane with him. Other valued M.I.T. friends include Brandon McElroy, Joel Johnson, Amy Draut, Wes Waters, Maureen Long, and Cam Wobus. My life outside of M.I.T. was greatly improved through interactions with several roommates. In particular, I wish to thank Ben Teply for his friendship during three great years at 115.5 Hampshire. I also thank Rebekah Cain for the support and companionship she offered during my last year in Cambridge. She made the completion of this phase in my life immensely more enjoyable.

I thank those who participated in my fantasy baseball league.

Finally, and most importantly, thank you to my family. The support, stability, and love you have granted me are directly responsible for who I am now. Thank you to my grandparents, in particular Martin Estep, for encouraging my interest in math and science during my childhood. My brother Jeff and sister Amy are two of my best friends in the world – thanks for everything. Thanks to Terry Foster for encouraging me to apply to M.I.T. and always believing in me. To my mother, Linda Straub, thank you for 27 years of never-ending love and support. I will never be able to repay all you have done for me. Words can not describe how much you mean to me.

Scientific Support

Shell Exploration and Production generously provided funds that supported the research contained in this thesis. Additional Shell funds supported my tuition and stipend while completing this degree.

Brunei-Shell Petroleum provided the seismic data from the Brunei continental margin. Carlos Pirmez was instrumental in obtaining that data and was also a great friend and colleague.

The National Center for Earth-surface Dynamics, an STC program of the National Science Foundation, under agreement number EAR-0120914, provided funds that supported my tuition and stipend while completing this degree.

Funding for the first year of this degree was provided by the Massachusetts Institute of Technology via a Presidential Fellowship.

Contents

<i>Abstract</i>	3
1 <i>Introduction</i>	9
2 <i>Quantifying the morphology and growth of levees in aggrading submarine channels</i>	14
3 <i>Addendum to chapter 2: Architecture of tributary channel network on the Champion Delta slope offshore Brunei Darussalam</i>	52
4 <i>Interactions between turbidity currents and topography in aggrading sinuous submarine channels: A laboratory study</i>	73
5 <i>How sinuosity can affect the total length of submarine channels</i>	149
6 <i>Constructional canyons built by sheet-like turbidity currents: Observations from offshore Brunei Darussalam</i>	167
7 <i>Conclusions</i>	193
<i>Bibliography</i>	196

Because a thing is difficult for you, do not therefore suppose it to be beyond mortal power. On the contrary, if anything is possible and proper for man to do, assume that it must fall within your own capacity.

Marcus Aurelius (121-180) Roman Emperor

The scientist does not study nature because it is useful; he studies it because he delights in it, and he delights in it because it is beautiful. If nature were not beautiful, it would not be worth knowing, and if nature were not worth knowing, life would not be worth living.

Jules Henri Poincaré (1854-1912) French mathematician.

Chapter 1

Introduction

Sediment deposition and erosion on the continental slope is dominated by the mechanics of turbidity current systems. Turbidity currents are defined as sediment gravity flows in which the gravitational driving force is supplied by an excess density associated with the suspension of particles. Turbidity currents can construct submarine canyons and channels that are similar in form to their terrestrial cousins. Sediment deposition from these flows construct expanded sections of sedimentary strata that preserve important records of past environmental conditions. In this work I advance our understanding of the interactions between turbidity currents and topography and therefore improve our ability to decipher the geological record preserved in their deposits. To accomplish this I utilized laboratory experiments, remote sensing of subsurface sedimentary deposits, and numerical analyses of targeted transport processes and sedimentary deposits. Quantitative measurements collected with these tools are used to study a range of conditions, spanning a flow spectrum from channelized currents to fully unconfined sheet-flows.

Very few direct observations exist defining turbidity current interactions with submarine channels and canyons (Best et al., 2005; Khripounoff et al., 2003; Xu et al., 2004) because infrequent occurrence, great water depths, and high current velocities make these measurements difficult to obtain. Due to the lack of direct measurements many scientists have utilized models developed for subaerial channelized flow as semi-quantitative guides for understanding submarine channel flow physics (Imran et al., 1999; Komar, 1969; Pirmez and Imran, 2003). Use of the terrestrial analog has been considered reasonable because rivers and submarine channels share similar scaling relationships for dimensions characterizing channel geometry (Pirmez, 1994). While these similarities are real, key differences in flow parameters also exist between the two environments. One critical difference is the ratio of current density to ambient-fluid density. For rivers, where the ambient fluid is air, this ratio equals 830. While in the deep ocean, where the ambient fluid is seawater, this ratio for turbidity currents typically ranges between 1.01-1.10. This difference in the density ratio reduces the ability of topography to guide flows in the

submarine environment (Kneller et al., 1991) and results in turbidity current heights that are often much greater than the relief of their guiding channels (Mohrig and Buttles, 2007).

Turbidity currents have been studied at laboratory scale for some time in flumes specifically designed to suppress systematic lateral variation in the flow field (Alexandar and Mulder, 2002; Brunt et al., 2004; Felix et al., 2005; Middleton, 1966; Parker et al., 1987; Simpson and Britter, 1979). These studies refined our understanding of the stream-wise evolution of perfectly confined turbidity currents (Brunt et al., 2004; Garcia, 1994; Gray et al., 2005) and their associated depositional trends (Alexandar and Mulder, 2002; Garcia, 1994; Middleton, 1966) and erosional (Pantin, 2001; Parker et al., 1987). Spreading associated with purely unconfined turbidity currents have also been studied in the laboratory (Choi and Garcia, 2001; Hauenstein and Dracos, 1984; Luthi, 1981; Mohrig and Buttles, 2007; Mohrig et al., 2005; Parsons et al., 2002; Violet et al., 2005). In this work, I capture the interactions between currents and topography most relevant to building depositional channel forms with experiments that target a middle ground between these end-member configurations.

In addition to laboratory experiments, I utilized seafloor topography and subsurface data from offshore Brunei Darussalam to quantify the architecture of turbidite deposits. Advances in imaging of the seafloor and continental slope subsurface over the last two decades are the result of improvements in geophysical exploration technologies including three-dimensional (3-D) seismic surveys. Many of these 3-D seismic surveys cover areas that are hundreds to thousands of km² in size and resolve strata defining many millions of years of continental-margin development. Stratigraphic horizons contained in these data volumes represent ‘snapshots’ of past depositional topographies. Analyses of these preserved topographies provide sedimentologists with temporal data to supplement spatial data contained in any single submarine digital elevation model. I utilized static depositional trends and stratigraphy from the Brunei Darussalam data set to infer dynamic interactions between topography and margin constructing turbidity currents.

In chapter two I use laboratory experiments and 3-D seismic data to quantify the morphodynamics of levees on submarine channels. Submarine levees are built from the overflow and deposition of sediment contained in turbidity currents. Levees are the primary topographic elements of self-formed channels and are thus a critical component of any

submarine landscape evolution model. Levees are also faithful records of channel history relative to channel-thalweg deposits that possess complicated stratigraphies associated with multiple episodes of local erosion. Despite their importance few studies have examined submarine levee morphology and growth (Dennielou et al., 2006; Skene et al., 2002). Using the 3-D seismic data from offshore Brunei Darussalam, I map the seafloor and several subsurface horizons beneath a tributary network of channels. I then create deposit thickness maps via sequential differencing of the mapped horizons and use these to characterize levee deposition patterns and quantify the change in levee morphology as a function of channel relief. My interpretation of map trends and associated constructional processes is guided by results from laboratory experiments. These experiments show that growth of levee-deposit thickness and taper is strongly influenced by the concentration profile of suspended sediment within a turbidity current. Rapid increases in levee-deposit thickness and taper are associated with channels that are shallow compared to the characteristic thickness of the constructing currents. Observations from Brunei Darussalam and the laboratory guide the development of a levee growth model that utilizes an advection-settling scheme coupled to a characteristic suspended-sediment concentration profile. Results from the laboratory experiments and levee growth model reveal a method for constraining turbidity-current heights from levee stratigraphy.

The submarine levees analyzed in chapter 2 are part of a tributary network of channels offshore Brunei Darussalam. In chapter 3 I use maps of present-day seafloor bathymetry and Quaternary deposit-thickness trends to characterize the stratigraphic architecture of this underreported style of submarine channel network. In addition, the data are used to pose several questions related to the evolution of submarine channel systems. These include: 1) What is the connection between the degree of channelization and rates of sedimentation; and 2) What controls the initiation and geometry of submarine channels that lack a direct connection to terrestrial channels?

In chapter 4 I turn my attention toward turbidity current interactions with aggrading sinuous submarine channels. Many deep marine channels are highly sinuous and persist for hundreds of kilometers, yet the processes by which these channels evolve are incompletely known. I report results from a laboratory experiment where I monitor the interactions of currents with channel bends at a reduced scale. The experiment documents the evolution of

a channel (initial sinuosity = 1.32) via deposition from 24 turbidity currents. Data collected during and following each flow includes high resolution maps of channel topography, profiles of current velocity, and profiles of suspended sediment concentration. These observations are used to test several commonly cited yet untested conceptual models of submarine channel evolution. Specifically, I quantify the magnitude of current superelevation in submarine channel bends and compare my measurements to equations describing superelevation driven by centrifugal acceleration. Measurements of current superelevation far exceed values estimated using these equations. I then derive a runup equation that accurately estimates the observations. This derivation highlights differences between submarine and terrestrial current-channel interactions which arise due to dissimilar excess densities for the sediment-transporting flows in the two environments. In-channel and channel-margin sedimentation patterns, including grain size, are also characterized.

In chapter 5 I use laboratory experiments to document the influence of channel-current interactions on turbidity-current runout length. Channels constructed by turbidity currents are the most common and dynamically significant topographic features found on the continental slope yet little is known about the processes that set channel length. The mechanism(s) allowing for the transport of sediment through sinuous submarine channels for great distances has puzzled scientists for decades. In attempting to explain this transport a contribution from the channel planform has until now never been considered. Measurements of currents traversing a straight and sinuous channel show enhanced turbulence and vertical mixing of suspended sediment at channel bends that reduces deposition rates, thereby increasing current runout lengths. This study demonstrates that increased form drag does not automatically decrease the transport efficiency of turbidity currents and provides an intriguing explanation for why almost all long submarine channels are moderately to highly sinuous in planform.

Finally, in chapter 6 I address interactions between sheet-like turbidity currents and a growing, shale-cored anticline. While channelized turbidity currents have received significant attention, several studies suggest that some currents move down continental margins as unchannelized flows (Field et al., 1999; Pickering et al., 1992; Wright et al., 1988). These flows can have current width to depth ratios exceeding 1000 and are referred

to as sheet-flow currents. I present sedimentation maps for a portion of the upper continental slope offshore Brunei Darussalam that I interpret as the product of deposition from sheet-flows. The interpreted sheet-flow deposits blanket an anticline that is dissected by several canyons. While the entire study region is a site of recent net deposition, local minimas in sedimentation are observed in the canyons and inter-canyon regions that are positioned on top of the anticline hinge. The magnitude of inter-canyon deposition has exceeded the sedimentation within canyons, causing canyon relief to increase through time. Growth of canyons via net sediment accumulation highlights differences in current-topography interactions found in submarine and terrestrial environments. Terrestrial canyon growth is always associated with net erosional conditions along the canyon axis. We hypothesize that the small excess density of sheet-flow turbidity currents allows for a significant fraction of a flow to traverse the inter-canyon highs rather than being routed through the canyon topographic lows. As a result, sediment is delivered to both canyon and inter-canyon regions by the same turbidity currents.

This thesis is written as four independent papers, each of which can stand on its own. A wide range of turbidity current flow conditions and time and length scales are considered, with the overarching goal of improving our understanding of seascape evolution. I have set out to accomplish this by refining the general understanding of how transport properties of turbidity currents are mediated by interactions with seafloor topography. Characterization of submarine channelized flows also provides the data necessary to compare against terrestrial systems in order to evaluate what processes are general versus environment specific in channelized landscapes.

Chapter 2

Quantifying the morphology and growth of levees in aggrading submarine channels

Kyle M. Straub^a and David Mohrig^b

^aDepartment of Earth, Atmosphere, and Planetary Sciences, Massachusetts Institute of Technology, 77 Massachusetts Avenue, Building 54-824, Cambridge, MA 02139

^bDepartment of Geological Sciences, The University of Texas at Austin, Austin, TX 78712

ABSTRACT

A network of submarine channels sharing planform attributes similar to river systems is located on the present-day continental slope offshore Brunei Darussalam. We mapped the seafloor and a shallow regional surface beneath the network of interest using an industry-grade 3D seismic survey. The subsurface horizon defines the geometry of a scarp and slide plane associated with a mass-failure event that reset the margin to an unchanneled state. A map of deposit thickness was created by differencing the seafloor and subsurface horizon, and this thickness data is used to unravel the growth of self-formed, leveed channels. With thickness and topographic data we have determined sedimentation trends; particularly relative rates of levee and overbank sedimentation as a function of lateral distance from the nearest channel centerline. We also use the deposition map to quantify the relationship between channel relief and levee taper. Levee steepness increases from 0.010 m/m to 0.050 m/m with a growth in channel depth from 5 to 50 m. Steepnesses increase at an ever diminishing rate for the deepest channels with sections of channel up to 72 m deep having a levee taper of only 0.056 m/m. We model levee growth using a simple advection settling model for currents with a vertical sediment concentration profile defined by the Rouse equation. This reproduces field and additional laboratory observations of levee growth and suggests that the most important parameters controlling levee morphodynamics are the degree of channel confinement and the vertical structure of suspended-sediment concentration profiles.

2.1. INTRODUCTION

Mapping of continental margins has revealed surfaces covered by numerous submarine channel systems (Damuth et al., 1983; Pirmez and Flood, 1995; Posamentier and Kolla, 2003). These channels are the dominant conduits for transport of terrigenous sediment into the deep sea and impart a first-order control on continental-slope topography (Kostic et al., 2002; Pirmez et al., 2000). Submarine channels are bounded over much of their length by prominent natural levees. These levees are built from the overspill and deposition of sediment contained in turbidity currents (Dennielou et al., 2006; Hay, 1987; Pirmez et al., 1997; Skene et al., 2002; Straub et al., submitted). In net aggradational settings, levees are the primary elements of self-formed channels and their deposits provide a cumulative record of channel history compared to deposits located in channel thalwegs where frequent episodes of local erosion can produce complicated stratigraphic histories. For self-formed channels the temporal and spatial growth of levees sets channel relief or depth. This relief in turn influences the degree to which turbidity currents are able to spill out of the confining channels and construct the regional overbank surface. Unfortunately, the wealth of geometric data defining the levees of submarine channels is not matched by an equivalent set of data defining the levee-building processes. Measurements of out-of-channel flow are less common than the small set of direct observations from turbidity currents confined to submarine channels themselves (Hay, 1987; Khripounoff et al., 2003; Xu et al., 2004). This paper links measurements of submarine levees and stratigraphy from the continental margin offshore Borneo with data from laboratory experiments that resolve the processes controlling submarine levee growth at reduced scale. Taken together these measurements motivate the development of a simple, quantitative sedimentation model that is intended to illuminate the basic morphodynamics of submarine levee growth.

Measurements from natural systems and laboratory experiments document numerous cases in which depositional submarine channels aggrade distances equal to or exceeding multiple channel depths while undergoing almost no change in channel planform shape and position (Deptuck et al., 2003; Posamentier, 2003; Straub et al., submitted). This nearly vertical climb of channel form in space requires rates of overbank sedimentation that are nearly equivalent to the in-channel deposition rates. Several

processes have been identified that can transfer some fraction of a channelized turbidity current onto the regional overbank surface, including flow splitting and flow spilling (Clark and Pickering, 1996; Piper and Normark, 1983; Straub et al., submitted). A portion of the sediment contained in these overbanking flows is deposited on and incorporated into the channel-bounding levees. Several authors have proposed that submarine levee architecture is controlled by 4 properties of the overbanking flow: 1) current height, H ; 2) current velocity, U ; 3) diameter and size distribution of suspended particles; and 4) structure of the suspended-sediment concentration profile (Pirmez and Imran, 2003; Skene et al., 2002; Straub et al., submitted). In this paper we focus on the control of these 4 properties as they relate to the evolution of the channel-levee taper. Levee taper is defined here as the change in deposit thickness over some specified distance measured at a right angle to the local direction of the channel centerline (Fig. 2.1). Levee taper is equal to the levee surface slope in the special case where the bank of the original channel form was both perfectly flat and horizontal. We analyze how taper changes during cases where levee growth is associated with both channel deepening and channel filling and relate these changes to properties of the channel-constructing turbidity currents. A better resolved understanding of levee morphodynamics will aid numerical formulations of seascape evolution that incorporate submarine channel processes.

Submarine levees have been the subject of several quantitative studies during the past ten years (Pirmez and Flood, 1995; Pirmez et al., 1997; Pirmez and Imran, 2003; Skene et al., 2002). Pirmez et al., (1997) and Pirmez and Imran (2003) focused on the temporal and spatial fining of particles composing levee deposits as a channel deepened. This change in deposit particle size was related to the progressive confinement of currents within the banks of the channel itself. These studies did not relate vertical trends in levee grain-size to the evolution of levee morphology. Skene et al. (2002) studied the morphology of submarine levees by comparing characteristics of levee thickness from 6 different channel systems from around the world. This study developed methods for measuring the spatial decay rate of levee thickness in both the flow direction parallel to the channel centerline and in cross-sections oriented perpendicular to the primary transport direction. Skene et al. (2002) calculated these spatial decay rates for only the total levee deposit, making no attempt to analyze how these parameters might have varied as channels

either deepened or filled. We aim here to develop a joint description of how levee deposit particle size and morphology co-evolve in response to changes in channel relief.

Submarine levees share many characteristics with terrestrial levees that develop on river banks. Levee height and width are proportional to channel depth in both environments (Adams et al., 2004; Cazanacli and Smith, 1998) and levee slope is influenced by the depth, velocity and particle sizes contained in overbanking flows (Filgueira-Rivera et al., in press; Pizzutto, 1987). Even though it is easy to access terrestrial levees, the processes controlling levee development in this environment are not correspondingly well resolved. The small surface slopes and tapers associated with terrestrial levees make it difficult to resolve differences in these properties (Brierley et al., 1997; Rowland et al., 2005). In addition, relatively little subsurface data has been collected over active or abandoned terrestrial channels, placing limits on the ability to study the temporal evolution of levee morphologies. Submarine levees on channels of comparable size are typically thicker, wider, and have larger tapers than those associated with rivers (Pirmez, 1994). These differences in levee properties are thought to be a consequence of the difference in density of the ambient fluid present in the two environments: ocean water is roughly 800 times denser than air and the ocean water is almost as dense as the sediment-transporting turbidity currents themselves. This small density contrast helps to promote turbidity-current heights that can be much greater than the relief of their guiding channels (Mohrig and Buttles, 2007), allowing for the continuous overspill of current and sediment onto the marine overbank surface (Clark and Pickering, 1996). Additionally, the low excess density of turbidity currents allows channel-levee complexes to super-elevate relative to their regional overbank surface by several channel depths (Peakall et al., 2000; Pirmez and Flood, 1995). This extreme degree of super-elevation is not observed in river systems where channel super-elevation equal to only a fraction of channel depth appears laterally unstable and is often associated with channel avulsion (Mohrig et al., 2000). It is our hope that an improved understanding of levee formation and growth in the submarine environment will also aid our quantitative and conceptual understanding of terrestrial levee dynamics and add to a general evolution model for self-formed channels.

2.2. CONTINENTAL MARGIN OFFSHORE BORNEO

The present-day continental slope offshore northern Borneo (Fig. 2.2) has been a passive margin since the late Miocene (Hiscott, 2001; Hutchison, 2004). The morphology of this continental margin is greatly influenced by sediment delivered from the Baram, Belait, and Tutong rivers (Hiscott, 2001; Hutchison, 2004). These three rivers are also responsible for building the Baram-Champion delta complex and construction of a continental shelf that is 50-70 km wide and underlain by 8-9 km of post-Eocene siliclastic sediments (Sandal, 1996). These sediments are derived from uplifted rocks of the Rajang-Crocker ranges in central Borneo. Erosion rates measured in these ranges are amongst the highest in the world and have resulted in high sediment-discharge rates to the South China Sea since the Eocene (Hutchison, 2004; Sandal, 1996).

In the study area the continental shelf-slope break occurs at a water-depth of ~200 m (Fig. 2.2b). The seabed then descends for the next roughly 60 km until reaching the floor of the Borneo Trough at a water depth of 2800 m. The upper slope is characterized by a relatively steep average gradient of 3.2° . Superimposed on this regional dipping surface are several tributary networks of submarine channels and a series of strike-parallel ridges. These ridges are the product of diapirism by mobile overpressured shale (Demyttenaere et al., 2000; Ingram et al., 2004; van Rensbergen et al., 1999). The combination of the high surface gradient and shale diapirism has led to multiple mass-failure events on the upper slope. Several head scarps documenting the release points for these large detachments are still visible on bathymetric maps of the present-day seafloor (Fig. 2.2b).

2.2.1. Seismic data set parameters

Our study of leveed submarine channels takes advantage of a 4000 km² industry-grade 3-D seismic volume covering the continental slope offshore Brunei Darussalam. The specific area is a tributary network of channels that covers 555 km² of this larger survey (Fig. 2.2b). We focused on the shallow sedimentary section positioned between the seafloor and a subsurface depth defined acoustically by an additional 0.3 seconds of two-way travel-time. The frequency roll-off for this portion of the seismic volume is near 80 Hz, providing a vertical resolution for buried deposits of ≤ 3 m. The entire survey was collected on a horizontal grid with 25 x 25 m² spacing. The seismic reflectors defining the seafloor and a

significant subsurface horizon were picked manually on every grid in-line in order to produce the highest quality set of digital elevation models for our study area.

2.2.2. Network of Leveed Channels

We focus on a relatively small channel network with a catchment that is approximately 6×24 km in the strike and dip directions (Fig. 2.2b). Even though this network is located directly down slope from the Champion shelf-edge delta, none of its channels can be directly traced to the terrestrial system. All submarine channels of detectable size initiate at positions 1 – 2 km down slope of the shelf break. These most proximal channels are presently situated approximately 250 m below mean sea-level. The distal end to the network is at 1200 m below mean sea-level. Channels possess a consistent pattern of growth. Channel relief or depth systematically increases from 0 m to an average value of 40 m over approximately the first 7 km down slope of the shelf-edge. Following this zone of consistent growth, the three largest channels in the network approach a constant relief for the remainder of their lengths. The long profile for Channel A (Fig. 2.2b) and the corresponding variation in channel relief or depth is presented in Figure 2.3. Subsurface imaging shows that channel relief is entirely the product of levee construction (Fig. 2.4). Seismic cross-sections oriented perpendicular to channels reveal higher amplitude reflectors in channel thalwegs compared to overbank surfaces, suggesting that channel deposits are coarser grained than levee and regional overbank deposits (Prather et al., 1998).

2.2.3. Pattern of sediment deposition within channel network

Producing a map of sediment deposition associated with the leveed channels requires the regional mapping of two surfaces, the seafloor and some prominent horizon in the shallow subsurface. Using the 3-D seismic volume we have mapped a shallow (<0.25 sec TWT below seafloor) regional surface beneath the network of interest. We chose to map the shallow subsurface reflector marked in Figure 2.4 because it possesses consistently strong reflection amplitude that allowed us to track the horizon beneath the majority of the network area. Inspection of a map of this surface (Fig. 2.5) reveals a dearth of local topography associated with paleo-channels, as well as a laterally persistent detachment

scarp and slide plane associated with a regionally extensive, mass-failure event ($>40 \text{ km}^2$). The detachment scarp preserves 30-50 m of relief suggesting a mass failure of comparable thickness. Down slope of the scarp are several long linear striations which were likely formed as the mass failure moved across the slide plain (Fig. 2.5). Further inspection of this map reveals a prominent band of high local slope extending from the south to the north corner. This feature represents a buried and partially healed detachment scarp associated with an even earlier mass-failure event. The seismically defined stratigraphy indicates that the network area has been the site of persistent sediment deposition since the release of the youngest mass-failure. Development of the leveed channels on top of the regional extensive and relatively smooth slide plane provides us with the simplest possible initial condition for studying the evolution of aggradational submarine channels and levee taper.

A map of sediment deposition associated with the channel network was created by differencing the seafloor and subsurface horizons. This map was converted from two-way travel-time to deposit thickness using a seismic velocity of 1700 m/s, the measured average velocity for the first 300 m of sediment at the nearest point of well control, 60 km to the southwest of our study area (van Rensbergen et al., 1999). Several observations can be made from this map of recent deposition (Fig. 2.5b). First, the primary control on interval thickness is simply distance from the shelf-edge, with sedimentation decreasing in the down slope direction. This depositional pattern is consistent with this region of Borneo margin undergoing progradation. In addition to this regional trend, the observed pattern of sedimentation is locally influenced by the high surface gradients associated with the most recent detachment scarp. Local minima in sediment deposition are positioned directly up-slope of the scarp while depositional thicks are located directly down slope of the scarp (Fig. 2.5b). Finally, thick levee deposits define the margins of every channel and indicate that this tributary network grew under net depositional conditions. In-channel deposition appears anti-correlated to local channel relief or depth (Fig. 2.3b). Sediment deposition on the beds of channels decreases rapidly over the same locations that channel depth is observed to rapidly increase. Both thalweg deposition and channel relief achieve approximately constant values at approximately the same downslope position (Fig. 2.3b).

The regional deposit thickness map (Fig. 2.5b) and seismic cross-sections (Fig. 2.4) reveal that the growth of channels A, B, and C (Fig. 2.2b) did not occur coevally. Rather,

sediment deposition at the terminus of channel B is consistent with transport in channel A, suggesting that channel B is older. Cross-cutting relationships imaged in the levee and overbank deposits of channel A and C suggest that channel A is also younger than channel C. Biostratigraphic control assembled from subsurface samples collected at petroleum exploration wells located roughly 60 km to the southwest of our study area strongly suggest that all of this sedimentation is of Quaternary age (Hiscott, 2001). Further refinement of the age for the studied depositional network will require coring within the study area itself.

2.2.4. Quantifying Overbank Deposition and Levee Growth

The map of deposit thickness throughout the submarine channel network contains the spatial information that defines levee form and sediment accumulation on the distal overbank surface. To characterize this depositional pattern we have performed the following analysis. First, we identified the location of every grid node on the thickness map that corresponds to a channel thalweg (Fig. 2.2C). With this network in place we calculated the path length to the nearest channel thalweg for every grid node on the map. This allowed us to examine every local measure of thickness as a function of distance from the closest channel thalweg. We then sorted and assembled all of the data points using this distance. The binning width was 25 m, the horizontal spacing associated with the 3-D seismic cube itself. Collapsing the data onto a single trendline allows us to capture both the mean depositional signal as well as the magnitude of variability about this trend associated with local topographic effects. Mean thickness and coefficient of variation, CV , defining both levee and background overbank deposition are presented in Figure 2.6.

The plot of average sediment thickness versus distance from a channel center allows us to define and characterize three depositional zones within the network. The first zone makes up the channels themselves. Average channel half-width is 125 m and over this distance deposit thickness increases from 65 m at the thalweg to 122 m at the levee crest (Fig. 2.6a). The second zone defines the average levee form and runs between 125 m to 2200 m from a channel centerline. Over this lateral distance, sediment thickness drops from 122m at the levee crest to 55 m its distal termination. It is not obvious where to place the distal end of the levee based only on mean thickness. We have refined the location by

taking advantage of the spatial structure in the coefficient of variation for deposit thickness. Coefficient of variation maintains an approximately constant, relatively large value for a distance up to 2200 m from a channel center. After this point values for CV systematically decrease with increasing separation from a channel. We take the transition from a roughly constant CV to a continuously decreasing one as defining the boundary between the levee and background overbank surface. We expect a greater variation in depositional thickness to be associated with focused levee deposition versus the background sedimentation building the regional overbank surface. Sedimentation on the distal overbank has produced a deposit with a nearly constant thickness of 55 m.

Analysis of the three depositional zones reveals two system properties that are particularly relevant to inferring behavior of the evolving network. First, sedimentation in channel thalwegs is only somewhat greater than the background deposition associated with the far-field overbank surface, 65 m versus 55 m, respectively. These nearly equal amounts of in-channel versus overbank deposition points to development of channels that are laterally stable and not prone to avulsion. Second, the characteristic width of the total levee package is 8.4 times the average channel width (Fig. 2.6a). As most channels in our study network are separated by less than 2 km from their closest neighboring channel, this levee distance suggests that some fraction of overbanking flow from currents moving down one channel is likely to re-enter an inactive or less neighboring channel and continue to move down slope.

Next we sought to unravel how levee morphology, specifically taper, evolved as channel relief increased. The vertical resolution associated with subsurface sediment bodies was not high enough to resolve this trend by measuring a succession of stacked levee deposits in seismic cross-section (Fig. 2.4). Because of this we regrouped the regional thickness data summarized in Figure 2.6a by relief of the nearest channel. By doing this we created a series of profiles defining deposit thickness as a function of distance from the nearest channel thalweg for 5-m increments of channel relief. Levee taper was measured from each of these profiles by measuring the change in total levee deposit thickness over a lateral distance equal to two channel widths. Previous studies have characterized levee slope or taper using spatial decay rates calculated by fitting exponential curves to the profiles (Pizzutto, 1987; Skene et al., 2002). Skene et al. (2002) compared

exponential and linear models which describe the decrease in levee thickness with distance away from a channel thalweg and found no statistically meaningful difference between the two models. We used the simpler linear model to determine how the average levee taper varies as a function of channel relief. Levee taper was found to systematically increase from 0.008 m/m to 0.041 m/m as channel relief or depth increased from 5 to 25 m. This increase in taper was not constant. Levee taper increased at an ever diminishing rate, with channel segments up to 72 m deep having a levee taper of only 0.056 m/m (Fig. 2.7). This pattern of rapid increase in levee taper when channel relief is small followed by slower increases in taper for higher-relief channels suggests a change in sedimentation properties for overbanking flow as the turbidity currents became relatively more confined within channels. In the following sections we use laboratory experiments and a numerical model to investigate the dynamics of levee growth and the influence of current properties in the evolution of levee taper as a function of channel relief.

2.3. LABORATORY EXPERIMENTS

Turbidity currents and their depositional and erosional patterns have been studied at laboratory scale for over 40 decades (Keevil et al., 2006; Middleton, 1966; Parker et al., 1987; Straub et al., submitted). The vast majority of these experiments have been conducted in flumes specifically designed to suppress across-flow variation in the flow field (Felix et al., 2005; Hallworth et al., 1993; Parker et al., 1987). These studies refined our understanding of the stream-wise evolution of two-dimensional turbidity currents. In recent years, several studies have examined depositional and erosional patterns associated with channel formation and growth (Mohrig and Buttle, 2007; Straub et al., submitted; Yu et al., 2006). We present laboratory results that focus on resolving at a reduced scale the growth of channel bounding levees. In particular, we monitor the depositional patterns, specifically deposit thickness, composition (grain size), and levee taper, resulting from the continuous overspill of an upper fraction of a turbidity current in a straight channel. Deposit properties resulting from this experiment were summarized by Mohrig et al. (2005) but were not systematically related to the streamwise velocity and suspended-sediment concentration profiles for the levee-building turbidity currents. We relate deposit properties to the following current properties, 1) fraction of total current thickness located

above the rim of the channel-confining levees, 2) vertical profiles of suspended sediment concentration, and 3) streamwise velocity profile. The over-arching aim of this experiment was to collect data relevant to the morphodynamics of levee growth that is missing in the static morphology and stratigraphy of natural settings such as offshore Brunei.

2.3.1. Experimental setup

Nine sediment-laden currents were released into a basin that is 5 m long, 5 m wide, and 1.2 m deep that remained filled with water throughout the experiment (Fig. 2.8). Before filling the basin with fresh water, a channel was constructed on its floor. The channel had a length of 3 m, had an initial relief of 50 mm, 30° channel side walls and maximum and minimum channel widths of 0.77 and 0.6 m respectively (Figure 2.9A). The initial channel was constructed from six 0.5 m long concrete forms placed flush end to end. The channel had no initial downstream bed slope. After traversing the 3.0 m long channel, each current spread out onto a short unconfined surface before plunging into a moat where it was removed from the basin via perforated pipes, thereby preventing current reflections off of the tank sidewalls.

All turbidity currents were composed of the same mixture of clear water and suspended sediment. This mixture produced currents that entered the channel with a bulk density of 1024 kg/m³. Crushed silica was used as sediment and had a cumulative grain size distribution characterized by a D1, D5, D16, D50, D84, D95, and D99 equal to nominal diameters of 1.4 μm, 2.4 μm, 6 μm, 29 μm, 59 μm, 89 μm, and 133 μm, respectively. The mixture of fresh water and sediment was introduced to the basin via a constant head tank that guaranteed steady input discharge throughout each individual release. Each current passed through a momentum extraction box before entering the channel. This box was 0.5 m by 0.5 m in planform and contained several vertical screens of 5 mm wire mesh which currents passed through prior to entering the experimental channel. The momentum extraction box ensured that each flow acted as a sediment-laden plume driven by buoyancy alone. Current thickness remained constant for all 9 runs at 90 mm, while current discharge and velocity varied from flow to flow between 1.5x 10⁻³ - 3.5 x 10⁻³ m³/sec and 50 mm/sec – 120 mm/sec. Representative input values for the densimetric Froude number ($Fr = \bar{u} / \sqrt{[(\rho_c / \rho_a) - 1]gH}$), Reynolds number ($Re = \bar{u}H / \nu$),

and buoyancy flux ($B_{f0} = \Delta\rho g u h b / \rho$) for each flow are presented in table 2.1, where \bar{u} is depth averaged velocity, ρ_c is current density, ρ_a is the ambient fluid density, g is gravitational acceleration, H is current thickness, ν is kinematic viscosity, and b channel width. Current duration varied between 245 – 576 sec.

Measurements of current velocity were collected using two Sontek Acoustic Doppler Velocimeters (ADV) and one Sontek Pulse-Coherent Acoustic-Doppler Velocity Profiler (PCADP). An ADV was positioned at the channel entrance and exit throughout the experiment. These devices recorded the 3-D velocity in a 10^{-6} m³ sampling volume located 50 mm above the channel bed at the channel centerline with a frequency of 10 Hz. Vertical profiles of velocity were collected during flow 8 at 2 distances from the channel entrance in the channel center. The PCADP measured velocity with a frequency of 0.25 Hz in sampling volumes that were 16 mm tall and varied between 0.004 to 0.006 m² in planform area with increasing distance from the instrument.

Maps of the channel form were collected prior to flow 1, and after flows 1, 2, 3, and 8 using the first hard returns from a 1MHz ultrasonic transducer connected to a pulse/receiver box. Each bathymetric map was built from 23,184 points collected on a grid with 14.1 mm spacing in the cross-stream and downstream directions. The precision at each location is better than 0.2 mm. This resolution makes it possible to successfully determine the patterns of sediment deposition associated with individual currents by differencing successive maps of channel topography.

Following the 9th current, the water level in the experimental basin was lowered, and the deposit was allowed to dry. After drying, the deposit was sampled for particle-size characterization. These samples were collected at 255 locations including sample locations centered on the left levee-crest located every 7 cm from the channel entrance. Samples were also collected from 6 cross-sections oriented perpendicular to the channel centerline. Samples came from the uppermost deposit and represent deposition associated with the final currents. The sediment samples were then analyzed with a Horiba LA-300 laser-particle-size analyzer (LPSA). The LPSA uses a diode laser to accurately measure a distribution of sizes from 0.001 to 0.3 mm in nominal diameter.

2.3.2. **Scaling**

Our experiment was conducted at a reduced scale relative to submarine channels. A comparison of our experiment to natural environments is performed using three components: 1) a geometric scaling of the channel topography itself; 2) a dynamic scaling of flow properties for estimating equivalence between model and natural flows; and 3) a dynamic scaling of sediment-transporting conditions for roughly comparing model and natural flows. The scaling is only intended to guide how experimental results might be applied to the interpretation of natural channels. Our experiment was not designed to simulate environmental conditions associated with the construction of channels offshore Brunei.

The geometric scaling for our experimental system was set at 1/1000. Maximum width, depth and length for the laboratory channel correspond to natural scales of 770 m, 50 m, and 3 km. The channel width/depth ratio measured 0.35 m from the channel entrance systematically increased from 15.4 to 42.8 through the course of the experiment. These values compare favorably with measurements from natural channels assembled by Pirmez and Imran (2003) and for the channels offshore Brunei.

The comparison between properties of the experimental and natural or prototype flows focuses on the densimetric Froude number. An approximate dynamic similarity between the model and a natural system is ensured by setting $Fr_{(\text{model})} = Fr_{(\text{prototype})}$ (Graf, 1971). Assuming a similar excess density for the experimental and natural currents, equality in densimetric Froude number is satisfied by prototype values for \bar{u} and H of 2.2 m/s and 50 m. Equality in densimetric Froude number also constrains the duration of a comparable natural current to be 2.8 hr. Reynolds numbers for the model and prototype cannot be matched. The characteristic Reynolds number for model currents was 6.4×10^3 while the characteristic value for a comparable natural current would be 3.0×10^8 . Fortunately the model-current value was sufficiently large to ensure the approximate Reynolds similarity for fully turbulent gravity currents proposed by Parsons and Garcia (1998).

Grain sizes used in the experiment can be compared to natural systems by the ratio w_s / u^* where w_s is a representative settling velocity for the particle class of interest and u^* is the shear velocity for the current. This scaling parameter was chosen because it best characterizes the degree to which particles of various sizes are suspended within the

transporting current, with w_s serving as the scale value for downward particle advection and u^* being the scale value for diffusion of particles up into the interior flow by turbulent eddies. Estimates of settling velocities for experimental particles were calculated using the method of Deitrich (1982). Shear velocity was calculated from estimates of bottom shear stress, τ_b , using

$$(1) \quad u^* = \sqrt{\frac{\tau_b}{\rho_c}}$$

and

$$(2) \quad \tau_b = \rho_c C_f \bar{u}^2$$

where C_f is a friction coefficient. We employed values of $C_{f(\text{prototype})} = 3 \times 10^{-3}$ and $C_{f(\text{model})} = 3 \times 10^{-2}$ to account for the weak dependence of bed friction coefficient with turbidity-current scale (Garcia, 1994; Parker et al., 1987). By satisfying the equality $w_s / u^*_{(\text{model})} = w_s / u^*_{(\text{prototype})}$ we found that D5, D50, and D95 for the experimental flows correspond to 7 μm , 101 μm , and 434 μm for flows at natural scale. This scaling of the suspended sediment suggests that the medium to very-coarse silt transported by the experimental currents is comparable to particles ranging from very coarse silt to medium sand in a natural system.

2.3.3. Experimental Results

The primary goal of this experiment was to characterize the patterns of sediment deposition from turbidity currents that construct submarine levees and to connect these patterns to properties of the flow field. The nine flows that traversed our experimental channel were all highly depositional, with very little re-entrainment of sediment. This resulted in deposition of sediment lamina with no internal structure and a fine-grained cap consisting of particles that did not settle out of the water column until after each current was finished. Sediment deposition in the mapped region represented a fraction of 25 – 30 % of the total sediment released into the basin. A majority of the sediment bypassed the mapped region, exiting the channel at its downstream end. For every flow event deposition in the channel exceeded deposition on channel banks (Fig. 2.9B&C), resulting in a channel that progressively lost relief over the course of the experiment. This loss of channel relief resulted in a progressive increase during the experiment in the fraction of current thickness

existing above the channel overbank surface because current thickness remained constant at 0.09 m throughout the experiment. At the start of the first flow 44 % of the current was situated above the overbank surface. At the end of flow 8, 81% of the current was situated above the overbank surface at a downstream location of 0.35 m from the channel entrance.

2.3.3.1. *Deposition on Channel Banks*

Deposition on the overbank surface produced levees that displayed systematic downstream trends in thickness, taper and composition. Levee taper was measured perpendicular to the channel direction and calculated using total-deposit thickness measurements, one at the levee crest and a second at a lateral position 0.2 m from the levee crest. This lateral distance equals 29 % of the channel width and therefore characterizes only the most proximal section of the constructional feature. We focus on the evolution of the left-bank levee. Topographic data measured there defines the spatial patterns of levee deposition (Fig. 2.10A). Near the channel entrance ($x=0.35$ m), overbanking flow resulted in deposition of a 15 mm thick levee that had a taper of 4.1×10^{-2} m/m. Both levee crest deposit thickness and taper decreased with increasing distance from the channel entrance. At 2.22 m from the channel entrance levee crest thickness and taper equaled 1.5 mm and 0.18×10^{-2} m/m. This represents a 96 % decrease in levee taper between the two positions.

Particle size distributions were measured along 6 transects oriented perpendicular to the channel direction. On these transects the deposit was sampled every 14 mm from 0 – 0.114 m from the levee crest (Fig. 2.10B). Median grain size, D50, of the levee crest deposit decreased from 41 μ m to 20 μ m between 0.35 – 2.69 m from the channel entrance. The change in D50 with lateral distance from the channel also systematically decreased. At 0.35 m from channel entrance, grain size decreased at 2.9×10^{-2} μ m/mm. At 2.69 m from the channel entrance the lateral decrease in median grain size for the levee deposit was 2.2×10^{-2} μ m/mm. This represents a 24 % decrease in the lateral fining of levee deposits between 0.35 and 2.69 m from the channel entrance, a much smaller percentage decrease than was measured for levee taper.

2.3.3.2. *Current Properties*

To quantify the influence of current properties on levee production we must first estimate profiles of streamwise velocity and suspended sediment concentration. Streamwise velocity profiles were collected using a Sontek PCADP situated at the channel centerline. The profiler measured the current structure of flow 8 at two downstream locations, 0.5 m and 1.5 m from the channel entrance. Mean current thickness remained constant over this distance and equaled 96 mm +/- 8 mm (Fig. 2.11). The vertical structure of the suspended-sediment concentration profile was reconstructed using properties of the levee crest deposit. This is done by assuming that mean deposition rate here was a function of the mean concentration and grain size of suspended sediment residing in the current at the levee-crest height above the channel bed. Since channel relief for flow 8 varied in the downstream direction (Fig. 2.9) we were able to collect a set of measurements defining how the solids in this current were distributed vertically within the current. Collapsing these data collected at many points in the downstream direction onto a single, representative concentration profile requires us to assume that this profile and other current properties are slowly varying with increasing distance from the source, an assumption supported by our direct measurements of current thickness and velocity profile. Sedimentation rate for strongly depositional currents can be approximated as:

$$(3) \quad \frac{\partial \eta}{\partial t} = w_s C_{nb}$$

where C_{nb} is the near-bed concentration (Parker et al., 1987). Deposition rate on levee crests is calculated by dividing the deposit thickness on levee crests by the combined run-time of the first 8 currents in our experiment. w_s is calculated for the median particle size deposited on levee crests using the method of Deitrich (1982). Using this data we rearranged Equation 3 to solve for C at current heights between 17 and 33 mm above the channel bed (Figure 2.11A). The reconstructed section of the concentration profile shows a rapid vertical decrease in concentration from 9.0×10^{-3} to 4.5×10^{-3} between 17 and 20 mm above the channel bed followed by a much less rapid decrease in concentration with increasing flow height. This rapid decrease in concentration is located at the same vertical position as the velocity maximum, confirming that there is little mixing of suspended sediment across this zone of low shear associated with the velocity maximum (Altinakar et al., 1996; Imran et al., 1999).

2.3.4. Interpretation of Laboratory Results

A notable property of our experimental system was the strong correlation between levee crest deposit thickness and levee taper. Both properties are plotted against the ratio of local channel relief to total current thickness, R/H , in Figure 2.12. This ratio describes the relative confinement of a current within the channel sidewalls at any point in the system. Values of levee-crest deposition and taper increase slowly as R/H drops from 0.49 to 0.32. Further decreases in R/H lead to rapid increases in levee-crest deposit thickness and levee taper. These observed patterns of change mimic the vertical structure of the estimated concentration profile (Fig. 2.11). The concentration profile shows vertical stratification that is much greater than the reconstructed vertical gradient for the settling velocity profile. As the fraction of current located above the levee crest increases, the concentration of sediment located above the levee crest will also increase, resulting in enhanced sediment discharge to the overbank regions. In highly aggradational settings, like our experiment, this will result in levee crest deposition rates that are a function of the degree of current confinement and current sediment concentration profile. We examine the connection between current confinement, sediment concentration profile, and levee taper in the following sections.

2.4. COMPARISON OF BRUNEI AND LABORATORY LEVEES

The formation and growth of levees offshore Brunei and in our laboratory experiment represent two end-member growth histories for levee evolution in aggradational settings. Levee growth offshore Brunei outpaced in-channel deposition, resulting in an increase of current confinement throughout evolution of the channels. In contrast, levee growth in our experimental channel was associated with progressive filling of a channel. As the channel filled, a larger fraction of each current was situated above the levee crest and therefore available to transition to overbank flow. We compare these two channel evolution styles by plotting levee taper as a function of local channel relief (R) divided by maximum channel relief within the evolving system (R_m) (Fig. 2.13A&B). We use R_m as a proxy for the vertical dimension of currents since no data on current thickness exists for offshore Brunei. The absolute magnitude of R/R_m may differ from R/H but we assume that these two

parameters are highly correlated and when plotted against levee taper both ratios will produce similar trends. In the offshore Brunei system, levee taper initially increases rapidly as R/R_m grows from a very small beginning value. A roll-over in this trend occurs at approximately $R/R_m = 0.04$ and levee taper increases less rapidly with further increases in R/R_m . In our laboratory experiment the growth in levee taper is initial small as R/R_m decreases from 1 to about 0.45. As R/R_m decreases further, levee taper rapidly increases. We use the similarity between the offshore Brunei and laboratory trends (Fig. 2.13C) to guide the formulation of a simple levee growth model so that we can further explore the connections between suspended-sediment concentration profile, particle settling and advection velocities, and the degree of current confinement that lead to levee construction.

2.5. LEVEE GROWTH MODEL

Inspection of submarine levees reveals that these topographic forms are primarily depositional features. In general, sediment collecting on these forms is not being substantial reworked by either the depositing or subsequent overbanking flows. Clearly this is a simplification but it provides us with a legitimate starting point for exploring submarine levee morphodynamics. We are going to assume that sediment added to levees is purely deposited from suspension fallout and that once a grain hits the bed it is transferred to the immobile substrate. Transfer to the immobile substrate precludes future mobilization as bedload or its wholesale removal via a later, net-erosional current. Under these environmental conditions we approximate the sediment transport and deposition on a levee surface using an advection-settling scheme. The vertical distribution of particle sizes and sediment concentrations are defined using the Rouse equation (1939). We are aware that the structures of suspended sediment profiles described by the Rouse equation are affected by the assumption that the transporting flow has a free surface. This obviously is not the case for turbidity currents where there can exist considerable mixing and turbulence production at the interface between the current and the overlying ambient fluid, seawater. In spite of this difference, similarity between predicted and experimental profiles (Garcia, 1994; Mohrig et al., 2005) has lead us to conclude that the Rouse equation is a useful starting point. Only that fraction of the current situated above the elevation of the levee crest is used in the advection-settling calculation. We envision currents with a given H , U_x ,

C_a , ρ_c , and grain size distribution leading to the growth of levees from an initially flat surface. During early channel growth, sedimentation from near-bed, relatively stratified overbanking flow will lead to levee deposits that have high tapers (Fig. 2.14A). As the channel grows due to levee construction, tapers of individual levee deposits will decrease as only the relatively homogeneous, better-mixed portions of the interior flow are available to leave the channel and build the levee (figs. 2.14B). During late stages of levee growth, individual deposits will have extremely low tapers because only the very well mixed uppermost portions of currents are able to empty onto the overbank surface (Fig. 2.14C).

Advection-settling models calculate the distance a particle will travel based on the velocity of the transporting fluid and w_s . The distance a particle travels is equal to:

$$(4) \quad x = U \frac{z_i}{w_s}$$

where z_i is the initial height of the particle above the local bed elevation. Advection-settling models for sediment transport are most accurate when w_s is large compared to instantaneous, upward-directed velocities associated with the turbulent flow. We assume that this condition is met for decelerating depositional currents moving across the levee and overbank surface. Several terrestrial studies (Adams et al., 2004; Asselmann and Middlekoop, 1995; Cazanacli and Smith, 1998; Filgueira-Rivera et al., in press) have concluded that levee form and composition are controlled by the advection and settling of particles contained in overbank flow.

We track levee elevation, η , in our model along a transect that is oriented perpendicular to the dominant flow direction. Levee deposition is influenced by current height, current velocity, the distribution of suspended particle sizes, and the structure of the suspended sediment concentration profile. We calculate a suspended-sediment concentration profile for the partially channelized flow based on input values of U_x , H , C_a , ρ_c , and a grain size distribution defined by 10 particle diameters. For each particle diameter we calculate a sediment concentration profile defined by the Rouse equation (1939):

$$(4) \quad C_z = C_a \left(\frac{H-z}{z} \left(\frac{z_a}{H-z_a} \right)^p \right)$$

where C_a is a reference concentration at a given elevation, z_a , and p is the Rouse number:

$$(5) \quad p = \frac{w_s}{ku^*}$$

where k is von Karman's constant (0.4), and u^* is the current shear velocity. u^* is calculated using equations 1 and 2, and values of $C_f = 3 \times 10^{-3}$ and $z_a = 0.8$ m. C_f value utilized in our model represents a coefficient of friction for field scale flows estimated by (Garcia, 1994). Model z_a value represents an elevation associated with possible field scale roughness elements. Deposition rate is calculated at each model node by summing of the deposition rates for each particle size included in the model:

$$(6) \quad \frac{\partial \eta}{\partial t} = \sum_i w_{si} C_{nbi}$$

where w_{si} and C_{nbi} represent the settling velocity and near bed concentration of each class i of particle diameter. C_{nb} at levee position x for each model time step is equal to:

$$(7) \quad C_{nbx} = C_a \left(\frac{H - z_x}{z_x} \left(\frac{z_a}{H - z_a} \right)^p \right)$$

where z_x is the vertical position in the current contributing suspended sediment to the levee surface at distance x from the levee crest. The value of z_x is calculated using the following advection-settling expression:

$$(8) \quad z_x = w_s \frac{x}{U_y} + z_{LC}$$

where z_{LC} represents the height of the current confining levee crest above the bed of the channel at each time step and U_y is the velocity at which sediment is advected laterally across the levee surface. As z_{LC} increases due to levee growth an ever increasing fraction of the suspended-sediment profile becomes confined within the channel walls and is no longer available for overbanking flow. We will begin our analysis assuming a constant value of $U_y = 0.43U_x$. This relationship has been shown by Parsons et al. (1998) to describe the lateral velocity for a purely unconfined flow in terms of the down slope directed velocity.

The levee growth model outlined above was used to investigate whether or not a reasonable combination of input values for U_x , H , C_a , and grain size distribution could produce a curve for levee taper growth that is similar to the trend measured from offshore Brunei (figs. 2.7 and 2.13A). We used a Monte Carlo scheme to search 100,000

combinations of the following 13 input parameters: U_x , H , C_a , and 10 particle sizes. We tracked the RMS error for each combination between our model result and the measured relationship from offshore Brunei. The RMS error was minimized by the set of parameters listed in Table 2.2 and visualized in Figure 2.15. Notice the similarity between the synthetic levee stratigraphy shown in Figure 2.15B and the seismically resolved stratigraphy shown in Figure 2.14D. The fit between the modeled levee-taper trend and the measured relationship of taper and channel relief is also quite good (Fig. 2.15C). The model shows that the observed roll-over in taper occurs at a channel relief sufficient to fully contain the highest gradient portion of the suspended-sediment concentration profile.

A general understanding of the relationship between current confinement and the ratio of lateral, overbank velocity to down channel, current velocity has not yet been developed. Spreading of a completely unconfined turbidity current over smooth surfaces has been studied by Luthi (1981), Hauenstein and Dracos (1984), and Choi and Garcia (2001). These studies found $0.25 < U_y/U_x < 1$ for currents with widely ranging initial conditions. The evolution of U_y/U_x as a function of R/H was monitored under one set of flow conditions during an experiment presented by Mohrig and Buttle (2007). They found that:

$$(9) \quad \frac{U_y}{U_x} = 0.60e^{-3.05(R/H)}$$

with $r^2 = 0.97$. We use Equation 9 to compare levee growth with a varying U_y/U_x against model results for which the ratio of U_y/U_x was held constant. The best-fit model parameters using the new expression for U_y/U_x are presented in Table 2.2. The two models produce indistinguishable results during early levee growth and only minor differences following the roll-over in levee taper (Fig. 2.16). Important for this study, though, the roll-over in the two curves happens at the same value of R .

2.6. DISCUSSION

2.6.1. Control of Concentration Profile on Levee Evolution

The combination of data from offshore Brunei, our laboratory experiment and our levee growth model indicate that the shape of a suspended-sediment concentration profile most

strongly influences the evolution of levee morphology. Previous studies have recognized the importance of lateral current velocity, current height, and suspended particle sizes in setting the morphology of levees (James, 1985; Pizzutto, 1987; Skene et al., 2002; Straub et al., submitted). None of these studies have attempted to evaluate how levee taper changes with variation in channel relief. This study reveals that levee taper growth is primarily a function of the shape of the supra-levee fraction of a current's vertical profile of sediment concentration. In our laboratory experiment we found that the relative growth in bulk levee taper was closely tied to the supra-levee fraction of turbidity current thickness. The reduction in channel relief due to high in-channel deposition rates eventually elevated the high velocity core above the channel sidewalls. This resulted in the lateral movement of some fraction of the highly stratified flow onto the overbank region (Fig. 2.11) and the construction of levees with high tapers. Our levee growth model indicates a similar control of current confinement in the rate of levee taper growth for channels that increase their relief through time. A measurable reduction in the rate of increasing levee taper occurs after the high concentration fraction of the flow is confined to the channel via levee and sidewall growth.

We propose that channel confinement has a more important role in submarine levee evolution than in terrestrial settings. This is because submarine channels are often built by currents that can be a number of times thicker than the channels that guide them (Hay, 1987; Mohrig and Buttles, 2007; Peakall et al., 2000). For systems where current thickness is often greater than channel relief, a continuous overspill onto the overbank surface via gravitational collapse of the supra-levee fraction of the flow can be expected (Piper and Normark, 1983). The large dynamic range in values of R/H for submarine channels compared to rivers appears to have associated with it a greater variability in the patterns of levee sedimentation and final topographic form. This difference in the range of values for R/H is primarily a consequence of the relative density differences between turbidity currents and seawater and river flow and air.

2.6.2. Implications for Using Levee Stratigraphy to Estimate Current Heights

The thickness of submarine channel-forming currents is difficult to measure directly due to great water depths and infrequent flow. In addition, the depth of submarine channels

bounded by levees offers only a minimum thickness for channel-building flows because turbidity currents are often much thicker than their guiding channel (Hay, 1987; Mohrig and Buttles, 2007; Peakall et al., 2000). This poses a considerable problem for modeling seascapes because current properties such as thickness are needed to accurately formulate and evaluate numerical models that simulate evolving submarine channels. Accurate estimates of paleo-current properties are also necessary to reconstruct environmental conditions associated with ancient channel systems. Komar (1969) and Pirmez and Imran (2003) estimated turbidity current velocities in two submarine channel systems using equations that required knowledge of current height. In these two studies, the absence of a way to accurately constrain current height led the authors to equate current thickness to channel depth in order to perform their calculations of velocity. We believe results from our study point out an improved method for estimating current height from preserved levee topography.

In our experiment levee taper increased as R/H decreased, due to greater deposition on the channel bed relative to the channel margins. The rate of taper growth rapidly increased after R/H fell below ~ 0.35 and a fraction of the high velocity and sediment-charged core of the currents was exposed to the supra-channel environment. Garcia (1994) and Altinakar et al. (1996) found that over a range of conditions, the high velocity core of turbidity currents is located between $0.2-0.4H$. In our experiment the location of the high velocity core was coincident with the interval where the concentration of suspended sediment rapidly changed. Once this most stratified portion of the current was elevated above the crest-lines of the channel levees, a rapid increase in levee taper occurred. Several other authors have observed a rapid change in the suspended-sediment concentration associated with the height of maximum velocity in turbidity currents (Buckee et al., 2000; Garcia and Parker, 1993; Parker et al., 1987) and have explained the connection as a result of minimal vertical mixing associated with low shear in the velocity maximum region (Buckee et al., 2000). We propose that the identification of the channel relief associated with a rapid roll-over or change in growth rate of levee taper defines containment of the high velocity and stratified core the characteristic turbidity current by channel sidewalls. This channel relief at the roll-over, R_{ro} , would therefore be $0.2H < R_{ro} < 0.4H$.

For channels located offshore Brunei, a roll-over in growth of levee taper occurs at a channel relief of 30 +/- 5 m. Applying the surrogate for current thickness described above, we estimate the characteristic thickness of turbidity currents building the Brunei channels to be greater than 75, but less than 150 m in thickness. It is worth noting that this height is somewhat less than the estimated thickness derived using our levee growth model. We speculate that this is a result of our method for computing suspended-sediment concentration profiles. Sediment concentration profiles in our model were calculated using the Rouse equation, directly applicable to flows possessing an upper, free surface. This condition does not hold for turbidity currents and to date no consensus has been reached on how to best mathematically define the concentration profiles for these flows. Work by Altinakar et al. (1996) suggest that the Rouse equation does a good job of estimating turbidity current concentration profiles from the channel bed up to the elevation of the velocity maximum. Above this height they theorize that the concentration profile is modified by shear and turbulence production at the interface of turbidity currents and the overlying ambient fluid. This modification could result in reduced sediment concentrations at levels above the velocity maximum compared to those estimated using the Rouse equation. Fortunately, the roll-over in levee taper occurs at a distance above the bed where the concentration profile does appear to be accurately modeled by the Rouse equation.

2.7. SUMMARY

In this study we use an industry grade, 3-D seismic volume to quantify the thickness of levee and regional overbank deposits that construct a tributary network of submarine channels in offshore Brunei. The initiation and growth of this channel network occurred following the release of a large mass-failure. This mass-failure left a 30-50 m high scarp and an unchannelized slide plane. Since the release of this mass-failure our study region has been a site of net deposition, allowing us to study the initiation and growth of channels from an unchannelized surface. Channel relief in this system is tied to the growth of prominent levees. These levees have an average half-width of 2.1 km, a distance much less than the average distance separating channels in this network. Levee taper was measured from plots of mean deposit thickness vs. distance from closest channel thalweg for channels of varying relief. We found that levee taper rapidly increased during

early levee growth than transitioned to a slower taper growth rate as channel relief exceeded approximately 30 m.

We monitored the growth of levees in a reduced-scale laboratory experiment. Nine turbidity currents with constant initial conditions were released into a straight channel. Preferential deposition in the channel compared to overbank surface resulted in an ever increasing fraction of the turbidity current being located above the crests of the channel-confining levees. After R/H decreased below a value of 0.35 the rate of levee taper growth rapidly increased. At these low values for R/H some fraction of the high velocity and highly stratified core of the turbidity currents was situated above the levee-crest and free to spread lateral onto the channel margins. The deposition from this highly stratified interval of the flow is the primary cause for the rapid growth in levee taper.

Using our observations from the laboratory experiment we developed a levee growth model based on an advection settling scheme coupled to a sediment concentration profile defined by the Rouse equation. We found that a reasonable set of flow conditions produced a levee taper growth history that is similar to the observed trend measured from offshore Brunei. In the model a roll-over to a lower growth rate for levee taper occurred following the lateral confinement of the highly stratified core flow by the thick channel-bounding levees.

The observations from offshore Brunei, our laboratory experiment and our levee growth model place useful quantitative constraints on the role of current thickness, sediment-concentration profiles and confinement on the morphology of channel-bounding levees in submarine landscapes. This information can be used to estimate the thickness of channel forming turbidity currents in regions where the tapers of levees at several stages of channel growth can be measured. We propose that a measured roll-over in a plot of levee taper vs. channel relief is the result of progressive confinement and that $0.2H < R_{ro} < 0.4H$. The ability to estimate a characteristic thickness or height for turbidity currents associated with construction of a modern or ancient channel network will aid both forward and inverse modeling of submarine channel evolution. Further study is required to refine this estimate of current thickness from levee taper, as well as to define the dynamics of levee growth in net erosional systems and to characterize how alternating between erosional and depositional conditions affects levee morphodynamics.

ACKKNOWLEGEMENTS

We thank Brunei Shell Petroleum for permission to publish seismic data from offshore Brunei Darussalam. Support for our research was provided by Shell International Exploration and Production Inc. and by the STC Program of the National Science Foundation via the National Center for Earth-Surface Dynamics under Agreement Number EAR-0120914. Carlos Pirmez and the Shell Turbidite Research Group provided valuable help and stimulating discussions in the early stages of the project.

NOMENCLATURE

b	channel width
C_f	friction coefficient
C_a	reference concentration
CV	Coefficient of Variation
Fr	Froude Number
g	gravitational acceleration
H	thickness of flow
k	von Karmens constant
p	Rouse number
R	channel relief
R_m	Maximum channel relief
Re	Reynolds number
t	time
U_x	down channel velocity
U_y	across channel velocity
\bar{u}	depth averaged velocity
u^*	shear velocity
w_s	particle settling velocity
z_a	reference elevation
ρ_a	ambient fluid density
ρ_c	current density
τ_b	bottom shear stress
η	bed elevation
ν	kinematic viscosity

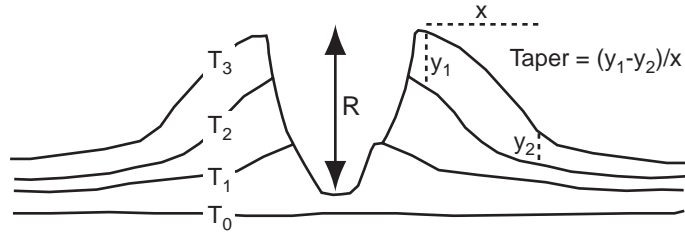


Figure 2.1. Definition sketch for the geometry of a levee.

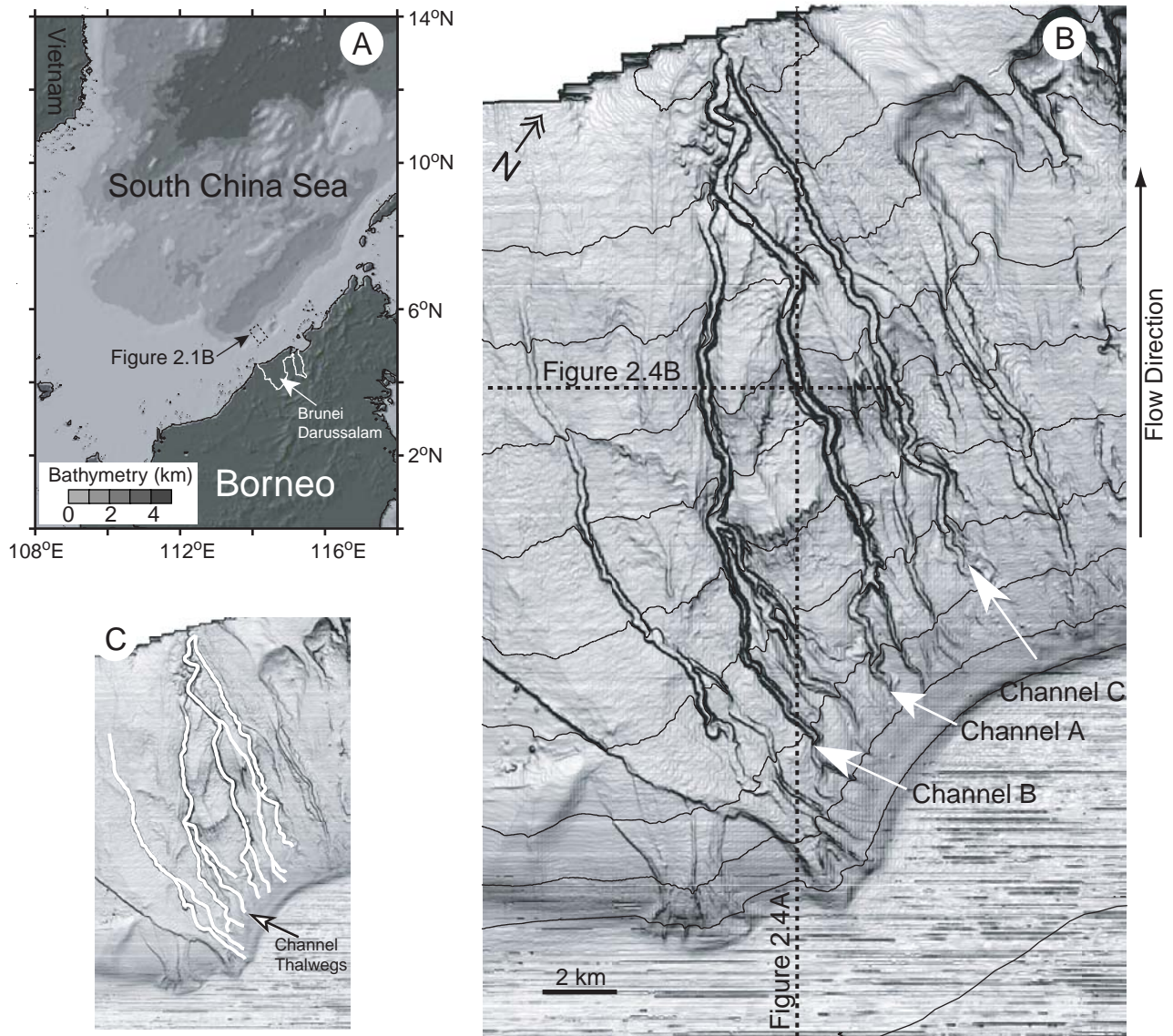


Figure 2.2. Maps of South China Sea and the study region. A) Regional bathymetry map for the South China Sea with location of study region offshore Brunei defined by dashed box. B) Slope map of study region highlighting the network of leaved submarine channels. This and other slope maps presented here were created by calculating the average absolute value for the local surface slope based on the surface elevations at each data bin and its eight immediate neighbors. High values of surface slope defining channel walls and detachment scarps have high gray-scale intensities (appear dark colored). Contour lines defining 100 m bathymetric intervals are superimposed on the dip map. Locations for seismic sections in Figure 4 are represented by dashed lines. Arrows and labels identify channels A, B, and C.

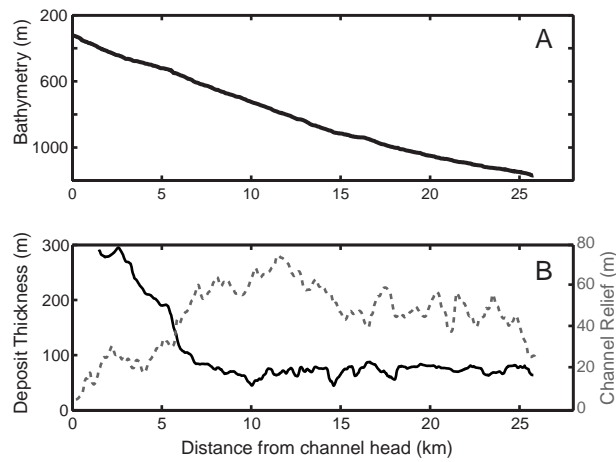


Figure 2.3. Downstream trends for Channel A thalweg. A) Profile of channel thalweg bathymetry following channel centerline as a function of distance from channel head. B) Channel relief and in-channel sediment thickness measured for interval between seafloor and mapped detachment surface as a function of distance from channel head.

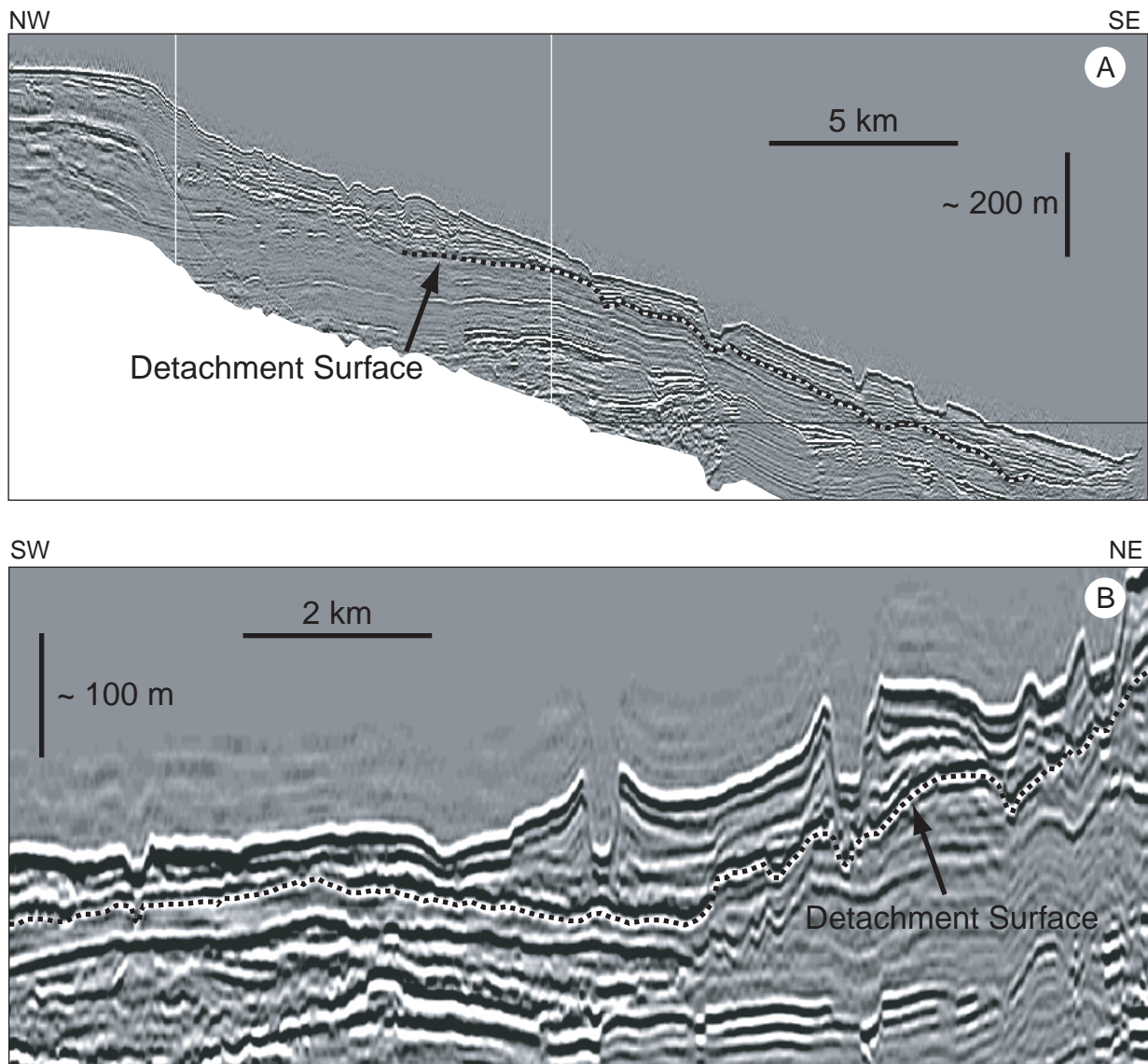


Figure 2.4. Characteristic dip and strike oriented seismic lines for study region showing a portion of the regional stratigraphy from the seafloor to below the area of interest in this study. Dashed lines follow subsurface detachment horizon created by mass-failure release which reset margin to an unchannelized state. A) Characteristic dip section spanning upper continental slope from present day continental shelf to 1200 m of water depth. B) Characteristic strike section. Section intersects two prominent channels at close to perpendicular angles to channel centerlines. Velocity increases with depth so vertical scale is an approximate vertical average for the section

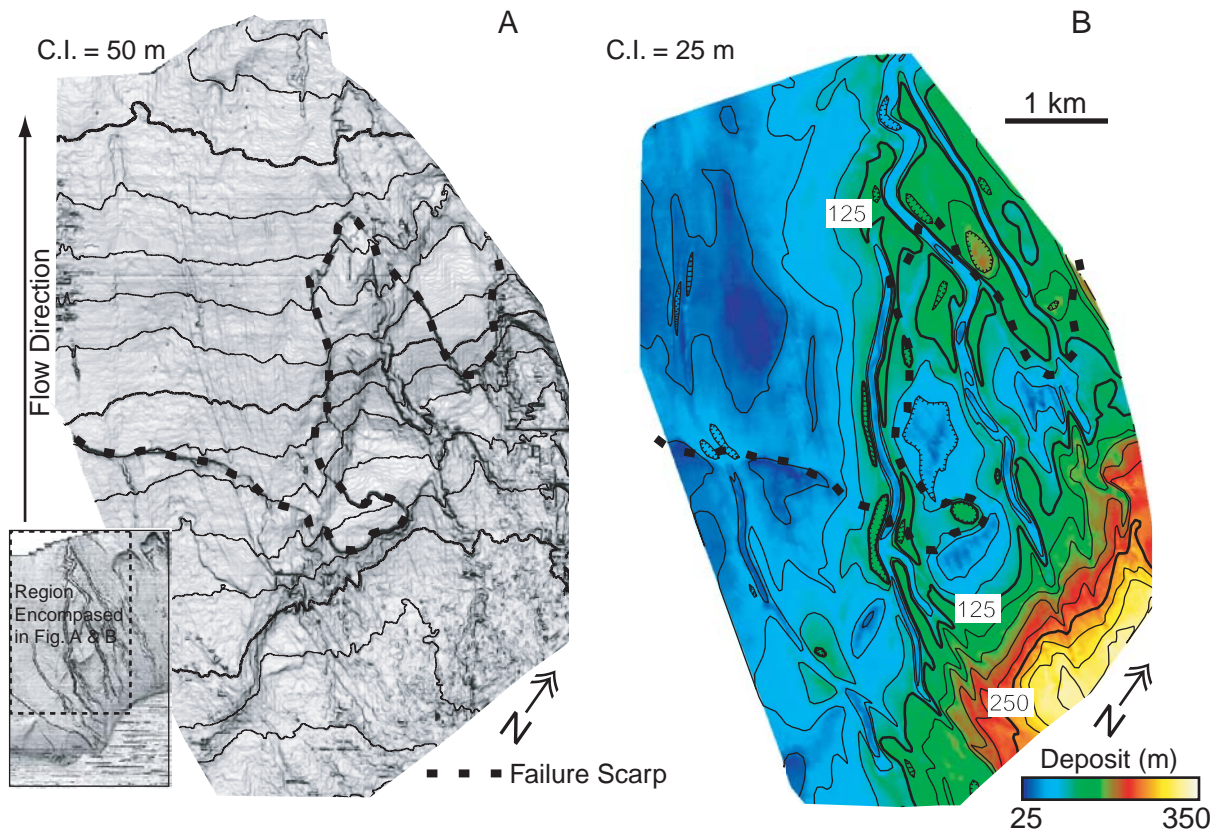


Figure 2.5. Maps of mapped subsurface seismic horizon and deposit thickness measured between seafloor and subsurface horizon. Dashed lines mark location of failure scarp. Insert delineates boundaries of two maps. A) Slope map of regionally mapped subsurface horizon. Horizon defines scarp and slide plane associated with release of mass-failure. Contours define depth below present day sea level. Contour interval is 50 m. B) Deposit thickness measured between seafloor and regionally mapped subsurface horizon. Contour interval is 25 m.

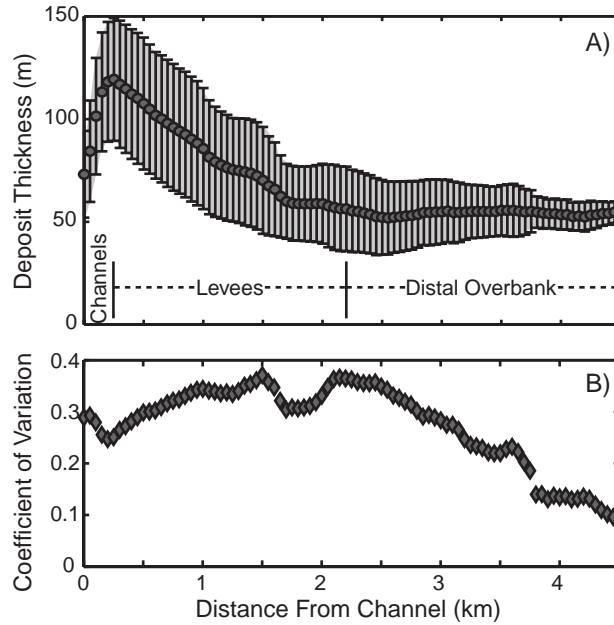


Figure 2.6. Change in deposit thickness as a function of shortest distance to a channel thalweg. A) Mean thickness of deposit measured in bins spaced every 25 m from closest channel thalweg. Error bars represent +/- one standard deviation of data in each bin. B) Coefficient of variation for deposit thickness sample bins.

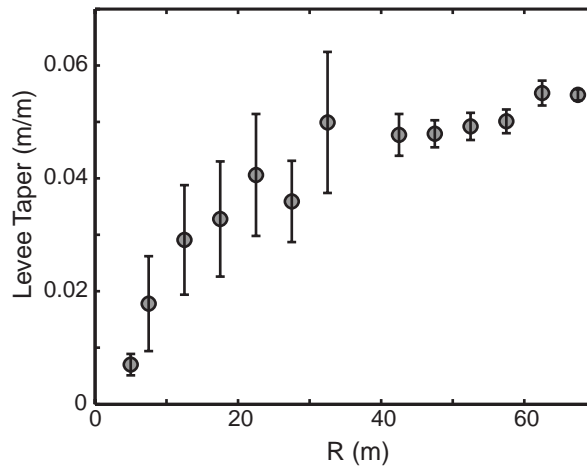


Figure 2.7. Change in the levee-deposit taper as a function of channel relief. Levee taper was defined from linear regression best-fit lines through plots of average cumulative deposit thickness vs. distance from channel. Taper was measured over a distance equivalent to two channel-widths for each value of channel relief. Error bars are plus and minus one standard deviation measured from variability in data defining deposit thickness vs. distance from channel plots for each bin of channel relief.

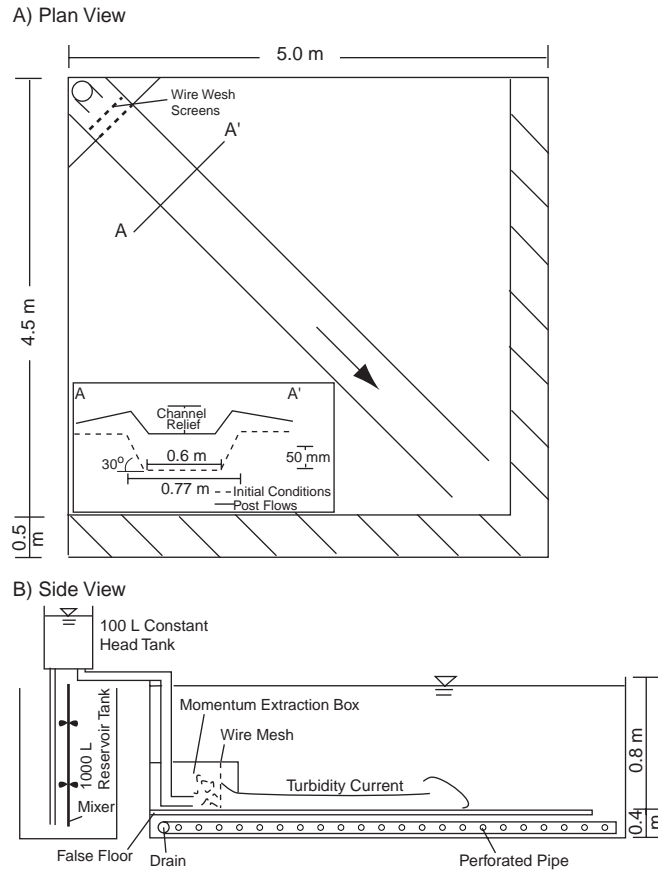


Figure 2.8. Schematic diagram of the experimental facility. A) Planview of the basin and the initial channel form. Each current passed through a momentum extraction box located in the top left basin corner prior to entering the channel. Diagonal lines mark the position of a moat for collecting a current following its passage through the channel avoiding reflections off of tank walls. The insert figure depicts an initial and final channel cross-section. B) Side view of the facility. Each current is mixed in a reservoir tank and pumped up into a constant head tank before entering the basin.

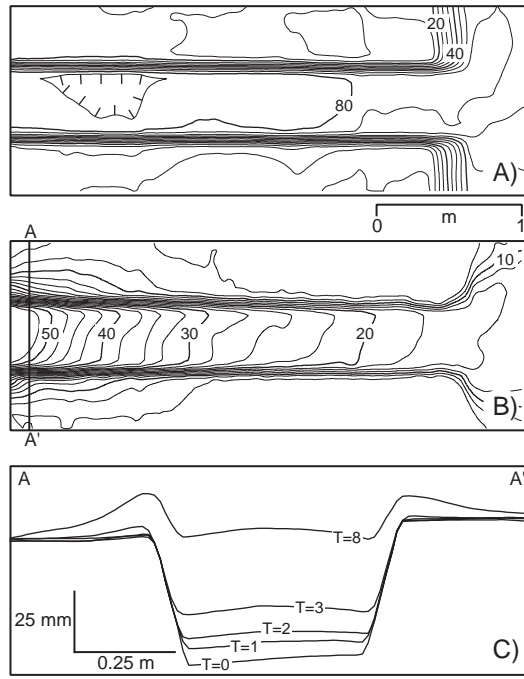


Figure 2.9. Maps and cross-section from the experimental channel. Channel flow was from the left to the right in each map. A: Topographic map of the initial channel form. Topography is defined as vertical distance between the bed and an overlying datum of constant elevation. Contour interval is 5 mm. B: Map of deposit thickness from sedimentation by 8 turbidity currents. This map is the difference between the initial channel form and the channel form following flow event 8. Contour interval equals 2.5 mm. C) Evolution of channel cross-sections located 0.35 m from channel entrance. Figure displays the original channel form plus successive forms following sedimentation by flows 1, 2, 3, and 8. Cross sections are oriented perpendicular to channel direction and oriented looking downstream.

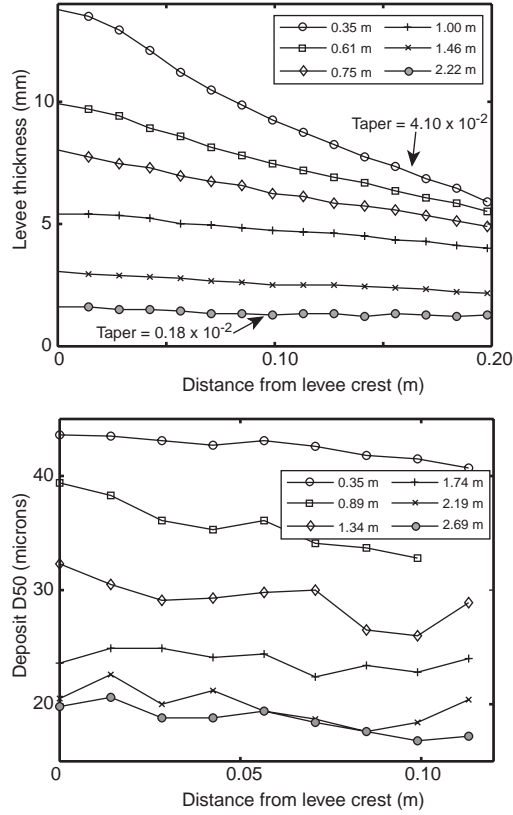


Figure 2.10. Cross-sectional profiles of the depositional levee at 6 different locations down the channel. A) Levee thickness and taper decrease with increasing distance from the channel entrance. B) D50 of levee deposit decrease with distance from channel entrance, but rate of D50 decrease with distance from levee crest changes negligibly with distance from channel entrance.

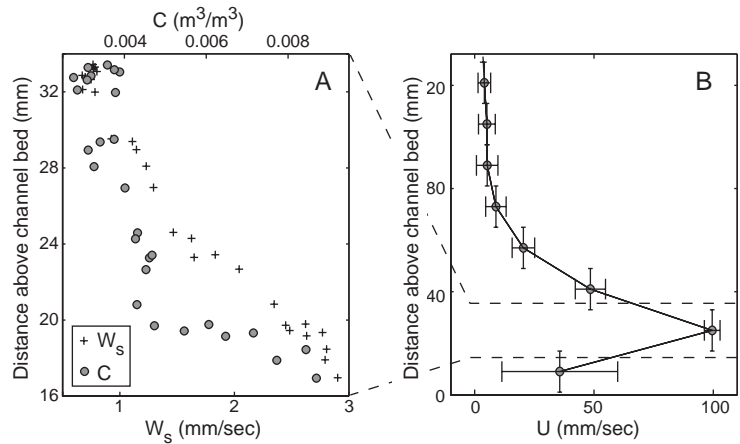


Figure 2.11. Vertical profiles of turbidity current properties. A) Estimated profiles of concentration and suspended particle settling velocity calculated from deposit properties of levee-crest and elevation difference between levee-crest and channel centerline. B) Profile of downstream velocity measured 0.5 m from channel entrance. Vertical error bars define the extent of each sampling volume while the horizontal error bars are plus and minus one standard deviation calculated using all values for current velocity collected in each sampling volume.

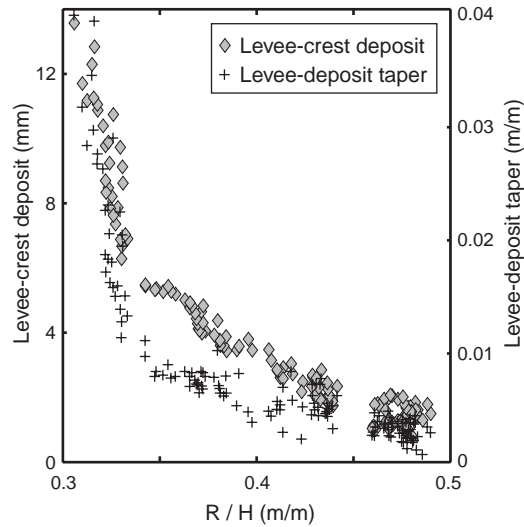


Figure 2.12. Comparison of change in both levee-crest deposit thickness and levee-deposit taper as a function of the ratio of local channel relief to current thickness.

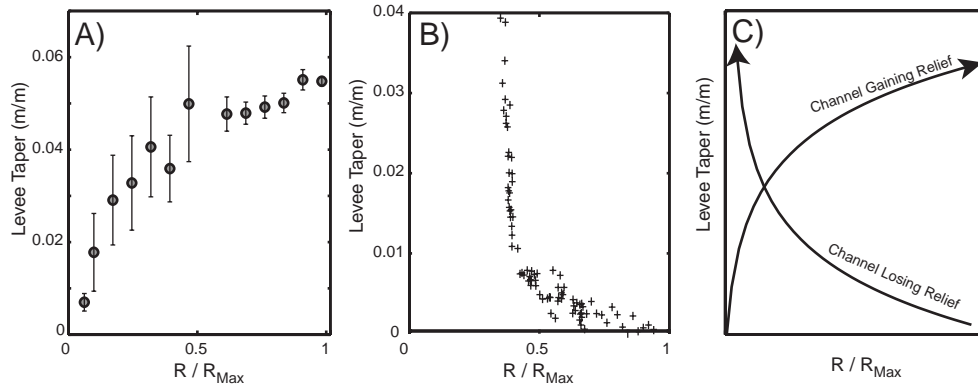


Figure 2.13. Evolution of levee tapers as a function of local channel relief divided by maximum channel relief for a give channel system. A) Levee tapers measured for channel network offshore Brunei. B) Levee tapers measured for laboratory experiment following flow 8. C) Schematic diagram illustrating channel in levee taper for channel systems that gain relief through time and channel systems that loss relief through time.

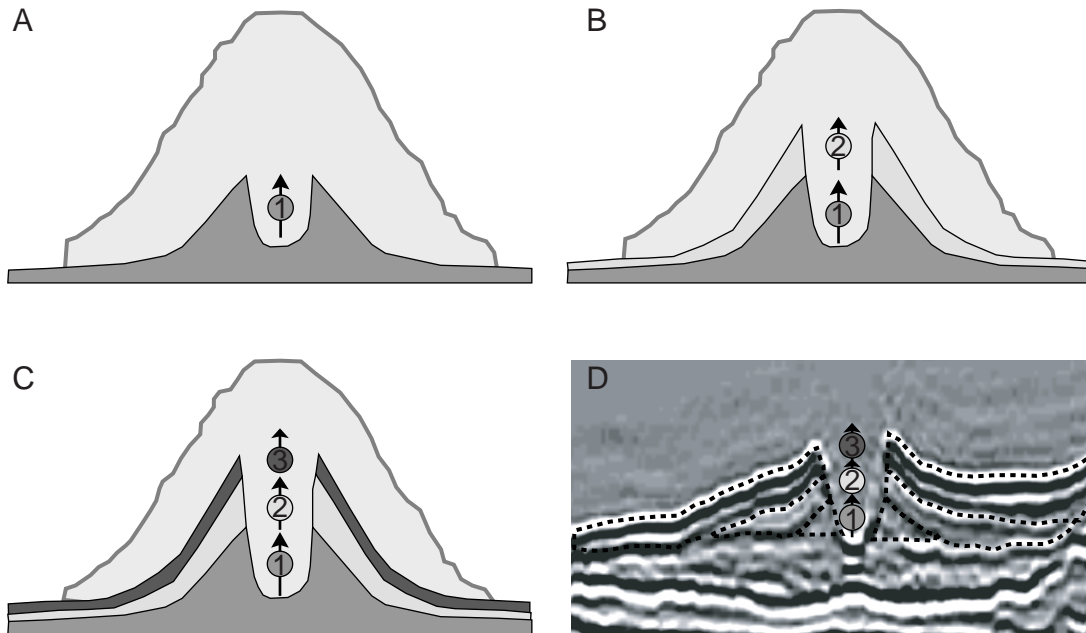


Figure 2.14. Schematic diagrams illustrating levee morphology evolution under aggradational conditions for by-pass turbidity currents. A) Initial channel formation and growth is associated with rapid increases in bulk levee taper. B) As channel relief increases due to levee deposition, taper of individual turbidite deposits decreases. C) As channel relief approaches current height, only fine grained well mixed upper portion of turbidity current is able to spread onto overbank surface. This results in levee deposits with low tapers. D) Seismic cross-section oriented perpendicular to axis of channel B offshore Brunei. Seismic stratigraphy is similar to progression suggested in panels A - C.

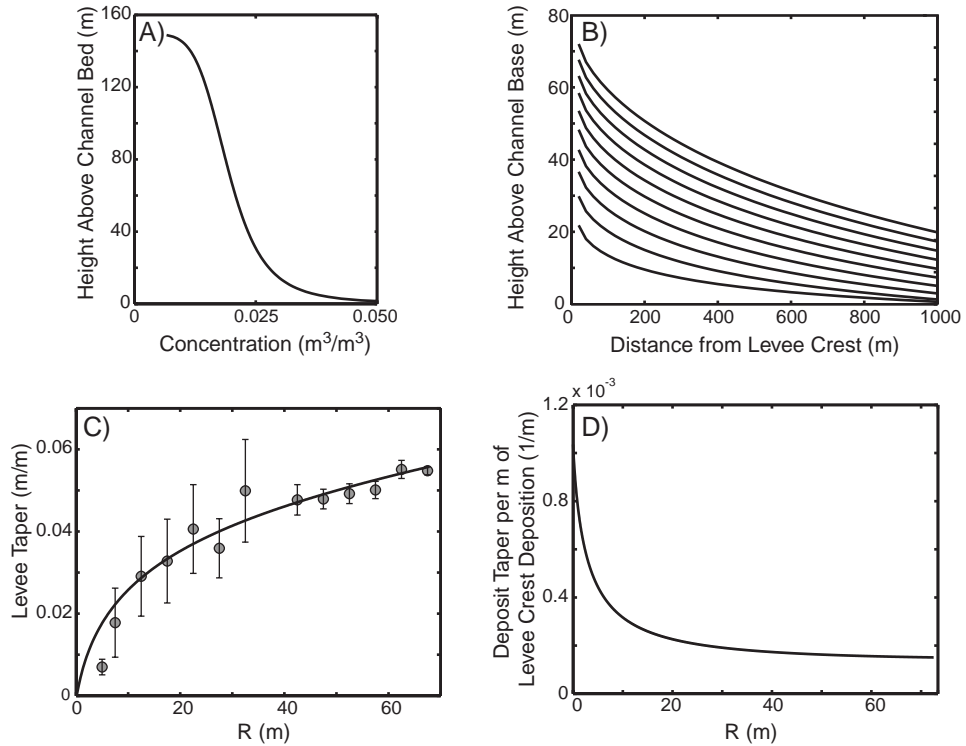


Figure 2.15. Results from levee growth model using input parameters detailed in Table 2.2. A) Cumulative vertical suspended sediment concentration profile for the 10 particle diameters. B) Evolution of levee topography at 10 equally spaced time steps. C) Comparison of model and Brunei levee taper as a function channel relief. Error bars are plus and minus one standard deviation measured from variability in data defining deposit thickness vs. distance from channel plots for each bin of channel relief. D) Change in model deposit taper per meter of levee crest deposition as a function of channel relief.

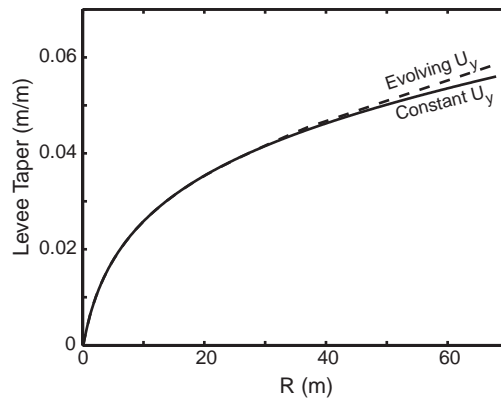


Figure 2.16. Comparison of levee taper growth as a function of channel relief for constant U_y model and temporally evolving U_y model.

Current	U(mm/sec)	Flow Duration (sec)	Fr	Re	B_{10} (m^4/sec^3)
1	50	576	0.34	4.5×10^3	7.08×10^{-4}
2	60	576	0.41	5.4×10^3	8.50×10^{-4}
3	55	504	0.37	5.0×10^3	7.79×10^{-4}
4	55	504	0.37	5.0×10^3	7.79×10^{-4}
5	50	504	0.34	4.5×10^3	7.08×10^{-4}
6	70	320	0.47	6.3×10^3	9.91×10^{-4}
7	110	245	0.74	9.9×10^3	15.6×10^{-4}
8	70	320	0.47	6.3×10^3	9.91×10^{-4}
9	120	248	0.81	11×10^3	17.0×10^{-4}

Table 2.1. Experimental flow conditions

U_x (m/sec)	3.4
H (m)	156
C_a	0.05
Particle Size 1 (μm)	86
Particle Size 2 (μm)	93
Particle Size 3 (μm)	96
Particle Size 4 (μm)	102
Particle Size 5 (μm)	112
Particle Size 6 (μm)	153
Particle Size 7 (μm)	211
Particle Size 8 (μm)	241
Particle Size 9 (μm)	265
Particle Size 10 (μm)	291
Fr	0.57

Table 2.2. Best fit model parameters for data fit presented in Figure 2.15

Chapter 3

Addendum to chapter 2: Architecture of a tributary channel network on the Champion Delta slope offshore Brunei Darussalam

Kyle M. Straub^a, David Mohrig^b & Carlos Pirmez^c

^aDepartment of Earth, Atmosphere, and Planetary Sciences, Massachusetts Institute of Technology, 77 Massachusetts Avenue, Building 54-824, Cambridge, MA 02139

^bDepartment of Geological Sciences, The University of Texas at Austin, Austin, TX 78712

^cShell International Exploration and Production, Inc., P.O. Box 481, Houston, TX 77001

3.1. INTRODUCTION

In chapter 2, I used laboratory experiments and a simple numerical model to interpret the evolution of submarine levees on the Champion Delta slope offshore Brunei Darussalam. Submarine channels analyzed in chapter 2 form a tributary network with no direct connection of to terrestrial channels. Few examples of tributary submarine channel networks disconnected from terrestrial channels exist in the literature. In this chapter, I use an industry-grade three dimensional (3-D) seismic volume to characterize the present morphology of this channel network and to characterize Quaternary depositional and erosional processes on this margin. These observations and measurements are used to pose several questions for future scientific study.

Technological advances over the last 25 years in acoustical sonar systems have revealed ubiquitous submarine channels on continental slopes (Damuth et al., 1983; Kenyon et al., 1995; Posamentier and Kolla, 2003). The majority of these channels initiate at the continental shelf edge as canyons that can have relief exceeding 400 m (Greene et al., 2002; Pirmez and Imran, 2003). Downslope of the canyon head, many channels branch and form distributary networks (Twitchell et al., 1995). Submarine canyons and distributary channel networks dominate studies of submarine channel types because they are conduits for coarse sediment that forms many large hydrocarbon reservoirs (Clemenceau et al., 2000; Deptuck et al., 2003). These channels are constructed by turbidity currents, defined as sediment gravity flows in which the gravitational driving

force is supplied by a suspension of particles supported by fluid turbulence. Channels are important elements to the construction of deep-sea fans because they act to laterally confine turbidity currents. This processes has been hypothesized to increase turbidity current runout length (Bouma et al., 1985) and reduce proximal fan deposition rates (Pirmez et al., 1997). Data characterizing this process, though, has yet to be quantified in a natural system.

Unlike frequently studied submarine channel types, the continental slope offshore Brunei Darussalam contains a tributary network of channels that do not currently connect to terrestrial channels. This network is located on the continental slope, downdip of the Champion delta front (Figure 3.1). This network configuration provides a natural system where channel relief can be compared to local and regional deposit thickness trends, allowing the relationship between these two variables to be quantified. Depositional and erosional processes on the Brunei margin also result in stratigraphy and seafloor morphology allowing the following questions to be addressed: 1) How do submarine channels initiate, and is there a relationship between channel head dimensions and channel-forming flow conditions; and 2) How do submarine channels interact with mass-wasting processes on a continental margin.

Channel initiation under net depositional conditions has been studied using reduced scale laboratory experiments and numerical models (Imran et al., 1998; Yu et al., 2006). In these studies, channel growth resulted from higher channel-margin deposition relative to deposition rates in the channel thalweg. The small absolute size of channels in the laboratory study of Yu et al. (2006) resulted in limited sampling of relationships between channel relief, flow conditions, and deposit thickness trends. These relationships were also not quantified in the numerical modeling study of Imran et al. (1998) due to problems with model boundary conditions that limited the study to channel initiation conditions.

3.2. CHAMPION DELTA – OFFSHORE BRUNEI DARUSSALAM

The present-day continental margin offshore Brunei Darussalam has been a passive margin since the late Miocene (Hiscott, 2001; Hutchison, 2004). Since subduction of the South China Sea Plate ceased in the late Miocene, the continental slope in our study region has primarily been altered by shale diapirism, release of mass-failure events, and deposition

from turbidity currents. Sediment is delivered to the continental shelf by three major rivers: the Baram, Belait, and Tutong rivers (Sandal, 1996). Sediment delivered by these rivers built a continental margin that is 50-70 km wide and underlain by 8-9 km of post Eocene siliclastic sediment (Hiscott, 2001). These sediments are derived from uplifted rocks of the Rajang-Crocker ranges in Central Borneo. Erosion rates measured in these ranges are amongst the highest in the world and have resulted in high sediment discharge rates to the South China Sea since the Eocene (Hutchison, 2004; Sandal, 1996). Offshore Brunei, the continental shelf-slope break occurs at a water-depth of ~200 m. The seabed then descends steeply to the floor of the Borneo Trough at 2800 m of water depth.

3.3. SEISMIC DATA SET PARAMETERS

A large industry-grade 3-D seismic volume, located on the continental slope offshore Brunei covers an area of 4000 km² (40 x 100 km²). Our study focuses on a smaller subset of the 3-D seismic survey covering an area of 555 km² which encompasses a tributary network of channels. In this study we focused on the top 0.4 seconds of two-way travel-time beneath the seafloor. For this portion of the 3-D data volume, the frequency roll-off is near 80 Hz (approximately a 3 m vertical resolution) and the horizontal bin spacing is 25 x 25 m². The seismic survey encompasses a channel network positioned directly down slope of the Champion Delta shelf-edge, which is approximately 6 km by 24 km in the strike and dip directions, respectively. Present-day water depths increase from approximately 250 m to 1200 m moving from the proximal to distal end of the network, respectively.

3.4. PRESENT-DAY CHANNEL NETWORK ARCHITECTURE

The present-day seafloor in our study area was mapped manually from each in-line of the 3-D industry seismic volume. Due to the regional slope of the continental margin, we visualize planform attributes of the channel network through maps of local slope. These maps are created by calculation of the average absolute local slope for each data bin and its 8 immediate neighbors (Fig. 3.1b). The present-day margin is characterized by several mass-failure scarps, shale-diapirs, and low sinuosity submarine channels. A swath profile of topography quantifies the mean topographical trend of the margin. This swath profile is constructed using measurements of bathymetry and shortest path length to shelf-edge

(defined as 280 m contour) calculated for each map grid node. The mean topography measured in 25 m bins from the shelf-edge define the swath profile. This swath profile is shown as Fig. 3.2A and a plot of the surface gradient along this profile is shown as Fig. 3.2B. Downslope gradient is calculated at each node using the elevation of the immediate upslope and downslope neighboring bins. The plot of swath surface gradient reveals a rapid increase in the gradient of the margin immediately downslope of the shelf-slope transition to 0.14 m/m. Surface gradient rapidly decreases with increasing downslope distance to a quasi-steady value of ~ 0.06 m/m.

In our study area we focus on 10 channels that begin 1-2 km down-slope of the shelf-edge. The four western most channels merge 7 km from the shelf-edge and the resulting channel continues down slope for another 10 km before channel relief rapidly diminishes to 0 m. The 6 eastern channels merge into 3 major channels approximately 10 km down slope of the shelf-edge. 27 km down slope of the shelf-edge these three channels merge into 1 channel. All 10 channels rapidly increase in channel relief from 0 m to an average relief of 40 m approximately 7 km down slope of the shelf-edge. Down slope of this rapid rise in channel relief, the 3 major trunk channels approach a constant relief for the remainder of their lengths. A plot of channel thalweg vertical profiles is presented as Figure 3.3. In this figure, profiles are aligned with distance from the distal most channel confluence in the network. Unlike many confluences in terrestrial tributary channel networks (Crosby and Whipple, 2006), gradients of low order streams at channel confluences are approximately equal to trunk channels. This pattern might suggest that multiple submarine channels are not active with any one flow event. In terrestrial channels, the decrease in stream slope observed downslope of channel confluences is often attributed to an increase in stream power associated with an increase in stream discharge (Whipple and Tucker, 1999). If only one channel is active during a flow event an increase in stream discharge would not occur at channel confluences. A second plausible explanation for the quasi-equal channel slopes upslope and downslope of confluences is that channel forming turbidity currents are not sufficiently powerful to alter the slope of the continental slope. This would result in channels that aggrade but do not affect the large scale topographical signature of the margin.

3.5. RECENT DEPOSITION AND EROSION PATTERNS

Using the 3-D seismic volume, we mapped two shallow (<0.4 sec TWT below seafloor) regional surfaces. These seismic horizons (CD1 and CD2) were selected because they have strong reflection amplitudes and are only cross-cut by local erosion in small patches (Fig. 3.4). These characteristics allow us to track the surfaces beneath the majority of the area encompassed by the 10 channels in the study region. Slope maps of these two surfaces are presented in figure 3.5. Maps of interpreted seismic horizons represent approximate paleo-bathymetry maps. Biostratigraphic dating from fossils preserved in petroleum exploration wells located 60 km to the southwest of the study region suggest that both mapped horizons are of Quaternary age (Hiscott, 2001). Both slope maps lack significant topographic signatures of channels. The prominent feature on both maps are failure scarps. On surface CD2 a failure scarp with 70-90 m of relief is oriented roughly north-south. On surface CD1 a failure scarp has 30-50 m of relief and has a significant degree of variability in planform orientation. Down slope of the failure scarp, several long linear striations exist which were likely formed during release of mass-failure events. Deposition of material released during these mass-failure events was not found in the study seismic volume. The region of the continental slope affected by the two mapped mass-failure scarps exceeds 40 km² per event. The identification of these large subsurface palaeo-failure scarps indicate that the continental slope morphology was influenced by frequent mass-failure releases during the Quaternary. The relative influence of mass-failures, turbidity currents and regional structures in setting the slope of the margin remain unknown.

Following the mass-failure release associated with the scarp present on surface C1, the continental slope down dip of the Champion delta has been a site of net deposition. A map of recent deposit thickness is shown in figure 3.6. This map was created by differencing the seafloor and subsurface horizon CD1. This map was converted from two-way travel time to thickness using a seismic velocity for the first 300 m below seafloor of 1700 m/sec. This seismic velocity was measured for the first 300 m beneath the seafloor, 60 km to the southwest of our study region (van Rensbergen et al., 1999). Several observations were made from the map of recent deposition. The first-order control on deposit thickness appears to be distance from the shelf-edge, with deposition decreasing with down slope distance. This suggests this region of the Borneo margin is currently

undergoing progradation. Deposition appears to be influenced by locally high surface gradients, associated with the subsurface mass-failure scarps. Relative local lows in deposition are present up slope of the scarp while local deposition highs are present down slope of the scarp.

Deposition occurring on an initially unchannelized surface allows for the quantification of correlations between channel deposit thickness, channel gradient, channel relief, and distance from the shelf-edge. A complete understanding of the interdependence of these parameters and their relation to the evolution of submarine channels is still unrealized. Long profiles of channel thalweg bathymetry, down-channel gradient, channel relief, and deposit thickness for channels A-C are presented in figures 3.7-3.9. Deposit thickness is measured between the present-day elevation of a channel thalweg and that same horizontal location on map CD1. Deposit thickness values were calculated from two-way travel times using a seismic velocity for the first 300 m below seafloor of 1700 m/sec. All three channel profiles show a rapid increase of channel relief from 0 to 5-7 km from their respective channel heads. This rapid increase in channel relief is spatially correlated with a rapid decrease of in-channel deposit thickness for all three channels. The negative correlation between deposit thickness and channel relief suggest that sediment transport capacity increases for channel forming turbidity currents as channels deepen. This increase in sediment transport capacity is likely linked to an increase in down-channel velocity associated with channel confinement, which reduces lateral current spreading (Mohrig and Buttle, 2007). Downslope of the region of initial increases in channel relief, all three channels reach an approximately constant channel relief for the remainder of the down slope region encompassed in our study area. The correlations between down channel gradient and channel relief are not as strong as the correlation between channel relief and deposit thickness. A weak positive correlation is observed, however, between channel relief and channel gradient. The sign of this correlation is the same as observed terrestrial observations of these two parameters (Church, 2006).

Recent deposit thickness trends on the Brunei Darussalam margin are a function of several factors. In chapter 2, I characterize how deposit thickness varies as a function of distance from a channel. Measurements of channel relief, gradient, and in-channel deposit thickness presented in figures 3.7-3.9 document trends related to channel axis, but do not

characterize controls on bulk deposit volumes relative to channel properties and distance from the shelf-edge. To characterize the control of distance from the shelf-edge on recent deposit thickness trends we performed the following analysis. For each grid node in a map of deposit thickness between surface CD1 and the seafloor (Fig. 3.6) we tracked the deposit thickness at that location and the shortest path length to the shelf-edge, defined as the 280 m contour of bathymetry. This data is sorted and binned by distance from the shelf-edge. Bin widths were equal to 200 m. We perform this analysis in the region contained within the channel basin boundary outlined in figure 3.1B. This boundary is defined as the margin delineating topographic area with a path of steepest descent that follows a route passing through the distal most confluence in the network of study. We choose this region to perform our analysis so that comparisons of deposit thickness to channel relief can be performed over regions of equal channelization. The mean deposit thickness vs. distance from shelf-edge for this region is presented in figure 3.10a. Mean deposit thickness decreases rapidly between 4-8 km from the shelf-edge and then approaches a near constant value of 80 m between 7-19 km from the shelf-edge. The observation of quasi-steady deposit thickness with distance from the shelf-edge is surprising. This distance from the shelf-edge spans a region of channel network confluences. This suggests that the decrease in total number of channels associated with increasing distance from the shelf-edge does not decrease the mean sediment deposition with distance from the shelf-edge.

Mean channel relief as a function of distance from the shelf-edge was calculated in a manner analogous to the method used to calculate mean deposit thickness. Channel depth was measured at 1921 channel cross-sections. Channel depth is defined as the difference in bathymetry between the channel thalweg and the average bathymetry of channel bounding levee crests. Shortest path length to shelf-edge was calculated for each channel cross-section. This data was used to calculate mean channel relief for 200 m bins of distance from shelf edge (Fig. 3.10B). Mean channel relief increases rapidly between 4-8 km from the shelf-edge and then approaches a near constant value of 45 m between 7-19 km from the shelf-edge.

Trends presented in figure 3.10 suggest that the correlation between deposit thickness and channel relief is stronger than the correlation with distance from the shelf-

edge. A cross-plot of mean deposit thickness vs. mean channel relief, sorted by bins of distance from shelf-edge, shows an apparent linear decrease between 20 – 50 m of channel relief (Fig. 3.11). This trend suggest that increasing the lateral confinement of turbidity currents in channels increases the transport efficiency of turbidity currents. This increase in transport efficiency reduces the volume of sediment deposited on the continental slope for a given distance from the continental shelf-edge.

3.6. CHANNEL INITIATION

Submarine channels on the continental slope offshore Brunei Darussalam do not connect to presently day terrestrial channels. A broad continental shelf, 50-70 km wide separates the present-day shoreline and the shelf-slope transition. Seismic cross-sections of continental shelf strata oriented parallel to the shelf-edge also do not reveal a clear connection of palaeo-shelf-channels connecting terrestrial to submarine channels (Fig. 3.12). If a direct connection of terrestrial systems to continental slope channels did not deliver sediment for channel forming turbidity currents, how was the sediment delivered and how did the submarine channels form? Previous studies of other continental margin submarine channels have lacked a direct terrestrial link. Proposed mechanisms for sediment delivery to these submarine channels include large storms that evacuate sediment stored on broad continental shelves to the continental slope (Puig et al., 2003), and breaching events along the shelf-slope transition (van den Berg et al., 2002). Several observations suggest that submarine channels in our study region formed as a result of sediment deposition from turbidity currents that initiated at the shelf edge, however the exact mechanism for initiation of turbidity currents at this site is still unknown. These observations include channels that all start at a similar distance downslope from the maximum downslope surface gradient (Fig. 3.13). This observation suggests a link between channel initiation and acceleration of currents over the shelf edge. The exact mechanism linking channel initiation and current acceleration over a shelf-edge is still unknown. Finally, channel width and depth measured at 176 channel cross-sections reveal an interesting trend when plotted against each other. Channel width increases with channel depth with a best fit linear slope of 5.5 m/m (Figure 3.14). This best fit trend does not suggest that channel width is zero when channel relief equal zero. The best fit y-intercept for this trend suggests

a minimum channel width of 180 +/- 50 m. Further study is needed to understand what properties control a minimum width for channels. An interesting recent study by Izumi (2004) found a control of submarine channel spacing on current thickness. A similar control on channel width might also exist and presents a future line of study.

3.7. SUMMARY

Mapping of the present-day seafloor morphology and architecture of submarine channel deposits on the continental slope offshore Brunei Darussalam have permitted a reconnaissance study of the formation and evolution of tributary channel networks. The main observations coupled with associated unresolved scientific questions from this study are as follows:

- a) Mapping of the seafloor and shallow subsurface offshore Brunei reveal a tributary network of submarine channels. This network has developed in a setting prone to frequent mass-failure events. Deposit thickness maps reveal that the present-day channel network developed under net depositional conditions spanning the time period following the last major mass-failure event on the margin. The cause of mass-failure events on this margin is still unknown, as is the degree of channelization on the margin prior to this last mass-failure event.
- b) Channel relief and channel thalweg deposit thickness are anti-correlated for the three largest channels in the network. A similar anti-correlation is observed for mean channel relief and mean deposit thickness as a function of distance from the shelf-edge. This observation suggests that sediment transport efficiency increases with increasing channel relief. The exact form of this physical relationship governing this observation cannot be deciphered with only deposit thickness and seafloor morphology trends contained within a 3-D seismic volume, and therefore pose an interesting line of future study.
- c) Submarine channels on the continental slope offshore Brunei Darussalam do not presently connect directly to terrestrial channels. Seismic cross-sections oriented parallel to the shelf-edge also do not reveal palaeo-shelf channels that could have connected submarine and terrestrial systems in sea level lowstands. Channels on

this continental margin initiate downslope of the shelf-edge and also downslope of the maximum observed slope gradients. A collection of channel width and depth measurements suggest that a minimum channel width exist at all channel heads in this system. A complete physical understanding of the channel initiation mechanisms on this margin remains unresolved.

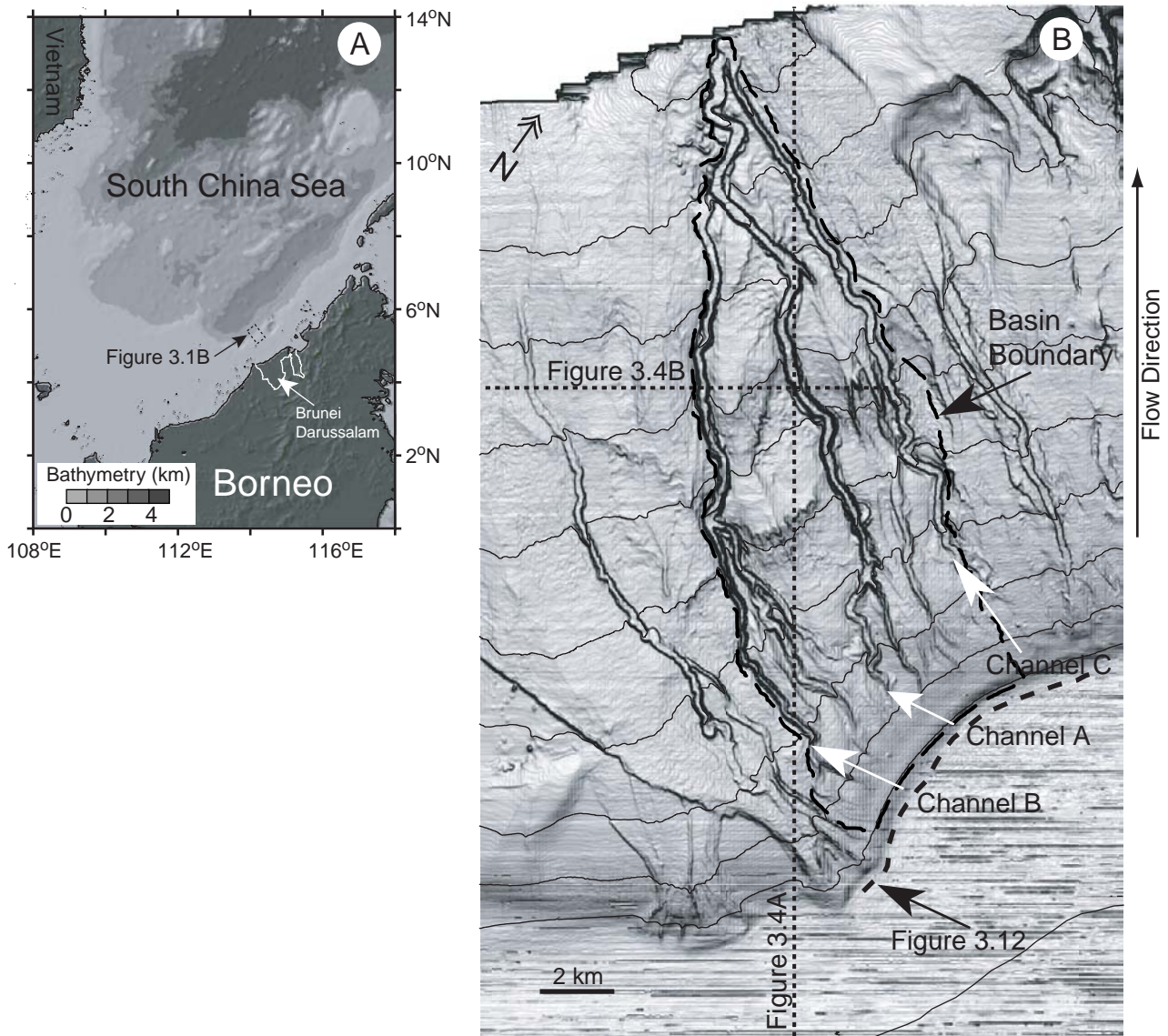


Figure 3.1. Maps of South China Sea and study region. A) Regional bathymetry map of South China Sea with location of study region offshore Brunei Darussalam defined by dashed box. B) Slope map of Brunei Darussalam continental shelf and slope with 100 m contours of bathymetry. Location of seismic cross-sections presented in figures 3.4 and 3.12 are illustrated with dotted lines. Channel network drainage basin boundary is illustrated with dashed line.

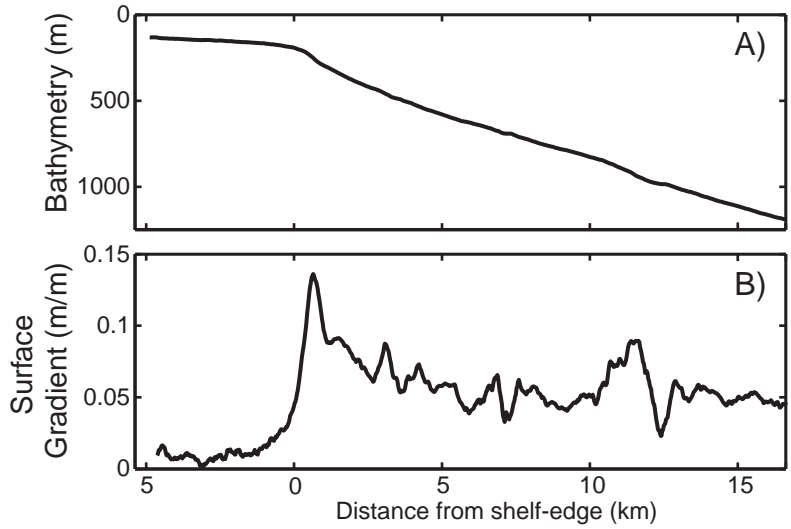


Figure 3.2. Bathymetry (A) and downslope surface gradient (B) swath profiles for region of Brunei continental shelf and slope offshore Champion delta.

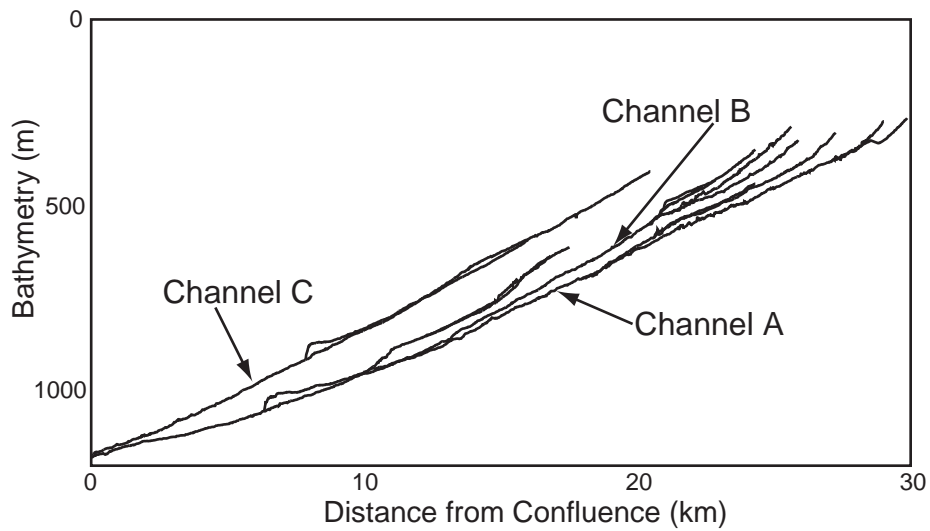


Figure 3.3. Long profiles of the 10 submarine channels that comprise the tributary channel network on the continental slope of the Champion delta. Channel profiles are measured against distance from most distal confluence in network.

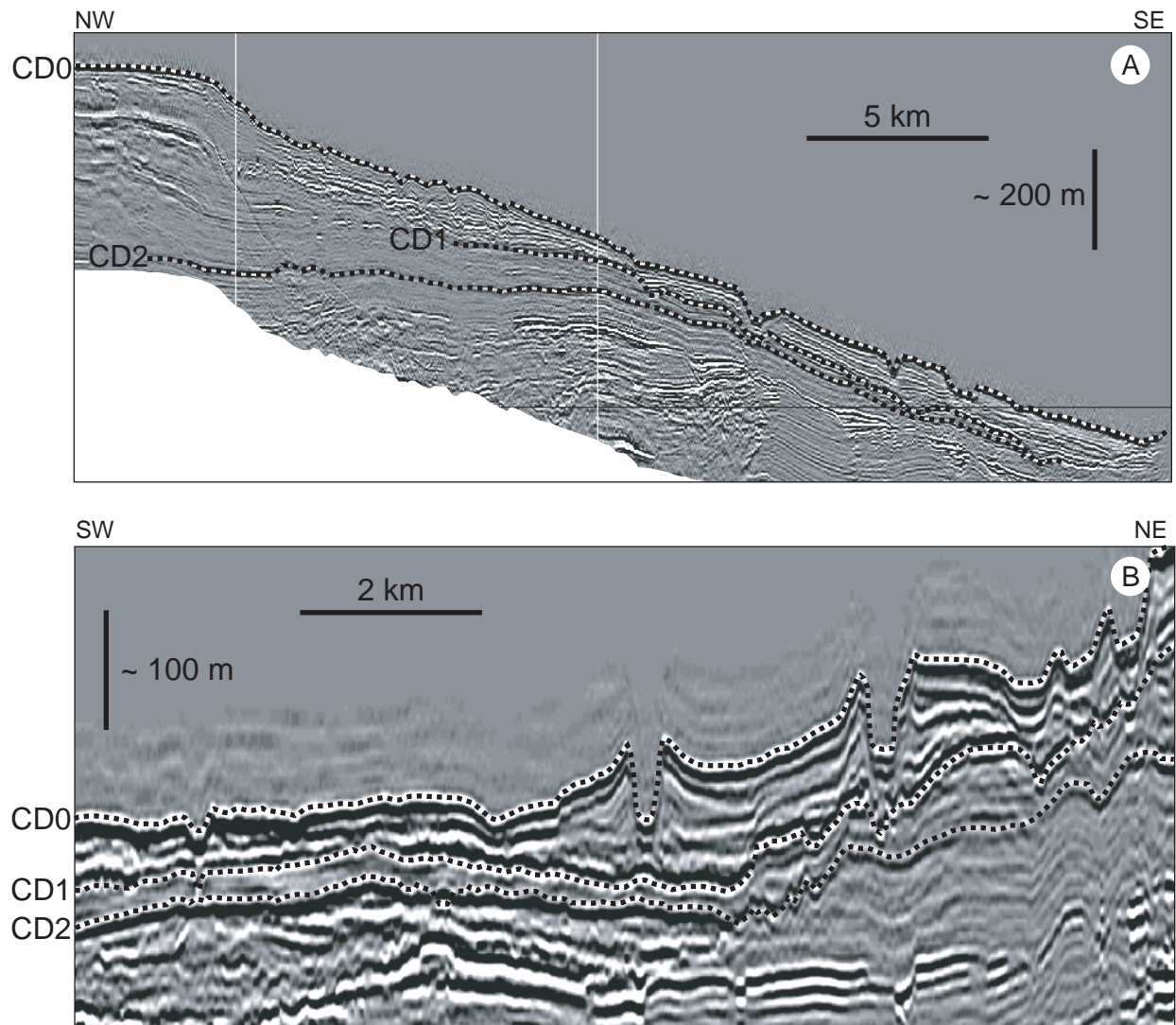


Figure 3.4. Characteristic dip and strike oriented seismic lines for study region showing a portion of the regional stratigraphy from the seafloor to below the area of interest in this study. Dashed lines labeled CD0-CD2 follow surface and subsurface seismic horizons that represent approximate palaeo-seafloor locations. Locations of seismic cross-sections are labeled on figure 3.1B. A) Characteristic dip section spanning upper continental slope from present-day continental slope to 1200 m of water depth. B) Characteristic strike section. Section intersects two prominent channels at close to perpendicular angles to channel centerlines. Velocity increases with depth so vertical scale is an approximate vertical average for the section.

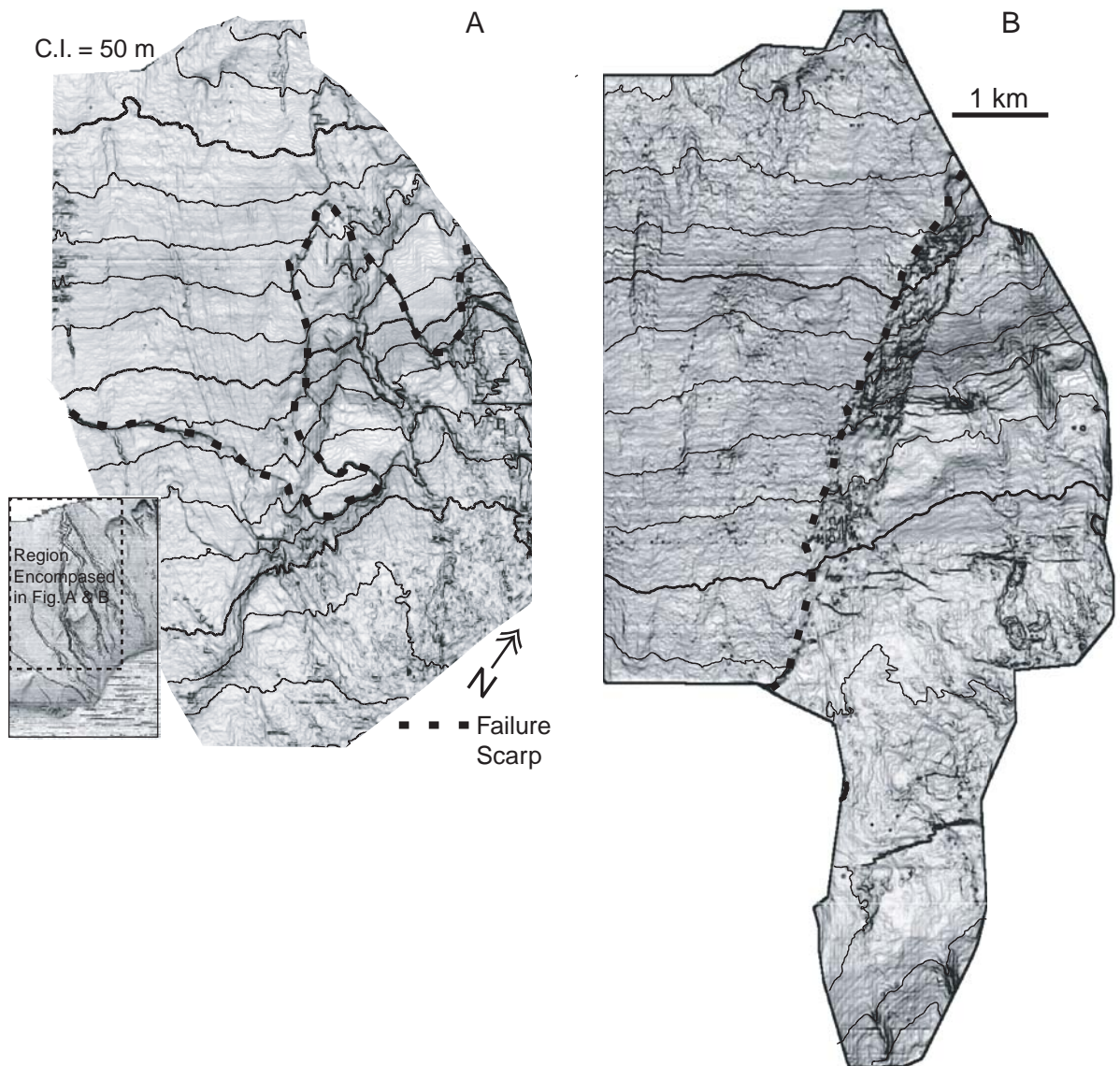


Figure 3.5. Maps of mapped subsurface seismic horizons CD1 (A) and CD2 (B). Dashed lines mark location of failure scarp. Insert delineates boundaries of two maps. A) Slope map of regionally mapped subsurface horizon CD1. Horizon defines scarp and slide plane associated with release of mass-failure. Contours define depth below present-day sea-level. Contour interval is 50 m. B) Slope map of regionally mapped subsurface horizon CD2. Horizon defines scarp and slide plane associated with release of mass-failure. Contours define depth below present-day sea-level. Contour interval is 50 m.

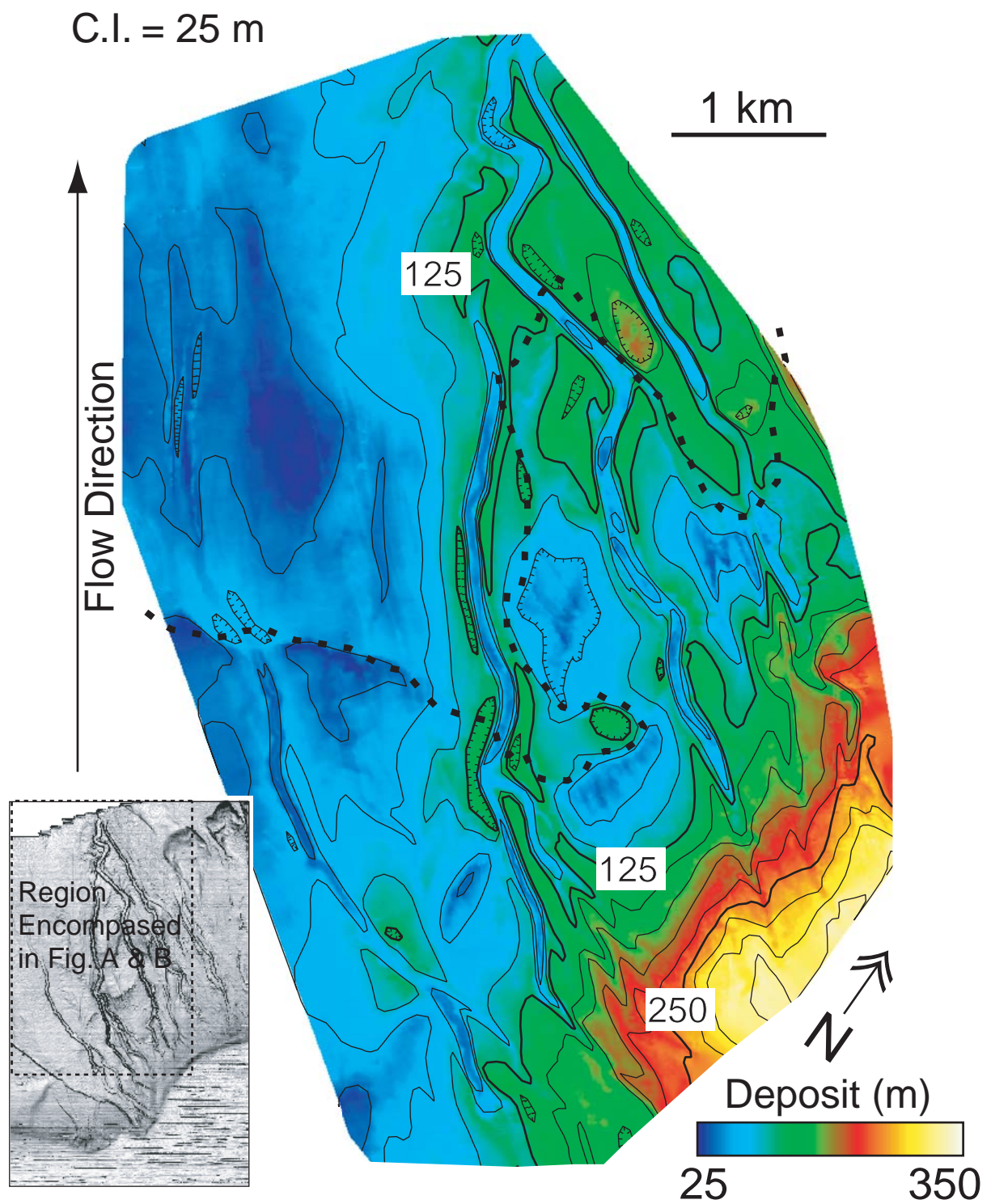


Figure 3.6. Map of deposit thickness measured between seafloor and subsurface horizon CD1. Contour interval is 25 m. Dashed line marks location of failure scarp. Insert delineates boundary of map.

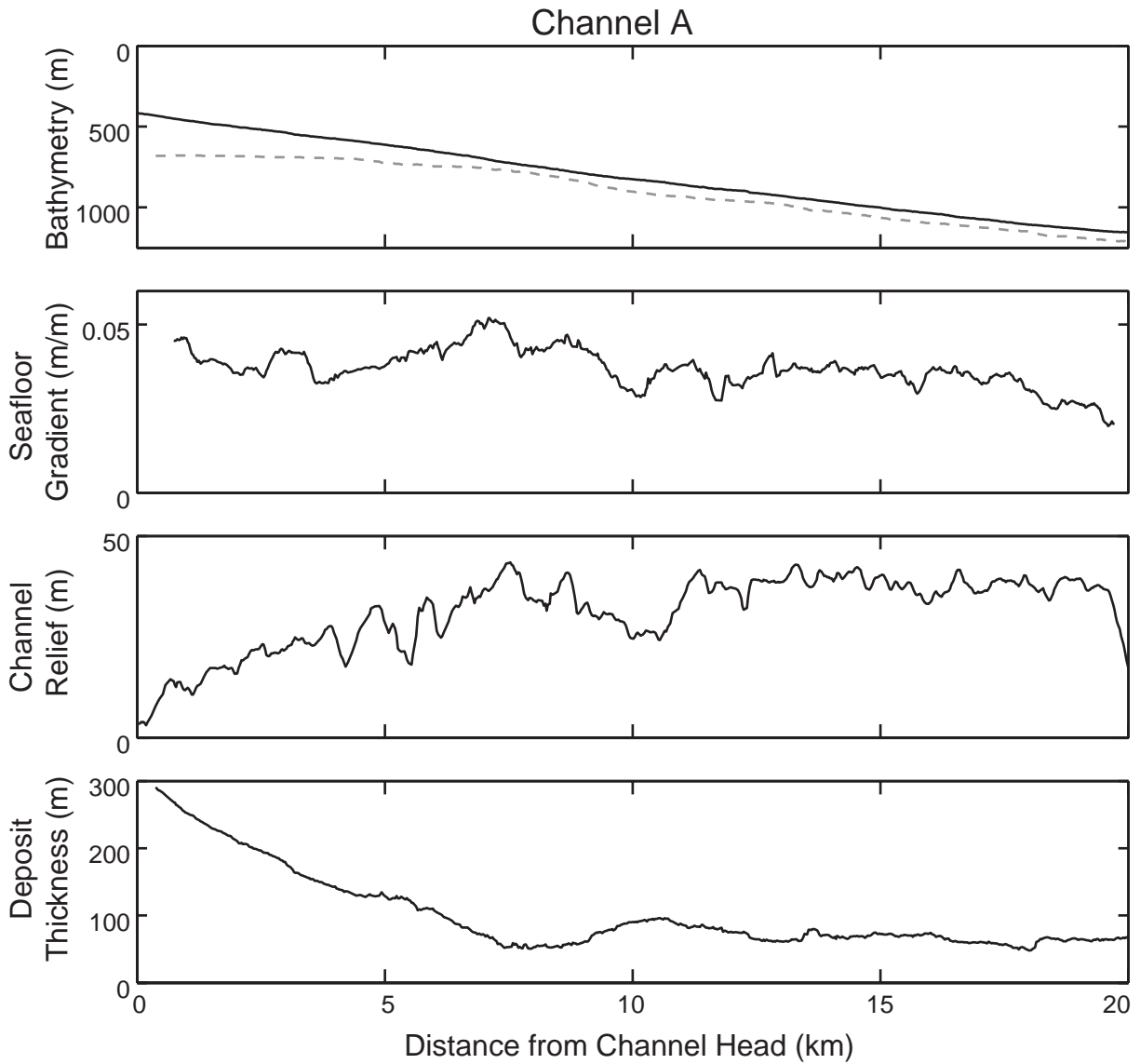


Figure 3.7. Downstream trends for Channel A thalweg. A) Profile of channel thalweg bathymetry following channel centerline as a function of distance from channel head. Dashed line represents bathymetry of surface CD1 below present day channel thalweg. B) Profile of present-day down channel surface gradient. C) Channel relief measured between the channel thalweg and average levee crest bathymetry as a function of distance from channel thalweg. D) In-channel sediment thickness measured for interval between seafloor and mapped subsurface horizon CD1 as a function of distance from channel head.

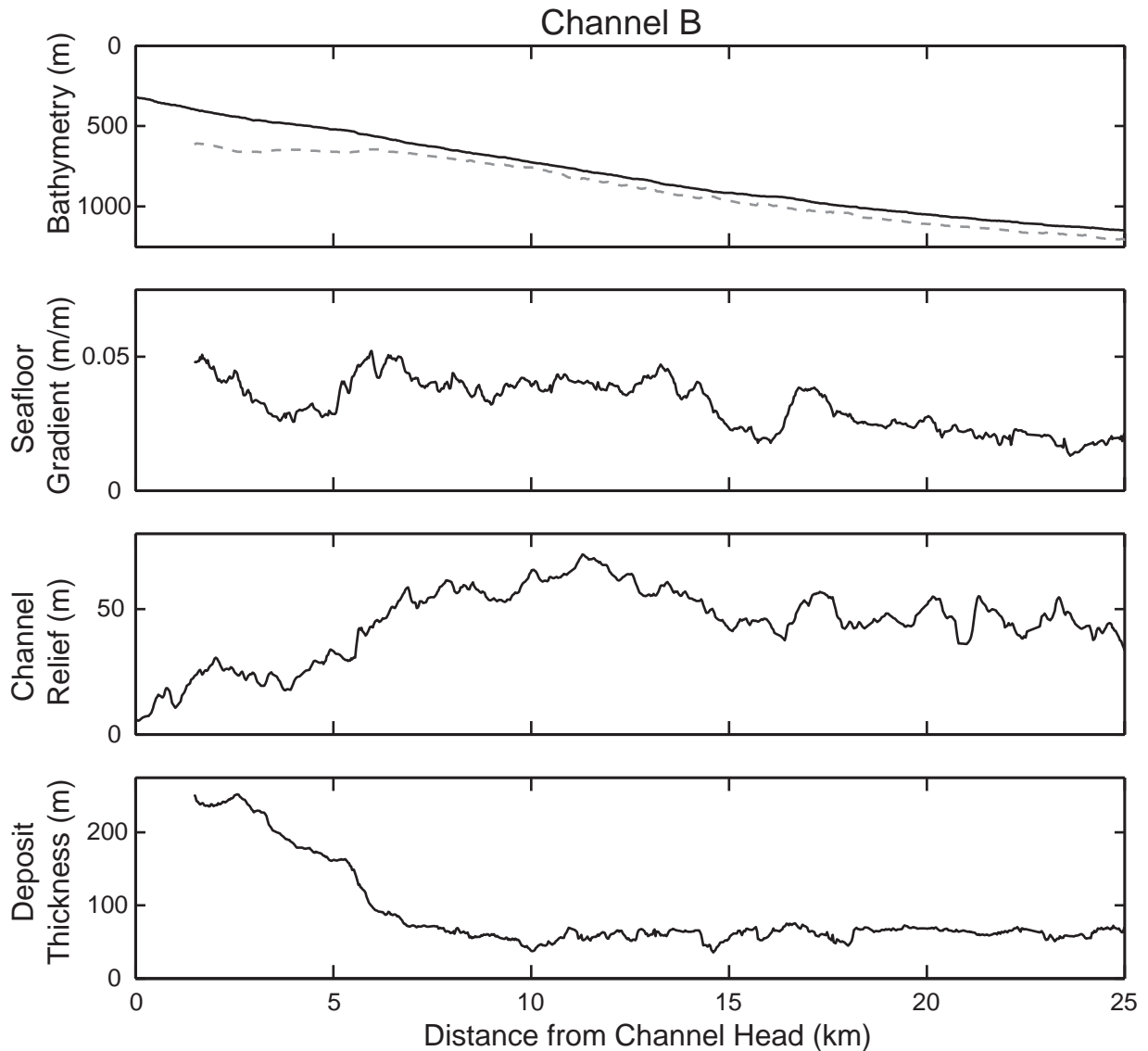


Figure 3.8. Downstream trends for Channel B thalweg. A) Profile of channel thalweg bathymetry following channel centerline as a function of distance from channel head. Dashed line represents bathymetry of surface CD1 below present day channel thalweg. B) Profile of present-day down channel surface gradient. C) Channel relief measured between the channel thalweg and average levee crest bathymetry as a function of distance from channel thalweg. D) In-channel sediment thickness measured for interval between seafloor and mapped subsurface horizon CD1 as a function of distance from channel head.

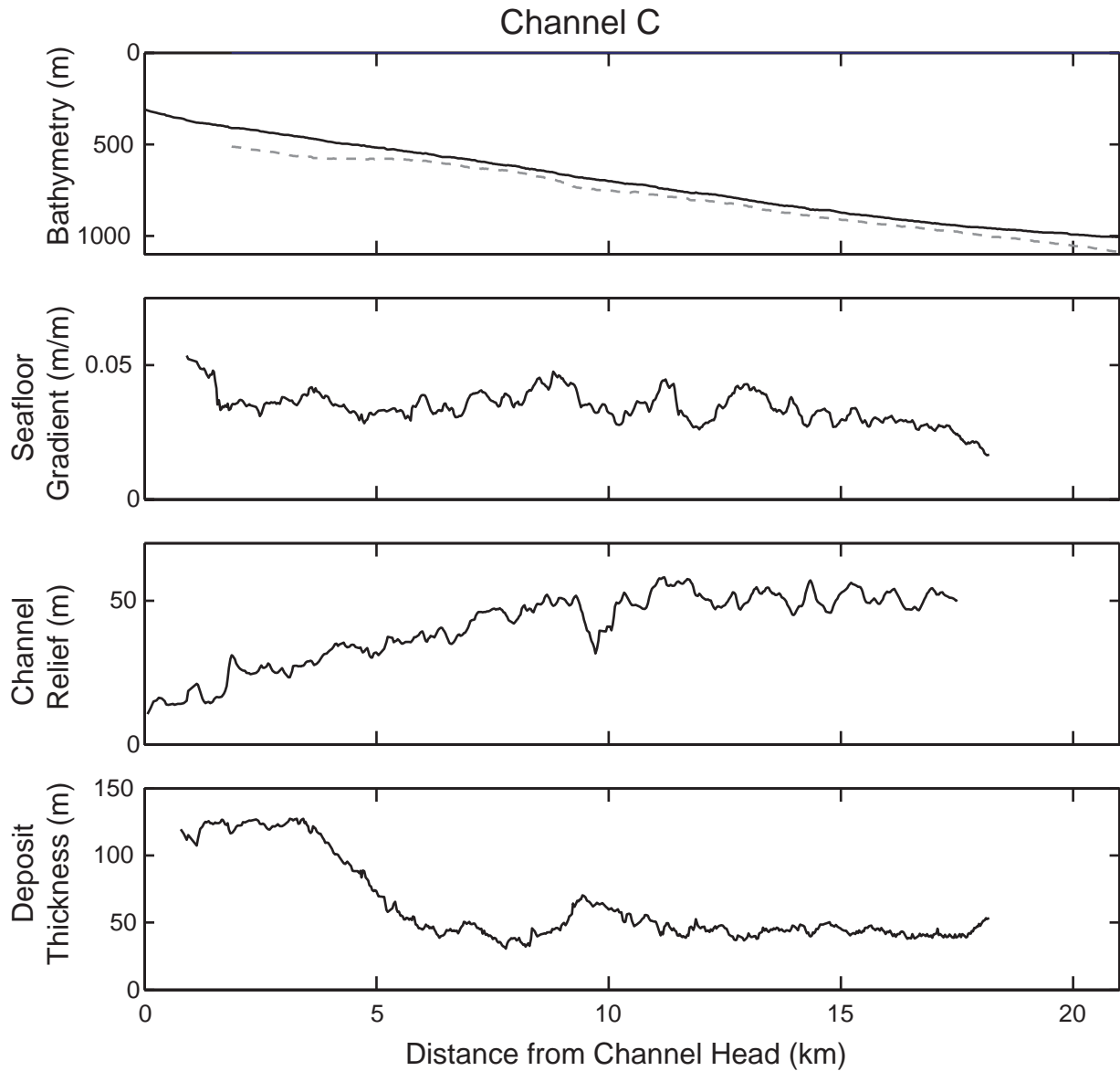


Figure 3.9. Downstream trends for Channel C thalweg. A) Profile of channel thalweg bathymetry following channel centerline as a function of distance from channel head. Dashed line represents bathymetry of surface CD1 below present day channel thalweg. B) Profile of present-day down channel surface gradient. C) Channel relief measured between the channel thalweg and average levee crest bathymetry as a function of distance from channel thalweg. D) In-channel sediment thickness measured for interval between seafloor and mapped subsurface horizon CD1 as a function of distance from channel head.

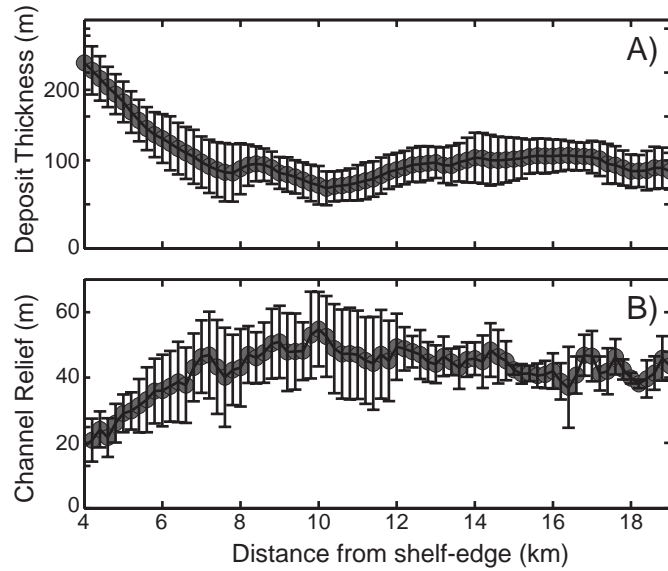


Figure 3.10. Change in deposit thickness and channel relief as a function of shortest distance to shelf-edge (defined as 280 m contour of bathymetry). Error bars represent +/- one standard deviation of data in each bin. A) Mean thickness of deposit measured in bins spaced 200 m from shelf-edge. B) Mean channel relief measured in bins spaced 200 m from shelf-edge. Channel relief trend computed from 1921 channel cross-sections.

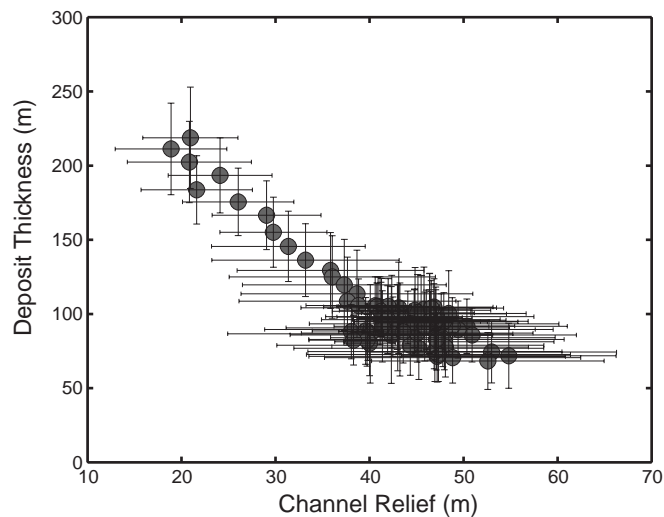


Figure 3.11. Cross plot of deposit thickness and channel relief data presented in figure 3.10. Horizontal and vertical error bars represent +/- one standard deviation of data in each bin.

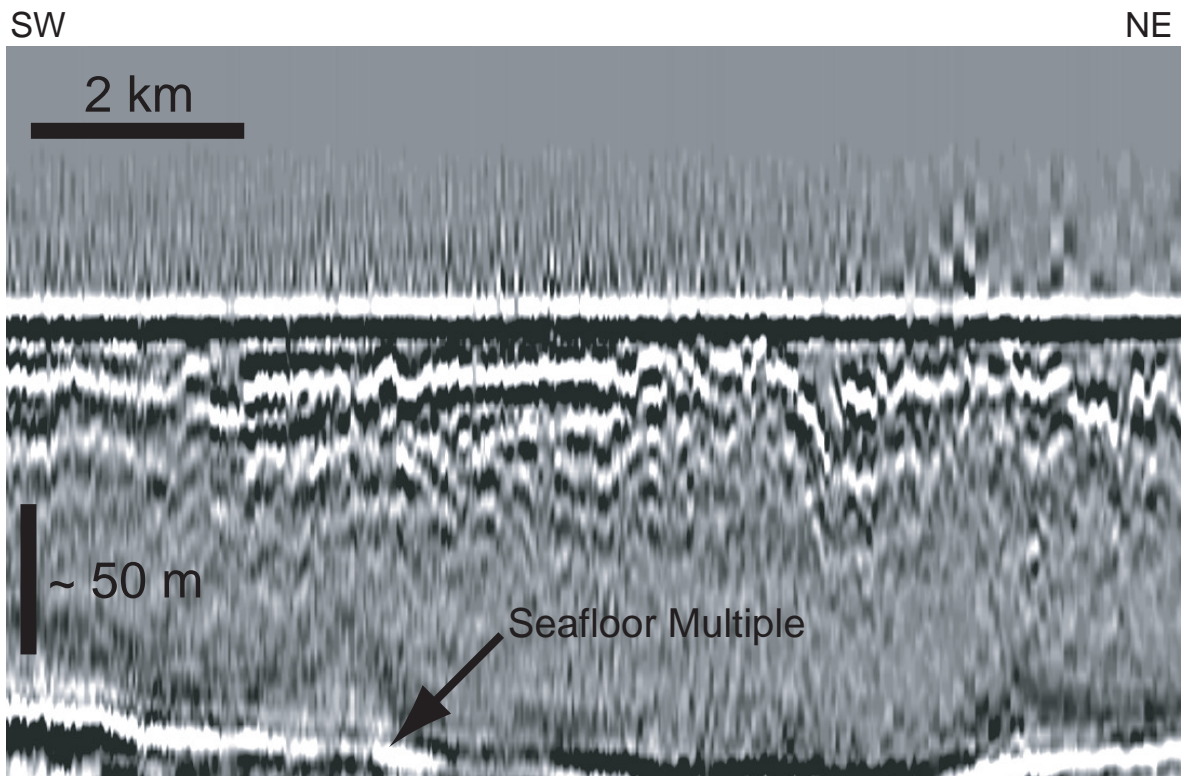


Figure 3.12. Characteristic seismic line oriented parallel to shelf-edge and located immediately upstream of shelf-slope transition. Location of seismic line is indicated in Fig. 3.1B. No channel features can be observed in cross-section that connect to location of present-day channels.

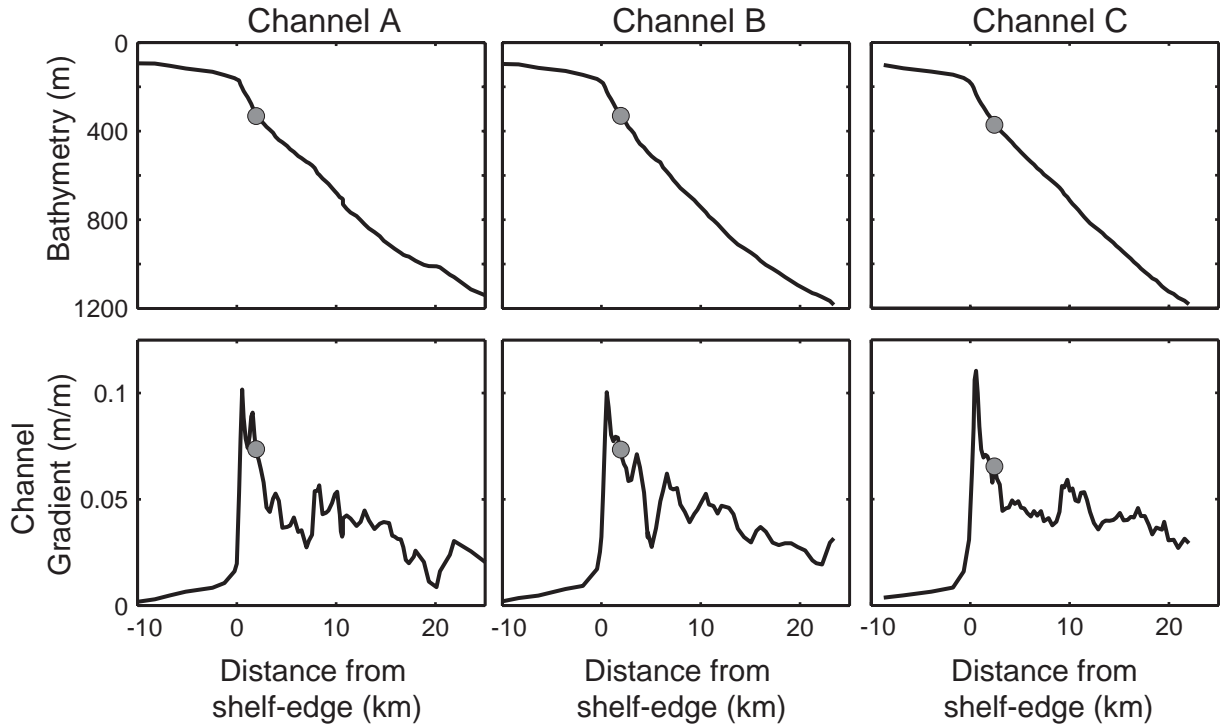


Figure 3.13. Long profiles of bathymetry and down-channel surface gradient for channels A-C with channel head location marked on each plot. Upslope of channel head, long profile represents steepest path of accent.

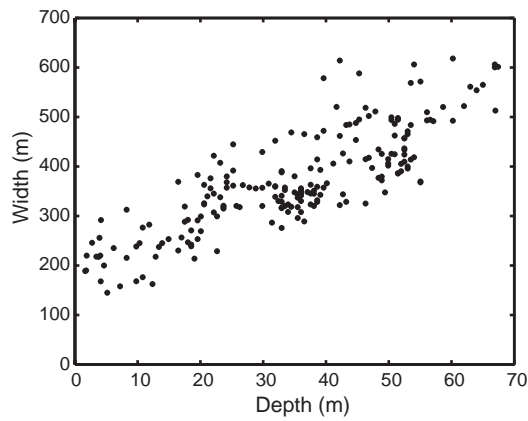


Figure 3.14. Channel width as a function of channel depth measured along 176 channel cross-sections of channels on slope of continental margin offshore Champion Delta.

Chapter 4

Interactions between turbidity currents and topography in aggrading sinuous submarine channels: A laboratory study

Kyle M. Straub^a, David Mohrig^{a,c}, James Buttles^{a,c}, Brandon McElroy^{a,c}, & Carlos Pirmez^b

^aDepartment of Earth, Atmosphere, and Planetary Sciences, Massachusetts Institute of Technology, 77 Massachusetts Avenue, Building 54-824, Cambridge, MA 02139

^bShell International Exploration and Production, Inc., P.O. Box 481, Houston, TX 77001

^cPresent Address: Department of Geological Sciences, The University of Texas at Austin, Austin, TX 78712

ABSTRACT

We present results from a laboratory experiment documenting the evolution of a sinuous channel form via sedimentation from 24 turbidity currents having constant initial conditions. The initial channel had a sinuosity of 1.32, a wavelength and amplitude of 1.95 m and 0.39 m, and three bends. All currents had a densimetric Froude number of 0.53 and an initial height equal to the channel relief at the start of the experiment. Large superelevation of currents was observed at bend apexes. This superelevation was 85-142% greater than the value predicted by a balance of centrifugal and pressure-gradient forces. An additional contribution to the superelevation was the runup of the current onto the outer banks of bends. This runup height is described by a balance between kinetic and potential energy. Runup resulted in deposition of coarse particles on levee crests that were indistinguishable from those deposited on the channel bottom. Deposit thickness and composition showed a strong cross-channel asymmetry. Thicker, coarser, steeper levees grew on the outer banks relative to the inner banks of bends. Zones of flow separation were observed downstream from bend apexes along inner banks and affected sedimentation patterns. Sedimentation from currents caused the channel to aggrade with almost no change in planform. However, channel relief decreased throughout the experiment because deposition on the channel bottom always exceeded deposition at levee crests. The first bend served as a filter for the properties of the channelized current, bringing discharge at

the channel entrance into agreement with the channel-cross-sectional area. Excess discharge exited the channel at this filtering bend and was lost to the overbank surface.

4.1. INTRODUCTION

Channels are the most significant morphologic feature of the submarine landscape on the continental slope. Many of these channels are highly sinuous in planform ($s \geq 1.3$) and persist from 10 km to 1000 km downslope, yet the processes by which these channels evolve and organize themselves are incompletely known. There are still very few direct observations of turbidity currents moving through sinuous channels (Hay, 1987; Khripounoff et al., 2003; Xu et al., 2004) because infrequent occurrence, great water depths, and high current velocities make measurements difficult to obtain. This paper presents results from a laboratory experiment where the interactions of currents with channel bends are directly monitored at a reduced scale. We focused on resolving processes controlling the construction of channel-margin levees and the nearly vertical aggradation of a channel with almost no change in its planform. This style of geometric and kinematic evolution is reported for many natural channels based on seismic imaging and analysis (Deptuck et al., 2003; Posamentier, 2003) and is a key component in a number of conceptual models for submarine channel evolution, including those by Peakall et al. (2000), Kneller (2003), and Pirmez and Imran (2003). Importantly, it is the style of channel evolution most closely linked to a significant addition of sediment mass to the submarine landscape.

The nearly vertical climb of channel forms in space through time requires rates of overbank sedimentation that are comparable to those within the channels themselves. The most commonly cited processes by which sediment is transferred from channelized turbidity currents to overbank flow are referred to as flow splitting and flow spilling (Clark and Pickering, 1996; Kassem and Imran, 2005; Peakall et al., 2000; Piper and Normark, 1983). Flow splitting describes a process where the upper fraction of the flow traveling above the channel detaches from the body of the current as it moves through a channel bend. This detachment takes place along the outer bank of a bend, and afterward the separated fraction of current is thought to move independently out across the overbank

surface (Piper and Normark, 1983). Flow spilling, on the other hand, is not a site specific mechanism. Flow spilling describes a process in which a supra-channel fraction of a current spreads laterally out across the overbank surface (Clark and Pickering, 1996). This lateral spreading primarily is interpreted as being a consequence of the gravitational collapse of the non-confined portion of the density current. Another recognized process that produces overbanking flow is referred to as inertial overspill by Hay (1987). Inertial overspill of currents at bends is specifically a result of spatial changes in channel width and takes place only when curvature of an outer bank exceeds that of the channel axis. The experiment presented here specifically investigates the consequences of the more general flow splitting and overspilling on construction of the overbank surface and channel-bounding levees. Recent conceptual models that describe the long-profile evolution of a current call on a systematic bias in the size of suspended particles that leave a channel. The effect is a coarsening in the particle-size distribution for the remaining channelized current with distance traveled (Peakall et al., 2000; Posamentier and Kolla, 2003). These conceptual models remain untested for natural systems but are tested here at laboratory scale.

Laboratory models exploring phenomena of landscape-evolving flows at reduced scale must resolve three separate but coupled fields in order to be complete: 1) the topography and composition of the evolving granular bed; 2) the sediment transport field; and 3) the flow field. In practice, even under controlled laboratory conditions, it is difficult to monitor the structure and evolution of all three fields equally as well. Typically attention is focused on one or two of the fields at the expense of the other(s) depending on the guiding motivation for the study. The experiment presented here focuses on evolution of the channel form and the composition of the sedimentary deposits that modify its topography. Measurements defining the other two fields were also collected but emphasis was placed on resolving the geometric and kinematic evolution of the vertically aggrading channel. We made this choice in order to generate data that is consistent with the greatest amount of information available for natural submarine channels, seismic images of their topography and their affiliated deposits.

Recent laboratory measurements reported by Corney et al. (2006) and Keevil et al. (2006) and numerical models of Imran et al. (1999), Kassem and Imran (2005) and Corney

et al. (2006) have provided quantitative descriptions or estimations of the flow fields associated with gravity currents traversing a series of sinuous channel bends. The laboratory measurements in particular make important contributions to defining both the structure of the mean flow and the turbulence intensities associated with these gravity currents. While this information is critical to developing a general understanding of the fluid dynamics, the absence of sediment transport and/or deposition in these studies prohibits direct observation of the co-evolution of turbidity currents and the channels they construct. Measurements of this co-evolution, connected through the sediment transport, are a necessary component for models of submarine landscape evolution. We present results from an experiment where strongly depositional currents modified a pre-existing channel by spatially varying patterns of sedimentation. These measurements are intended to serve as a benchmark for developing and calibrating fully 3-D numerical models of flow through sinuous submarine channels. At the present time, numerical models describing channelized 3-D turbidity currents either assume the currents are completely confined to the channel (Das et al., 2004; Imran et al., 1999) or assume they are conservative and therefore unable to evolve the channel form (Imran et al., 2002; Kassem and Imran, 2005). The experiment presented here targets a middle ground between these end-member configurations in an attempt to capture the interactions between currents and topography most relevant to building depositional channel forms.

Due to a lack of direct measurements of the interactions of currents with submarine channels, many scientists have focused on reconstructing flow conditions by interpreting depositional and erosional patterns preserved in seafloor topography and in sedimentary deposits (Bouma, 2000; Gardner et al., 2003; Komar, 1969; Lee et al., 2002; Middleton, 1993; Pirmez, 1994; Pirmez et al., 2000; Pirmez and Imran, 2003; Shor et al., 1990). Models developed for subaerial channelized flow have been applied as semi-quantitative guides for understanding the physics of flow through sinuous submarine channels (Imran et al., 1999; Komar, 1969; Pirmez and Imran, 2003). For example, Komar (1969) estimated a mean stream-wise velocity for turbidity currents that moved through the Monterey Canyon by assuming the unequal heights of levees running along the outer and inner banks of channel bends recorded a cross-channel superelevation of currents that was set by the balance between centrifugal and pressure-gradient forces. Use of the terrestrial

analog has been considered reasonable because rivers and submarine channels have been found to share the same scaling relationships between meander wavelength, radius of curvature, and bend amplitude (Clark et al., 1992; Hay et al., 1983; Leopold and Wolman, 1960; Pirmez, 1994). While the similarities in geometry between channels of the two environments do exist, both computational (Corney et al., 2006; Kassem and Imran, 2005) and experimental (Keevil et al., 2006) analyses point to key differences between the flow fields of terrestrial versus submarine sinuous channels. One consequence of these differences is the relatively high rate of overbank sedimentation in the submarine environment allowing nearly vertical climb of submarine channel forms (Hackbarth and Shew, 1994; Kneller, 2003; Peakall et al., 2000; Posamentier et al., 2000; Stelling et al., 1985). High rates of overbank sedimentation are most pronounced along the outer banks of channel bends in the submarine where thick channel levees are deposited (Hay, 1987; Pirmez and Flood, 1995; Posamentier and Kolla, 2003; Prior et al., 1987). We are interested in determining which processes account for this apparent increase in overbank sedimentation. In this sense, our laboratory results can be used to examine differences between subaerial and subaqueous flows moving through sinuous channels and provide an opportunity to better understand channelized landscapes in general.

4.2. EXPERIMENTAL SETUP

Twenty-four sediment laden currents were released into a basin that is 5 m long, 5 m wide and 1.2 m deep that remained filled with water throughout the experiment (Figure 4.1). Before filling the basin with water, a channel was built on its floor with a sinuosity of 1.32 and a planform described by a sine-generated curve that has been shown to reproduce the shape of many subaerial and subaqueous channels (Langbein and Leopold, 1966; Pirmez, 1994). This curve describes the local direction of the channel centerline, φ , as a function of streamwise distance, x :

$$(1) \quad \varphi = \omega \sin \frac{x}{X_t} 2\pi$$

where ω is the maximum angle at which the centerline deviates from the mean downstream direction and X_t is the centerline distance associated with one channel wavelength. Our channel was designed with $\omega = 55^\circ$, $X_t = 3.4$ m, and a bend wavelength and amplitude of

1.95 m and 0.39 m, respectively. Channel sidewalls and banks were constructed from a 15:1 mixture of sand and cement mortar. The original channel was trapezoidal in cross-section with an initial depth of 0.11 m and basal and top widths of 0.20 m and 0.40 m, respectively (Fig. 4.1). The channel was built with no downstream bed slope. After traversing the 4.2 m long channel, each current spread out onto a short unconfined surface before plunging into a moat where it was removed from the basin via perforated pipes, thereby preventing current reflections off of the tank sidewalls.

All turbidity currents were composed of the same mixture of clear water, dissolved CaCl_2 and suspended sediment. This mixture produced currents that entered the channel with an absolute density of 1021 kg/m^3 and an excess density of 2.1 % relative to the fresh water that filled the basin. Thirty-three percent of this excess density was due to suspended sediment and 67 % was from the dissolved salt. The sediment consisted of 60 % blown silica (ballotini) and 40 % crushed silica flour by weight with a cumulative size distribution where D1, D5, D10, D16, D25, D50, D75, D84, D90, D95, and D99 equaled nominal diameters of 1.7 μm , 3.1 μm , 12.9 μm , 18 μm , 23 μm , 31 μm , 41 μm , 46 μm , 52.1 μm , 60 μm , and 80 μm , respectively (Figure 4.2). Dissolved salt was used to simulate the finest portion of suspended sediment within natural turbidity currents, a fraction that is transported to the distal end of a system without loss via deposition. The mixture of water, sediment and dissolved salt was introduced to the basin via a constant head tank that guaranteed steady input discharge throughout each individual release. Each current passed through a momentum extraction box before entering the channel. This box was 0.5 m by 0.5 m in planform and contained several vertical screens of 5 mm wire mesh which currents passed through prior to entering the experimental channel. The momentum extraction box ensured that each flow acted as a sediment-laden plume driven by buoyancy alone. Current thickness and discharge at the channel entrance were held constant for all 24 runs at values of 0.11 m and $4.7 \times 10^{-3} \text{ m}^3/\text{sec}$. Representative input values for the densimetric Froude number ($Fr = \bar{u} / \sqrt{[(\rho_c / \rho_a) - 1]gH}$), Reynolds number ($Re = \bar{u}H / \nu$), and buoyancy flux ($B_{f0} = \Delta\rho g u h b / \rho$) were 0.53, 8.2×10^3 and $5.3 \times 10^{-4} \text{ m}^4/\text{s}^3$, respectively, where \bar{u} is depth averaged velocity, ρ_c is current density, ρ_a is the ambient fluid density, g is gravitational acceleration, H is current thickness, ν is kinematic

viscosity, and b channel width. The duration of each current was 5.3 ± 0.1 minutes. The flow of currents out of the momentum extraction box and into the experimental channel represents a similar transition made by erosional currents confined in canyons to depositional currents in aggradational channels.

Measurements of current velocity were collected using two Sontek Acoustic Doppler Velocimeters (ADV) and one Sontek Pulse-Coherent Acoustic-Doppler Velocity Profiler (PCADP). An ADV was positioned at the channel entrance and exit throughout the experiment. These devices recorded the 3-D velocity in a 10^{-6} m³ sampling volume located 50 mm above the channel bed at the channel centerline with a frequency of 10 Hz. Vertical profiles of velocity were measured at many locations inside and outside of the channel using only one of the three transducers on the PCADP. In particular, we measured the magnitude of the velocity in overbank regions. The PCADP measured velocity with a frequency of 0.25 Hz in sampling volumes that were 16 mm tall and varied between 0.004 to 0.006 m² in planform area with increasing distance from the instrument. In particular, the PCADP was stationed overbank at the apexes of bends 1 and 3 as well as at the channel inflection points between the three bends. This arrangement assured the capture of any changes in velocity and thickness of the currents as the channel-form evolved. Data collected during each flow included the ADV and PCADP measurements, some sampling of the developing suspended-sediment concentration and grain-size profiles within currents, and digital video of currents as seen from directly overhead. A 15 ml pulse of dye was released at the channel entrance for each current about 2 minutes following the start of each flow. These pulses were captured on overhead video and analysis of their advection through the system yields close to a synoptic representation of the channelized-overbank flow field (Figure 4.3).

Maps of the channel form following each experimental current were produced using the first hard returns from a 1MHz ultrasonic transducer connected to a pulse/receiver box. Each bathymetric map was built from 27,600 points collected on a grid with 5 mm spacing in the cross-stream and 40 mm spacing in the downstream direction. The precision at each location is better than 0.2 mm. This resolution makes it possible to successfully determine the patterns of sediment deposition associated with individual currents by differencing successive maps of channel topography.

Following the 24th current, the water level in the experimental basin was lowered, and the deposit was allowed to dry. After drying, the deposit was sampled for particle-size characterization. These samples were collected at 211 locations along 13 channel cross-sections oriented perpendicular to the channel centerline. At most of these locations, the deposit was divided into a lower, middle, and upper sample. The sediment samples were then analyzed with a Horiba LA-300 laser-particle-size analyzer (LPSA). The LPSA uses a diode laser to accurately measure a distribution of sizes from 0.001 to 0.3 mm in nominal diameter.

4.2.1. Scaling

Our experiment was conducted at a reduced scale relative to submarine channels. It is therefore important to discuss how our model system compares to the natural environment. This comparison has three components: 1) a simple geometric scaling of the relatively static channel topography; 2) a dynamic scaling of flow properties for estimating equivalence between model and natural flows; and 3) a dynamic scaling of the sediment transport in order to roughly compare particle sizes being moved by the model and natural flows. The scaling is only intended to guide how experimental results might be applied to the interpretation of natural channels. Our experiment was not designed to simulate environmental conditions associated with a specific system but rather was carried out to better understand the depositional consequences of interactions between turbidity currents and channels.

The geometric scaling for our experiment was chosen to be 1/1000. Maximum width, depth and length for the laboratory channel therefore correspond to natural scales of 400 m, 110 m and 3.5 km. Bend amplitude and wavelength correspond to natural scales of 390 m and 1.95 km. The wavelength/amplitude ratio was 6.5 and the channel width/depth ratio measured at the inflection point between bend apex 1 and 2 systematically increased from 3.6 to 8.0 through the course of the experiment. These values compare favorably with measurements from natural channels assembled by Pirmez and Imran (2003): wavelength/amplitude ranges between 0.4 and 8.0, and values of width/depth for the Amazon submarine channel tightly cluster around 10. A comparison of our channel

geometry to the Amazon submarine system and recent numerical and experimental studies is found in Table 4.1.

The comparison between properties of the experimental and natural or prototype flows focuses on the densimetric Froude number. An approximate dynamic similarity between the model and a natural system is ensured by setting $Fr_{(\text{model})} = Fr_{(\text{prototype})}$ (Graf, 1971). Assuming a similar excess density for the experimental and natural currents, equality in densimetric Froude number is satisfied by prototype values for \bar{u} and H of 2.5 m/s and 110 m. Equality in densimetric Froude number also constrains the duration of a comparable natural current (T) to be 2.7 hr. Reynolds numbers for the model and prototype cannot be matched. The characteristic Reynolds number for model currents was 8.2×10^3 while the characteristic value for a comparable natural current would be 3.0×10^8 . Fortunately the model-current value was sufficiently large to ensure the approximate Reynolds similarity for fully turbulent gravity currents proposed by Parsons and García (1998).

Grain sizes used in the experiment can be compared to natural channels by estimating equivalent sediment transporting conditions between the two systems. Since the predominant mode of transport is suspended load, we make the dynamic comparison by matching the ratio w_s / u^* where w_s is a representative settling velocity for the particle class of interest and u^* is the shear velocity for the current. This scaling parameter was chosen because it best characterizes the degree to which particles of various sizes are suspended within the transporting current, with w_s serving as the scale value for downward particle advection and u^* being the scale value for the effective diffusion of particles into the interior flow by turbulent eddies. Estimates of settling velocities for experimental particles were calculated using the method of Deitrich (1982). Particle settling velocities for D5, D10, D50, D90, and D95 equaled 5.1×10^{-5} m/s, 1.3×10^{-4} m/s, 7.8×10^{-4} m/s, 2.0×10^{-3} m/s, and 2.7×10^{-3} m/s respectively. Shear velocity was calculated from estimates of bottom shear stress, τ_b , using

$$(2) \quad u^* = \sqrt{\frac{\tau_b}{\rho_c}}$$

and

$$(3) \quad \tau_b = \rho_c C_f \bar{u}^2$$

where C_f is a friction coefficient. We employed values of $C_{f(\text{prototype})} = 3 \times 10^{-3}$ and $C_{f(\text{model})} = 3 \times 10^{-2}$ to account for the weak dependence of bed friction coefficient with turbidity-current scale (Garcia, 1994; Parker et al., 1987). Calculated experimental values for $w_s/u^*_{(D5)}$, $w_s/u^*_{(D10)}$, $w_s/u^*_{(D50)}$, $w_s/u^*_{(D90)}$, and $w_s/u^*_{(D95)}$ are 3.6×10^{-4} , 9.5×10^{-3} , 5.6×10^{-2} , 1.5×10^{-1} , and 1.9×10^{-1} . All five of these values are much less than 1, the minimum value for significant suspension transport originally reported by Bagnold (1966). By satisfying the equality $w_s/u^*_{(\text{model})} = w_s/u^*_{(\text{prototype})}$ we estimate that D5, D10, D50, D90, and D95 for the experimental flows correspond to particle sizes of 9 μm , 41 μm , 113 μm , 207 μm , and 251 μm for flows at natural scale.

4.3. EXPERIMENTAL RESULTS

The primary goal of this experiment was to characterize the patterns in sediment deposition associated with turbidity currents moving through a sinuous channel. We were particularly interested in determining how channel curvature, distance from the source, and the relative thickness of currents controlled the patterns of deposit thickness and grain-size composition, both inside and outside of the channel. Sedimentation was primarily from the rain of suspended sediment onto the bed. Once deposited there was almost no reworking of the sediment by bedload transport. Ripples were observed on the levee bounding the outer margin of bend 1 and in the channel thalweg at bends 2 and 3. Using measurements of ripple height, wavelength, and migration rate (Simons et al., 1965) we estimate the downstream bedload transport in the channel thalweg at bend 2 to be $1 \pm 0.5 \times 10^{-8}$ m^2/sec . The per unit width suspended load flux measured just down channel of bend 2 was 2×10^{-5} m^2/sec , or 2000 times greater than the bedload flux. The deposit building the rest of channel form was relatively smooth with no indication of reworking by bedload transport. Sectioning the deposit revealed that each flow laid down a sediment lamina with no observable internal structure and a fine-grained cap consisting of particles that did not settle out from the water column until after each current was finished. These laminae represented the solids lost from each current during its traverse of the channel segment and this sediment volume was small when compared to the total amount carried by a current. The deposited fraction was very close to 10 % for the early currents and had increased to 15% by current 24. A majority of the sediment bypassed the mapped region, exiting the

channel at its downstream end. Evolution of channel topography associated with this limited amount of sediment deposition on the channel bed, sidewalls and banks is described below.

4.3.1. Deposition on Channel Bed and Sidewalls

We observed a systematic decrease in the thickness and grain size of the channel centerline deposit with distance from the deposit entrance point (Figs. 4.4, 4.5A, 4.6). Deposit sorting improved with distance traveled as D90 decreased by 40 μm over the study reach while D10 decreased by only 10 μm (Fig. 4.6). Superimposed on these basic streamwise trends are systematic, cross-channel variations in deposit thickness and its accompanying particle size. In every bend the location of the thickest and coarsest grain deposit was always displaced laterally from the centerline toward the outer bank (Figs. 4.4 and 4.6). To compare the magnitude of this skewing we digitized the path of maximum deposit thickness and grain size in the experimental channel from cross-sections oriented perpendicular to the channel centerline (Fig. 4.7). The path of maximum particle size defines the cross-over from inner to outer bank as occurring just downstream from the points of channel inflection. These points of cross-over are associated with a narrowing or necking of the contour lines defining the coarsest-grain deposit on the channel bottom (Fig. 4.6b).

Sediment deposition was not limited to the bed of the channel. Sediment also accumulated on the channel sidewalls. During early flows the sediment deposited on the steep sidewalls (45°) was unstable and remobilized as grain flows that accumulated at the base of sidewalls. Remobilization of some fraction of sidewall deposits continued until the sidewall had been completely regraded to a new slope of about 21° , close to the particle angle of repose. Sediment layers deposited by currents following the regrading were not remobilized as grain flows (Figure 4.8). Regrading of the sidewall slopes systematically reduced the width of the channel bottom (Fig. 4.8).

4.3.2. Deposition on Channel Banks

Deposition on the overbank surface displayed down-system trends that were roughly similar to those already described within the channel; thickness of the deposit and grain

size decreased with distance from the channel entrance. Superimposed on these trends was a pronounced asymmetry in deposit properties that varied with local curvature of the channel. The outer banks of all three bends were sites of pronounced levee construction (Fig. 4.8). These wedge-like overbank deposits were not evenly distributed about the bend apex (Fig. 4.4). Position of the thickest levee deposit at the 1st, 2nd, and 3rd bend was displaced downstream from the point of maximum channel curvature by distances of 0.12 m, 0.10 m, and 0.12 m (Fig. 4.4). Overbank deposits that accumulated directly across the channel on the inner banks of bends were in general, thinner, finer grained, and less wedge-like in cross-section (Fig. 4.8). Specific measurements defining the differences in overbank sedimentation between outer and inner banks of bends are presented below.

Surface slopes of the constructional overbank surface varied with the local channel curvature. Values of this slope were measured at the end of the experiment along transects running perpendicular to the local centerline direction. These transects revealed that levees forming along the outer banks of bends have higher slopes than those developed along the inner banks (Fig. 4.5c). The maximum surface slope for outer-bank levees at bends 1, 2 and 3 were 0.10, 0.12, and 0.06. The maximum slope measured for the affiliated inner-bank levees at bends 1, 2 and 3 were 0.06, 0.01, and -0.04.

The measured surface slopes provide a reasonably accurate estimate of the wedge-like geometry associated with the overbank deposits because they accumulated on an original surface that was close to horizontal. This is not often the case for natural surfaces, making levee taper a superior measure of cross-sectional form. We define levee taper as the change in deposit thickness over a specified distance running perpendicular to the local direction of the channel centerline. Tapers for outer-bank levees are calculated using the deposit thicknesses at levee crests and at positions located 0.15 m outboard from the crests. These measures defined the spatial rate of change in overbank deposition associated with a distance equal to the channel half-width. The evolutions of levee taper associated with deposition by all 24 currents are presented in Figure 4.9. This figure clearly shows a cumulative increase in taper as the total thickness of the levee deposit grew. The final values for levee taper at the outer-banks of bends 1, 2 and 3 were 0.13, 0.17, and 0.11. These values are substantially different from values associated with inner-bank overbank deposits at the apexes of the three bends. Final values for levee taper at the inner-banks of

bends 1, 2, and 3 were 1.5×10^{-3} , -16.1×10^{-3} , and -2.9×10^{-3} . Overbank deposits at the inner banks of bends were characterized by approximately constant local thicknesses rather than wedge-like cross-sectional geometries (Fig. 4.8). These thicknesses represented only a fraction of the accumulation measured directly across the channel. The ratios of the inner-to-outer levee-crest deposit thickness taken at the apexes of bends 1, 2 and 3 were 3.2, 6.0, and 4.6.

Particle analyses of inner- and outer-bank levee deposits establish spatial patterns in grain-size distribution (Fig. 4.6) that are consistent with the previously described levee geometries. Particles comprising the levee-crest deposits at the outer banks of bends are consistently coarser grained than the channel-edge deposits located directly cross-channel on the inner bank (Figure 4.10). In fact, the outer-bank deposits are so coarse as to be indistinguishable in composition from deposits laid down on the bed of the channel. All sizes of particles available for deposition on the channel bottom were also available for constructing the crests of outer-bank levees. The same condition did not hold for distribution of particles comprising the inner-bend overbank deposits. The coarsest particles found at the bed of the channel are not present at the inner banks of bends (Fig. 4.10). This difference between the particle-size distributions mirrors the difference in deposit thickness at inner- and outer-bank levee crests. Differences in the cross-sectional geometry of inner- and outer-bend overbank deposits are also reflected in their particle compositions. Figure 4.11 summarizes these grain-size trends by focusing on the apexes of bends 1 and 2. The outer-bank deposits possess systematic reductions in median particle size with distance away from the channel edge. Inner-bank deposits display no trend with distance from the channel. These spatial trends in median particle size emulate the measured values for levee taper along the outer and inner banks of the channel.

Successive measurements from all three outer-bank levee deposits show that bend 1 evolved differently from bends 2 and 3. The total amount and grain size of sediment deposited at the outer bank of bend 1 increased with each flow while these properties remained approximately constant at the two downstream bends. These differences in levee evolution are highlighted by comparing bend 1 with bend 3 in Figure 4.12. Deposit thickness at the bend 1 levee crest remained a roughly constant 9 mm per flow for the first six currents and then began to systematically increase with each current thereafter (Fig.

4.12a). The final current deposited a 15 mm layer of sediment on the outer-bank levee of bend 1. In comparison, no temporal trend in deposition rate was observed at bend 2 and bend 3. For example, a roughly constant deposition rate of 6×10^{-1} mm per flow was measured for all 24 currents on the outer-bank levee of bend 3 (Fig. 4.12a). These temporal changes in levee deposition rate are matched by temporal changes in median particle size of the levee deposits. The grain size of levee deposits increases from the early to intermediate and then later currents at bend 1 (Fig. 4.12b) while no such change was measured at bends 2 and 3. For example, levee deposits associated with the early, intermediate and later currents record essentially no change in median particle size at the outer-bank of bend 3 (Fig. 4.12b).

4.3.3. Changing Channel Morphology

The rate of sediment deposition on the bed of the channel always exceeded the rates of deposition on the adjacent overbank surface. As a result, the local channel depth or relief decreased at each point along the centerline throughout the experiment. We define this relief as the difference in elevation between the highest levee crest and the channel centerline. The bed of the channel at the entrance to the study reach had aggraded to an elevation nearly 75% of the original channel depth by the end of the experiment while maintaining about 50 % of its original local relief. The channel bed at the end of the study reach aggraded only 34 % its original depth but retained 75 % of its relief. Channel relief was preserved because losses due to sedimentation on the bed were offset by levee construction. Figure 4.5b shows three local maxima in channel relief that correspond to local maxima in levee deposition at the outer-banks of bends 1, 2 and 3. Rapid levee growth along the outer banks of these bends slowed down the loss of channel relief and thereby maintained channel integrity at the very locations where currents are most likely to exit the channel. The local minima in channel relief correspond to the inflection points between the three bends.

Preferential sediment deposition along the outer banks of channel bends led to an asymmetry in channel cross-sectional shape (Fig. 4.8). This preferential deposition on one side of bends also produced a relative straightening of the channel centerline and a 3 % reduction in channel sinuosity over the course of the experiment. The small change in plan

form is associated with an average vertical displacement of the channel bed equal to nearly one-half of its original depth. This vertical climb with little distortion of the channel plan form is very similar to evolutions of many submarine sinuous channels (Hackbarth and Shew, 1994; Kneller, 2003; Peakall et al., 2000; Posamentier et al., 2000; Stelting et al., 1985).

4.3.4. Flow Velocity Data

Vertical velocity profiles were collected at the inflection point between bends 1 and 2 for currents 2, 3, 4, 14, and 16 and at the inflection point between bends 2 and 3 for currents 17, 19, and 23 (Fig. 4.4a). In channel velocity measurements were made in the direction of the channel centerline, which did not necessarily correspond to the direction of maximum velocity. Resulting profiles of mean downstream velocity for these currents are presented in Figure 4.13. Estimates of current thickness using the velocity profiles collected at site ADP2 (Fig. 4.4a) show this property was relatively insensitive to change in local channel relief. Total current thickness for flows 2, 3 and 4 is $1.12 \pm 0.08 \times 10^{-1}$ m and for flows 14 and 16 was $0.96 \pm 0.08 \times 10^{-1}$ m. Local channel relief associated with these same five currents is 0.109 m, 0.106 m, 0.103 m, 0.077 m, and 0.073 m. The maximum velocity associated with these five currents shows no systematic variation and was measured at $1.16 \pm 0.17 \times 10^{-1}$ m/s. Local channel relief at site ADP4 (Fig. 4.4a) was measured to be 0.078 m, 0.074 m, and 0.069 m for currents 17, 19, and 23, respectively. No systematic change in total current thickness or maximum velocity can be resolved between these series of flows and are simply measured to be $1.05 \pm 0.08 \times 10^{-1}$ m and $1.24 \pm 0.13 \times 10^{-1}$ m/s (Fig. 4.13b). In summary, there are essentially no resolvable changes in current thickness or maximum velocity between the sites ADP2 and ADP4 (Fig. 4.4a) even though the channel form itself evolved. The only notable change was in the vertical structure of the velocity profile between the two measurement sites. Profiles collected at site ADP4 consistently possessed lower values for streamwise velocity above the velocity maximum than were measured at site ADP2 (Fig. 4.13).

The path of the high velocity core was measured using overhead digital video of dye pulses injected into the body of flows 2, 4, 8, 10, 11, 12, 13, 15, 17, 20, and 22. For each flow the location of the leading edge of a dye pulse was digitized every second from

the time of dye release until the dye pulse front reached the channel exit. The average path of the high velocity core from the 11 measured flow paths is compared to the channel centerline, path of maximum deposit thickness, and grain size in Figure 4.7. The maximum separation between the position of the high velocity core and the channel centerline occurs at the apexes of bends 1, 2, and 3.

Flow moving out onto the overbank surface at the outer banks of bends 1 and 3 was monitored with the PCADP during currents 5, 6, 7, 10, 12, 13, 15, 20, 22, and 24 (Fig. 4.4A). Overbank velocity profiles were oriented in the direction of maximum velocity as estimated from the leading edge of injected dye pulses captured on overhead video. At the apex of bend 1, the mean current velocity for overbanking flow steadily increased from approximately 0.015 ± 0.009 m/s early in the experiment to 0.035 ± 0.006 m/s near the end of the experiment (Fig. 4.12C). This increase is associated with a decrease in channel relief at bend 1 from 0.098 m to 0.060 m. No equivalent change in mean overbank velocity was measured at bend 3 (Fig. 4.12c). The local overbank velocity here maintained a nearly constant value of 0.009 ± 0.007 m/s, even though the local channel relief dropped from 0.099 m to 0.075 m between currents 5 and 24.

4.3.5. Zones of Flow Separation

Channel depositional patterns were also affected by zones of flow separation along the inner banks of bends. The current separated from the inner wall immediately downstream from a bend apex and reattached to the sidewall just downstream from the inflection point. These zones were resolved using injections of dye into the bodies of currents. Video of these injections documents a lag in the arrival of dye to the interior of these zones followed by a lag in its release back to the core flow where it is rapidly advected out of the system. Figure 4.14 is an example of a separation zone defined by dye intensity.

4.4.6. Current Superelevation

The upper surface of a turbidity current at any channel cross-section was not associated with a single elevation, but varied laterally between channel banks as a function of channel curvature. In this study, we focused on the surface elevation at channel-bend apexes and specifically measured the change in surface elevation for the current at the outer channel

bank and the channel center line. Following Engelund (1974) and Imran et al. (1999), we call this cross-stream variation in surface elevation the current superelevation. Measuring the local surface elevation is a two step process. First, local current thickness was measured using the PCADP. This thickness is then transformed into an elevation by adding it to the local bed topography. Local surface elevations were measured at locations marked ADP2, ADP3, ADP4, and ADP5 on Figure 4.4. This calculation uses the surface elevation measured at the inflection point as a proxy for the centerline elevation at the bend apex. This assumption is supported by the nearly constant current thickness measured at the 1st and 2nd inflection points. Using these measurements, current superelevations of 34 +/- 8 mm and 26 +/- 8mm are estimated for the 2nd and 3rd bends, respectively, which equates to approximately 25% of the total current thickness at the channel centerline.

An independent estimate of current superelevation was made using overhead photography. Injected dye images were converted into maps of current thickness using the Lambert-Beer law of light absorption:

$$(4) \quad I = I_0 10^{-\alpha l c}$$

where I is intensity of dye after passing through a given material, I_0 is the maximum intensity of dye, α is an absorption coefficient, l is the distance light passes through material, and c is the concentration of absorbing species (Starn, 1981). For our analysis, we injected red dye into currents and measured the intensity of red in images collected from stills of digital video defined by red, green and blue color maps. For each analyzed image, we subtracted the intensity of red dye present in a video frame prior to the injection of the dye. We assume a I_0 of 255 on a red, green and blue color map. Values for α and c are then calibrated at locations where current thickness has been measured with a PCADP. Rearranging Eq. 4 to solve for l allows us to create maps of current thickness from frames of digital video. Maps of current thickness were then added to local topography to create maps of surface elevation associated with the top of the current. This method gives a superelevation of 49 mm at the 1st bend and 47 mm at the 2nd bend. Plots showing the superelevation at the apexes of bend 1 and 2 are presented in Figure 4.15.

4.4. INTERPETATION

4.4.1. Superelevation in Channel Bends

The superelevation of flows measured at bends 2 and 3 was approximately equal to 25% of the total current thickness. This fraction is large compared to those measured for flows in river bends. For example, field measurements by Dietrich and Whiting (1989) resolve a superelevation equal to 1% of the total flow depth and laboratory data analyzed by Smith and McLean (1984) show a superelevation equal to only 8% of the mean flow depth. In order to understand these differences in degree of cross-channel superelevation it is prudent to revisit the dynamics of channelized flow that produces it, beginning with rivers. The cross-stream difference in water surface elevation at river bends is a well known phenomenon typically ascribed to the balance between a centrifugal force and a restoring pressure gradient force (Engelund, 1974; Johannesson and Parker, 1989; Rozovskii, 1961; Yen and Yen, 1971). Describing superelevation solely as the consequence of this balance is a result of the manner in which the equations of motion for flow in a bed have traditionally been simplified to make them amenable to stability analyses (Nelson and Smith, 1989). Specifically, it has been assumed that vertical velocities are negligible and the equation describing the balance of vertical momentum in the flow can be reduced to the hydrostatic condition; a condition requiring that vertical accelerations be sufficiently small that they can be set to zero without accumulating significant error (Nelson and Smith, 1989). It is recognized that this simplification to the flow field accrues significant error in the vicinity of steep channel sidewalls, where vertical accelerations are always important, but these non-hydrostatic effects have been left out of full descriptions for the flow field by arguing that these defects are local in nature, have a small effect on the overall flow pattern, and their addition would complicate the theory substantially from a mathematical point of view without adding much new physical insight (Johannesson and Parker, 1989; Smith and McLean, 1984). The developing theory of Imran et al. (1999) and Corney et al. (2006) has adopted this simplifying assumption of a hydrostatic condition to the flow of turbidity currents in channel bends. Our laboratory data calls into question the use of this simplifying assumption by highlighting patterns of flow and sedimentation that are consistent with significant vertical accelerations associated with runup of the high-velocity cores of currents onto channel sidewalls. In the subsequent sections, we explore the various forces contributing to the large superelevations seen in our experiment.

4.4.2. Centrifugal Contribution

The cross-stream difference in water surface elevation observed in river bends is typically ascribed to the balance between a centrifugal force and a restoring pressure gradient force (Engelund, 1974; Johannesson and Parker, 1989; Rozovskii, 1961; Yen and Yen, 1971). This relationship is based on two assumptions: 1) all fluid remains contained within the channel while traversing the bend and 2) streamlines always run parallel to the channel centerline and banks (Engelund, 1974; Johannesson and Parker, 1989; Rozovskii, 1961; Yen and Yen, 1971). In this framework, cross-channel flow can only be produced by a centrifugal force. The surface slope balancing this outward directed flow is:

$$(5) \quad S = \alpha \frac{H}{r_0} Fr^2$$

where r_0 denotes the channel centerline radius of curvature and α is a parameter very near unity (Engelund, 1974; Johannesson and Parker, 1989; Rozovskii, 1961). This equation can be rearranged to solve for current superelevation, Δz , measured between the channel centerline and outer bank:

$$(6) \quad \Delta z = \alpha b \frac{\bar{u}^2}{2r_0 \left(\frac{\rho_c - \rho_a}{\rho_c} \right) g}$$

. Using Equation 6, a superelevation of 14 mm is predicted at the apexes of our experimental bends. Parameters used for this calculation are $r_0 = 0.59$ m, $b = 0.40$ m, $\bar{u} = 0.08$ m/sec, $\rho_c = 1016$ kg/m³, and $\rho_a = 1000$ kg/m³. Values for ρ_c and \bar{u} are for measured conditions at the inflection point between bends 2 and 3.

Estimates of current superelevation using Equation 6 substantially underestimate the measured values. The estimated value is only 41% of the current superelevation at bend 2 and 54% at bend 3. This underestimate is not surprising given the fact that streamlines were observed to cross the channel centerline (Fig. 4.7) and a portion of the current exited the channel along the outer bank of each bend (Fig. 4.3), therefore violating the assumptions embedded in equations 5 and 6. The direction of turbidity current helical flow in submarine channel bends has been debated in recent laboratory (Corney et al., 2006) and computational studies (Kassem and Imran, 2005). These studies focus on the sense of

cross-stream flow resulting from flow superelevation and associated implications for sediment transport. We investigate movement of the basal current up the outer sidewall and out of the channel resulting from runup of turbidity currents in the following section. The consequences of runup on patterns and compositions of overbank deposits are also presented.

4.4.3. Runup Contribution

The experiment provides clear evidence for superelevation resulting from the runup of currents onto the outer banks of all channel bends. Particle size data from deposits record this runup of the basal part of the currents onto outer sidewalls in all bends as seen in Figure 4.6. In addition, this runup is captured by the path of the high velocity core relative to the channel centerline. At channel bends the high velocity core deviates from the channel centerline, and moves toward the outer channel bend wall. This runup can be understood by simply balancing the kinetic energy of a current against the potential energy gained as it moves up a sloping sidewall (Chow, 1959; Hungr et al., 1984; Kirkgoz, 1983). Any parcel of current has a kinetic energy per unit volume equal to $\frac{1}{2}\rho_c u^2$, and an associated maximum runup height, Δz , associated with its kinetic energy being completely converted to a potential energy equal to $(\rho_c - \rho_a)g\Delta z$. The resulting expression for Δz is

$$(7) \quad \Delta z = \frac{\rho_c u^2}{(\rho_c - \rho_a)2g}$$

and represents an upper limit to the runup elevation because energy losses due to friction are neglected. We estimate maximum runup by calculating Δz specifically associated with the high momentum cores of currents. To do this, we use measured values of $u = 0.11$ m/s, $\rho_c = 1019$ kg/m³, and $\rho_a = 1000$ kg/m³. Inserting these values into Equation 7 yields $\Delta z = 33$ mm at bend apexes. The measured superelevation of currents in bends exceeds that calculated with either Equation 6 or 7. Clearly additional study is required to fully understand the cross-channel flow within turbidity currents moving through channel bends.

4.4.4. Implications for Flow Splitting

Observations of current runups at outer banks of bends is inconsistent with the proposed occurrence of flow splitting that assumes the discharge lost at bends is restricted to some upper fraction of the currents (Peakall et al., 2000; Piper and Normark, 1983). This interpretation is untested and not consistent with grain size data collected on the bed of the channel and the levee crest (Fig. 4.6, Fig. 4.10). These data seem to require that the basal current become elevated to the height of the levee crests at all three bends. The resultant overbank flow had a composition equivalent to that of the entire channelized current rather than only some upper portion. We acknowledge that flow splitting can occur, but data from this experiment shows that this model does not always provide an accurate description for the compositional evolution of currents traversing sinuous channels. Replacement or placement of limits on the applicability of the flow splitting model to these systems has important implication for which particle sizes are tapped by overbank sedimentation and therefore the composition of a channelized current with distance from its source.

Previous studies investigating turbidity current flow in channel bends assumed that flow streamlines were parallel to the channel centerline (Keevil et al., 2006). Flow directed towards the outer banks of channel bends was assumed to result from centrifugal induced cross-stream flow. Runup provides another mechanism for transport of coarse sediment to the outer banks of channel bends. This mechanism does not necessitate a strong centrifugal induced cross-stream basal flow directed toward the outer banks of channel bends. Our observations of the path of the high velocity core, deposit particle size patterns, and estimate of superelevation using equation 7 suggests that runup is often the dominant transport mechanism of coarse sediment to outer channel bend levees.

4.4.5. First Bend as a Filter

Systematic increases in mean overbank velocity and levee crest sedimentation were measured for successive currents at the first bend (Fig. 4.12). These same properties did not vary throughout the experiment at bends 2 and 3. This difference suggests that the first bend acted as a filter on currents traversing the sinuous channel. The thickness of each current as it entered the channel was roughly 0.12 m. At the beginning of the experiment, this thickness approximately matched the local channel relief, but sediment deposition by successive currents partially infilled the channel and decreased this relief. This resulted in a

greater fraction of the current being elevated above the levee crest as it entered the first bend where it spilled onto the overbank surface resulting in the trends seen in Figure 4.12. The increasing amount of overbank sedimentation, the coarsening of the overbank deposit, and the increasing velocities for the overbank flow are all consistent with an ever greater fraction of a current exiting the channel at this position. This loss of current at the first bend reduced the discharge of the remaining channelized flow producing a current that was roughly compatible with the cross-sectional area of the evolving channel. The lack of systematic trends in overbank sedimentation and flow measured at bend 2 and bend 3 (Fig. 4.12) are consequences of these adjusted currents. The substantial differences between the measured trends at bend 1 versus bend 2 and bend 3 illustrate the effectiveness of a single bend as a filter on passing currents.

This experimental result highlights an internal process that almost certainly limits the variability in properties of turbidity currents traversing sinuous submarine channels. In particular, this filter is envisioned to reduce the natural variability in current discharges entering a system by adjusting higher discharge cases. Laterally confined currents in canyons that empty into aggrading sinuous channel forms can be expected to undergo adjustments to their discharge over a small number of high-amplitude bends. This process of current filtering by channel bends might provide a partial explanation for the slowly varying dimensions of many aggrading leveed submarine channels with distance down slope (Pirmez and Imran, 2003).

4.5. DISCUSSION

4.5.1. Control of Curvature on Channel Evolution

One of the most striking results of this experiment is the high deposition rates that occur along the outer banks of bends. This sedimentation pattern is quite different than expected patterns of deposition in sinuous rivers (Engelund, 1974; Imran et al., 1999; Rozovskii, 1961; Yen and Yen, 1971) (Fig. 4.16) but compatible with results from a numerical model for fully channelized turbidity currents by Das et al. (2004). We think the differences in patterns are the result of differences in the primary mode of sediment transport in the two environments. In rivers bedload transport dominates the evolution of channel morphology

including the development and growth of point bars (Deitrich and Whiting, 1989). Bedload transport does not cover the relatively steep outer banks of bends, leaving these sidewalls exposed to erosion by the moving fluid. A depositional turbidity current can mantle the entire channel form with a layer of sediment that settled onto the bed from suspension. These layers dominate the stratigraphy of our experimental channel, confirming that fallout of grains carried in suspension primarily controlled the morphological evolution of our channel. Following Das et al. (2004), we conclude that sedimentation rates were greatest where near-bed suspended-sediment concentrations were greatest, along the outer versus inner banks of channel bends. Higher deposition rates towards the outer banks of bends decreased channel sinuosity from 1.32 to 1.27, over the course of the experiment. This reduction in sinuosity was associated with the nearly vertical climb of the channel form. Channels that aggrade vertically with little change in their planform are commonly observed on the seafloor (Hackbarth and Shew, 1994; Peakall et al., 2000; Posamentier et al., 2000). The close connection between aggrading channel forms and minimal change in channel sinuosity strongly suggests that the production of sinuosity must be associated with net-erosional or non-depositional turbidity currents (Das et al., 2004).

Zones of flow separation were observed at the inner banks of bends immediately downstream from bend apexes, even though the experimental channel was smoothly varying in form and had a constant width. These zones of flow separation (Fig. 4.14) can have deposition rates that are measurably lower from those in the adjacent active channel (Fig. 4.8) and their deposits are finer grained (Fig. 4.6). Unlike deposit patterns in our experiment, zones of flow separation in terrestrial channels are often sites of local highs in deposit thickness resulting from cross-stream bedload transport into region of low velocity (Ferguson et al., 2003). The limited transport of fluid and sediment into and out of these separation zones is not adequately resolved by our experiment but our deposit thickness trends give some clues to their origin. Deposition dominated by suspension fallout combined with deposition patterns indicating weak near bed cross-stream flow suggest minimal exchange of fluid between the separation zones and remainder of channelized flow. A coupling between high suspended sediment concentration and the high velocity core would then result in thicker deposits in high velocity zones bordering the separation zones. We speculate that zones of flow separation are common in natural submarine

channels and accurate interpretation of deposits accumulated on the inner banks of bends requires consideration of the possibility that this sedimentation occurred in such zones of low current velocity.

4.5.2. Submarine Levee Construction

3-D seismic imaging of submarine channels has provided the geological community with a great deal of geometric data defining the structure of levees and associated overbank deposits (Clemenceau et al., 2000; Pirmez and Flood, 1995; Skene et al., 2002). Of relevance to this study, measured levee tapers from several natural systems compare favorably to tapers of levees deposited during our experiment (Figure 4.17). Unfortunately the wealth of geometric data is not matched by a comparable quantity of core, outcrop or experimental data characterizing the composition of these deposits or the processes through which they are constructed, with notable exceptions including Mohrig and Buttles (2007) and Mohrig et al. (2005). Inverting for overbank processes using particle size measurements from cores is difficult because most cores that sample levees have been collected several kilometers from the channel axis (Hiscott et al., 1997; Pirmez et al., 1997). One exception is found in core and seismic data presented by Clemenceau et al. (2000) that shows levee deposits from the Ram/Powell field in the Gulf of Mexico composed of particles with a size distribution that is similar to the associated channel filling sands. Even with this data, Clemenceau (2000) were unable to correlate individual overbank deposits to specific channel filling deposits as we report in the experiments herein. Outcrop studies that characterize the interaction of turbidity currents with channel bends are also rare due to the inherent difficulty in determining the position and orientation of a roughly two-dimensional exposure within a three-dimensional channel form (Gardner et al., 2003; Morris and Busby-Spera, 1990). However, an outcrop study of the Carboniferous Ross Formation in southwest Ireland, concluded that the crests of levees built from the spillover of channelized currents were as coarse as the channelized deposits themselves (Lien et al., 2003).

The present experimental results show a clear relationship between the character of the overbank flow and the geometry and composition of the levees that are constructed. The levees that develop on the inner banks of all bends are relatively thin, have small

tapers (Fig. 4.8) and show little change in grain size (Fig. 4.11) with distance from the levee crest. All of these properties are consistent with well-mixed vertical profiles having little change in suspended sediment concentration and particle size with distance above the overbank surface. These current properties are representative of the relatively fine-grained and dilute upper flow that resides above the channel where it was free to spread laterally, moving onto the overbank surface. A different structure was observed for the overbank flow at the outer banks of bends. Levees that developed at these sites were relatively thick, had high tapers (Fig. 4.8), and showed systematic reductions in grain size with distance away from the levee crest-line (Fig. 4.11). All of these trends are consistent with construction by overbank flows having vertically stratified profiles for grain size and suspended-sediment concentration. As previously stated, these profiles contain all of the particle sizes found in the basal channelized current; a consequence of current running up and out of the channel at the outer banks of bends.

The growth of levees at the outer banks of bends varied as a function of bend number. These changes can be related to the evolving suspended sediment profiles. Figure 4.9 shows that the amount of sediment available to build levees decreased from bend 1 to bend 3. This reduction in sedimentation was accompanied by a decrease in deposit grain size (Fig. 4.6). In spite of this, levee tapers remain high which suggests that the stratification was preserved within the overbanking flow even when the amount and sizes of sediment are diminishing.

The construction of thick levees on the outer banks of bends plays an important role in preserving the channel relief through time. As shown in Figure 4.5b, construction of the outer bank levees keeps the local channel relief high at points where runup and loss of current are significant. This pattern of levee growth allowed the channel to remain a flow conduit while experiencing large amounts of vertical aggradation, a pattern often seen in acoustic images of submarine channels (Hackbarth and Shew, 1994; Posamentier, 2003).

Our experiment clearly shows a connection between the flow field, channel planform, and evolution of channel morphology. This result stands in contrast to statements by Skene et al. (2002) whose study of natural levees on submarine channels concludes that there are no connection between local channel planform and levee morphology. The disagreement points out a need for the collection and analysis of

additional data from natural and experimental channels as well as a need to collect data with sufficient resolution and density to confirm the presence or absence of these correlations.

4.5.3. Implications for Using Levee Heights to Estimate Current Velocities

Komar (1969) proposed a model that relates channel morphology to the physical characteristics of channel-building currents by using the differences in levee crest elevation at the outer and inner banks of bends as a proxy for current superelevation and connecting it to a centrifugal acceleration experienced by the channel-building currents with Equation 6. This method has recently been used by Pirmez and Imran (2003) to estimate characteristic current velocities in the sinuous Amazon Submarine Channel. The results of our study suggest that the simple force balance described by Equation 6 underestimates the current superelevation and consequently, when used as an inversion tool, overestimate current velocities. The estimates for mean current velocity in 12 channel bends described by Komar (1969) are 30 % greater when using Equation 6 versus Equation 7. We understand that the runup expression for superelevation (Eq. 7) is incomplete, but it provides some measure of the possible systematic error associated with Komar method. The result points to a need for continued investigation of flow in submarine channel bends with a variety of configurations. Only after this is completed can the depositional records preserved in levees be used to more accurately constrain seascape forming conditions.

4.6. SUMMARY

In this experiment, we monitored the interactions between 24 turbidity currents and an aggrading sinuous channel. All currents were depositional with sedimentation occurring by suspension fallout. This sedimentation systematically reduced channel relief because deposition on the channel bottom was always somewhat greater than that on the channel bounding levees. The sedimentation pattern was skewed towards the outer banks of bends, which produced a slight reduction in sinuosity of the channel form as it aggraded. Sedimentation on the crest of levees at the outer banks of bends was 3-4 times greater than that found on the inner banks and enhanced deposition on outer banks minimized the reduction of channel relief at the sites where we measured the greatest loss of channelized

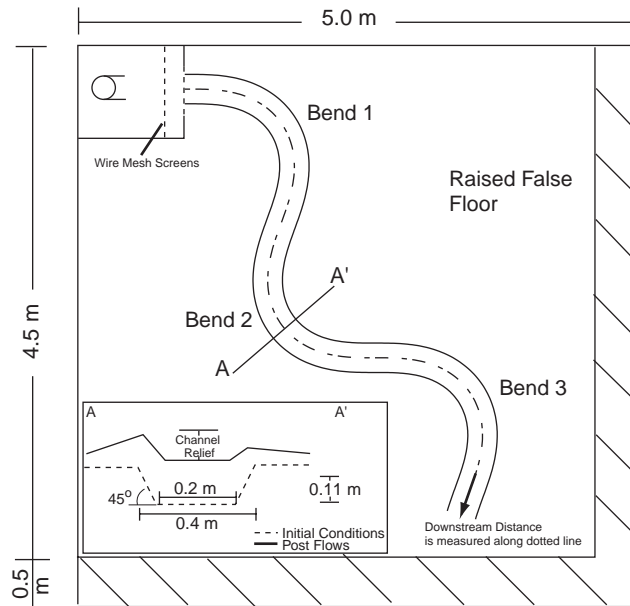
current to the overbank surface. The growth of levees at the outer banks of bends helped preserve the integrity of the channel form to act as a conduit for future flows. A cross-channel asymmetry in deposit particle sizes was also measured. This asymmetry was large enough that levee crest deposits on the outer banks of bends were as coarse as sediment deposited in the channel thalweg.

The measured superelevations of currents across bend apexes are 85% -142% greater than values predicted using a standard balance between the centrifugal and pressure gradient forces (Eq. 6). Particle sizes on the channel banks point to a large runup of the currents at these zones of high curvature. We propose that the high superelevations measured in the experimental bends is a combination of the well-known centrifugal contribution and a runup associated with the momentum of a current (Eq. 7). Streamwise velocities for turbidity currents and rivers are comparable, but the runup of turbidity currents is significantly greater due to their low excess density when compared to the ambient fluid. The value of $\rho_c / (\rho_c - \rho_a)$ for rivers roughly equals 1, while this ratio for turbidity currents ranges between 10 and 100. Its representative value for our experiment was 33. The large runup for turbidity currents and the deposition of coarse particles to the outer banks of our channel bends suggest that some portion of the basal current can exit the channel at bends. This result contradicts conceptual models of the downstream coarsening of currents due to flow splitting (Peakall et al., 2000; Posamentier and Kolla, 2003). Further studies are needed to quantify how changes in channel sinuosity affect the relative contributions of runup and the centrifugal force in setting the cross-stream superelevation. As long as direct measurements from turbidity currents remain few and technically difficult to obtain, results from this study and other channelized experiments will prove valuable in determining the interactions between currents and natural topography that lead to construction of the seascape.

ACKNOWLEDGEMENTS

Support for our research was provided by Shell International Exploration and Production Inc. and by the STC Program of the National Science Foundation via the National Center for Earth-Surface Dynamics under Agreement Number EAR-0120914. We thank Jim Best, Gareth Keevil, and Peter Talling for their thorough reviews and suggestions.

A) Plan View



B) Side View

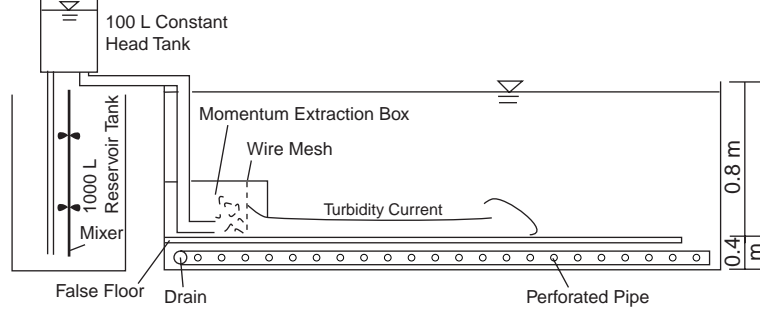


Figure 4.1. Schematic diagram of the experimental facility. A) Planview of the basin and the initial channel form. Each current passed through a momentum extraction box located in the top left basin corner prior to entering the channel. Diagonal lines mark the position of a moat for collecting a current following its passage through the channel avoiding reflections off of tank walls. The insert figure depicts an initial and final channel cross-section. B) Side view of the facility. Each current is mixed in a reservoir tank and pumped up into a constant head tank before entering the basin.

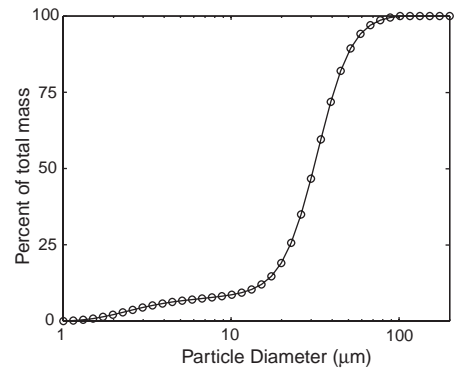


Figure 4.2. Particle size distribution for sediment discharged into experimental basin.



Figure 4.3. Turbidity current spilling onto the overbank surface along the outer banks of bend 1 (upper photo) and bend 2 (lower photo). Waves developed at the interface between the current and the ambient fluid are visible in the photograph from each bend. Overbank flow is visible from dye injected into the body at the beginning of the channel. Flow is from the upper left to lower right in both pictures.

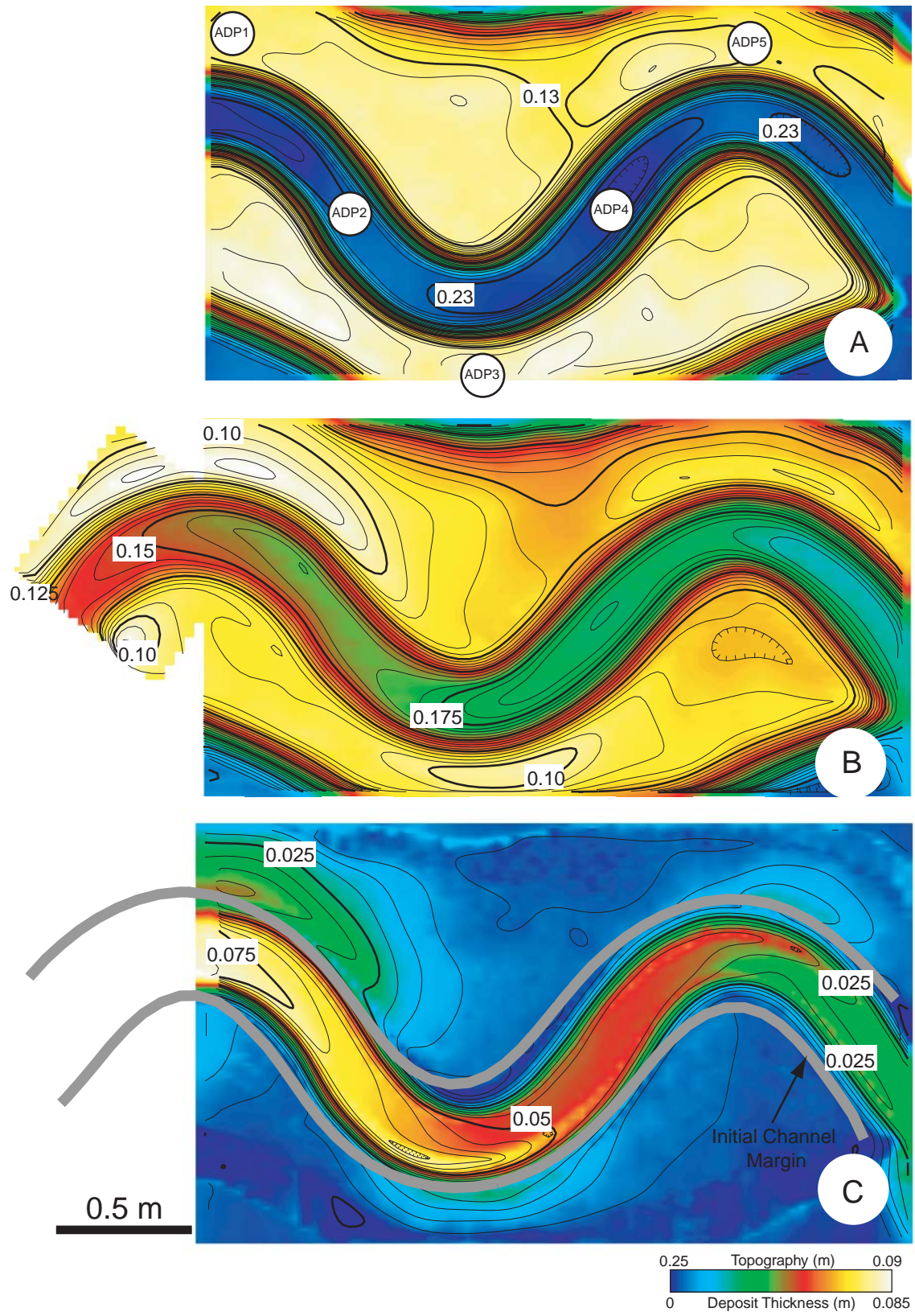


Figure 4.4. Maps from the experimental channel. Channel flow was from the left to the right in each map. A: Topographic map of the initial channel form. Topography is defined as vertical distance between the bed and an overlying datum of constant elevation. Contour interval is 5 mm. Locations of PCADP measurements discussed in text are marked on the map. Velocity profiles collected at the ADP2 and ADP3 locations were used to constrain current superelevation at bend 2 and profiles at ADP4 and ADP5 were used to constrain superelevation at bend 3. B: Topographic map of the final channel form following sedimentation by 24 currents. Channel filling and pronounced levee growth along the outer banks of the 3 bends are clearly defined. Contour interval is 5 mm. C: Map of deposit thickness from sedimentation by 24 turbidity currents. This map is the difference between maps (A) and (B). Contour interval equals 5 mm. Gray bold lines represent location of channel margin prior to deposition by flow 1.

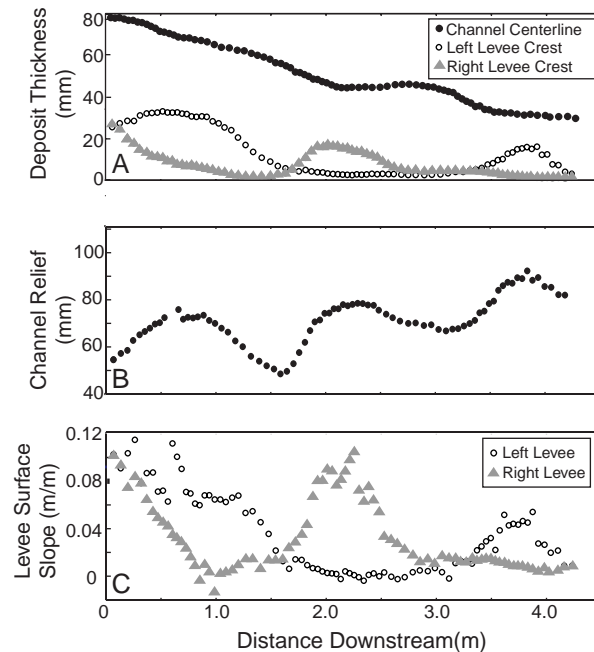


Figure 4.5. Downstream trends following sedimentation by 24 currents. A) Deposit thickness as a function of distance along the channel centerline. Levee-crest deposits were measured on cross-sections oriented perpendicular to the local direction of the channel centerline. Left and right levee refer to the left-hand and right-hand margins of the channel when looking downstream. B) Channel relief as a function of distance along the channel centerline. Relief was measured using channel cross-sections cut at right angles to the local centerline direction and equaled the elevation difference between the channel bed at the centerline and the taller of the two levee crests on that particular cross-section. C) Levee surface slopes as a function of distance along the channel centerline. Surface slopes were measured on channel cross-sections cut orthogonal to the local centerline direction.

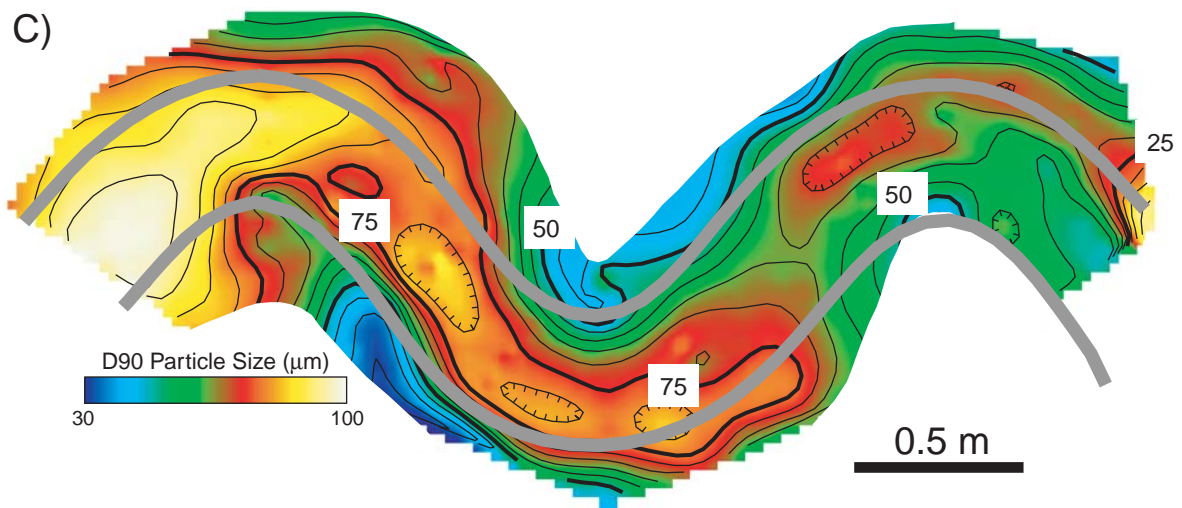
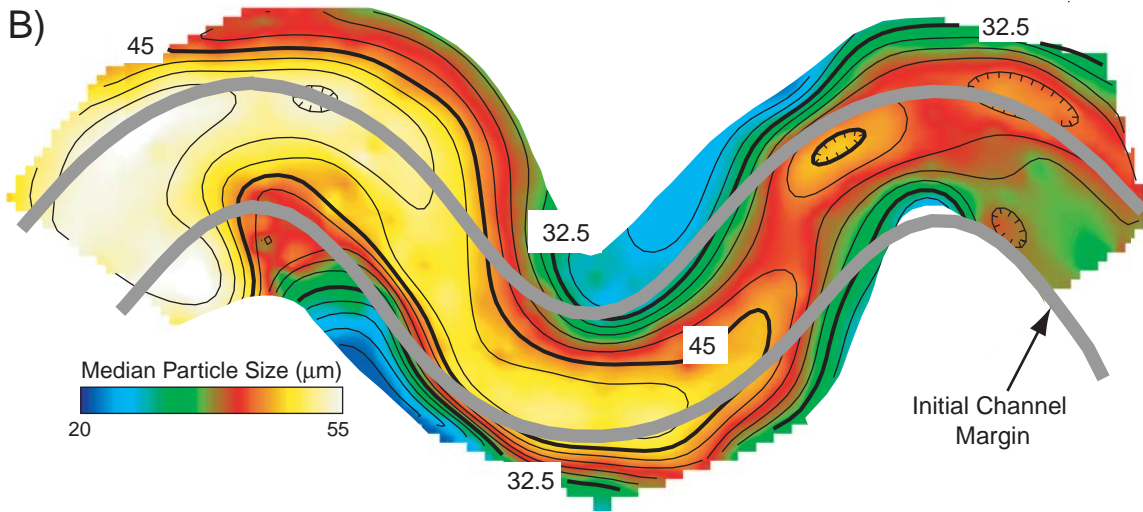
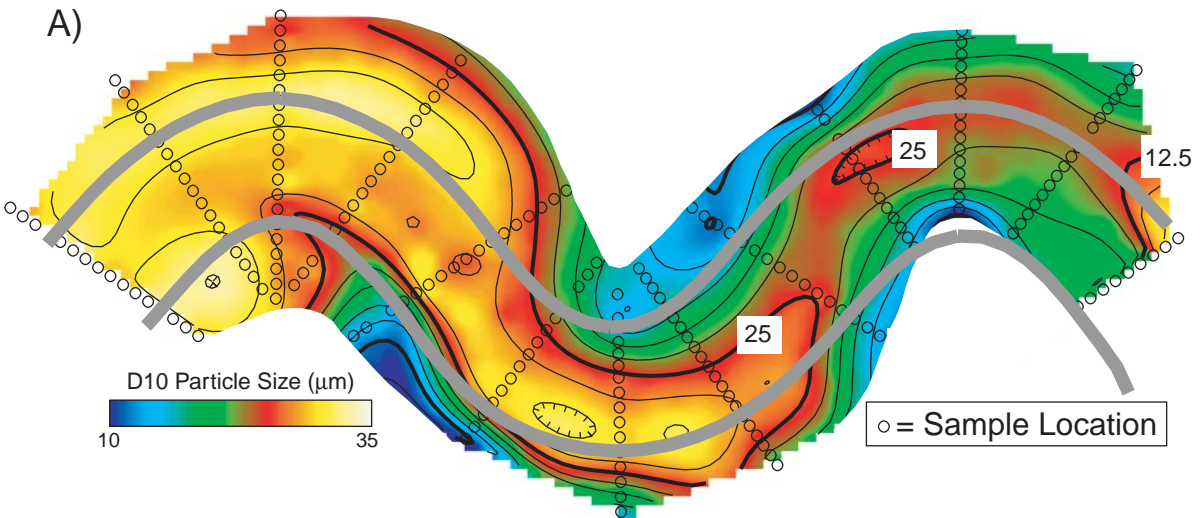


Figure 4.6. Maps of particle size for the total sedimentary deposit. Circles in (A) mark the 211 locations where vertically integrated sediment samples were collected for particle size analysis. Channel flow was from the left to the right in each map. A: Nominal diameter associated with particles composing the 10th percentile of the local deposit (D10). Contour interval equals 2.5 m. B: Nominal diameter associated with the median particle size for the local deposit (D50). Contour interval equals 2.5 m. C: Nominal diameter associated with particles composing the 90th percentile of the local deposit (D90). Contour interval equals 5.0 m. Gray bold lines in all three maps represent location of initial channel margin.

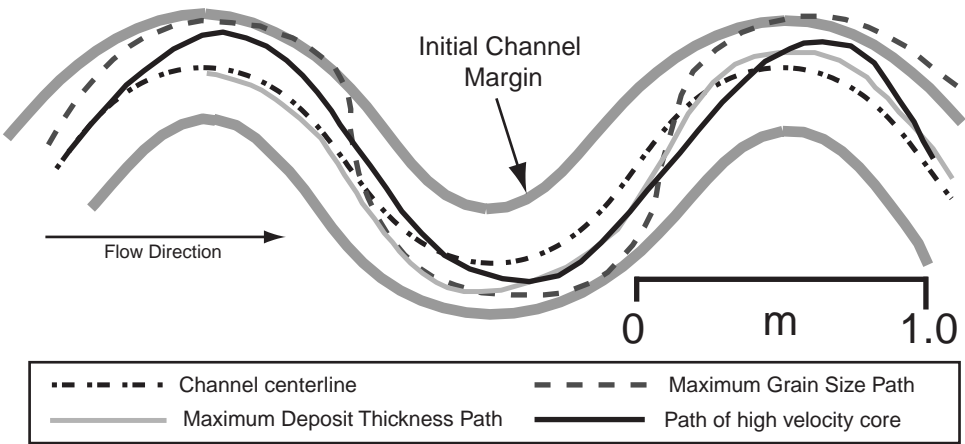


Figure 4.7. Downstream paths of maximum deposit thickness, maximum particle size, and high velocity core compared to the channel centerline. Path of high velocity core represents average path of high velocity core measured for flows 2, 4, 8, 10, 11, 12, 13, 15, 17, 20, and 22.

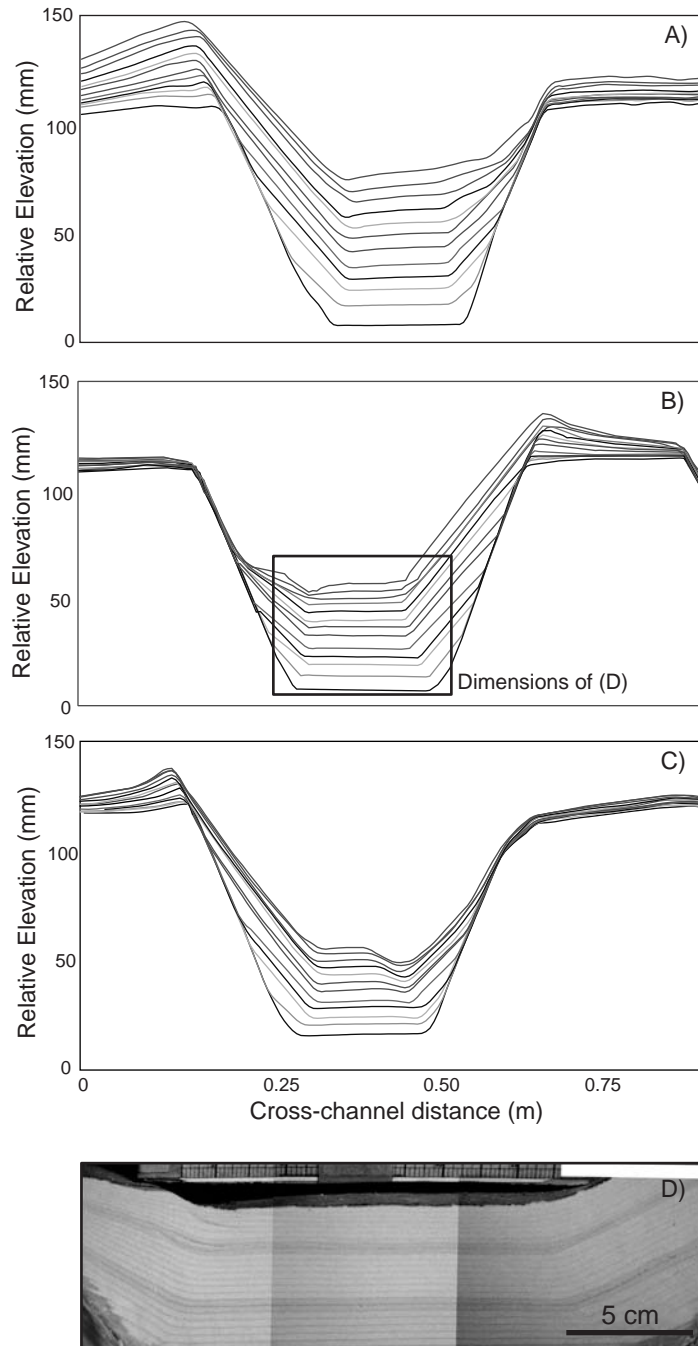


Figure 4.8. Evolution of channel cross-sections located at the apexes of the first (A), second (B), and third (C) bends. Each figure displays the original channel form plus successive forms following sedimentation by two currents. All cross sections are oriented perpendicular to the local centerline direction and oriented looking downstream. D: Photograph of sectioned deposit at 2nd bend apex.

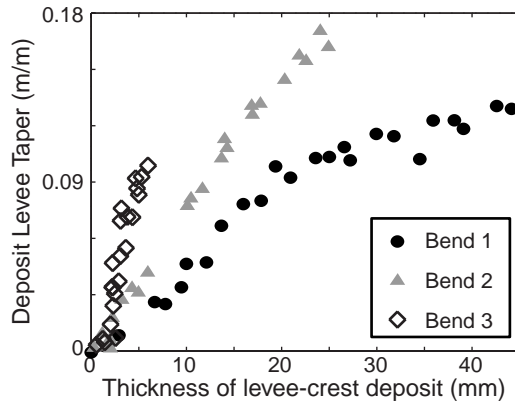


Figure 4.9. Change in the levee-deposit taper as a function of deposit thickness at the levee crest. Measurements were collected following each current at the locations marked ADP1 (bend 1), ADP3 (bend 2) and ADP5 (bend 3) in Figure 4.4a.

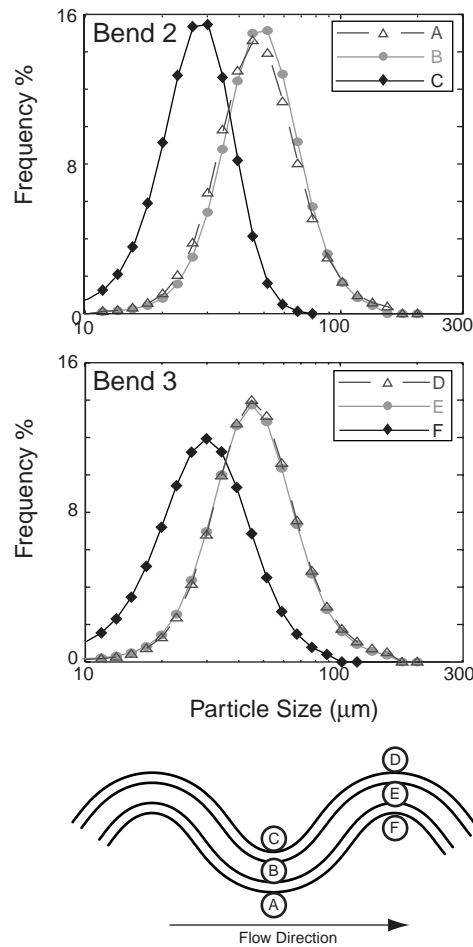


Figure 4.10. Measured particle-size distributions for deposits at the apices of bends 2 and 3. Location for each sediment sample is shown on the map at the bottom of the figure. At bend 2 there was essentially no difference in grain size between the outer-bank levee crest (A) and the channel bed at the centerline (B). Sediment deposited on the inner-bank levee crest (C) was substantially finer grained than (A) and (B). At bend 3 there was essentially no difference in grain size between the outer-bank levee crest (D) and the channel bed at the centerline (E). Sediment deposited on the inner-bank levee crest (F) was substantially finer grained than at the outer-bank (D) and centerline (E).

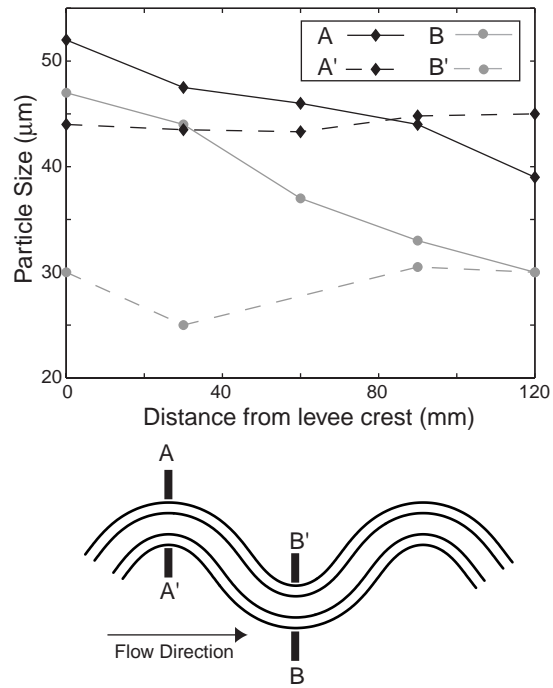


Figure 4.11. Change in median particle size of levee deposits as a function of distance from the levee crest. Solid lines indicate measurements taken from the outer banks of channel bends 1 and 2, while dashed lines indicate measurements from inner banks of the bends. Locations of these transects are drawn on the map at the bottom of the figure.

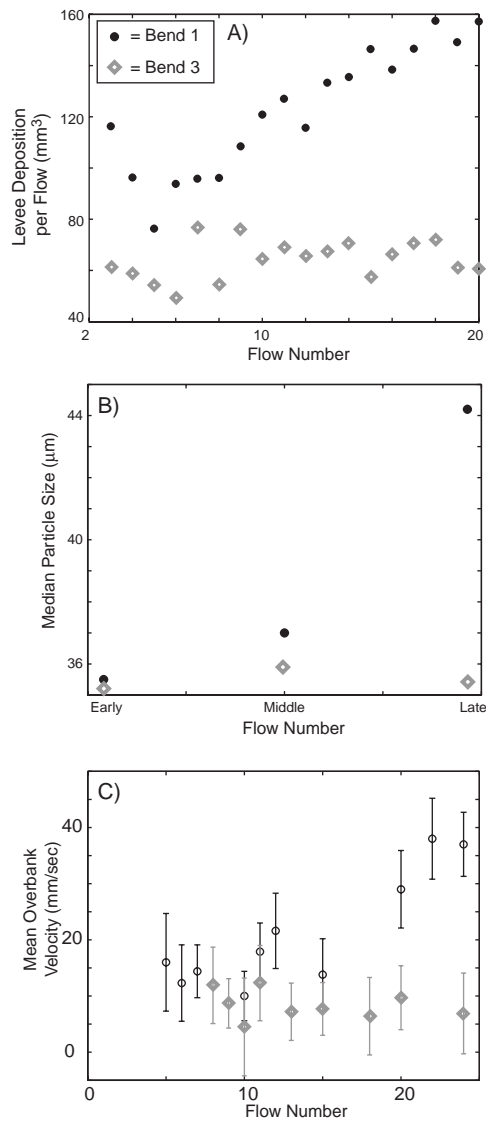
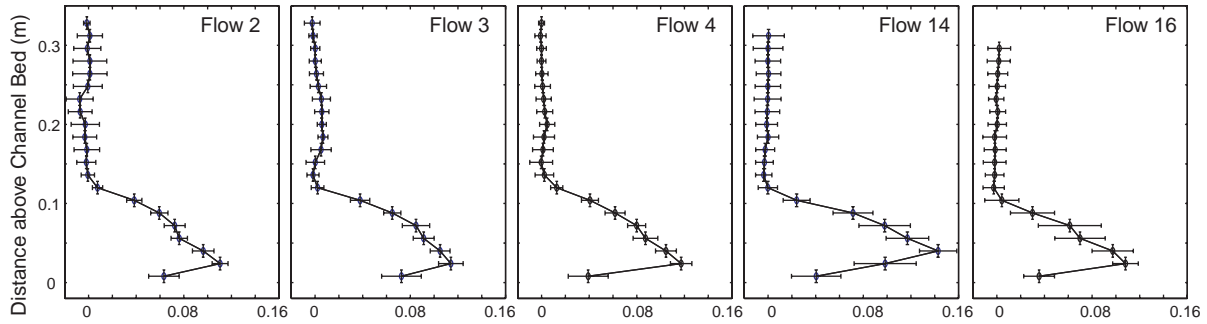


Figure 4.12. Temporal change in levee construction and levee-constructing flows at the outer banks of bends 1 and 3. These locations for bend 1 and bend 3 are labeled as sites ADP1 and ADP5 in Figure 4.4a. A: Volume of sediment deposited on the proximal levee as a function of current number. The volume corresponds to a swath of levee measured from 0.3 m upstream to 0.3 m downstream of the bend apex. Each point here represents a box-car averaging of deposit from three successive flows. B: Median particle size for the levee crest deposit on the outer bank of bend apices 1 and 3. C: Vertically averaged velocity for flow moving out across overbank surface at sites ADP1 and ADP5 (Fig. 4.4a). Velocity was measured using the PCADP and reported error bars represent plus and minus one standard deviation in the values for mean velocity collected every 4 seconds throughout the duration of each flow.

A) 1st Inflection Point



B) 2nd Inflection Point

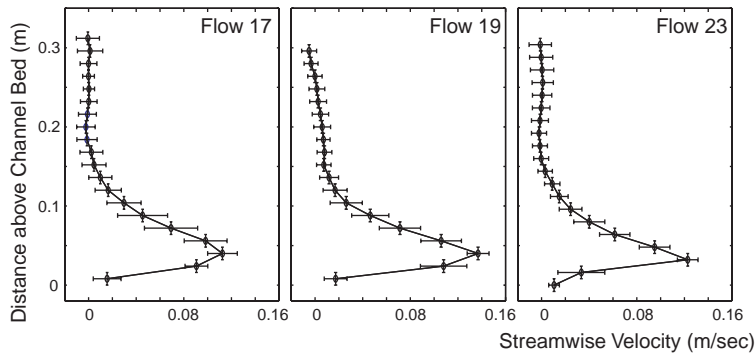


Figure 4.13. Profiles of downstream velocity for various currents measured at the channel centerline using the PCADP. Vertical error bars define the extent of each sampling volume while the horizontal error bars are plus and minus one standard deviation calculated using all values for current velocity collected in each sampling volume. A: Velocity profiles for a sequence of currents collected at the inflection point marked ADP2 in Figure 4.4a. B: Velocity profiles for currents measured at the channel inflection point marked ADP4 in Figure 4.4a.

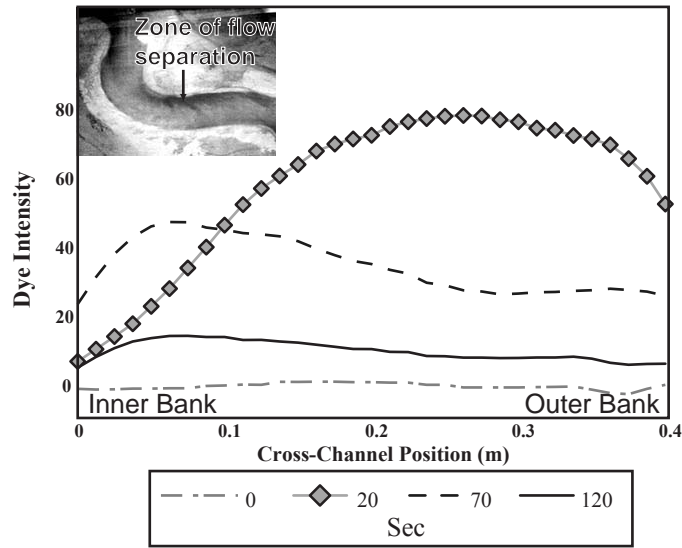


Figure 4.14. Defining a separation zone immediately downstream from the apex of bend 2 using time and space variation in tracer intensity recorded in digital photographs. Intensity of red dye released into a turbidity current was measured for each pixel across the channel at the streamwise position labeled ADP4 in Figure 4.4a ($x=0\text{m}$ =left channel edge, $x=0.4\text{m}$ =right channel edge). The line labeled 0 sec defines red intensity across the channel at the time immediately preceding arrival of the dye pulse. Lines 20, 70 and 120 sec describe the cross-stream variation in dye intensity 20, 70, and 120 s after passage of the leading edge of the dye plug. The zone of flow separation developed along the left-hand (inner) channel bank is defined here by relatively low dye concentrations at 20 s and relatively high dye concentrations at 70 s. The inset photo depicts the separation zone at the time roughly equal to 70 s and arrow indicates center of flow separation zone.

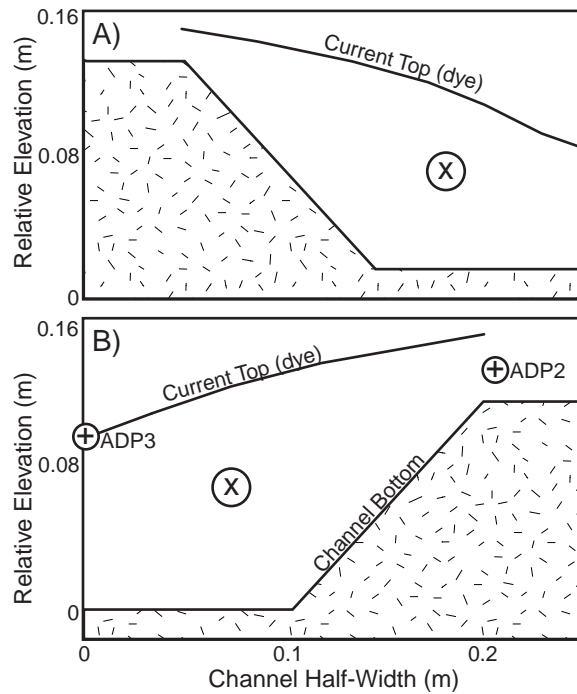


Figure 4.15. Measurements defining current superlevation at bends 1 and 2. A: Estimate of cross-channel elevation for the top of a current from analysis of dye injections recorded by overhead photographs at bend 1. This analysis suggests that the top of the current at the outer channel bank ($x = 0.2$ m) is elevated 4.9 cm above the top of the current at the channel centerline ($x = 0$ m). B: Estimate of cross-channel elevation for the top of a current from both dye-injection analysis and direct detection at bend 2. Dye analysis suggests that the top of the current at the outer channel bank ($x = 0.2$ m) is elevated 0.047 m above the top of the current at the channel centerline ($x = 0$ m). Relative elevations for the current top measured using the PCADP are labeled points ADP2 and ADP3. These point measurements define a difference in elevation between the outer bank and channel centerline of 0.024 cm.

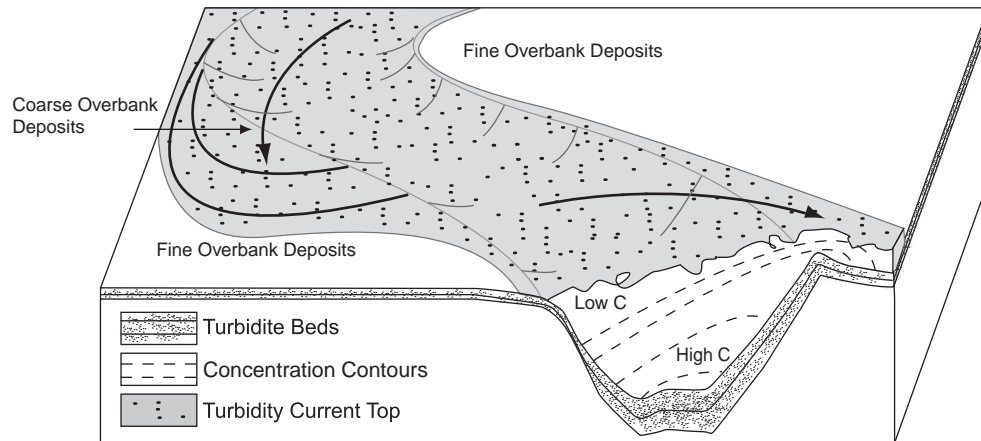
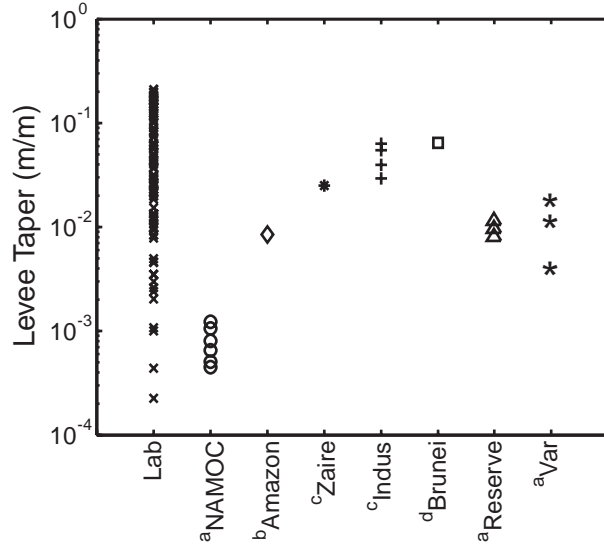


Figure 4.16. Schematic illustration of turbidity current flow in a sinuous channel. Arrows indicate direction of overbanking flow. Greater deposition occurs on outer bank relative to inner channel bank as a result of runup.



^aSkene, 1998; ^bPirmez et al., 1995;
^cDeptuck et al., 2003; ^dDemyttenaere et al., 2000

Figure 4.17. Comparison of experimental levee tapers following flow 24 with levee tapers measured from studies of 7 natural systems.

Table 4.1. Comparison of our experimental channel and currents to earlier theoretical and laboratory studies

	Kassem and Imran 2005	Das et. al 2004	Keevil et. al 2006	Present Study	Amazon ^{a,b}
	1.13	1.3	1.36	1.32	1.2-2.6
v/W	10	9.4	5.09	5	3-7
v/r_0	4.4	7.8	3.1	3.3	3-6
r_0/W	2.3	1.6	1.6	1.5	1-1.5
W/D	$\leq 10.6^*$	5.5	1.8	3.6-8.0	9-25
Downstream slope	0.08°	0.3°	3°	$0-1.20^\circ$	$0.14-0.40^\circ$
Sidewall slope	90°	90°	79°	$21-45^\circ$	$15-25^\circ$
Froude Number	1.22	1.46	0.63	0.53	0.5-0.8

* Currents were completely confined to channel; ^aPirmez and Flood, 1995; ^bPirmez et al., 2003

Table 4.2. Comparison of model and prototype flow characteristics

	model	prototype
U (m/s)	0.08	2.5
H (m)	0.12	120
T (hr)	8.8×10^{-2}	2.7
Fr	0.53	0.53
Re	8.2×10^3	3×10^8
C_f	3×10^{-2}	3×10^{-3}
u^* (m/s)	0.014	0.14
$w_s(D50)$ (m/s)	7.8×10^{-4}	8.1×10^{-3}
$w_s(D50)/u^*$	5.6×10^{-2}	5.6×10^{-2}
$D50$ (μm)	31	113

APPENDIXES

Appendix 1: Nomenclature

Appendix 2: Topographic maps from the experimental channel. Channel flow was from the left to the right in each map. Topography is defined as a vertical distance between the bed and an overlying datum of constant elevation. Contour interval is 10 mm. Coordinate system is defined by labeled X and Y locations of three map corners on Flow 1 map.

Appendix 3: Tables defining vertical profiles of velocity measured in the dominant (U_x) flow direction and standard deviation, σ , of U_x . X and Y locations defining horizontal position of PCADP probe correspond to coordinate system defined in Appendix 2.

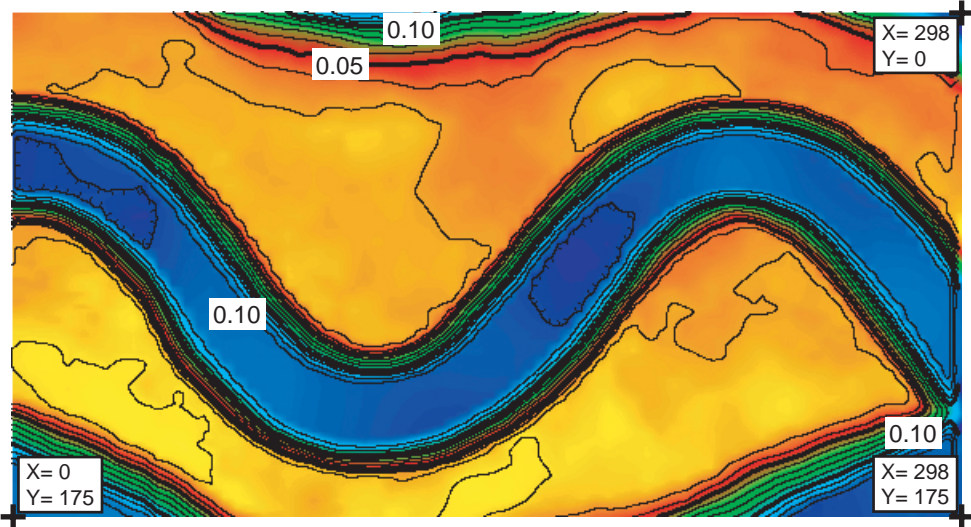
Appendix 4: Tables defining particle size distributions for deposits at 211 locations in experimental basin. X and Y locations defining horizontal position of particle size distributions correspond to coordinate system defined in Appendix 2.

APPENDIX 1

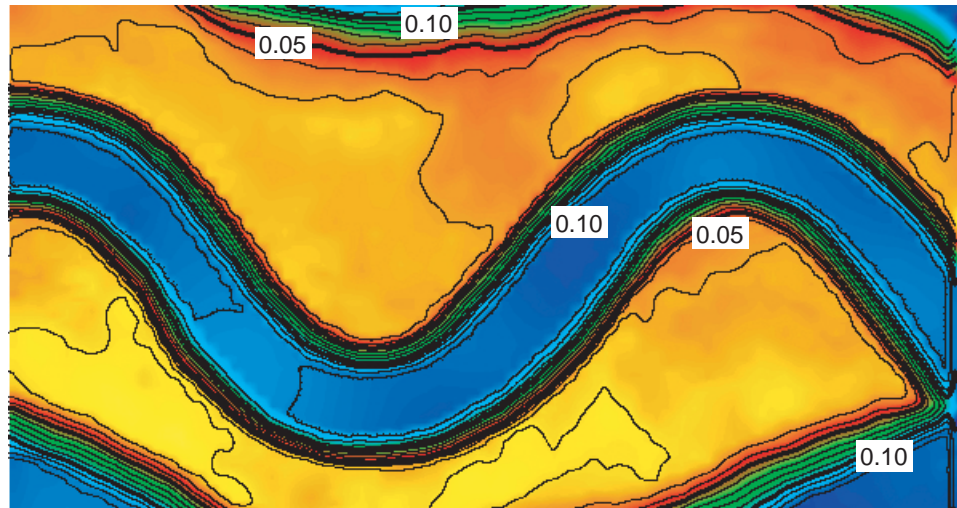
α	absorption coefficient
b	channel width
B_{θ}	buoyancy flux
c	<i>concentration of absorbing species</i>
C_f	bed friction coefficient
g	acceleration due to gravity
H	thickness of flow
Fr	Froude number
φ	angle of channel center-line relative to mean downstream direction
I	dye intensity
L	distance light passes through material
Re	Reynolds number
ρ_a	the density of the ambient water
ρ_c	the bulk density of the flow
r_0	channel centerline radius of curvature
S	Slope
T	Flow duration
τ_b	bottom shear stress
u	streamwise velocity
u^*	shear velocity
ν	kinematic viscosity
w_s	particle settling velocity
ω	maximum angle channel centerline makes with mean downstream direction
x	downstream distance
X_t	total downstream meander length
z	height above channel bed

APPENDIX 2

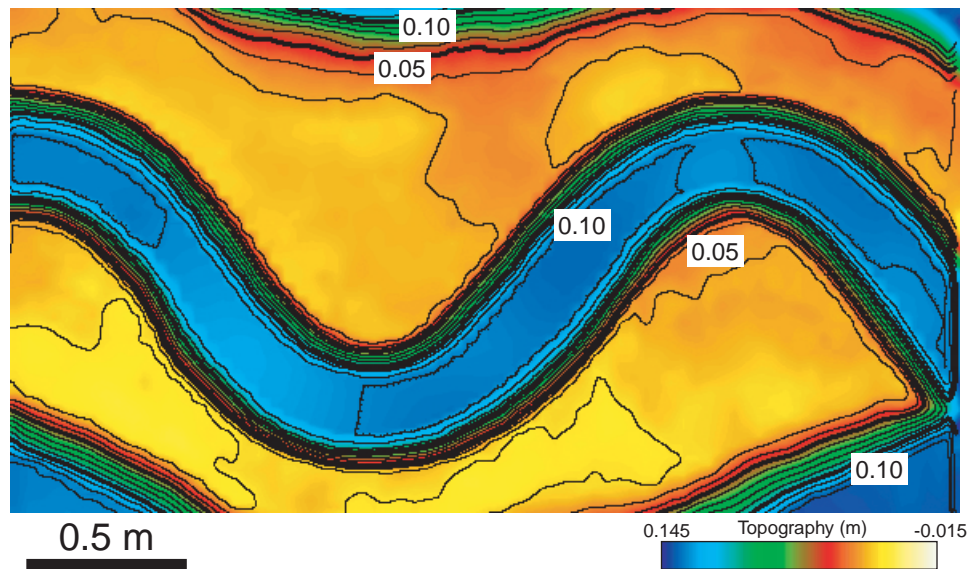
Flow 1



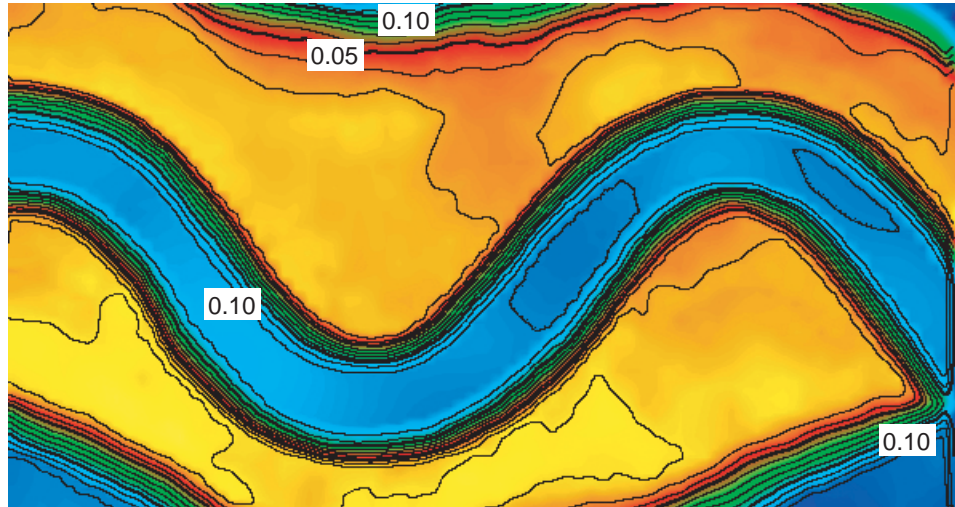
Flow 2



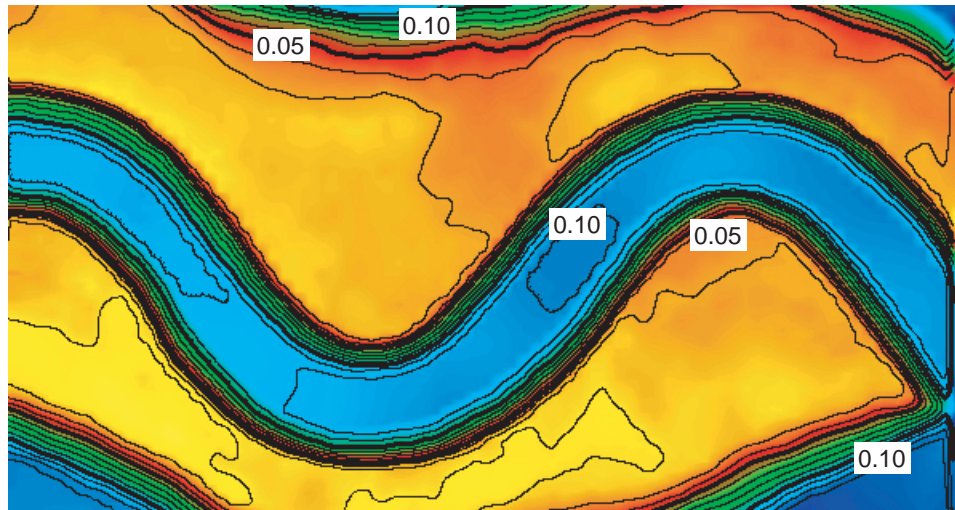
Flow 3



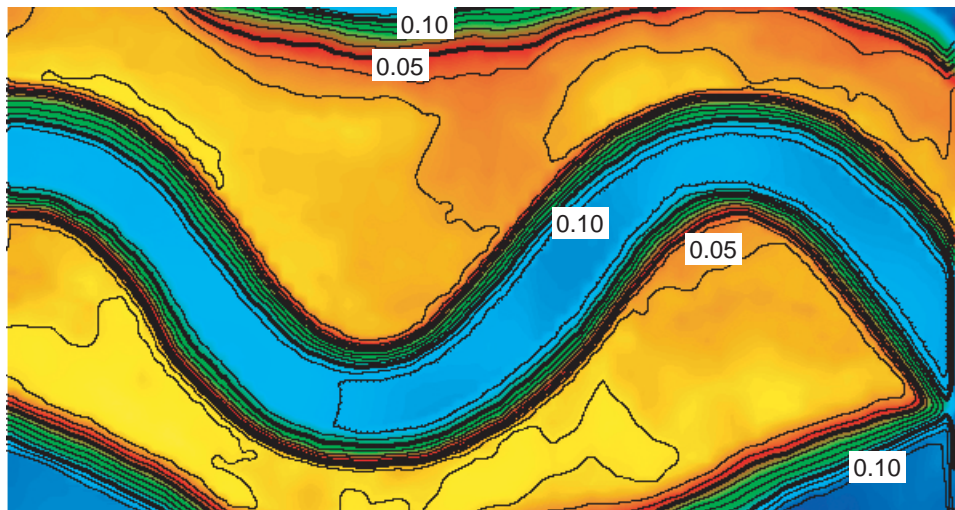
Flow 4



Flow 5



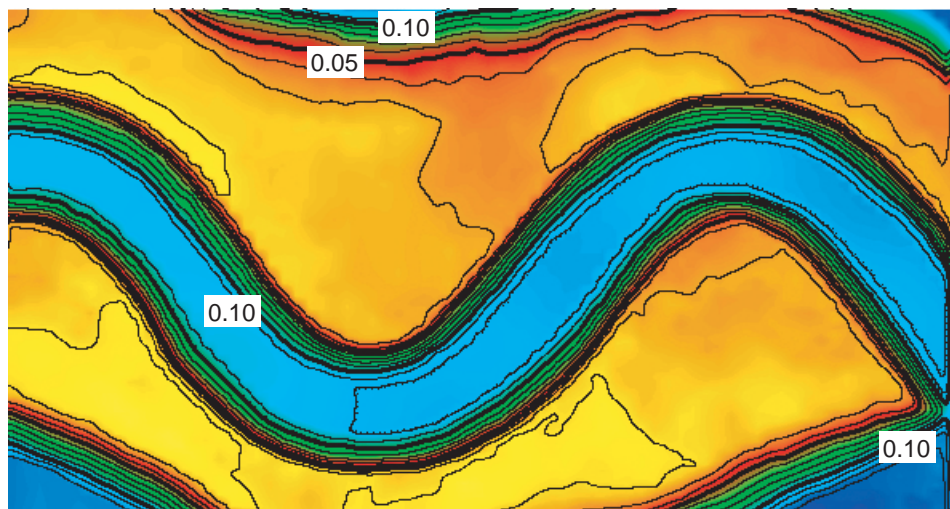
Flow 6



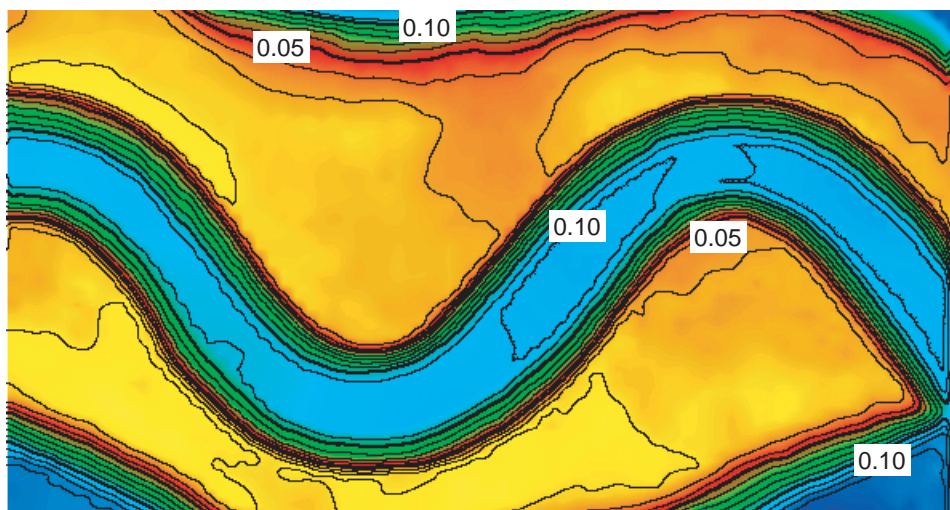
0.5 m

0.145 Topography (m) -0.015

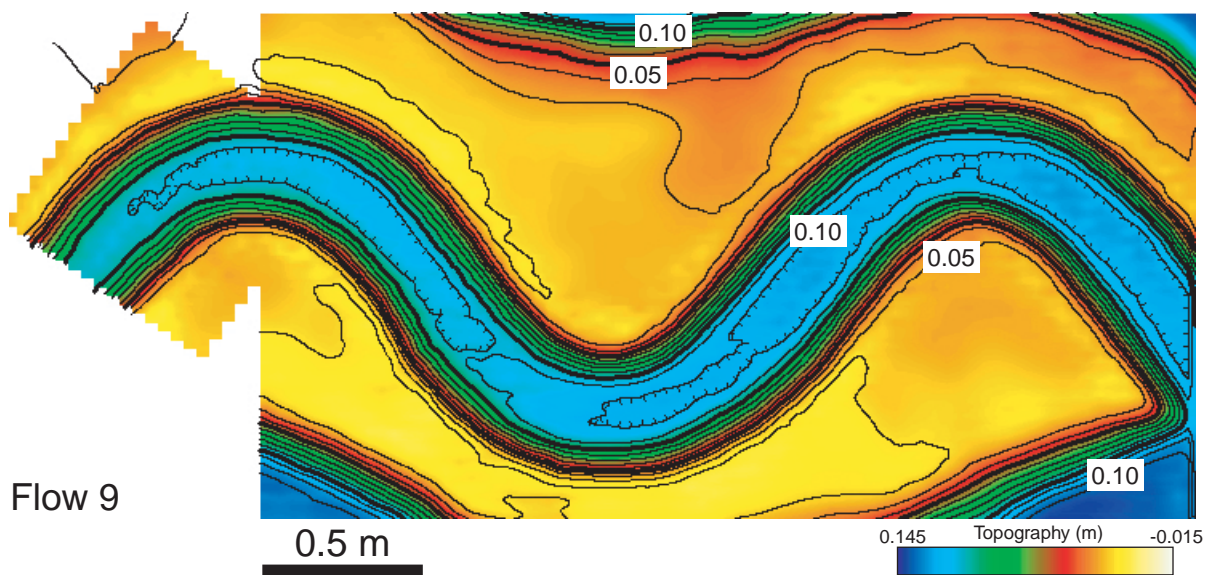
Flow 7

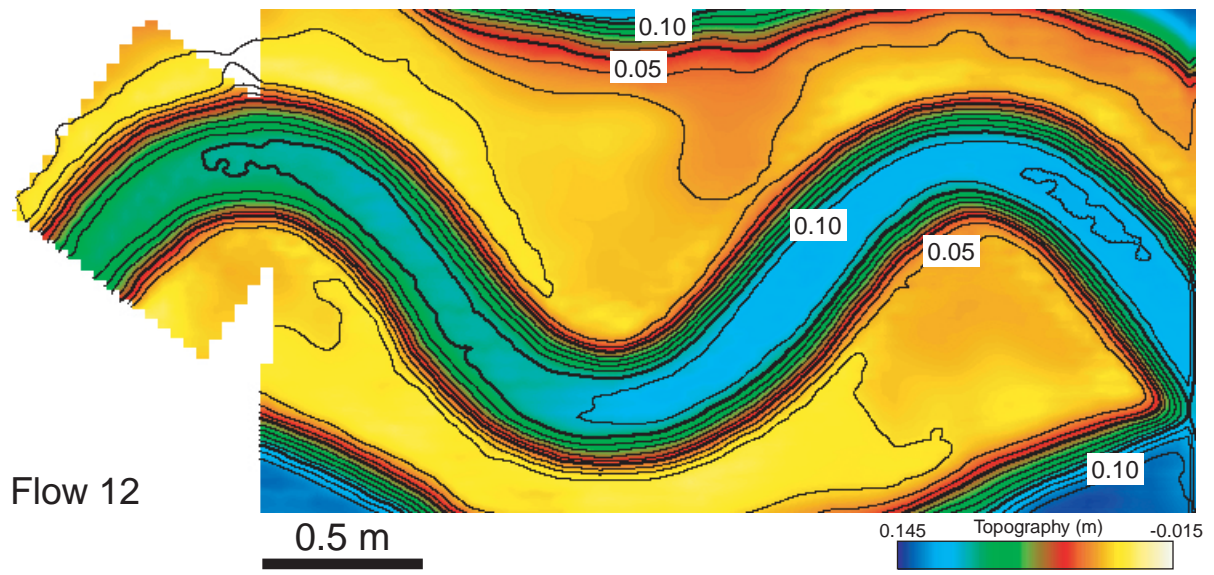
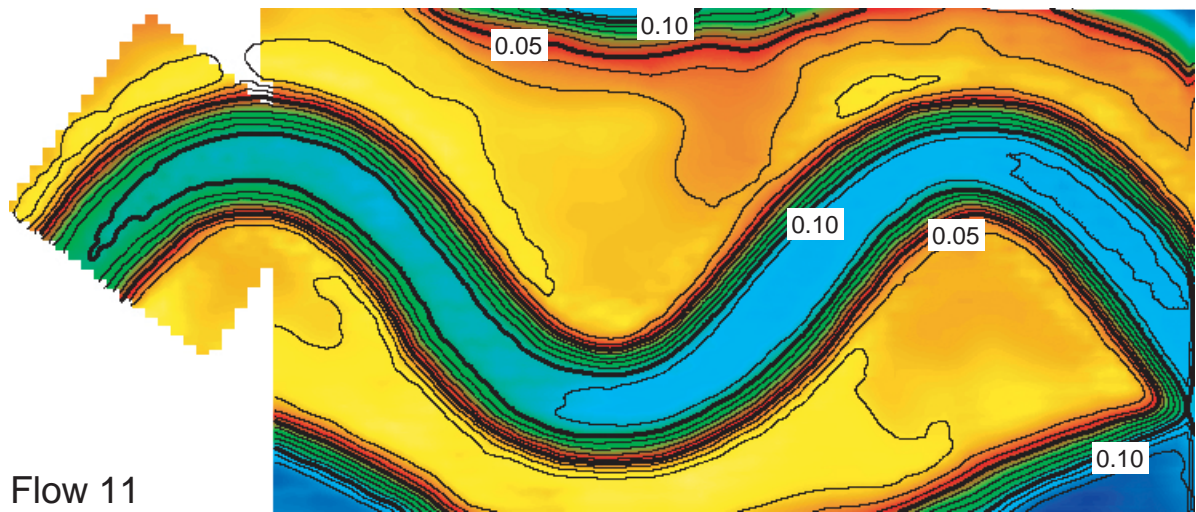
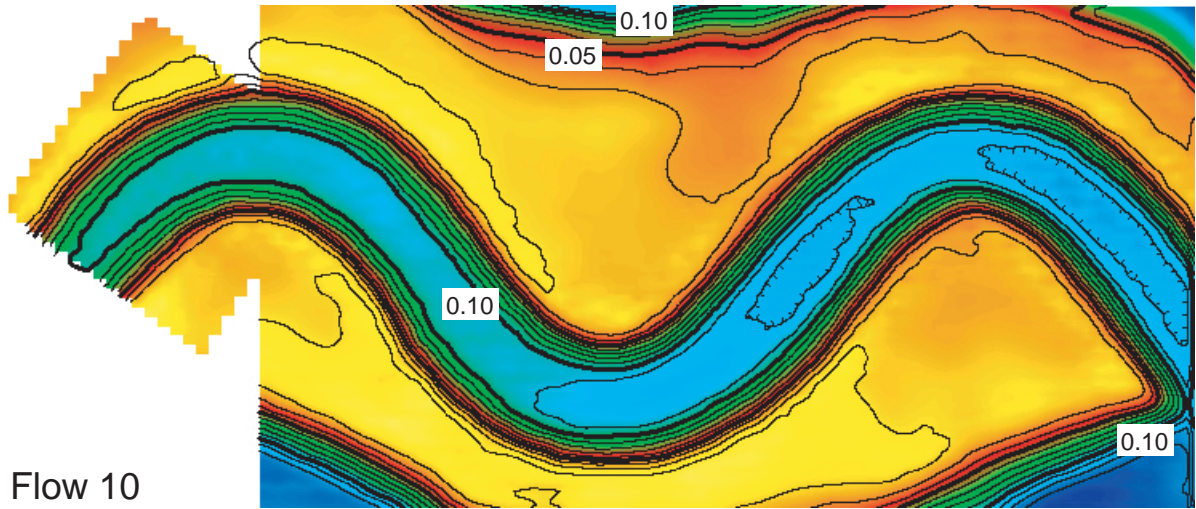


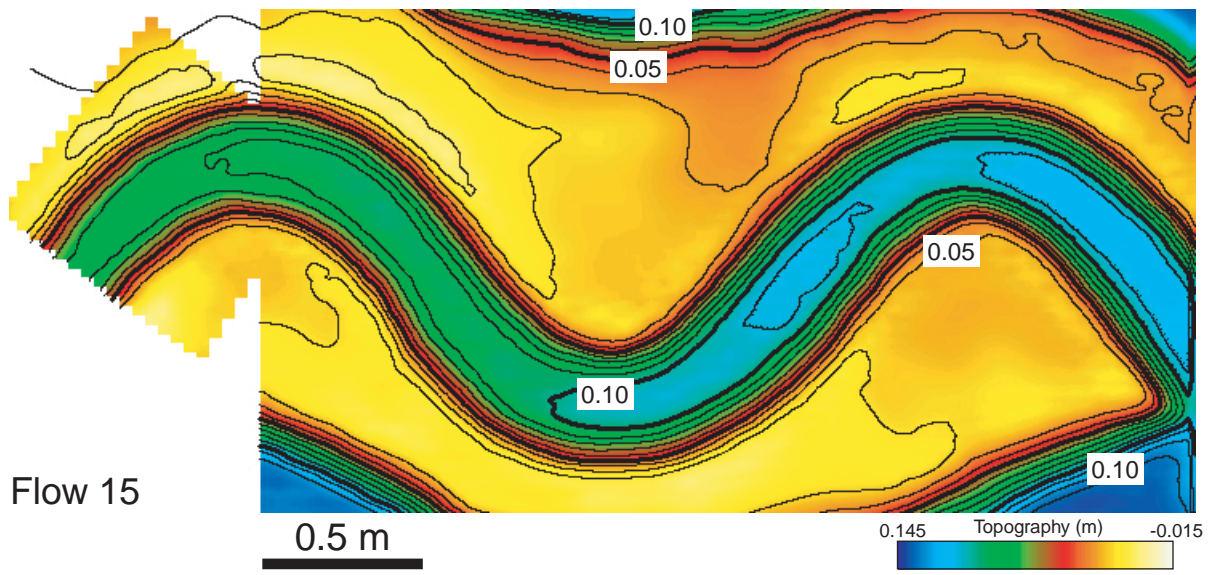
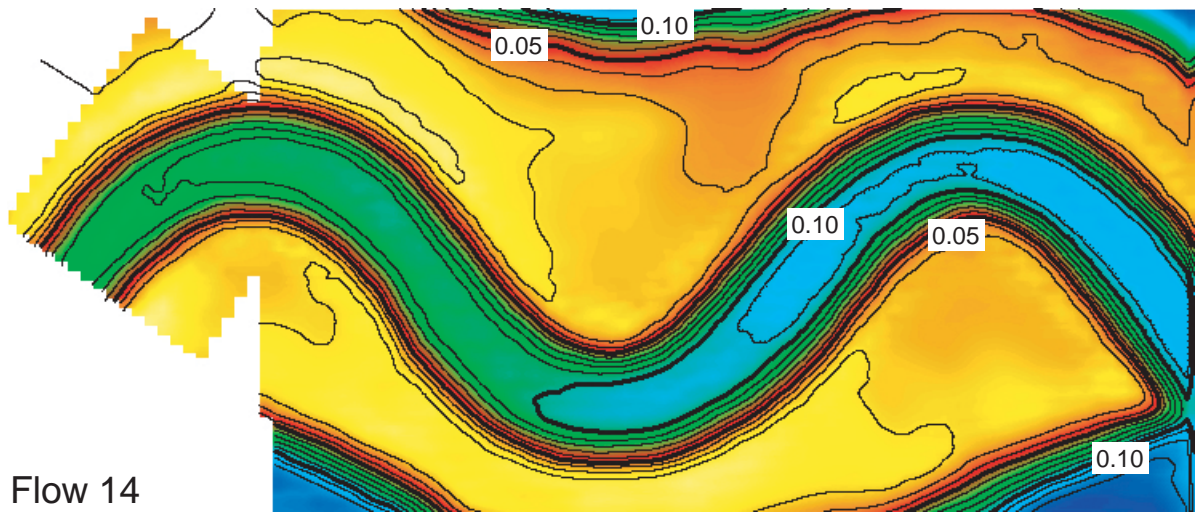
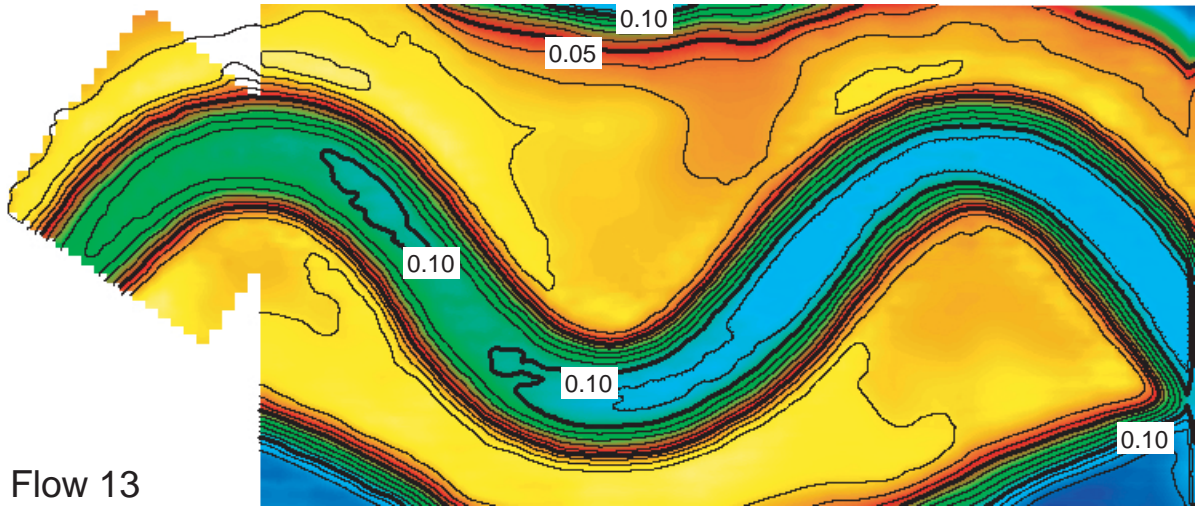
Flow 8

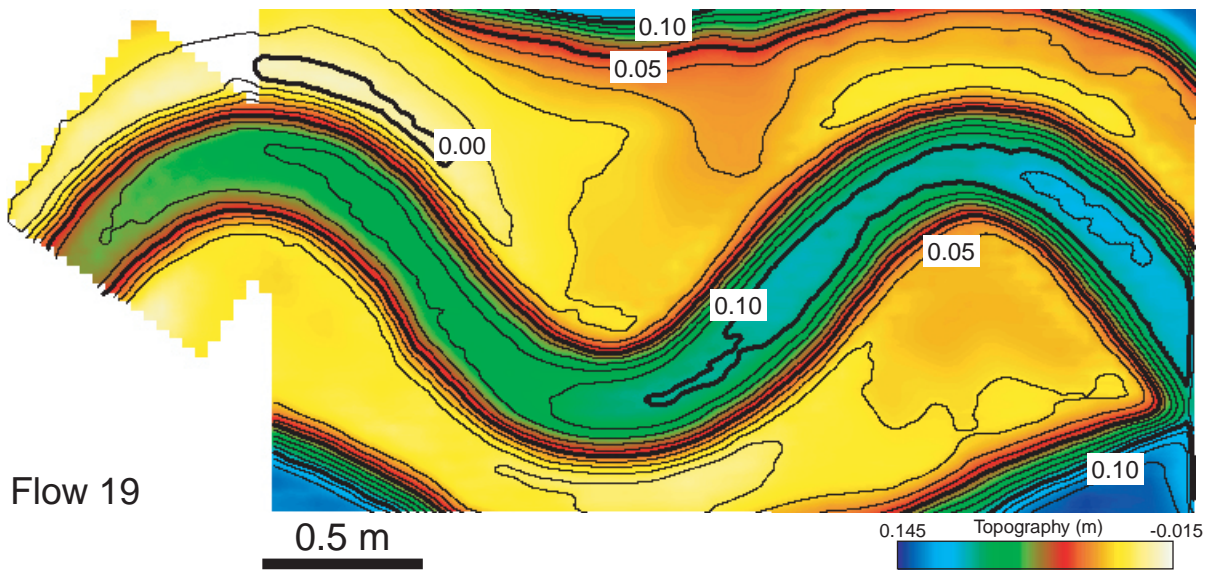
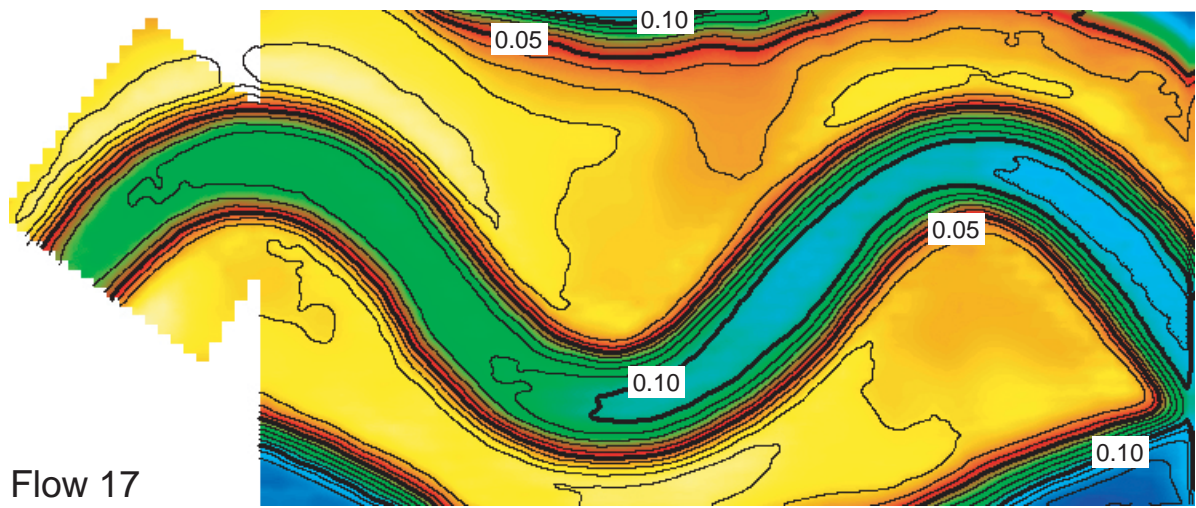
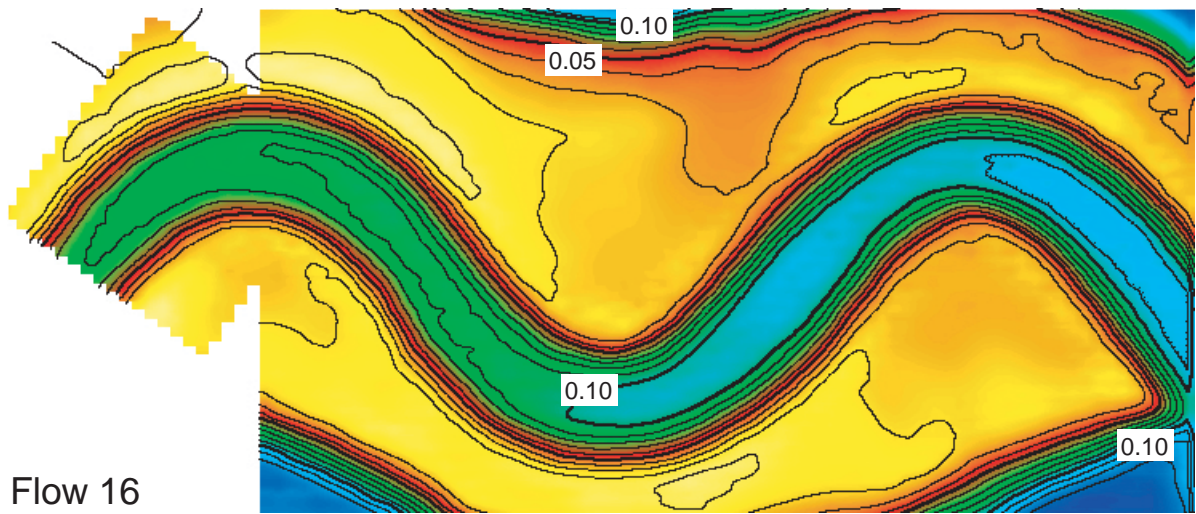


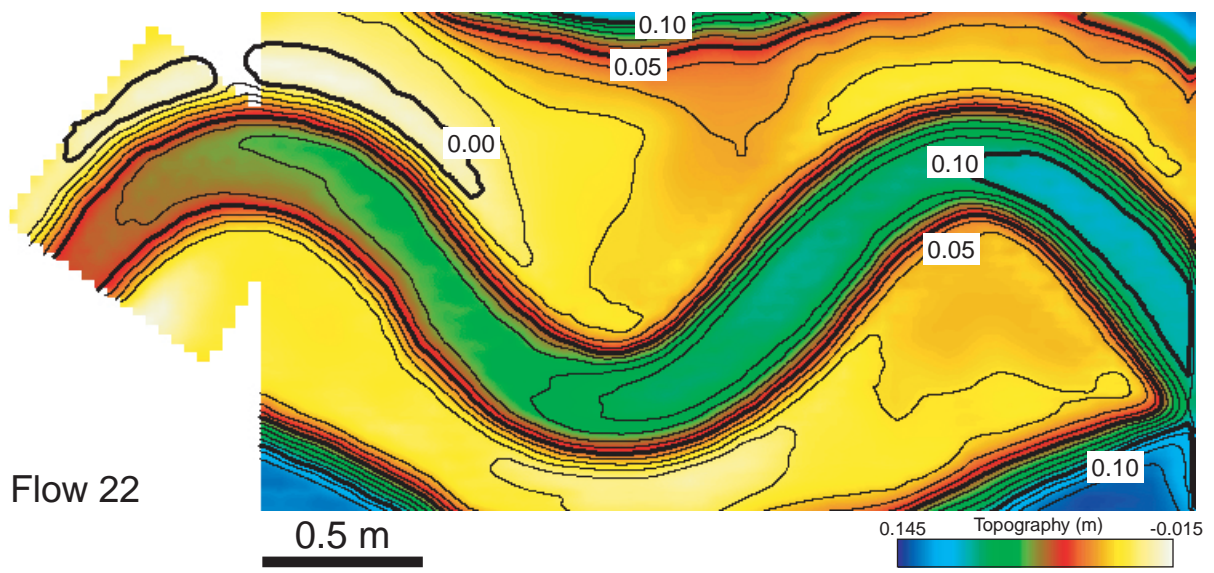
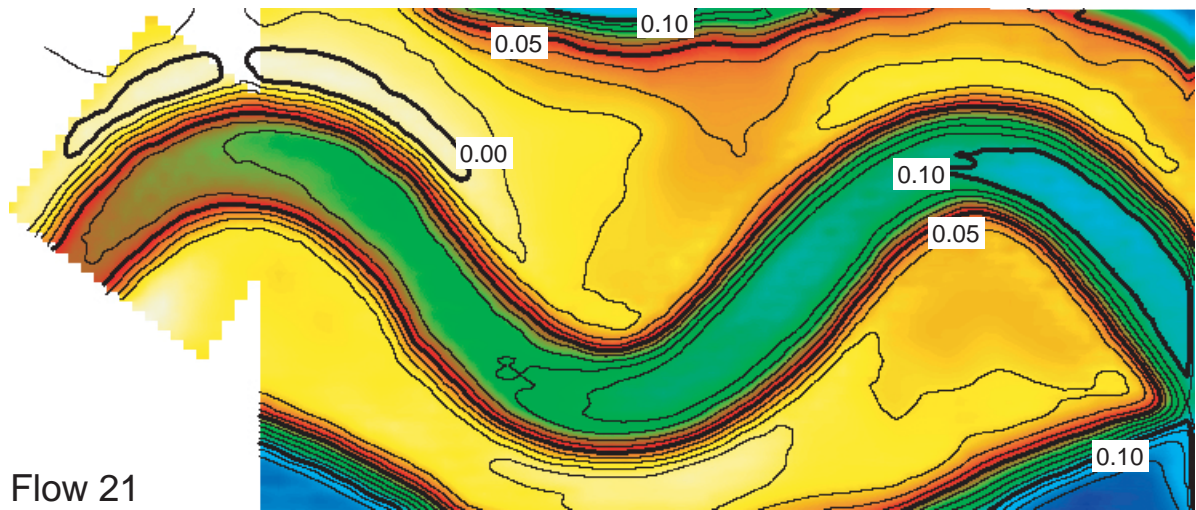
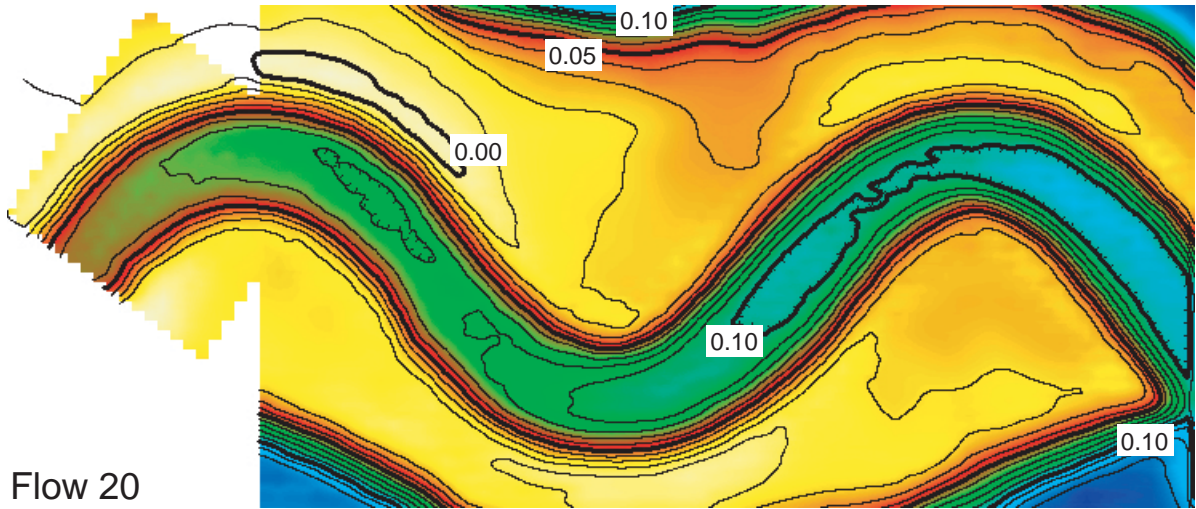
Flow 9

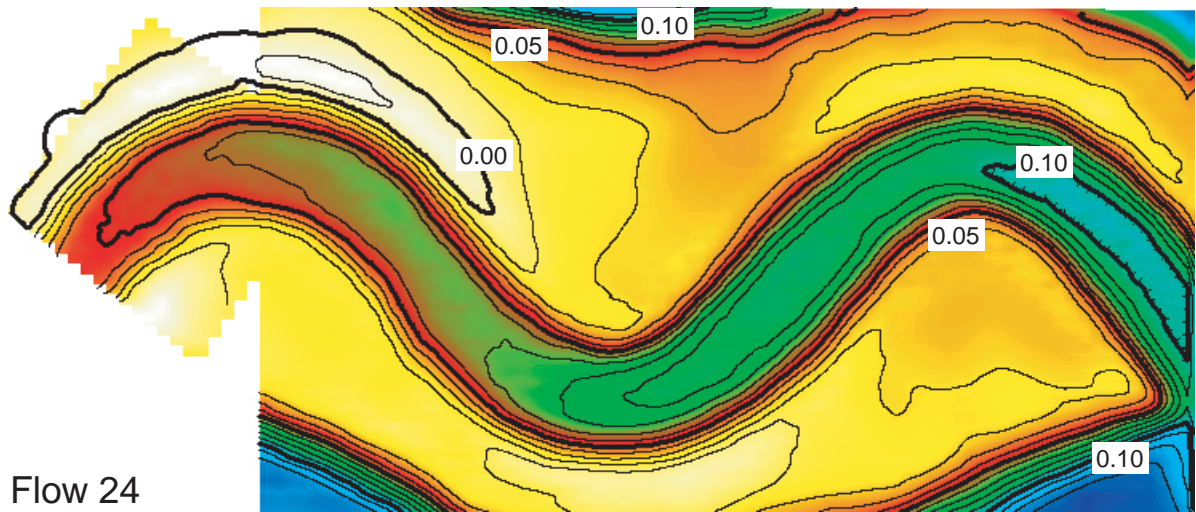
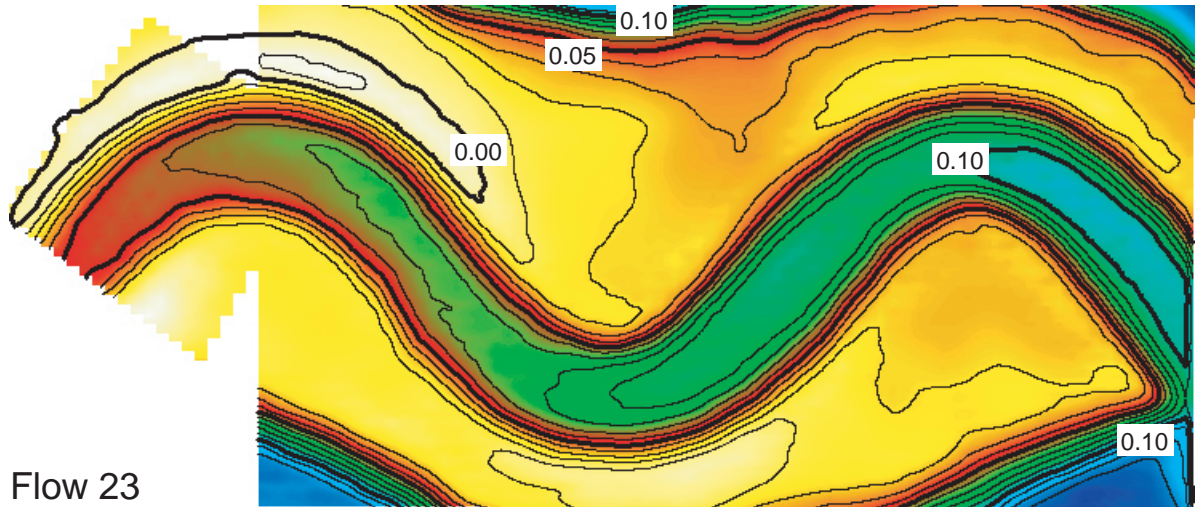












0.5 m

0.145 Topography (m) -0.015

APPENDIX 3

Flow #	2	3	4	5	6
X Location	65.6	65.6	65.6	27.3	27.3
Y Location	102.7	102.7	102.7	27.7	27.7

Height Above Bed (m)	U _x									
	(m/sec)	σ (m/sec)								
0.200	-0.002	0.011	0.007	0.004	0.004	0.008	-0.001	0.003	0.008	0.007
0.184	-0.002	0.008	0.005	0.009	0.002	0.009	-0.001	0.003	0.007	0.005
0.168	-0.001	0.006	0.000	0.008	0.001	0.009	0.000	0.002	0.006	0.007
0.152	0.008	0.004	-0.002	0.005	0.000	0.010	0.000	0.003	0.005	0.007
0.136	0.038	0.006	0.002	0.005	0.003	0.008	0.000	0.003	0.004	0.007
0.120	0.059	0.007	0.038	0.008	0.013	0.005	0.000	0.003	0.004	0.006
0.104	0.072	0.009	0.065	0.007	0.040	0.010	0.002	0.005	0.003	0.007
0.088	0.076	0.007	0.085	0.012	0.061	0.011	0.001	0.005	0.000	0.008
0.072	0.096	0.009	0.091	0.009	0.080	0.008	0.001	0.006	-0.002	0.010
0.056	0.110	0.007	0.105	0.008	0.088	0.010	-0.001	0.011	-0.003	0.013
0.040	0.063	0.013	0.114	0.010	0.104	0.011	0.006	0.013	0.004	0.013
0.024	0.040	0.017	0.073	0.017	0.116	0.012	0.028	0.014	0.025	0.010
0.008	0.021	0.011	0.025	0.008	0.042	0.017	0.015	0.006	0.009	0.007

Flow #	7	8	9	10	10
X Location	27.3	243.1	243.1	27.3	243.1
Y Location	27.7	26.3	26.3	27.7	26.3

Height Above Bed (m)	U _x									
	(m/sec)	σ (m/sec)								
0.200	0.000	0.005	-0.001	0.004	-0.004	0.003	0.002	0.007	0.000	0.013
0.184	0.001	0.005	0.003	0.004	-0.001	0.004	-0.001	0.008	-0.002	0.012
0.168	0.001	0.006	0.007	0.006	0.002	0.004	0.000	0.008	0.000	0.012
0.152	0.003	0.006	0.003	0.006	0.003	0.005	0.000	0.008	0.001	0.013
0.136	0.004	0.006	0.003	0.005	0.002	0.004	-0.004	0.009	0.001	0.012
0.120	0.005	0.007	-0.001	0.007	0.001	0.006	-0.002	0.010	0.001	0.012
0.104	0.003	0.006	-0.005	0.003	-0.001	0.010	-0.003	0.010	0.002	0.012
0.088	0.002	0.006	-0.005	0.004	-0.004	0.008	-0.005	0.008	0.001	0.010
0.072	0.001	0.006	-0.005	0.005	0.001	0.010	-0.006	0.009	0.004	0.010
0.056	0.003	0.007	-0.001	0.003	0.000	0.013	-0.004	0.008	0.004	0.009
0.040	0.023	0.007	0.007	0.007	0.001	0.013	0.002	0.008	0.003	0.009
0.024	0.019	0.004	0.018	0.004	0.013	0.010	0.030	0.012	0.011	0.005
0.008	0.012	0.005	0.011	0.004	0.012	0.007	0.000	0.003	0.002	0.002

Flow #	11	11	12	13	13
X Location	27.3	243.1	27.3	27.3	243.1
Y Location	27.7	26.3	27.7	27.7	26.3

Height Above Bed (m)	U _x (m/sec)	σ (m/sec)								
0.200	0.005	0.009	0.001	0.009	-0.001	0.008	-0.003	0.005	-0.001	0.015
0.184	0.002	0.008	0.003	0.009	0.000	0.009	0.000	0.006	-0.008	0.035
0.168	0.001	0.008	0.005	0.011	0.002	0.009	0.001	0.007	0.002	0.014
0.152	-0.001	0.008	0.004	0.010	0.002	0.010	0.002	0.007	0.006	0.015
0.136	0.000	0.009	0.004	0.010	0.000	0.008	0.003	0.007	0.006	0.014
0.120	-0.002	0.010	0.000	0.010	-0.001	0.007	0.002	0.007	0.003	0.013
0.104	-0.001	0.010	-0.004	0.010	-0.001	0.007	0.003	0.008	0.007	0.012
0.088	-0.002	0.008	-0.005	0.011	-0.001	0.007	0.003	0.005	0.008	0.011
0.072	-0.001	0.008	-0.003	0.011	-0.003	0.008	0.006	0.005	0.010	0.009
0.056	0.000	0.008	-0.002	0.011	-0.003	0.010	0.011	0.005	0.015	0.007
0.040	0.013	0.013	-0.002	0.006	0.008	0.010	0.016	0.003	0.024	0.007
0.024	0.038	0.008	0.017	0.005	0.042	0.008	0.019	0.004	0.018	0.002
0.008	0.008	0.007	0.005	0.005	0.015	0.004	0.019	0.002	0.014	0.002

Flow #	14	15	15	16	17
X Location	65.6	243.1	27.3	65.6	177.9
Y Location	102.7	26.3	27.7	102.7	84.7

Height Above Bed (m)	U _x (m/sec)	σ (m/sec)								
0.200	-0.001	0.009	0.003	0.003	0.001	0.012	-0.001	0.010	-0.002	0.008
0.184	0.000	0.009	-0.001	0.002	0.002	0.010	-0.002	0.010	-0.001	0.009
0.168	-0.002	0.008	-0.005	0.002	0.000	0.009	-0.003	0.011	0.002	0.010
0.152	-0.003	0.007	-0.008	0.002	0.000	0.008	-0.001	0.008	0.005	0.010
0.136	-0.004	0.007	-0.009	0.001	0.000	0.007	-0.002	0.009	0.010	0.010
0.120	0.000	0.008	-0.010	0.001	-0.001	0.007	0.001	0.016	0.016	0.011
0.104	0.024	0.011	-0.008	0.001	-0.002	0.006	0.026	0.020	0.030	0.014
0.088	0.071	0.017	-0.006	0.001	-0.005	0.005	0.054	0.029	0.045	0.021
0.072	0.098	0.022	-0.005	0.001	-0.010	0.006	0.063	0.025	0.069	0.022
0.056	0.117	0.018	-0.002	0.001	-0.007	0.010	0.088	0.025	0.098	0.018
0.040	0.143	0.016	0.002	0.002	0.023	0.011	0.096	0.026	0.112	0.012
0.024	0.098	0.026	0.018	0.002	0.020	0.006	0.040	0.013	0.091	0.010
0.008	0.040	0.021	0.006	0.000	0.013	0.003	0.032	0.030	0.016	0.012

Flow #	18	19	20	20	22
X Location	243.1	177.9	243.1	27.3	27.3
Y Location	26.3	84.7	26.3	27.7	27.7

Height Above Bed (m)	U _x (m/sec)	σ (m/sec)								
0.200	-0.006	0.010	0.006	0.007	0.000	0.007	0.002	0.011	-0.001	0.010
0.184	-0.005	0.010	0.007	0.006	0.000	0.006	0.001	0.012	0.000	0.011
0.168	-0.002	0.008	0.008	0.006	0.001	0.006	0.000	0.012	0.001	0.012
0.152	0.002	0.008	0.007	0.006	0.001	0.006	-0.001	0.012	0.000	0.011
0.136	0.006	0.008	0.012	0.008	0.000	0.007	-0.001	0.010	0.001	0.010
0.120	0.007	0.008	0.017	0.010	0.000	0.008	-0.002	0.010	-0.001	0.009
0.104	0.006	0.009	0.026	0.013	0.001	0.008	-0.003	0.008	-0.002	0.010
0.088	0.007	0.007	0.046	0.016	0.000	0.009	-0.004	0.008	-0.004	0.010
0.072	0.007	0.006	0.071	0.017	-0.001	0.009	-0.007	0.008	-0.008	0.008
0.056	0.006	0.009	0.106	0.017	-0.002	0.006	-0.006	0.007	-0.002	0.008
0.040	0.006	0.008	0.137	0.009	0.000	0.007	0.002	0.007	0.019	0.009
0.024	0.014	0.007	0.108	0.020	0.017	0.011	0.027	0.011	0.064	0.011
0.008	0.012	0.005	0.017	0.010	0.007	0.003	0.010	0.002	0.031	0.008

Flow #	23	24	24
X Location	177.9	27.3	243.1
Y Location	84.7	27.7	26.3

Height Above Bed (m)	U _x (m/sec)	σ (m/sec)	U _x (m/sec)	σ (m/sec)	U _x (m/sec)	σ (m/sec)
0.200	-0.002	0.006	0.000	0.015	-0.002	0.015
0.184	-0.001	0.006	0.000	0.015	0.001	0.014
0.168	0.000	0.006	0.000	0.016	0.005	0.012
0.152	0.003	0.006	0.000	0.016	0.007	0.010
0.136	0.009	0.006	0.000	0.017	0.006	0.008
0.120	0.015	0.007	-0.001	0.016	0.005	0.007
0.104	0.024	0.010	-0.001	0.016	0.001	0.006
0.088	0.040	0.013	0.000	0.016	-0.004	0.005
0.072	0.061	0.013	0.000	0.016	-0.005	0.004
0.056	0.095	0.013	0.002	0.018	-0.003	0.005
0.040	0.123	0.009	0.009	0.021	0.002	0.006
0.024	0.033	0.020	0.013	0.020	0.018	0.008
0.008	0.010	0.004	0.010	0.027	0.005	0.000

APPENDIX 4

Sample #	A1	A2	A3	A4	A5	A6	A7	A8	A-1	A-2	A-3
X Location	-54.8	-58.9	-63.0	-67.1	-71.2	-75.3	-79.4	-83.5	-50.7	-46.6	-42.5
Y Location	89.2	86.3	83.4	80.6	77.7	74.8	72.0	69.1	92.1	94.9	97.8

Grain Size (μm)	%	%	%	%	%	%	%	%	%	%	%
	Finner										
1.0	0.0	0.0	0.0	0.0	0.0	0.0	0.0	0.0	0.0	0.0	0.0
1.2	0.0	0.0	0.0	0.1	0.1	0.0	0.0	0.1	0.0	0.0	0.0
1.3	0.1	0.1	0.1	0.3	0.3	0.1	0.1	0.3	0.1	0.1	0.2
1.5	0.3	0.3	0.3	0.5	0.5	0.3	0.3	0.5	0.3	0.4	0.4
1.7	0.6	0.6	0.6	0.6	0.7	0.5	0.5	0.8	0.6	0.6	0.6
2.0	0.9	0.8	0.8	0.8	0.9	0.7	0.7	1.1	0.9	0.9	0.9
2.3	1.2	1.1	1.1	0.9	1.2	0.9	0.9	1.3	1.2	1.2	1.1
2.6	1.4	1.3	1.3	0.9	1.4	1.0	1.1	1.6	1.4	1.5	1.4
3.0	1.7	1.6	1.4	0.9	1.5	1.1	1.2	1.7	1.7	1.7	1.6
3.4	1.9	1.7	1.5	0.9	1.7	1.1	1.2	1.9	1.9	1.9	1.7
3.9	2.0	1.9	1.5	0.9	1.7	1.1	1.2	2.0	2.0	2.1	1.8
4.5	2.2	2.0	1.5	0.9	1.7	1.1	1.2	2.0	2.1	2.2	1.8
5.1	2.2	2.1	1.5	0.9	1.7	1.1	1.2	2.0	2.1	2.2	1.8
5.9	2.2	2.1	1.5	0.9	1.7	1.1	1.2	2.0	2.1	2.2	1.8
6.7	2.2	2.1	1.5	0.9	1.7	1.1	1.2	2.0	2.1	2.2	1.8
7.7	2.2	2.1	1.5	0.9	1.7	1.1	1.2	2.0	2.1	2.2	1.8
8.8	2.2	2.1	1.5	0.9	1.7	1.1	1.2	2.0	2.1	2.2	1.8
10.1	2.2	2.1	1.5	0.9	1.7	1.1	1.2	2.0	2.1	2.2	1.8
11.6	2.2	2.2	1.5	0.9	1.7	1.1	1.2	2.0	2.1	2.2	1.8
13.2	2.2	2.4	1.5	0.9	1.7	1.1	1.2	2.0	2.3	2.3	1.8
15.2	2.3	2.6	1.5	0.9	1.8	1.1	1.4	2.2	2.4	2.5	1.9
17.4	2.5	3.0	1.7	0.9	2.1	1.3	1.6	2.5	2.7	2.9	2.1
19.9	3.0	3.6	2.0	0.9	2.6	1.6	2.1	3.2	3.2	3.5	2.5
22.8	3.8	4.7	2.7	1.1	3.5	2.2	3.1	4.5	4.1	4.7	3.3
26.1	5.3	6.8	4.0	1.8	5.4	3.6	5.1	7.1	5.8	6.8	4.8
29.9	8.1	10.2	6.6	3.3	8.9	6.3	8.8	11.8	8.8	10.4	7.8
34.3	12.9	15.8	11.3	6.8	14.8	11.1	14.9	19.6	13.7	16.2	13.1
39.2	20.5	24.0	18.8	13.5	23.7	18.6	23.7	30.7	21.2	24.3	21.4
44.9	31.0	34.7	29.4	24.6	35.5	28.8	34.5	44.5	31.2	34.6	32.8
51.5	43.8	47.0	42.3	39.9	49.1	40.6	46.0	59.0	43.0	46.3	46.2
59.0	57.3	59.5	55.8	57.0	62.4	52.5	56.6	72.1	55.3	57.8	59.9
67.5	69.7	70.7	68.2	72.7	73.9	62.9	65.4	82.3	66.6	68.3	72.0
77.3	79.8	79.7	78.4	84.5	82.8	71.2	72.1	89.4	76.0	77.0	81.6
88.6	87.1	86.4	85.9	92.1	89.0	77.4	77.1	93.8	83.3	83.7	88.4
101.5	92.1	91.2	91.2	96.3	93.2	81.9	80.7	96.5	88.7	88.8	93.0
116.2	95.4	94.5	94.7	98.4	96.0	85.1	83.5	98.1	92.7	92.7	95.9
133.1	97.5	96.9	97.1	99.5	97.7	87.6	85.7	99.1	95.6	95.5	97.8
152.5	98.8	98.5	98.6	100.0	99.0	89.5	87.5	99.7	97.7	97.7	99.0
174.6	99.6	99.5	99.5	100.0	99.6	91.1	89.1	100.0	99.0	98.9	99.6
200.0	100.0	100.0	100.0	100.0	100.0	92.5	90.6	100.0	99.6	99.6	100.0
229.1	100.0	100.0	100.0	100.0	100.0	93.7	92.1	100.0	100.0	100.0	100.0
262.4	100.0	100.0	100.0	100.0	100.0	94.9	93.5	100.0	100.0	100.0	100.0
300.5	100.0	100.0	100.0	100.0	100.0	96.0	94.9	100.0	100.0	100.0	100.0

Sample #	A-4	A-5	A-6	A-7	A-8	B1	B2	B3	B4	B5	B6
X Location	-38.4	-34.3	-30.2	-26.1	-22.0	-26.5	-29.4	-32.2	-35.0	-37.8	-40.7
Y Location	100.7	103.5	106.4	109.3	112.1	59.3	55.2	51.1	47.0	42.9	38.7

Grain Size (μm)	%	%	%	%	%	%	%	%	%	%	%
	Finner										
1.0	0.0	0.0	0.0	0.0	0.0	0.0	0.0	0.0	0.0	0.0	0.0
1.2	0.0	0.1	0.0	0.1	0.0	0.0	0.1	0.0	0.1	0.0	0.1
1.3	0.1	0.3	0.2	0.3	0.2	0.1	0.3	0.1	0.3	0.2	0.3
1.5	0.3	0.5	0.3	0.5	0.4	0.4	0.5	0.3	0.5	0.4	0.5
1.7	0.5	0.7	0.6	0.7	0.6	0.6	0.7	0.6	0.7	0.6	0.8
2.0	0.7	0.9	0.8	1.0	0.9	0.9	1.0	0.8	1.0	0.8	1.0
2.3	0.9	1.1	1.0	1.2	1.2	1.2	1.3	1.1	1.2	1.0	1.2
2.6	1.1	1.2	1.2	1.3	1.4	1.5	1.5	1.3	1.3	1.2	1.3
3.0	1.2	1.4	1.4	1.4	1.5	1.8	1.7	1.5	1.5	1.4	1.4
3.4	1.2	1.4	1.5	1.4	1.7	2.0	1.9	1.6	1.5	1.4	1.4
3.9	1.2	1.4	1.5	1.4	1.7	2.2	2.0	1.6	1.5	1.4	1.4
4.5	1.2	1.4	1.5	1.4	1.7	2.3	2.0	1.6	1.5	1.4	1.4
5.1	1.2	1.4	1.5	1.4	1.7	2.4	2.0	1.6	1.5	1.4	1.4
5.9	1.2	1.4	1.5	1.4	1.7	2.4	2.0	1.6	1.5	1.4	1.4
6.7	1.2	1.4	1.5	1.4	1.7	2.4	2.0	1.6	1.5	1.4	1.4
7.7	1.2	1.4	1.5	1.4	1.7	2.4	2.0	1.6	1.5	1.4	1.4
8.8	1.2	1.4	1.5	1.4	1.7	2.4	2.0	1.6	1.5	1.4	1.4
10.1	1.2	1.4	1.5	1.4	1.7	2.4	2.0	1.6	1.5	1.4	1.4
11.6	1.2	1.4	1.5	1.4	1.7	2.4	2.0	1.6	1.5	1.4	1.4
13.2	1.2	1.4	1.5	1.4	1.7	2.5	2.0	1.6	1.5	1.4	1.4
15.2	1.2	1.4	1.5	1.4	1.7	2.7	2.1	1.6	1.5	1.4	1.4
17.4	1.2	1.5	1.6	1.6	1.9	2.9	2.4	1.7	1.6	1.5	1.6
19.9	1.4	1.8	1.8	1.9	2.3	3.4	2.8	2.0	2.0	1.9	2.1
22.8	1.9	2.4	2.4	2.6	3.1	4.2	3.7	2.5	2.8	2.7	3.2
26.1	2.8	3.7	3.5	4.1	4.9	5.8	5.5	3.7	4.6	4.4	5.5
29.9	4.8	6.2	5.9	7.3	8.4	8.7	8.9	6.1	8.2	7.7	10.1
34.3	8.6	10.9	10.3	13.2	14.7	13.8	14.8	10.6	14.7	13.5	17.9
39.2	15.0	18.5	17.7	23.0	24.6	21.8	24.0	18.5	25.0	22.5	29.4
44.9	24.6	29.2	28.5	36.4	37.8	33.1	36.5	30.1	38.8	34.6	43.8
51.5	37.0	42.2	41.7	52.0	52.8	46.8	51.0	44.6	54.6	48.4	58.8
59.0	50.7	55.8	55.8	67.2	67.1	61.2	65.4	60.0	69.6	61.9	72.1
67.5	63.8	68.3	68.6	79.7	78.8	74.1	77.7	73.7	81.7	73.4	82.4
77.3	74.8	78.5	78.9	88.4	87.2	84.1	86.7	84.1	90.0	82.3	89.5
88.6	83.2	86.0	86.4	93.9	92.6	90.9	92.6	91.1	94.9	88.5	93.9
101.5	89.2	91.2	91.6	97.0	95.9	95.1	96.1	95.2	97.6	92.7	96.6
116.2	93.2	94.7	94.9	98.6	97.8	97.5	98.1	97.6	99.0	95.6	98.1
133.1	95.9	97.1	97.2	99.5	98.9	98.8	99.1	98.9	99.7	97.5	99.1
152.5	97.7	98.6	98.7	100.0	99.6	99.6	99.7	99.6	100.0	98.8	99.7
174.6	98.9	99.5	99.5	100.0	100.0	100.0	100.0	100.0	100.0	99.6	100.0
200.0	99.6	100.0	100.0	100.0	100.0	100.0	100.0	100.0	100.0	100.0	100.0
229.1	100.0	100.0	100.0	100.0	100.0	100.0	100.0	100.0	100.0	100.0	100.0
262.4	100.0	100.0	100.0	100.0	100.0	100.0	100.0	100.0	100.0	100.0	100.0
300.5	100.0	100.0	100.0	100.0	100.0	100.0	100.0	100.0	100.0	100.0	100.0

Sample #	B7	B8	B9	B-1	B-2	B-3	B-4	B-5	B-6	B-7	B-8
X Location	-43.5	-46.3	-49.2	-23.7	-20.9	-18.0	-15.2	-12.4	-9.5	-6.7	-3.9
Y Location	34.6	30.5	26.4	63.5	67.6	71.7	75.8	79.9	84.1	88.2	92.3

Grain Size (μm)	%	%	%	%	%	%	%	%	%	%	%
	Finner										
1.0	0.0	0.0	0.0	0.0	0.0	0.0	0.0	0.0	0.0	0.0	0.0
1.2	0.1	0.1	0.1	0.0	0.0	0.0	0.1	0.1	0.0	0.1	0.1
1.3	0.3	0.3	0.3	0.1	0.1	0.1	0.3	0.3	0.1	0.3	0.3
1.5	0.6	0.6	0.6	0.3	0.3	0.3	0.5	0.5	0.3	0.5	0.5
1.7	0.8	0.9	0.9	0.6	0.6	0.5	0.7	0.8	0.5	0.7	0.7
2.0	1.1	1.2	1.3	0.9	0.9	0.7	0.9	1.0	0.7	1.0	1.0
2.3	1.3	1.5	1.6	1.2	1.1	0.9	1.1	1.2	0.9	1.2	1.2
2.6	1.5	1.8	1.8	1.5	1.3	1.1	1.2	1.4	1.1	1.4	1.4
3.0	1.7	2.0	2.0	1.7	1.5	1.3	1.3	1.5	1.2	1.5	1.5
3.4	1.8	2.2	2.2	2.0	1.7	1.4	1.3	1.5	1.2	1.5	1.5
3.9	1.8	2.3	2.3	2.1	1.8	1.4	1.3	1.5	1.2	1.5	1.5
4.5	1.8	2.3	2.3	2.3	1.8	1.4	1.3	1.5	1.2	1.5	1.5
5.1	1.8	2.3	2.3	2.4	1.8	1.4	1.3	1.5	1.2	1.5	1.5
5.9	1.8	2.3	2.3	2.4	1.8	1.4	1.3	1.5	1.2	1.5	1.5
6.7	1.8	2.3	2.3	2.4	1.8	1.4	1.3	1.5	1.2	1.5	1.5
7.7	1.8	2.3	2.3	2.4	1.8	1.4	1.3	1.5	1.2	1.5	1.5
8.8	1.8	2.3	2.3	2.4	1.8	1.4	1.3	1.5	1.2	1.5	1.5
10.1	1.8	2.3	2.3	2.4	1.8	1.4	1.3	1.5	1.2	1.5	1.5
11.6	1.8	2.3	2.3	2.4	1.8	1.4	1.3	1.5	1.2	1.5	1.5
13.2	1.8	2.4	2.4	2.5	1.9	1.4	1.3	1.5	1.2	1.5	1.5
15.2	1.9	2.6	2.7	2.7	2.1	1.5	1.3	1.5	1.2	1.5	1.5
17.4	2.1	3.0	3.3	3.0	2.4	1.8	1.3	1.6	1.4	1.6	1.7
19.9	2.6	3.9	4.5	3.5	3.0	2.2	1.5	2.0	1.8	2.0	2.0
22.8	3.7	5.9	7.1	4.4	4.2	2.9	2.0	2.8	2.6	2.6	2.7
26.1	6.1	9.9	12.1	6.1	6.4	4.4	3.1	4.5	4.3	4.1	4.3
29.9	10.9	17.1	20.4	9.2	10.2	7.2	5.3	8.3	7.6	7.2	7.5
34.3	19.2	28.4	32.4	14.3	16.3	12.0	9.7	15.2	13.3	12.9	13.6
39.2	31.9	43.3	47.0	22.1	25.2	19.3	17.3	26.4	21.9	22.1	23.4
44.9	47.7	59.5	61.8	32.6	36.4	29.2	28.5	41.4	32.8	35.0	37.1
51.5	64.1	74.1	74.5	45.1	48.9	41.1	42.8	58.1	44.8	50.1	52.8
59.0	78.1	85.2	84.0	58.1	61.1	53.5	58.0	73.4	56.0	64.9	67.9
67.5	88.0	92.3	90.3	69.9	71.7	65.1	71.7	85.0	65.4	77.3	80.1
77.3	94.0	96.3	94.2	79.6	80.2	74.8	82.4	92.4	72.4	86.3	88.7
88.6	97.3	98.5	96.6	86.7	86.5	82.4	89.7	96.5	77.6	92.1	93.9
101.5	98.9	99.5	98.0	91.7	91.1	88.1	94.3	98.6	81.3	95.6	96.9
116.2	99.6	100.0	98.9	95.0	94.4	92.2	97.0	99.6	84.0	97.7	98.6
133.1	100.0	100.0	99.6	97.2	96.7	95.3	98.6	100.0	86.1	98.9	99.5
152.5	100.0	100.0	100.0	98.7	98.5	97.6	99.5	100.0	87.9	99.6	100.0
174.6	100.0	100.0	100.0	99.5	99.5	98.9	100.0	100.0	89.4	100.0	100.0
200.0	100.0	100.0	100.0	100.0	100.0	99.6	100.0	100.0	90.9	100.0	100.0
229.1	100.0	100.0	100.0	100.0	100.0	100.0	100.0	100.0	92.3	100.0	100.0
262.4	100.0	100.0	100.0	100.0	100.0	100.0	100.0	100.0	93.6	100.0	100.0
300.5	100.0	100.0	100.0	100.0	100.0	100.0	100.0	100.0	95.0	100.0	100.0

Sample #	B-9	C1	C2	C3	C4	C5	C6	C7	C8	C9	C10
X Location	-1.0	4.2	4.3	4.4	4.4	4.5	4.6	4.7	4.8	4.8	4.9
Y Location	96.4	49.7	44.7	39.7	34.7	29.7	24.7	19.7	14.7	9.7	4.7

Grain Size (μm)	%	%	%	%	%	%	%	%	%	%	%
	Finner										
1.0	0.0	0.0	0.0	0.0	0.0	0.0	0.0	0.0	0.0	0.0	0.0
1.2	0.1	0.0	0.1	0.1	0.0	0.1	0.1	0.1	0.1	0.1	0.1
1.3	0.3	0.1	0.3	0.3	0.2	0.3	0.3	0.3	0.3	0.3	0.3
1.5	0.5	0.3	0.6	0.5	0.4	0.5	0.5	0.5	0.5	0.5	0.5
1.7	0.7	0.6	0.9	0.8	0.6	0.7	0.8	0.7	0.8	0.7	0.8
2.0	1.0	0.9	1.2	1.0	0.9	1.0	1.1	1.0	1.1	1.0	1.1
2.3	1.2	1.2	1.5	1.3	1.2	1.2	1.3	1.2	1.3	1.2	1.3
2.6	1.3	1.5	1.8	1.6	1.4	1.4	1.6	1.4	1.6	1.4	1.5
3.0	1.5	1.7	2.0	1.8	1.6	1.6	1.8	1.6	1.8	1.6	1.7
3.4	1.5	2.0	2.2	2.0	1.8	1.8	2.0	1.7	1.9	1.7	1.9
3.9	1.5	2.1	2.3	2.1	2.0	1.9	2.1	1.8	2.0	1.7	1.9
4.5	1.5	2.2	2.3	2.1	2.0	1.9	2.1	1.8	2.0	1.7	1.9
5.1	1.5	2.2	2.3	2.1	2.0	1.9	2.1	1.8	2.0	1.7	1.9
5.9	1.5	2.2	2.3	2.1	2.0	1.9	2.1	1.8	2.0	1.7	1.9
6.7	1.5	2.2	2.3	2.1	2.0	1.9	2.1	1.8	2.0	1.7	1.9
7.7	1.5	2.2	2.3	2.1	2.0	1.9	2.1	1.8	2.0	1.7	1.9
8.8	1.5	2.2	2.3	2.1	2.0	1.9	2.1	1.8	2.0	1.7	1.9
10.1	1.5	2.2	2.3	2.1	2.0	1.9	2.1	1.8	2.0	1.7	1.9
11.6	1.5	2.2	2.3	2.1	2.0	1.9	2.1	1.8	2.0	1.7	1.9
13.2	1.5	2.2	2.4	2.1	2.0	1.9	2.2	2.0	2.0	1.7	1.9
15.2	1.5	2.4	2.7	2.2	2.1	2.0	2.5	2.2	2.1	1.8	2.0
17.4	1.6	2.6	3.1	2.5	2.4	2.3	2.9	2.6	2.4	2.1	2.3
19.9	2.0	3.1	4.0	2.9	2.9	2.8	3.8	3.3	2.9	2.6	3.0
22.8	2.7	4.0	5.8	3.8	3.8	3.9	5.4	4.7	4.0	3.8	4.4
26.1	4.4	5.6	9.2	5.8	5.6	5.9	8.4	7.2	6.2	6.2	7.3
29.9	7.8	8.8	15.4	9.5	8.9	9.6	13.6	11.7	10.6	11.0	12.8
34.3	14.3	14.3	25.2	16.2	14.6	15.8	21.7	18.9	18.1	19.2	21.8
39.2	24.7	22.9	38.3	26.6	23.4	25.1	32.8	29.1	29.3	31.4	34.6
44.9	39.1	34.8	53.2	40.7	35.2	37.0	46.1	41.9	43.3	46.5	49.9
51.5	55.5	48.8	67.7	56.4	49.0	50.4	59.7	55.7	58.1	62.1	65.1
59.0	70.9	62.8	79.6	71.1	62.7	63.3	71.9	68.3	71.3	75.4	77.8
67.5	83.1	74.9	88.0	82.6	74.5	74.3	81.6	78.6	81.4	85.3	86.8
77.3	91.1	84.0	93.4	90.3	83.6	82.8	88.5	86.1	88.4	91.6	92.6
88.6	95.8	90.2	96.5	94.9	89.9	88.7	93.2	91.2	92.9	95.4	95.9
101.5	98.2	94.1	98.2	97.4	93.9	92.8	96.1	94.5	95.8	97.5	97.8
116.2	99.4	96.6	99.1	98.8	96.5	95.6	97.9	96.7	97.5	98.7	98.9
133.1	100.0	98.1	99.7	99.5	98.1	97.4	99.0	98.1	98.7	99.5	99.5
152.5	100.0	99.1	100.0	100.0	99.1	98.8	99.6	99.1	99.5	100.0	100.0
174.6	100.0	99.7	100.0	100.0	99.7	99.6	100.0	99.7	100.0	100.0	100.0
200.0	100.0	100.0	100.0	100.0	100.0	100.0	100.0	100.0	100.0	100.0	100.0
229.1	100.0	100.0	100.0	100.0	100.0	100.0	100.0	100.0	100.0	100.0	100.0
262.4	100.0	100.0	100.0	100.0	100.0	100.0	100.0	100.0	100.0	100.0	100.0
300.5	100.0	100.0	100.0	100.0	100.0	100.0	100.0	100.0	100.0	100.0	100.0

Sample #	C-1	C-2	C-3	C-4	C-5	C-6	C-7	C-8	C-9	C-10	D1
X Location	4.1	4.1	4.0	3.9	3.8	3.7	3.7	3.6	3.5	3.4	34.6
Y Location	54.7	59.7	64.7	69.7	74.7	79.7	84.7	89.7	94.7	99.7	60.2

Grain Size (μm)	%	%	%	%	%	%	%	%	%	%	%
	Finner										
1.0	0.0	0.0	0.0	0.0	0.0	0.0	0.0	0.0	0.0	0.0	0.0
1.2	0.0	0.0	0.0	0.1	0.1	0.1	0.1	0.1	0.1	0.1	0.1
1.3	0.1	0.2	0.2	0.3	0.3	0.3	0.3	0.3	0.3	0.3	0.3
1.5	0.3	0.4	0.4	0.6	0.5	0.5	0.6	0.5	0.5	0.5	0.5
1.7	0.6	0.7	0.6	1.0	0.8	0.8	0.9	0.8	0.8	0.8	0.9
2.0	0.9	1.0	0.9	1.4	1.1	1.0	1.1	1.1	1.0	1.1	1.3
2.3	1.2	1.3	1.2	1.7	1.3	1.3	1.4	1.4	1.3	1.3	1.7
2.6	1.5	1.6	1.5	2.1	1.5	1.5	1.6	1.6	1.5	1.5	2.1
3.0	1.8	1.9	1.7	2.4	1.7	1.7	1.8	1.8	1.7	1.7	2.5
3.4	2.1	2.2	1.9	2.6	1.9	1.8	1.9	2.0	1.8	1.9	2.8
3.9	2.3	2.4	2.0	2.8	2.0	1.8	1.9	2.1	1.9	2.0	3.0
4.5	2.4	2.6	2.0	2.9	2.0	1.8	1.9	2.1	1.9	2.0	3.2
5.1	2.5	2.8	2.0	3.0	2.0	1.8	1.9	2.1	1.9	2.0	3.3
5.9	2.5	2.9	2.0	3.0	2.0	1.8	1.9	2.1	1.9	2.0	3.5
6.7	2.5	3.0	2.0	3.0	2.0	1.8	1.9	2.1	1.9	2.0	3.5
7.7	2.5	3.1	2.0	3.0	2.0	1.8	1.9	2.1	1.9	2.0	3.5
8.8	2.5	3.2	2.0	3.0	2.0	1.8	1.9	2.1	1.9	2.0	3.5
10.1	2.5	3.4	2.0	3.0	2.0	1.8	1.9	2.1	1.9	2.0	3.5
11.6	2.5	3.5	2.0	3.1	2.0	1.8	1.9	2.1	1.9	2.0	3.6
13.2	2.7	3.8	2.0	3.3	2.1	1.9	1.9	2.3	2.0	2.0	3.7
15.2	2.9	4.1	2.2	3.7	2.3	2.2	2.0	2.5	2.2	2.1	4.0
17.4	3.2	4.6	2.5	4.4	2.7	2.7	2.3	2.9	2.7	2.4	4.4
19.9	3.8	5.5	3.0	5.7	3.6	3.6	2.9	3.8	3.6	3.0	5.2
22.8	4.8	6.9	4.2	8.5	5.4	5.6	4.2	5.7	5.4	4.3	6.7
26.1	6.8	9.4	6.5	13.7	8.7	9.5	7.2	9.3	8.9	7.0	9.5
29.9	10.4	13.5	10.8	22.8	14.8	16.1	13.2	15.6	15.2	12.0	14.6
34.3	16.3	19.8	17.9	36.2	24.3	26.4	23.7	25.6	25.0	20.5	23.1
39.2	25.1	28.8	28.2	52.8	37.3	39.8	38.8	39.0	38.0	32.7	35.4
44.9	36.8	40.1	41.1	69.5	52.2	54.8	56.5	54.2	52.6	47.6	50.5
51.5	50.2	52.7	55.0	83.0	66.6	68.9	73.1	68.6	66.3	62.9	66.1
59.0	63.5	65.1	67.8	91.8	78.5	80.2	85.5	80.3	77.5	76.1	79.3
67.5	75.1	75.7	78.2	96.6	87.0	88.1	93.1	88.4	85.5	85.7	88.6
77.3	83.8	83.9	85.7	98.7	92.5	93.1	97.0	93.4	90.9	92.0	94.3
88.6	89.9	89.7	90.9	99.6	95.7	96.1	98.8	96.3	94.2	95.6	97.3
101.5	93.9	93.6	94.3	100.0	97.6	97.8	99.6	98.0	96.4	97.7	98.9
116.2	96.4	96.2	96.5	100.0	98.8	98.9	100.0	99.0	97.8	98.9	99.6
133.1	98.0	97.9	98.0	100.0	99.5	99.5	100.0	99.6	98.8	99.6	100.0
152.5	99.1	99.0	99.1	100.0	100.0	100.0	100.0	100.0	99.6	100.0	100.0
174.6	99.7	99.7	99.7	100.0	100.0	100.0	100.0	100.0	100.0	100.0	100.0
200.0	100.0	100.0	100.0	100.0	100.0	100.0	100.0	100.0	100.0	100.0	100.0
229.1	100.0	100.0	100.0	100.0	100.0	100.0	100.0	100.0	100.0	100.0	100.0
262.4	100.0	100.0	100.0	100.0	100.0	100.0	100.0	100.0	100.0	100.0	100.0
300.5	100.0	100.0	100.0	100.0	100.0	100.0	100.0	100.0	100.0	100.0	100.0

Sample #	D2	D3	D4	D5	D6	D7	D8	D9	D10	D11	D-1
X Location	37.6	40.5	43.4	46.4	49.3	52.2	55.2	58.1	61.0	63.9	31.7
Y Location	56.2	52.1	48.1	44.0	40.0	35.9	31.9	27.8	23.8	19.7	64.3

Grain Size (μm)	%	%	%	%	%	%	%	%	%	%	%
	Finner										
1.0	0.0	0.0	0.0	0.0	0.0	0.0	0.0	0.0	0.0	0.0	0.0
1.2	0.0	0.0	0.1	0.0	0.1	0.1	0.1	0.2	0.1	0.1	0.0
1.3	0.2	0.2	0.3	0.1	0.3	0.3	0.3	0.4	0.3	0.4	0.1
1.5	0.4	0.4	0.5	0.3	0.5	0.5	0.5	0.7	0.6	0.7	0.4
1.7	0.6	0.6	0.8	0.5	0.7	0.8	0.8	1.0	0.9	1.0	0.6
2.0	0.9	0.9	1.1	0.8	0.9	1.0	1.2	1.4	1.2	1.4	1.0
2.3	1.2	1.2	1.4	1.0	1.1	1.3	1.4	1.7	1.6	1.8	1.3
2.6	1.5	1.5	1.6	1.2	1.3	1.5	1.7	2.0	1.8	2.2	1.6
3.0	1.8	1.7	1.8	1.3	1.5	1.7	1.9	2.2	2.1	2.5	2.0
3.4	2.0	1.9	2.0	1.5	1.6	1.9	2.0	2.3	2.3	2.7	2.3
3.9	2.2	2.0	2.1	1.6	1.6	2.0	2.2	2.5	2.4	2.9	2.5
4.5	2.3	2.0	2.1	1.6	1.6	2.0	2.2	2.5	2.4	3.0	2.7
5.1	2.3	2.0	2.1	1.6	1.6	2.0	2.2	2.5	2.4	3.0	2.8
5.9	2.3	2.0	2.1	1.6	1.6	2.0	2.2	2.5	2.4	3.0	3.0
6.7	2.3	2.0	2.1	1.6	1.6	2.0	2.2	2.5	2.4	3.0	3.1
7.7	2.3	2.0	2.1	1.6	1.6	2.0	2.2	2.5	2.4	3.0	3.1
8.8	2.3	2.0	2.1	1.6	1.6	2.0	2.2	2.5	2.4	3.0	3.1
10.1	2.3	2.0	2.1	1.6	1.6	2.0	2.2	2.5	2.4	3.0	3.2
11.6	2.3	2.0	2.1	1.6	1.6	2.0	2.2	2.5	2.4	3.1	3.3
13.2	2.4	2.0	2.1	1.7	1.6	2.1	2.2	2.5	2.6	3.3	3.5
15.2	2.6	2.2	2.3	1.9	1.7	2.4	2.3	2.6	2.9	3.7	3.7
17.4	2.9	2.4	2.6	2.2	2.0	2.8	2.7	3.1	3.5	4.4	4.1
19.9	3.4	2.8	3.3	2.9	2.6	3.7	3.4	4.1	4.8	6.1	4.8
22.8	4.5	3.7	4.7	4.0	3.8	5.5	4.9	6.6	7.3	9.3	6.0
26.1	6.6	5.6	7.5	6.2	6.1	8.7	8.0	11.8	12.0	15.3	8.2
29.9	10.6	9.4	12.6	10.0	10.4	14.3	13.8	21.6	19.7	25.3	12.0
34.3	17.6	16.2	21.1	16.0	17.4	23.0	23.3	36.9	30.9	39.2	18.3
39.2	28.3	26.9	33.3	24.5	27.5	34.7	36.6	55.7	44.4	55.4	27.5
44.9	42.3	41.5	48.1	35.1	40.3	48.4	52.2	73.8	58.2	71.0	39.4
51.5	57.8	57.7	63.2	46.7	54.2	62.0	67.3	87.1	70.4	83.2	53.0
59.0	72.2	72.7	76.4	57.7	67.0	73.7	79.7	94.7	79.7	91.3	66.2
67.5	83.3	84.1	86.1	67.1	77.5	82.7	88.3	98.2	86.2	95.9	77.4
77.3	90.7	91.4	92.3	74.3	85.2	89.0	93.6	99.5	90.5	98.3	85.7
88.6	95.0	95.6	96.0	79.6	90.6	93.2	96.6	100.0	93.4	99.4	91.4
101.5	97.4	97.8	98.0	83.3	94.1	95.9	98.3	100.0	95.4	100.0	94.9
116.2	98.8	99.0	99.0	85.9	96.4	97.6	99.2	100.0	96.8	100.0	97.1
133.1	99.5	99.6	99.6	87.9	97.9	98.8	99.7	100.0	98.0	100.0	98.6
152.5	100.0	100.0	100.0	89.4	99.0	99.6	100.0	100.0	99.1	100.0	99.5
174.6	100.0	100.0	100.0	90.6	99.7	100.0	100.0	100.0	99.7	100.0	100.0
200.0	100.0	100.0	100.0	91.8	100.0	100.0	100.0	100.0	100.0	100.0	100.0
229.1	100.0	100.0	100.0	92.8	100.0	100.0	100.0	100.0	100.0	100.0	100.0
262.4	100.0	100.0	100.0	93.9	100.0	100.0	100.0	100.0	100.0	100.0	100.0
300.5	100.0	100.0	100.0	95.0	100.0	100.0	100.0	100.0	100.0	100.0	100.0

Sample #	D-2	D-3	D-4	D-6	D-7	D-8	D-9	E1	E2	E3	E4
X Location	28.8	25.8	22.9	15.3	12.4	9.4	4.9	61.6	65.7	69.8	73.9
Y Location	68.3	72.4	76.4	87.0	91.0	95.1	4.7	89.2	86.3	83.4	80.6

Grain Size (μm)	%	%	%	%	%	%	%	%	%	%	%
	Finner										
1.0	0.0	0.0	0.0	0.0	0.1	0.0	0.0	0.0	0.0	0.0	0.0
1.2	0.0	0.1	0.1	0.1	0.3	0.1	0.2	0.1	0.0	0.0	0.1
1.3	0.2	0.3	0.3	0.3	0.5	0.4	0.4	0.3	0.2	0.2	0.3
1.5	0.4	0.5	0.6	0.4	0.7	0.6	0.7	0.5	0.4	0.4	0.5
1.7	0.6	0.8	1.0	0.6	1.0	1.0	1.1	0.9	0.7	0.7	0.8
2.0	1.0	1.1	1.4	0.9	1.2	1.3	1.4	1.2	1.0	1.0	1.2
2.3	1.3	1.4	1.8	1.0	1.4	1.7	1.8	1.6	1.3	1.3	1.5
2.6	1.6	1.6	2.2	1.2	1.6	2.0	2.1	2.0	1.7	1.6	1.8
3.0	1.9	1.8	2.6	1.3	1.8	2.3	2.3	2.3	2.0	1.9	2.0
3.4	2.2	2.0	2.9	1.4	1.9	2.5	2.5	2.6	2.2	2.1	2.2
3.9	2.4	2.1	3.1	1.4	2.1	2.7	2.7	2.8	2.5	2.3	2.4
4.5	2.5	2.1	3.3	1.4	2.2	2.9	2.8	3.0	2.6	2.4	2.5
5.1	2.6	2.1	3.5	1.4	2.2	3.0	2.8	3.1	2.8	2.4	2.5
5.9	2.6	2.1	3.6	1.4	2.2	3.1	2.8	3.1	2.9	2.4	2.5
6.7	2.6	2.1	3.8	1.4	2.2	3.2	2.8	3.1	3.0	2.4	2.5
7.7	2.6	2.1	3.9	1.4	2.3	3.4	2.8	3.1	3.1	2.4	2.5
8.8	2.6	2.1	4.1	1.4	2.4	3.5	2.8	3.1	3.3	2.4	2.5
10.1	2.6	2.1	4.2	1.4	2.6	3.7	2.9	3.1	3.4	2.4	2.5
11.6	2.6	2.1	4.5	1.4	2.9	4.0	3.1	3.1	3.5	2.4	2.5
13.2	2.7	2.2	4.9	1.6	3.4	4.5	3.5	3.2	3.8	2.5	2.5
15.2	2.9	2.4	5.6	1.8	4.3	5.5	4.3	3.4	4.1	2.7	2.6
17.4	3.2	2.9	6.7	2.3	5.9	7.2	5.9	3.8	4.6	3.0	2.9
19.9	3.7	4.0	8.7	3.3	8.9	10.3	9.2	4.5	5.5	3.6	3.5
22.8	4.8	6.1	12.1	5.2	13.8	15.7	15.7	5.8	7.0	4.7	4.7
26.1	6.9	10.3	17.6	8.8	21.5	24.3	27.2	8.3	9.7	6.8	7.2
29.9	10.8	17.4	25.8	15.1	32.3	36.2	43.9	13.0	14.1	10.7	11.8
34.3	17.7	28.3	36.6	24.9	45.5	50.4	63.2	21.0	20.8	17.1	19.5
39.2	28.4	42.3	49.3	38.2	59.6	65.0	80.5	32.8	30.2	26.8	30.8
44.9	42.5	57.5	62.1	53.2	72.5	77.5	91.8	47.7	41.8	39.5	45.1
51.5	58.4	71.5	73.5	67.8	82.8	86.7	97.4	63.4	54.3	53.7	60.2
59.0	73.0	82.4	82.5	79.8	90.0	92.7	99.4	77.0	66.2	67.3	73.6
67.5	84.3	89.8	89.0	88.2	94.5	96.2	100.0	87.0	76.2	78.6	83.9
77.3	91.7	94.3	93.3	93.5	97.2	98.1	100.0	93.3	83.8	86.7	90.8
88.6	95.9	96.8	96.1	96.5	98.7	99.1	100.0	96.8	89.3	92.1	95.0
101.5	98.0	98.3	97.8	98.2	99.5	99.7	100.0	98.6	93.1	95.4	97.4
116.2	99.1	99.1	98.9	99.1	100.0	100.0	100.0	99.5	95.7	97.5	98.8
133.1	99.7	99.6	99.6	99.6	100.0	100.0	100.0	100.0	97.5	98.7	99.5
152.5	100.0	100.0	100.0	100.0	100.0	100.0	100.0	100.0	98.8	99.5	100.0
174.6	100.0	100.0	100.0	100.0	100.0	100.0	100.0	100.0	99.6	100.0	100.0
200.0	100.0	100.0	100.0	100.0	100.0	100.0	100.0	100.0	100.0	100.0	100.0
229.1	100.0	100.0	100.0	100.0	100.0	100.0	100.0	100.0	100.0	100.0	100.0
262.4	100.0	100.0	100.0	100.0	100.0	100.0	100.0	100.0	100.0	100.0	100.0
300.5	100.0	100.0	100.0	100.0	100.0	100.0	100.0	100.0	100.0	100.0	100.0

Sample #	E5	E6	E7	E8	E9	E10	E-1	E-2	E-3	E-4	E-5
X Location	78.0	82.1	86.2	90.3	94.4	98.5	57.6	53.5	49.4	45.3	41.2
Y Location	77.7	74.8	72.0	69.1	66.2	63.4	92.0	94.9	97.8	100.7	103.5

Grain Size (μm)	%	%	%	%	%	%	%	%	%	%	%
	Finner										
1.0	0.0	0.0	0.0	0.0	0.0	0.0	0.0	0.0	0.0	0.0	0.0
1.2	0.1	0.1	0.1	0.1	0.1	0.1	0.0	0.0	0.1	0.1	0.2
1.3	0.3	0.3	0.3	0.3	0.3	0.4	0.2	0.1	0.3	0.4	0.4
1.5	0.6	0.6	0.6	0.6	0.6	0.7	0.4	0.3	0.5	0.7	0.7
1.7	0.9	1.0	1.0	1.0	1.0	1.1	0.7	0.6	0.8	1.2	1.1
2.0	1.2	1.3	1.3	1.3	1.3	1.6	1.0	0.8	1.1	1.7	1.6
2.3	1.5	1.7	1.7	1.7	1.7	2.0	1.4	1.1	1.5	2.2	2.1
2.6	1.7	2.0	2.0	2.0	2.0	2.4	1.7	1.3	1.8	2.7	2.5
3.0	1.9	2.2	2.2	2.2	2.3	2.7	2.0	1.6	2.0	3.2	3.0
3.4	2.1	2.4	2.4	2.4	2.5	3.0	2.3	1.8	2.2	3.6	3.4
3.9	2.2	2.5	2.6	2.6	2.7	3.2	2.5	1.9	2.4	3.9	3.8
4.5	2.2	2.5	2.6	2.7	2.8	3.4	2.7	2.0	2.6	4.2	4.2
5.1	2.2	2.5	2.6	2.7	2.8	3.5	2.8	2.2	2.7	4.4	4.5
5.9	2.2	2.5	2.6	2.7	2.8	3.5	2.9	2.2	2.7	4.5	4.8
6.7	2.2	2.5	2.6	2.7	2.8	3.5	2.9	2.2	2.7	4.7	5.1
7.7	2.2	2.5	2.6	2.7	2.8	3.5	2.9	2.2	2.7	4.8	5.5
8.8	2.2	2.5	2.6	2.7	2.8	3.5	2.9	2.2	2.7	5.0	6.0
10.1	2.2	2.5	2.6	2.7	2.8	3.7	2.9	2.2	2.7	5.2	6.7
11.6	2.2	2.5	2.6	2.8	2.9	3.9	2.9	2.3	2.8	5.4	7.9
13.2	2.2	2.6	2.7	3.0	3.1	4.2	3.1	2.4	3.0	5.9	9.6
15.2	2.4	2.8	2.9	3.3	3.4	4.8	3.3	2.7	3.3	6.6	12.4
17.4	2.7	3.2	3.4	4.0	4.1	5.9	3.6	3.1	3.9	8.0	16.9
19.9	3.5	4.1	4.5	5.5	5.6	8.2	4.2	3.8	5.0	10.6	23.7
22.8	5.0	6.0	6.6	8.6	8.5	12.4	5.3	5.0	6.9	15.4	33.3
26.1	8.2	9.8	10.9	14.4	14.1	19.6	7.4	7.1	10.2	23.3	45.5
29.9	13.9	16.8	18.6	24.2	23.4	30.7	11.2	10.7	15.8	35.2	59.2
34.3	23.1	28.0	30.3	38.1	36.9	45.1	17.6	16.5	24.2	50.2	72.4
39.2	35.5	43.2	45.4	54.6	53.1	60.8	27.4	24.7	35.4	66.1	83.4
44.9	49.8	60.0	61.5	70.6	69.2	75.0	40.2	35.5	48.3	79.9	91.2
51.5	63.7	75.1	75.7	83.3	82.1	85.8	54.7	47.6	61.3	89.6	95.9
59.0	75.2	86.4	86.2	91.6	90.8	92.7	68.6	59.8	72.8	95.3	98.4
67.5	83.8	93.3	92.8	96.2	95.8	96.6	80.0	70.6	81.8	98.2	99.5
77.3	89.6	97.0	96.6	98.5	98.3	98.6	88.1	79.3	88.2	99.5	100.0
88.6	93.4	98.8	98.5	99.5	99.5	99.5	93.3	85.8	92.6	100.0	100.0
101.5	95.8	99.6	99.5	100.0	100.0	100.0	96.3	90.5	95.4	100.0	100.0
116.2	97.5	100.0	100.0	100.0	100.0	100.0	98.0	93.8	97.3	100.0	100.0
133.1	98.6	100.0	100.0	100.0	100.0	100.0	99.1	96.3	98.6	100.0	100.0
152.5	99.5	100.0	100.0	100.0	100.0	100.0	99.7	98.1	99.5	100.0	100.0
174.6	100.0	100.0	100.0	100.0	100.0	100.0	100.0	99.1	100.0	100.0	100.0
200.0	100.0	100.0	100.0	100.0	100.0	100.0	100.0	99.7	100.0	100.0	100.0
229.1	100.0	100.0	100.0	100.0	100.0	100.0	100.0	100.0	100.0	100.0	100.0
262.4	100.0	100.0	100.0	100.0	100.0	100.0	100.0	100.0	100.0	100.0	100.0
300.5	100.0	100.0	100.0	100.0	100.0	100.0	100.0	100.0	100.0	100.0	100.0

Sample #	E-6	E-7	E-8	F1	F2	F3	F4	F6	F7	F8	F9
X Location	37.1	33.0	28.9	86.1	89.0	92.0	94.9	99.6	102.5	105.4	108.4
Y Location	106.4	109.3	112.1	118.3	114.3	110.2	106.2	99.7	95.6	91.6	87.5

Grain Size (μm)	%	%	%	%	%	%	%	%	%	%	%
	Finner										
1.0	0.0	0.1	0.1	0.0	0.0	0.0	0.0	0.0	0.0	0.1	0.0
1.2	0.1	0.3	0.3	0.0	0.0	0.1	0.1	0.1	0.2	0.3	0.2
1.3	0.3	0.5	0.5	0.2	0.2	0.3	0.4	0.3	0.4	0.6	0.4
1.5	0.5	0.9	0.8	0.4	0.4	0.5	0.7	0.4	0.7	0.9	0.7
1.7	0.7	1.3	1.1	0.7	0.7	0.8	1.1	0.6	1.1	1.3	1.1
2.0	1.0	1.7	1.5	1.0	1.0	1.2	1.5	0.8	1.5	1.7	1.4
2.3	1.3	2.2	1.9	1.3	1.4	1.6	2.0	1.0	1.8	2.1	1.8
2.6	1.5	2.7	2.3	1.6	1.8	1.9	2.4	1.2	2.2	2.4	2.2
3.0	1.8	3.1	2.7	1.8	2.1	2.2	2.8	1.3	2.5	2.7	2.5
3.4	2.0	3.5	3.1	2.1	2.4	2.5	3.1	1.4	2.8	3.0	2.7
3.9	2.2	3.8	3.4	2.2	2.6	2.7	3.3	1.4	3.0	3.2	2.9
4.5	2.4	4.1	3.7	2.4	2.8	2.9	3.5	1.4	3.2	3.3	3.0
5.1	2.6	4.4	4.0	2.5	3.0	3.0	3.7	1.4	3.3	3.4	3.2
5.9	2.8	4.6	4.4	2.5	3.1	3.0	3.8	1.4	3.4	3.4	3.3
6.7	3.0	4.9	4.7	2.5	3.1	3.0	3.9	1.4	3.6	3.4	3.4
7.7	3.2	5.2	5.2	2.5	3.1	3.0	3.9	1.4	3.7	3.5	3.5
8.8	3.5	5.5	5.8	2.5	3.1	3.0	4.0	1.4	3.9	3.7	3.7
10.1	4.0	6.1	6.7	2.5	3.1	3.0	4.1	1.5	4.1	3.9	3.9
11.6	4.8	6.9	8.1	2.6	3.2	3.1	4.3	1.8	4.5	4.2	4.3
13.2	6.0	8.4	10.3	2.7	3.3	3.2	4.6	2.2	5.2	4.8	5.0
15.2	8.0	10.8	13.8	3.0	3.6	3.5	5.2	3.1	6.6	5.9	6.4
17.4	11.3	15.0	19.1	3.4	4.0	3.9	6.2	4.9	9.2	8.3	9.1
19.9	16.1	21.9	26.8	4.3	4.8	4.7	8.1	8.2	14.0	12.9	14.2
22.8	22.8	32.3	36.9	5.9	6.1	6.2	11.7	13.8	22.3	21.1	23.0
26.1	31.0	46.0	49.0	8.8	8.6	9.0	18.1	21.9	34.9	34.0	36.3
29.9	39.7	61.6	61.8	13.9	12.8	14.1	28.3	32.0	51.1	50.9	53.3
34.3	47.8	76.2	73.6	22.0	19.5	22.6	42.1	42.4	68.1	68.6	70.7
39.2	54.4	87.5	83.3	33.2	29.1	34.7	58.0	51.6	82.5	83.3	84.8
44.9	59.3	94.5	90.3	46.8	41.0	49.6	73.0	58.5	92.1	92.7	93.6
51.5	62.5	98.1	94.8	60.8	54.0	64.9	84.7	63.2	97.2	97.5	97.9
59.0	64.7	99.5	97.5	73.3	66.2	78.1	92.3	66.2	99.3	99.4	99.5
67.5	66.1	100.0	98.9	82.9	76.3	87.6	96.5	68.1	100.0	100.0	100.0
77.3	67.1	100.0	99.6	89.6	84.0	93.5	98.6	69.4	100.0	100.0	100.0
88.6	67.9	100.0	100.0	93.8	89.4	96.9	99.5	70.3	100.0	100.0	100.0
101.5	68.5	100.0	100.0	96.4	93.2	98.6	100.0	71.1	100.0	100.0	100.0
116.2	69.3	100.0	100.0	97.9	95.7	99.5	100.0	71.9	100.0	100.0	100.0
133.1	70.1	100.0	100.0	98.9	97.5	100.0	100.0	72.8	100.0	100.0	100.0
152.5	71.2	100.0	100.0	99.6	98.9	100.0	100.0	73.9	100.0	100.0	100.0
174.6	72.7	100.0	100.0	100.0	99.6	100.0	100.0	75.3	100.0	100.0	100.0
200.0	74.9	100.0	100.0	100.0	100.0	100.0	100.0	77.3	100.0	100.0	100.0
229.1	77.8	100.0	100.0	100.0	100.0	100.0	100.0	80.0	100.0	100.0	100.0
262.4	81.6	100.0	100.0	100.0	100.0	100.0	100.0	83.3	100.0	100.0	100.0
300.5	85.9	100.0	100.0	100.0	100.0	100.0	100.0	87.1	100.0	100.0	100.0

Sample #	F-1	F-2	F-3	F-4	F-5	F-6	F-7	G1	G2	G3	G4
X Location	83.2	80.2	77.3	74.4	71.4	68.5	65.6	115.6	115.6	115.5	115.4
Y Location	122.4	126.4	130.5	134.5	138.6	142.6	146.7	126.1	122.1	118.1	114.1

Grain Size (μm)	%	%	%	%	%	%	%	%	%	%	%
	Finner										
1.0	0.0	0.0	0.0	0.0	0.0	0.0	0.0	0.0	0.0	0.0	0.0
1.2	0.0	0.0	0.1	0.0	0.1	0.2	0.2	0.0	0.1	0.1	0.1
1.3	0.1	0.2	0.3	0.2	0.3	0.4	0.4	0.2	0.3	0.3	0.4
1.5	0.3	0.4	0.6	0.4	0.6	0.8	0.8	0.4	0.5	0.6	0.7
1.7	0.6	0.6	1.0	0.6	0.9	1.2	1.3	0.7	0.8	1.0	1.2
2.0	0.9	1.0	1.4	0.9	1.3	1.7	1.9	1.0	1.2	1.4	1.7
2.3	1.2	1.3	1.8	1.2	1.7	2.3	2.5	1.3	1.6	1.9	2.3
2.6	1.4	1.6	2.1	1.5	2.1	2.8	3.1	1.6	2.0	2.3	2.8
3.0	1.7	1.9	2.4	1.8	2.4	3.2	3.8	1.9	2.3	2.6	3.4
3.4	1.9	2.1	2.6	2.0	2.7	3.6	4.4	2.2	2.7	2.9	3.8
3.9	2.0	2.3	2.8	2.1	2.9	4.0	5.0	2.4	2.9	3.1	4.2
4.5	2.1	2.4	2.9	2.2	3.1	4.2	5.5	2.5	3.2	3.3	4.5
5.1	2.1	2.5	2.9	2.2	3.2	4.5	6.0	2.7	3.4	3.4	4.8
5.9	2.1	2.5	2.9	2.2	3.2	4.7	6.4	2.8	3.5	3.5	5.0
6.7	2.1	2.5	2.9	2.2	3.2	4.9	6.9	2.8	3.7	3.5	5.2
7.7	2.1	2.5	2.9	2.2	3.2	5.1	7.4	2.8	3.8	3.5	5.4
8.8	2.1	2.5	2.9	2.2	3.2	5.3	8.1	2.8	4.0	3.5	5.6
10.1	2.1	2.5	2.9	2.2	3.2	5.6	9.0	2.8	4.2	3.6	5.9
11.6	2.1	2.5	3.0	2.2	3.3	6.2	10.3	2.9	4.4	3.8	6.3
13.2	2.1	2.6	3.2	2.4	3.5	7.0	12.3	3.0	4.7	4.1	7.0
15.2	2.3	2.8	3.5	2.5	3.8	8.5	15.7	3.3	5.1	4.7	8.0
17.4	2.6	3.1	4.1	2.8	4.3	11.3	21.3	3.7	5.9	5.7	9.8
19.9	3.0	3.6	5.3	3.4	5.2	16.2	30.2	4.4	7.1	7.7	12.8
22.8	4.0	4.6	7.8	4.6	7.1	24.2	43.0	5.7	9.1	11.3	18.0
26.1	5.9	6.6	12.4	6.8	10.5	36.1	58.9	8.2	12.6	17.3	25.9
29.9	9.4	10.3	20.2	11.0	16.7	51.3	75.1	12.6	18.1	26.3	37.0
34.3	15.5	16.9	31.8	18.1	26.4	67.4	88.0	19.9	26.3	38.0	50.6
39.2	24.9	27.1	46.3	28.7	39.6	81.3	95.6	30.4	37.0	51.0	64.8
44.9	37.7	40.9	61.7	42.3	54.9	90.9	98.8	43.7	49.5	63.5	77.5
51.5	52.3	56.4	75.3	57.1	69.7	96.3	99.8	58.1	62.3	73.9	87.0
59.0	66.5	71.0	85.6	70.8	81.7	98.8	100.0	71.2	73.6	81.8	93.2
67.5	78.3	82.6	92.3	81.6	89.9	99.7	100.0	81.6	82.5	87.4	96.8
77.3	86.8	90.3	96.2	89.0	94.8	100.0	100.0	88.8	88.8	91.1	98.6
88.6	92.3	95.0	98.3	93.7	97.5	100.0	100.0	93.3	93.1	93.7	99.6
101.5	95.6	97.5	99.4	96.5	98.9	100.0	100.0	96.1	95.8	95.5	100.0
116.2	97.6	98.8	100.0	98.1	99.6	100.0	100.0	97.8	97.5	96.9	100.0
133.1	98.8	99.6	100.0	99.0	100.0	100.0	100.0	98.8	98.7	98.1	100.0
152.5	99.6	100.0	100.0	99.7	100.0	100.0	100.0	99.6	99.5	99.1	100.0
174.6	100.0	100.0	100.0	100.0	100.0	100.0	100.0	100.0	100.0	99.7	100.0
200.0	100.0	100.0	100.0	100.0	100.0	100.0	100.0	100.0	100.0	100.0	100.0
229.1	100.0	100.0	100.0	100.0	100.0	100.0	100.0	100.0	100.0	100.0	100.0
262.4	100.0	100.0	100.0	100.0	100.0	100.0	100.0	100.0	100.0	100.0	100.0
300.5	100.0	100.0	100.0	100.0	100.0	100.0	100.0	100.0	100.0	100.0	100.0

Sample #	G5	G6	G8	G9	G10	G-1	G-2	G-3	G-4	G-5	G-6
X Location	115.4	115.3	115.2	115.1	115.2	115.7	115.8	115.9	115.9	116.0	116.1
Y Location	110.1	106.1	98.1	94.1	92.0	131.1	136.1	141.1	146.1	151.1	156.1

Grain Size (μm)	%	%	%	%	%	%	%	%	%	%	%
	Finner										
1.0	0.0	0.1	0.0	0.0	0.0	0.0	0.0	0.0	0.0	0.0	0.0
1.2	0.1	0.3	0.2	0.2	0.2	0.0	0.1	0.0	0.1	0.1	0.1
1.3	0.3	0.6	0.4	0.4	0.4	0.2	0.3	0.2	0.3	0.3	0.3
1.5	0.6	0.9	0.7	0.6	0.8	0.4	0.5	0.4	0.5	0.5	0.6
1.7	0.9	1.4	1.0	0.9	1.2	0.7	0.7	0.7	0.9	0.8	0.9
2.0	1.3	1.9	1.4	1.2	1.6	1.1	1.0	1.0	1.2	1.2	1.3
2.3	1.6	2.4	1.8	1.5	2.1	1.4	1.3	1.3	1.6	1.5	1.7
2.6	2.0	2.9	2.1	1.8	2.5	1.8	1.6	1.6	1.9	1.8	2.0
3.0	2.3	3.4	2.4	2.0	2.9	2.1	1.8	1.9	2.2	2.1	2.4
3.4	2.6	3.8	2.7	2.3	3.2	2.3	2.0	2.1	2.4	2.4	2.6
3.9	2.9	4.2	2.9	2.5	3.5	2.5	2.2	2.3	2.6	2.5	2.8
4.5	3.1	4.6	3.1	2.6	3.7	2.7	2.4	2.4	2.7	2.7	3.0
5.1	3.4	4.9	3.3	2.8	3.9	2.8	2.5	2.4	2.7	2.8	3.1
5.9	3.6	5.2	3.5	2.9	4.0	2.8	2.6	2.4	2.7	2.8	3.1
6.7	3.8	5.5	3.7	3.1	4.2	2.8	2.6	2.4	2.7	2.8	3.1
7.7	4.1	5.9	3.9	3.3	4.4	2.8	2.6	2.4	2.7	2.8	3.1
8.8	4.5	6.5	4.1	3.6	4.7	2.8	2.6	2.4	2.7	2.8	3.1
10.1	5.1	7.3	4.5	4.0	5.0	2.8	2.7	2.4	2.7	2.8	3.1
11.6	5.9	8.5	5.1	4.6	5.5	2.8	2.8	2.4	2.7	2.9	3.2
13.2	7.2	10.6	6.1	5.8	6.4	2.9	3.0	2.5	2.7	3.1	3.4
15.2	9.4	14.2	8.0	7.7	7.9	3.1	3.3	2.7	2.9	3.3	3.7
17.4	12.8	20.1	11.1	11.2	10.6	3.4	3.8	3.0	3.2	3.7	4.3
19.9	18.1	29.3	16.3	16.8	15.1	3.9	4.6	3.5	3.8	4.5	5.4
22.8	25.5	42.0	24.2	25.1	22.2	5.1	6.1	4.7	5.0	6.0	7.4
26.1	34.9	57.3	35.2	36.2	32.3	7.3	8.6	6.9	7.6	8.8	11.2
29.9	45.8	72.8	48.4	49.0	44.7	11.7	12.9	11.2	12.6	13.5	17.7
34.3	56.7	85.4	62.2	61.6	58.1	19.4	19.5	18.5	21.1	21.2	27.5
39.2	66.4	93.6	74.6	72.5	70.4	31.3	28.9	29.5	33.8	32.0	40.5
44.9	74.2	97.8	84.3	80.4	80.4	46.6	40.5	43.8	49.7	45.1	55.1
51.5	79.9	99.4	91.0	85.7	87.5	63.0	53.1	59.2	66.0	58.9	69.0
59.0	83.7	99.9	95.2	88.8	92.1	77.4	65.1	73.1	79.7	71.3	80.3
67.5	86.2	100.0	97.6	90.5	95.0	87.6	75.3	83.8	89.2	81.2	88.3
77.3	87.7	100.0	98.9	91.4	96.8	93.9	83.0	90.9	94.8	88.2	93.4
88.6	88.7	100.0	99.6	91.9	98.0	97.2	88.6	95.2	97.7	92.8	96.4
101.5	89.4	100.0	100.0	91.9	98.7	98.8	92.5	97.5	99.1	95.7	98.1
116.2	89.9	100.0	100.0	91.9	99.3	99.6	95.2	98.8	99.7	97.6	99.1
133.1	90.3	100.0	100.0	91.9	99.7	100.0	97.2	99.6	100.0	98.8	99.6
152.5	90.7	100.0	100.0	91.9	100.0	100.0	98.7	100.0	100.0	99.6	100.0
174.6	91.1	100.0	100.0	91.9	100.0	100.0	99.5	100.0	100.0	100.0	100.0
200.0	91.6	100.0	100.0	91.9	100.0	100.0	100.0	100.0	100.0	100.0	100.0
229.1	92.2	100.0	100.0	91.9	100.0	100.0	100.0	100.0	100.0	100.0	100.0
262.4	92.9	100.0	100.0	92.3	100.0	100.0	100.0	100.0	100.0	100.0	100.0
300.5	93.9	100.0	100.0	92.9	100.0	100.0	100.0	100.0	100.0	100.0	100.0

Sample #	G-7	G-8	G-9	H1	H2	H3	H4	H5	H6	H7	H8
X Location	116.2	116.3	116.3	142.6	140.4	138.1	135.8	133.6	131.3	129.0	126.8
Y Location	161.1	166.1	171.1	119.2	115.9	112.6	109.3	106.0	102.7	99.4	96.1

Grain Size (μm)	%	%	%	%	%	%	%	%	%	%	%
	Finner										
1.0	0.0	0.0	0.0	0.0	0.0	0.0	0.0	0.1	0.0	0.1	0.1
1.2	0.1	0.2	0.2	0.1	0.1	0.1	0.1	0.3	0.2	0.3	0.3
1.3	0.4	0.4	0.4	0.3	0.3	0.3	0.4	0.6	0.4	0.5	0.5
1.5	0.7	0.8	0.8	0.5	0.5	0.6	0.7	0.9	0.7	0.9	0.8
1.7	1.1	1.2	1.3	0.8	0.9	1.0	1.1	1.3	1.2	1.3	1.2
2.0	1.5	1.7	1.9	1.2	1.3	1.4	1.6	1.7	1.6	1.8	1.7
2.3	2.0	2.3	2.4	1.5	1.7	1.9	2.1	2.1	2.2	2.2	2.1
2.6	2.5	2.8	3.0	1.9	2.1	2.4	2.6	2.5	2.7	2.7	2.5
3.0	2.9	3.2	3.5	2.2	2.5	2.8	3.1	2.9	3.1	3.1	2.9
3.4	3.3	3.6	3.9	2.5	2.8	3.2	3.5	3.2	3.6	3.5	3.3
3.9	3.5	4.0	4.3	2.8	3.1	3.6	3.8	3.5	3.9	3.8	3.6
4.5	3.8	4.2	4.5	3.0	3.3	3.8	4.1	3.8	4.3	4.1	3.8
5.1	3.9	4.5	4.8	3.2	3.5	4.0	4.3	4.0	4.6	4.3	4.0
5.9	4.1	4.7	5.0	3.3	3.6	4.2	4.5	4.3	4.9	4.6	4.3
6.7	4.2	4.9	5.2	3.5	3.7	4.3	4.7	4.5	5.2	4.8	4.5
7.7	4.3	5.1	5.4	3.6	3.7	4.5	4.9	4.8	5.6	5.1	4.8
8.8	4.4	5.4	5.7	3.8	3.7	4.6	5.1	5.2	6.1	5.4	5.1
10.1	4.6	5.8	6.0	3.9	3.8	4.8	5.4	5.8	6.8	6.0	5.7
11.6	4.8	6.4	6.6	4.1	4.0	5.1	5.8	6.7	7.9	6.7	6.5
13.2	5.2	7.4	7.5	4.4	4.2	5.4	6.4	8.3	9.6	8.0	7.9
15.2	5.8	9.0	9.2	4.9	4.5	6.0	7.5	10.8	12.3	10.2	10.3
17.4	7.0	11.7	12.2	5.6	5.1	7.0	9.3	14.9	16.7	13.7	14.2
19.9	9.1	16.2	17.4	6.8	6.1	8.7	12.6	21.3	23.2	19.3	20.5
22.8	13.0	23.1	25.8	8.9	8.0	11.8	18.1	30.5	32.3	27.4	29.6
26.1	19.5	32.8	37.8	12.4	11.5	17.0	26.6	42.4	43.5	38.1	41.3
29.9	29.6	44.8	52.6	17.8	17.4	25.0	38.2	55.8	56.0	50.6	54.6
34.3	43.0	57.6	67.9	25.8	26.7	36.2	52.2	69.0	68.1	63.3	67.7
39.2	58.2	69.7	80.9	36.3	39.3	49.8	66.3	80.3	78.6	74.5	78.9
44.9	72.5	79.5	90.1	48.4	53.8	64.0	78.6	88.6	86.6	83.2	87.2
51.5	83.9	86.6	95.6	60.6	68.0	76.5	87.6	94.0	92.1	89.4	92.7
59.0	91.6	91.4	98.3	71.5	79.8	86.0	93.5	97.1	95.6	93.4	96.1
67.5	96.0	94.5	99.5	80.2	88.2	92.3	96.8	98.8	97.7	96.0	98.0
77.3	98.4	96.4	100.0	86.6	93.4	96.0	98.6	99.6	98.9	97.5	99.1
88.6	99.5	97.7	100.0	91.1	96.5	98.0	99.5	100.0	99.6	98.5	99.6
101.5	100.0	98.5	100.0	94.1	98.1	99.1	100.0	100.0	100.0	99.2	100.0
116.2	100.0	99.1	100.0	96.2	99.1	99.7	100.0	100.0	100.0	99.7	100.0
133.1	100.0	99.6	100.0	97.8	99.6	100.0	100.0	100.0	100.0	100.0	100.0
152.5	100.0	100.0	100.0	99.0	100.0	100.0	100.0	100.0	100.0	100.0	100.0
174.6	100.0	100.0	100.0	99.6	100.0	100.0	100.0	100.0	100.0	100.0	100.0
200.0	100.0	100.0	100.0	100.0	100.0	100.0	100.0	100.0	100.0	100.0	100.0
229.1	100.0	100.0	100.0	100.0	100.0	100.0	100.0	100.0	100.0	100.0	100.0
262.4	100.0	100.0	100.0	100.0	100.0	100.0	100.0	100.0	100.0	100.0	100.0
300.5	100.0	100.0	100.0	100.0	100.0	100.0	100.0	100.0	100.0	100.0	100.0

Sample #	H9	H10	H-1	H-2	H-3	H-4	H-5	H-6	H-7	H-8	H-9
X Location	124.5	122.2	144.9	147.2	149.4	151.7	153.9	156.2	158.5	160.7	163.0
Y Location	92.8	89.5	122.5	125.8	129.1	132.4	135.7	139.0	142.3	145.6	148.9

Grain Size (μm)	%	%	%	%	%	%	%	%	%	%	%
	Finner										
1.0	0.1	0.0	0.0	0.0	0.0	0.0	0.0	0.0	0.0	0.0	0.0
1.2	0.3	0.2	0.0	0.0	0.1	0.1	0.0	0.1	0.1	0.1	0.1
1.3	0.6	0.4	0.2	0.2	0.3	0.3	0.2	0.3	0.3	0.3	0.4
1.5	0.9	0.7	0.4	0.4	0.6	0.5	0.4	0.5	0.6	0.6	0.7
1.7	1.3	1.1	0.8	0.7	0.9	0.8	0.7	0.8	0.9	0.9	1.0
2.0	1.7	1.5	1.2	1.1	1.3	1.2	1.0	1.2	1.3	1.4	1.4
2.3	2.2	1.9	1.6	1.5	1.6	1.5	1.3	1.5	1.7	1.8	1.8
2.6	2.6	2.3	2.1	1.9	2.0	1.9	1.7	1.8	2.0	2.2	2.2
3.0	3.0	2.6	2.5	2.2	2.3	2.2	2.0	2.0	2.3	2.5	2.5
3.4	3.3	2.9	2.8	2.5	2.6	2.4	2.2	2.2	2.6	2.8	2.8
3.9	3.6	3.2	3.1	2.7	2.8	2.6	2.4	2.3	2.8	3.0	3.1
4.5	3.8	3.4	3.3	2.9	2.9	2.7	2.5	2.4	3.0	3.2	3.3
5.1	4.1	3.7	3.4	3.0	3.1	2.8	2.6	2.4	3.1	3.4	3.4
5.9	4.2	3.8	3.5	3.0	3.2	2.8	2.6	2.4	3.1	3.5	3.6
6.7	4.5	4.0	3.6	3.0	3.2	2.8	2.6	2.4	3.1	3.6	3.7
7.7	4.7	4.3	3.6	3.0	3.2	2.8	2.6	2.4	3.1	3.7	3.9
8.8	5.0	4.6	3.6	3.0	3.2	2.8	2.6	2.4	3.1	3.8	4.1
10.1	5.5	5.0	3.6	3.0	3.3	2.8	2.6	2.4	3.2	3.9	4.3
11.6	6.3	5.7	3.8	3.0	3.5	2.8	2.6	2.4	3.3	4.1	4.6
13.2	7.7	6.8	3.9	3.1	3.7	3.0	2.8	2.6	3.5	4.5	5.2
15.2	10.0	8.7	4.2	3.3	4.1	3.2	3.0	2.8	3.9	5.0	6.1
17.4	14.1	12.0	4.6	3.7	4.8	3.7	3.3	3.3	4.6	6.0	7.8
19.9	20.6	17.3	5.5	4.3	6.0	4.5	4.0	4.4	5.8	7.8	10.7
22.8	30.2	25.3	7.1	5.6	8.2	6.1	5.3	6.5	8.1	11.2	15.5
26.1	42.7	36.0	10.1	7.9	12.1	9.2	7.7	10.5	12.1	17.0	23.1
29.9	56.8	48.9	15.5	12.3	18.5	14.6	12.1	17.6	18.8	26.3	33.7
34.3	70.5	62.2	24.5	19.7	27.8	23.2	19.3	28.6	28.7	39.1	46.6
39.2	81.7	74.3	37.3	30.8	39.8	35.3	29.7	43.1	41.4	54.2	60.4
44.9	89.8	83.8	52.9	45.0	53.4	49.6	42.7	59.0	55.3	69.2	73.1
51.5	94.7	90.5	68.6	60.3	66.6	64.0	56.7	73.5	68.5	81.6	83.1
59.0	97.5	94.7	81.6	74.1	77.7	76.4	69.5	84.5	79.3	90.2	90.1
67.5	99.0	97.3	90.5	84.5	86.0	85.6	79.7	91.7	87.2	95.4	94.6
77.3	99.7	98.7	95.6	91.4	91.6	91.7	87.1	95.8	92.3	98.1	97.2
88.6	100.0	99.5	98.2	95.5	95.2	95.4	92.0	97.9	95.5	99.4	98.7
101.5	100.0	100.0	99.5	97.7	97.3	97.5	95.1	99.1	97.5	100.0	99.5
116.2	100.0	100.0	100.0	98.9	98.6	98.8	97.2	99.7	98.7	100.0	100.0
133.1	100.0	100.0	100.0	99.6	99.5	99.5	98.5	100.0	99.5	100.0	100.0
152.5	100.0	100.0	100.0	100.0	100.0	100.0	99.5	100.0	100.0	100.0	100.0
174.6	100.0	100.0	100.0	100.0	100.0	100.0	100.0	100.0	100.0	100.0	100.0
200.0	100.0	100.0	100.0	100.0	100.0	100.0	100.0	100.0	100.0	100.0	100.0
229.1	100.0	100.0	100.0	100.0	100.0	100.0	100.0	100.0	100.0	100.0	100.0
262.4	100.0	100.0	100.0	100.0	100.0	100.0	100.0	100.0	100.0	100.0	100.0
300.5	100.0	100.0	100.0	100.0	100.0	100.0	100.0	100.0	100.0	100.0	100.0

Sample #	H-10	H-11	I1	I2	I3	I4	I5	I6	I7	I8	I-1
X Location	165.3	167.5	168.3	164.2	160.1	156.0	151.9	147.8	143.7	139.6	172.3
Y Location	152.2	155.4	89.2	86.3	83.5	80.6	77.7	74.8	72.0	69.1	92.1

Grain Size (μm)	%	%	%	%	%	%	%	%	%	%	%
	Finner										
1.0	0.0	0.1	0.0	0.0	0.0	0.0	0.0	0.1	0.1	0.0	0.0
1.2	0.1	0.3	0.1	0.1	0.1	0.1	0.1	0.3	0.3	0.2	0.0
1.3	0.3	0.6	0.3	0.3	0.3	0.3	0.4	0.6	0.6	0.4	0.2
1.5	0.5	0.9	0.5	0.6	0.6	0.7	0.7	1.0	1.1	0.7	0.4
1.7	0.8	1.4	0.8	1.0	1.1	1.1	1.2	1.6	1.6	1.0	0.8
2.0	1.0	1.9	1.2	1.4	1.6	1.6	1.7	2.2	2.3	1.3	1.2
2.3	1.3	2.4	1.6	1.8	2.1	2.1	2.2	2.9	2.9	1.7	1.7
2.6	1.5	2.8	2.0	2.3	2.6	2.7	2.8	3.5	3.6	2.0	2.1
3.0	1.8	3.2	2.3	2.7	3.1	3.2	3.4	4.2	4.3	2.3	2.6
3.4	1.9	3.6	2.7	3.1	3.6	3.7	3.9	4.8	4.8	2.5	2.9
3.9	2.1	3.9	3.0	3.5	3.9	4.1	4.3	5.3	5.3	2.7	3.2
4.5	2.2	4.1	3.2	3.7	4.2	4.4	4.7	5.8	5.8	2.9	3.5
5.1	2.2	4.3	3.4	4.0	4.4	4.7	5.1	6.3	6.2	3.1	3.6
5.9	2.2	4.5	3.6	4.2	4.6	4.9	5.4	6.8	6.6	3.3	3.8
6.7	2.2	4.7	3.7	4.3	4.8	5.1	5.7	7.3	7.1	3.5	3.9
7.7	2.2	4.9	3.9	4.5	5.0	5.4	6.1	8.0	7.6	3.7	4.0
8.8	2.2	5.1	4.1	4.7	5.1	5.6	6.5	8.9	8.2	4.0	4.1
10.1	2.2	5.5	4.3	4.9	5.4	5.9	7.1	10.2	9.2	4.5	4.2
11.6	2.3	6.1	4.5	5.2	5.6	6.3	7.9	12.2	10.7	5.3	4.3
13.2	2.5	7.2	4.8	5.6	6.1	6.9	9.2	15.3	13.2	6.8	4.5
15.2	2.9	9.2	5.4	6.2	6.8	7.9	11.1	20.0	17.0	9.3	4.8
17.4	3.6	12.9	6.2	7.1	7.9	9.6	14.2	26.9	22.9	13.6	5.3
19.9	4.9	19.7	7.5	8.7	10.0	12.5	19.0	36.1	31.4	20.2	6.2
22.8	7.4	30.7	9.8	11.4	13.7	17.2	26.0	47.4	42.4	29.5	7.9
26.1	11.8	46.2	13.5	15.9	19.8	24.6	35.4	59.6	55.0	40.9	11.0
29.9	19.1	64.0	19.2	22.8	28.9	35.1	46.8	71.4	67.8	52.9	16.5
34.3	29.9	80.1	27.5	32.6	41.3	48.2	59.1	81.3	79.0	63.9	25.5
39.2	43.5	91.3	38.1	44.9	55.5	62.3	70.7	88.7	87.5	72.7	38.1
44.9	58.5	97.0	50.1	58.2	69.5	75.2	80.4	93.7	93.2	78.8	53.3
51.5	72.3	99.2	62.2	70.7	81.2	85.3	87.6	96.7	96.7	82.8	68.6
59.0	83.1	99.9	72.8	80.9	89.5	92.1	92.5	98.5	98.5	85.3	81.3
67.5	90.5	100.0	81.3	88.3	94.6	96.1	95.6	99.5	99.5	86.8	90.2
77.3	94.9	100.0	87.4	93.1	97.5	98.3	97.4	100.0	100.0	87.8	95.4
88.6	97.4	100.0	91.6	96.0	98.9	99.4	98.6	100.0	100.0	88.5	98.1
101.5	98.8	100.0	94.5	97.8	99.6	100.0	99.2	100.0	100.0	89.1	99.4
116.2	99.6	100.0	96.5	98.9	100.0	100.0	99.7	100.0	100.0	89.6	100.0
133.1	100.0	100.0	97.9	99.6	100.0	100.0	100.0	100.0	100.0	90.1	100.0
152.5	100.0	100.0	99.0	100.0	100.0	100.0	100.0	100.0	100.0	90.8	100.0
174.6	100.0	100.0	99.7	100.0	100.0	100.0	100.0	100.0	100.0	91.5	100.0
200.0	100.0	100.0	100.0	100.0	100.0	100.0	100.0	100.0	100.0	92.4	100.0
229.1	100.0	100.0	100.0	100.0	100.0	100.0	100.0	100.0	100.0	93.7	100.0
262.4	100.0	100.0	100.0	100.0	100.0	100.0	100.0	100.0	100.0	95.1	100.0
300.5	100.0	100.0	100.0	100.0	100.0	100.0	100.0	100.0	100.0	96.8	100.0

Sample #	I-2	I-3	I-4	I-5	I-6	I-7	I-8	J1	J2	J3	J4
X Location	176.4	180.5	184.6	188.7	192.8	196.9	201.0	196.5	194.3	192.0	189.7
Y Location	94.9	97.8	100.7	103.5	106.4	109.3	112.1	59.3	56.0	52.8	49.5

Grain Size (μm)	%	%	%	%	%	%	%	%	%	%	%
	Finner										
1.0	0.0	0.0	0.0	0.0	0.0	0.0	0.0	0.0	0.0	0.0	0.0
1.2	0.0	0.0	0.1	0.1	0.1	0.2	0.1	0.0	0.0	0.0	0.1
1.3	0.2	0.2	0.3	0.3	0.4	0.4	0.4	0.2	0.2	0.1	0.3
1.5	0.4	0.4	0.5	0.6	0.7	0.7	0.7	0.4	0.4	0.3	0.6
1.7	0.8	0.7	0.9	1.0	1.1	1.1	1.0	0.7	0.8	0.5	0.9
2.0	1.2	1.1	1.3	1.4	1.5	1.6	1.5	1.1	1.2	0.7	1.3
2.3	1.6	1.5	1.6	1.8	2.0	2.1	1.9	1.5	1.6	0.9	1.8
2.6	2.0	1.9	2.0	2.2	2.6	2.5	2.4	1.9	2.1	1.1	2.3
3.0	2.5	2.2	2.4	2.6	3.0	3.0	2.8	2.3	2.5	1.3	2.7
3.4	2.9	2.6	2.6	2.9	3.5	3.4	3.2	2.7	2.9	1.5	3.0
3.9	3.2	2.8	2.9	3.1	3.9	3.8	3.6	3.0	3.2	1.6	3.3
4.5	3.5	3.0	3.0	3.4	4.2	4.1	3.9	3.2	3.4	1.8	3.5
5.1	3.7	3.2	3.2	3.5	4.5	4.4	4.3	3.4	3.6	1.8	3.7
5.9	3.9	3.3	3.3	3.7	4.8	4.6	4.6	3.5	3.7	1.8	3.9
6.7	4.1	3.4	3.3	3.8	5.1	4.9	4.9	3.6	3.8	1.8	4.0
7.7	4.3	3.5	3.3	3.9	5.4	5.2	5.2	3.8	4.0	1.8	4.1
8.8	4.4	3.6	3.3	4.1	5.9	5.6	5.7	3.9	4.1	1.8	4.2
10.1	4.6	3.7	3.4	4.2	6.4	6.2	6.4	4.0	4.2	1.8	4.3
11.6	4.9	3.9	3.5	4.5	7.2	7.1	7.4	4.2	4.4	1.8	4.5
13.2	5.2	4.1	3.7	4.8	8.4	8.5	8.9	4.4	4.6	1.9	4.7
15.2	5.7	4.4	4.0	5.4	10.4	10.8	11.3	4.8	4.9	2.1	5.1
17.4	6.5	4.9	4.7	6.4	13.5	14.5	15.1	5.4	5.5	2.5	5.7
19.9	7.8	5.8	5.8	8.2	18.5	20.3	20.7	6.4	6.5	3.3	6.7
22.8	9.9	7.5	7.9	11.3	25.7	28.8	28.5	8.3	8.5	4.8	8.8
26.1	13.3	10.4	11.7	16.5	35.6	39.9	38.3	11.5	12.0	7.5	12.4
29.9	18.6	15.4	17.9	24.4	47.6	52.9	49.3	16.8	18.2	12.3	18.7
34.3	26.3	23.1	27.2	35.3	60.5	66.1	60.3	24.7	28.0	20.1	28.4
39.2	36.4	33.5	39.2	48.3	72.6	77.7	70.0	35.3	41.4	31.0	41.5
44.9	48.0	46.0	52.5	61.8	82.6	86.6	77.7	47.5	57.0	43.9	56.6
51.5	59.9	58.9	65.3	73.9	89.8	92.5	83.3	59.9	72.0	57.0	71.2
59.0	70.6	70.5	76.0	83.3	94.5	96.1	87.1	70.8	84.0	67.9	82.9
67.5	79.3	79.7	83.9	89.8	97.2	98.1	89.7	79.4	91.8	75.8	90.9
77.3	85.9	86.4	89.5	94.0	98.7	99.1	91.4	85.7	96.3	80.7	95.7
88.6	90.6	91.0	93.1	96.5	99.6	99.7	92.6	90.2	98.5	83.6	98.2
101.5	93.9	94.1	95.6	98.1	100.0	100.0	93.5	93.4	99.5	85.2	99.4
116.2	96.2	96.3	97.3	99.0	100.0	100.0	94.2	95.6	100.0	86.2	100.0
133.1	97.8	97.8	98.5	99.6	100.0	100.0	94.9	97.4	100.0	86.9	100.0
152.5	99.0	99.0	99.5	100.0	100.0	100.0	95.6	98.8	100.0	87.4	100.0
174.6	99.6	99.6	100.0	100.0	100.0	100.0	96.2	99.6	100.0	87.8	100.0
200.0	100.0	100.0	100.0	100.0	100.0	100.0	97.0	100.0	100.0	88.3	100.0
229.1	100.0	100.0	100.0	100.0	100.0	100.0	97.8	100.0	100.0	88.9	100.0
262.4	100.0	100.0	100.0	100.0	100.0	100.0	98.6	100.0	100.0	89.7	100.0
300.5	100.0	100.0	100.0	100.0	100.0	100.0	99.5	100.0	100.0	90.7	100.0

Sample #	J5	J6	J7	J8	J9	J-1	J-2	J-3	J-4	J-5	J-6
X Location	187.5	185.2	182.9	180.7	182.7	198.8	201.1	203.3	205.6	207.9	210.1
Y Location	46.2	42.9	39.6	36.3	35.1	62.6	65.9	69.2	72.5	75.8	79.1

Grain Size (μm)	%	%	%	%	%	%	%	%	%	%	%
	Finner										
1.0	0.0	0.0	0.0	0.1	0.1	0.0	0.0	0.0	0.0	0.0	0.0
1.2	0.1	0.1	0.2	0.3	0.3	0.0	0.1	0.1	0.1	0.1	0.1
1.3	0.3	0.3	0.4	0.6	0.6	0.2	0.3	0.3	0.4	0.3	0.4
1.5	0.6	0.5	0.8	0.9	1.0	0.4	0.5	0.6	0.7	0.6	0.6
1.7	1.0	0.8	1.3	1.4	1.6	0.7	0.9	0.9	1.1	1.0	1.0
2.0	1.5	1.2	1.8	1.9	2.2	1.0	1.3	1.3	1.5	1.5	1.4
2.3	1.9	1.6	2.4	2.5	2.9	1.4	1.8	1.7	2.0	2.0	1.8
2.6	2.3	1.9	3.0	3.1	3.6	1.8	2.3	2.2	2.4	2.4	2.2
3.0	2.7	2.3	3.6	3.6	4.4	2.2	2.7	2.5	2.8	2.9	2.6
3.4	3.0	2.5	4.1	4.2	5.1	2.5	3.1	2.9	3.1	3.4	3.0
3.9	3.3	2.8	4.6	4.6	5.7	2.8	3.4	3.1	3.4	3.7	3.3
4.5	3.5	2.9	5.0	5.0	6.3	3.1	3.7	3.4	3.5	4.1	3.5
5.1	3.6	3.1	5.3	5.4	6.9	3.3	3.9	3.5	3.7	4.3	3.8
5.9	3.7	3.2	5.6	5.8	7.5	3.5	4.1	3.7	3.8	4.6	4.0
6.7	3.7	3.3	6.0	6.2	8.2	3.7	4.2	3.8	3.9	4.8	4.2
7.7	3.7	3.3	6.4	6.8	9.0	3.9	4.4	3.9	4.0	5.1	4.5
8.8	3.7	3.4	6.8	7.4	10.0	4.1	4.5	4.1	4.2	5.4	4.8
10.1	3.8	3.5	7.4	8.5	11.6	4.4	4.6	4.2	4.3	5.7	5.2
11.6	4.0	3.7	8.3	10.0	13.9	4.7	4.8	4.5	4.5	6.2	5.9
13.2	4.3	4.0	9.7	12.6	17.4	5.1	5.1	4.8	4.9	7.0	7.0
15.2	4.8	4.6	11.9	16.7	22.7	5.7	5.5	5.3	5.5	8.2	8.9
17.4	5.7	5.5	15.5	23.2	30.4	6.7	6.2	6.3	6.6	10.2	12.0
19.9	7.5	7.3	21.0	32.8	40.8	8.2	7.3	7.9	8.8	13.6	17.0
22.8	11.0	10.5	29.0	45.3	53.3	10.6	9.5	10.7	12.9	19.1	24.3
26.1	17.3	15.7	39.5	59.9	66.6	14.2	13.3	15.5	19.9	27.3	34.2
29.9	27.5	23.6	51.8	74.0	78.7	19.5	19.8	22.7	30.5	38.4	45.8
34.3	41.4	34.0	64.3	85.6	88.1	26.6	29.7	32.4	44.4	51.8	57.7
39.2	57.6	45.7	75.6	93.2	94.3	35.3	43.1	44.1	59.8	65.7	68.3
44.9	72.9	57.1	84.4	97.3	97.6	45.0	58.2	56.4	74.0	77.9	76.5
51.5	84.8	66.7	90.6	99.2	99.2	54.9	72.7	67.5	85.0	87.3	82.1
59.0	92.5	73.9	94.5	99.8	99.8	64.1	84.2	76.7	92.2	93.4	85.5
67.5	96.7	78.9	96.9	100.0	100.0	72.2	91.9	83.6	96.3	96.9	87.6
77.3	98.7	82.3	98.3	100.0	100.0	79.0	96.2	88.5	98.5	98.7	88.7
88.6	99.6	84.6	99.1	100.0	100.0	84.6	98.4	91.9	99.5	99.6	89.4
101.5	100.0	86.3	99.6	100.0	100.0	89.1	99.5	94.4	100.0	100.0	89.8
116.2	100.0	87.6	100.0	100.0	100.0	92.7	100.0	96.2	100.0	100.0	89.8
133.1	100.0	88.7	100.0	100.0	100.0	95.5	100.0	97.7	100.0	100.0	89.8
152.5	100.0	89.8	100.0	100.0	100.0	97.7	100.0	98.9	100.0	100.0	89.8
174.6	100.0	90.8	100.0	100.0	100.0	98.9	100.0	99.6	100.0	100.0	89.8
200.0	100.0	91.9	100.0	100.0	100.0	99.6	100.0	100.0	100.0	100.0	89.8
229.1	100.0	93.1	100.0	100.0	100.0	100.0	100.0	100.0	100.0	100.0	90.2
262.4	100.0	94.3	100.0	100.0	100.0	100.0	100.0	100.0	100.0	100.0	90.8
300.5	100.0	95.5	100.0	100.0	100.0	100.0	100.0	100.0	100.0	100.0	91.6

Sample #	J-7	K1	K2	K3	K4	K5	K6	K7	K8	K9	K10
X Location	212.4	227.2	227.3	227.4	227.4	227.5	227.6	227.6	227.7	227.7	227.8
Y Location	82.4	49.7	45.7	41.7	37.7	33.7	29.7	25.7	21.7	17.7	13.7

Grain Size (μm)	%	%	%	%	%	%	%	%	%	%	%
	Finner										
1.0	0.0	0.0	0.0	0.0	0.0	0.0	0.0	0.0	0.0	0.0	0.0
1.2	0.1	0.1	0.1	0.0	0.0	0.1	0.1	0.1	0.1	0.1	0.1
1.3	0.4	0.3	0.3	0.2	0.2	0.3	0.3	0.3	0.4	0.4	0.3
1.5	0.7	0.5	0.5	0.4	0.4	0.7	0.5	0.6	0.7	0.7	0.6
1.7	1.2	0.8	0.8	0.7	0.7	1.0	0.9	1.0	1.1	1.2	1.0
2.0	1.7	1.2	1.2	1.1	1.1	1.5	1.2	1.4	1.5	1.7	1.4
2.3	2.3	1.6	1.5	1.5	1.5	1.9	1.6	1.9	2.0	2.3	1.9
2.6	2.9	1.9	1.9	1.9	1.9	2.4	2.0	2.4	2.4	2.8	2.3
3.0	3.5	2.3	2.2	2.3	2.2	2.7	2.3	2.8	2.7	3.3	2.7
3.4	4.0	2.6	2.5	2.6	2.5	3.0	2.5	3.2	3.0	3.8	3.0
3.9	4.4	2.8	2.7	2.9	2.8	3.2	2.7	3.5	3.2	4.1	3.3
4.5	4.8	3.0	2.9	3.1	2.9	3.4	2.9	3.8	3.4	4.4	3.5
5.1	5.1	3.2	3.1	3.2	3.1	3.5	3.0	4.0	3.5	4.7	3.7
5.9	5.4	3.3	3.3	3.3	3.2	3.5	3.0	4.1	3.5	4.9	3.9
6.7	5.6	3.4	3.4	3.4	3.3	3.5	3.0	4.3	3.5	5.1	4.0
7.7	5.9	3.4	3.6	3.4	3.3	3.5	3.0	4.4	3.5	5.3	4.2
8.8	6.2	3.4	3.7	3.4	3.3	3.5	3.0	4.6	3.5	5.5	4.4
10.1	6.6	3.5	3.9	3.6	3.4	3.5	3.0	4.7	3.7	5.8	4.6
11.6	7.2	3.7	4.1	3.7	3.6	3.7	3.1	4.9	3.9	6.1	5.0
13.2	8.1	3.9	4.4	3.9	3.8	3.9	3.3	5.2	4.2	6.7	5.6
15.2	9.4	4.2	4.9	4.2	4.1	4.3	3.7	5.7	4.8	7.7	6.5
17.4	11.7	4.7	5.6	4.7	4.7	5.1	4.3	6.5	6.1	9.4	8.3
19.9	15.5	5.8	6.9	5.7	5.7	6.7	5.5	8.0	8.6	12.5	11.3
22.8	21.5	7.6	9.0	7.5	7.6	9.9	7.9	10.6	13.7	17.6	16.4
26.1	30.4	11.0	12.5	10.8	11.0	15.8	12.4	15.1	22.8	25.7	24.4
29.9	42.3	16.8	18.0	16.5	16.7	25.5	19.9	22.4	36.8	37.1	35.6
34.3	56.1	25.6	26.1	25.4	25.3	39.0	31.1	32.8	54.6	51.1	49.4
39.2	69.9	37.7	36.7	37.7	36.8	55.0	45.4	45.8	72.5	65.5	63.8
44.9	81.6	51.6	49.0	52.2	49.9	70.5	60.7	59.9	86.4	78.2	76.7
51.5	90.0	65.4	61.3	66.7	62.9	82.9	74.5	72.9	94.6	87.6	86.5
59.0	95.2	77.0	72.2	78.8	74.0	91.1	85.0	83.1	98.3	93.6	92.9
67.5	98.0	85.6	80.9	87.5	82.5	95.9	91.8	90.1	99.6	97.0	96.6
77.3	99.4	91.2	87.2	93.1	88.4	98.3	95.8	94.5	100.0	98.7	98.5
88.6	100.0	94.7	91.5	96.3	92.3	99.5	97.9	97.0	100.0	99.6	99.5
101.5	100.0	96.8	94.4	98.1	94.9	100.0	99.1	98.4	100.0	100.0	100.0
116.2	100.0	98.1	96.4	99.1	96.8	100.0	99.7	99.2	100.0	100.0	100.0
133.1	100.0	99.0	97.9	99.6	98.1	100.0	100.0	99.7	100.0	100.0	100.0
152.5	100.0	99.6	99.0	100.0	99.1	100.0	100.0	100.0	100.0	100.0	100.0
174.6	100.0	100.0	99.7	100.0	99.7	100.0	100.0	100.0	100.0	100.0	100.0
200.0	100.0	100.0	100.0	100.0	100.0	100.0	100.0	100.0	100.0	100.0	100.0
229.1	100.0	100.0	100.0	100.0	100.0	100.0	100.0	100.0	100.0	100.0	100.0
262.4	100.0	100.0	100.0	100.0	100.0	100.0	100.0	100.0	100.0	100.0	100.0
300.5	100.0	100.0	100.0	100.0	100.0	100.0	100.0	100.0	100.0	100.0	100.0

Sample #	K11	K-1	K-2	K-3	K-4	K-5	L1	L2	L3	L4	L6
X Location	227.9	227.2	227.1	227.1	227.0	226.9	259.0	261.3	263.7	266.1	270.8
Y Location	9.7	53.7	57.7	61.7	65.7	69.7	58.4	55.2	52.0	48.8	42.3

Grain Size (μm)	%	%	%	%	%	%	%	%	%	%	%
	Finner										
1.0	0.0	0.0	0.0	0.1	0.0	0.0	0.0	0.0	0.0	0.0	0.0
1.2	0.2	0.1	0.1	0.3	0.2	0.2	0.2	0.1	0.0	0.1	0.1
1.3	0.4	0.3	0.3	0.5	0.4	0.5	0.4	0.3	0.2	0.3	0.3
1.5	0.8	0.6	0.6	0.8	0.7	0.9	0.7	0.6	0.4	0.6	0.6
1.7	1.2	0.9	0.9	1.1	1.1	1.4	1.1	1.0	0.8	1.0	1.0
2.0	1.8	1.3	1.4	1.4	1.6	2.1	1.5	1.4	1.2	1.5	1.4
2.3	2.4	1.7	1.8	1.7	2.1	2.8	2.0	1.9	1.6	1.9	1.9
2.6	3.0	2.1	2.3	2.0	2.6	3.6	2.3	2.3	2.0	2.4	2.3
3.0	3.6	2.5	2.7	2.3	3.0	4.3	2.7	2.6	2.4	2.8	2.7
3.4	4.2	2.8	3.1	2.6	3.3	5.0	2.9	2.9	2.6	3.2	3.1
3.9	4.6	3.1	3.4	2.8	3.6	5.7	3.1	3.2	2.9	3.5	3.4
4.5	5.0	3.3	3.7	3.0	3.8	6.3	3.3	3.3	3.0	3.7	3.6
5.1	5.4	3.5	3.9	3.2	4.0	6.8	3.4	3.5	3.2	3.9	3.7
5.9	5.7	3.7	4.0	3.4	4.2	7.4	3.4	3.6	3.2	4.0	3.9
6.7	6.0	3.9	4.2	3.6	4.3	7.9	3.4	3.6	3.2	4.1	4.0
7.7	6.4	4.0	4.3	3.8	4.4	8.6	3.4	3.6	3.2	4.2	4.1
8.8	6.8	4.2	4.5	4.0	4.6	9.4	3.4	3.6	3.2	4.3	4.2
10.1	7.3	4.4	4.7	4.3	4.8	10.5	3.4	3.7	3.2	4.5	4.3
11.6	8.1	4.6	4.9	4.6	5.1	12.0	3.5	3.8	3.3	4.6	4.5
13.2	9.3	4.9	5.2	5.1	5.6	14.3	3.6	4.0	3.5	4.9	4.8
15.2	11.3	5.4	5.8	5.9	6.5	17.8	4.0	4.4	3.8	5.3	5.2
17.4	14.4	6.3	6.7	7.2	8.2	22.9	4.6	5.1	4.3	6.1	6.0
19.9	19.4	7.7	8.3	9.3	11.4	30.1	6.1	6.5	5.4	7.6	7.4
22.8	26.7	10.1	11.2	12.6	16.9	39.5	9.3	9.2	7.4	10.3	10.1
26.1	36.8	14.1	16.1	17.8	25.7	50.8	15.8	14.4	11.4	15.2	14.7
29.9	49.0	20.4	23.8	25.3	38.1	62.7	27.7	23.2	18.2	23.1	22.3
34.3	62.0	29.6	34.6	35.1	52.9	73.9	45.2	36.2	28.8	34.5	33.1
39.2	74.0	41.3	47.9	46.7	67.7	83.3	65.1	52.4	42.7	48.5	46.6
44.9	83.7	54.3	61.9	58.8	80.1	90.1	82.1	68.7	58.0	63.2	60.9
51.5	90.6	67.0	74.5	69.9	88.9	94.6	92.7	82.0	72.0	76.0	73.8
59.0	94.9	77.6	84.2	79.0	94.3	97.3	97.7	90.9	82.7	85.7	83.7
67.5	97.5	85.6	90.8	85.9	97.2	98.8	99.5	95.9	89.8	91.9	90.4
77.3	98.8	91.0	94.8	90.6	98.8	99.6	100.0	98.3	94.0	95.7	94.6
88.6	99.6	94.5	97.1	93.9	99.6	100.0	100.0	99.5	96.5	97.8	97.0
101.5	100.0	96.7	98.4	96.1	100.0	100.0	100.0	100.0	97.9	98.9	98.4
116.2	100.0	98.1	99.2	97.6	100.0	100.0	100.0	100.0	98.9	99.6	99.2
133.1	100.0	99.0	99.7	98.7	100.0	100.0	100.0	100.0	99.5	100.0	99.7
152.5	100.0	99.6	100.0	99.5	100.0	100.0	100.0	100.0	100.0	100.0	100.0
174.6	100.0	100.0	100.0	100.0	100.0	100.0	100.0	100.0	100.0	100.0	100.0
200.0	100.0	100.0	100.0	100.0	100.0	100.0	100.0	100.0	100.0	100.0	100.0
229.1	100.0	100.0	100.0	100.0	100.0	100.0	100.0	100.0	100.0	100.0	100.0
262.4	100.0	100.0	100.0	100.0	100.0	100.0	100.0	100.0	100.0	100.0	100.0
300.5	100.0	100.0	100.0	100.0	100.0	100.0	100.0	100.0	100.0	100.0	100.0

Sample #	L7	L8	L9	L10	L11	L12	L-1	L-2	L-3	L-4	L-5
X Location	273.1	275.5	277.9	280.3	282.6	285.0	256.6	254.2	251.8	249.4	247.1
Y Location	39.1	35.8	32.6	29.4	26.2	23.0	61.7	64.9	68.1	71.3	74.5

Grain Size (μm)	%	%	%	%	%	%	%	%	%	%	%
	Finner										
1.0	0.0	0.0	0.0	0.0	0.0	0.0	0.0	0.0	0.0	0.0	0.0
1.2	0.1	0.1	0.1	0.1	0.2	0.2	0.1	0.1	0.1	0.1	0.1
1.3	0.3	0.3	0.4	0.4	0.4	0.4	0.3	0.3	0.3	0.3	0.4
1.5	0.6	0.6	0.7	0.7	0.8	0.8	0.6	0.6	0.6	0.6	0.7
1.7	0.9	1.0	1.2	1.2	1.3	1.3	1.0	1.0	1.1	1.0	1.1
2.0	1.3	1.5	1.7	1.7	1.8	1.8	1.4	1.5	1.6	1.5	1.5
2.3	1.8	2.0	2.2	2.2	2.3	2.4	1.9	1.9	2.1	2.0	2.0
2.6	2.2	2.4	2.7	2.7	2.9	2.9	2.4	2.4	2.7	2.5	2.5
3.0	2.6	2.9	3.2	3.2	3.3	3.4	2.8	2.8	3.2	2.9	3.0
3.4	2.9	3.2	3.6	3.6	3.7	3.9	3.2	3.2	3.6	3.3	3.4
3.9	3.2	3.5	3.9	3.9	4.0	4.3	3.5	3.5	4.0	3.7	3.7
4.5	3.4	3.7	4.2	4.1	4.3	4.5	3.7	3.7	4.3	4.0	4.0
5.1	3.6	3.8	4.4	4.3	4.4	4.8	3.9	3.9	4.5	4.2	4.2
5.9	3.8	4.0	4.5	4.4	4.6	5.0	4.1	4.1	4.7	4.4	4.4
6.7	3.9	4.1	4.7	4.6	4.8	5.2	4.2	4.2	4.9	4.6	4.6
7.7	4.0	4.2	4.8	4.7	4.9	5.4	4.4	4.4	5.0	4.7	4.8
8.8	4.2	4.3	4.9	4.9	5.1	5.7	4.5	4.5	5.2	4.9	5.0
10.1	4.3	4.5	5.2	5.1	5.3	6.0	4.7	4.7	5.4	5.1	5.3
11.6	4.5	4.7	5.5	5.4	5.7	6.5	4.9	4.9	5.7	5.4	5.7
13.2	4.8	5.0	5.9	5.9	6.4	7.3	5.2	5.2	6.1	5.8	6.3
15.2	5.3	5.5	6.8	6.9	7.5	8.7	5.7	5.8	6.9	6.5	7.3
17.4	6.1	6.5	8.3	8.5	9.8	11.1	6.5	6.8	8.1	7.7	9.0
19.9	7.6	8.3	11.2	11.6	13.9	15.2	8.0	8.6	10.5	9.8	11.8
22.8	10.2	11.7	16.3	17.0	21.1	22.1	10.7	12.0	14.8	13.6	16.6
26.1	14.6	17.6	24.6	25.6	32.3	32.1	15.2	17.9	22.0	19.9	24.1
29.9	21.6	26.9	36.5	37.7	47.3	45.2	22.5	27.4	33.1	29.6	34.6
34.3	31.6	39.6	51.1	52.2	63.8	59.8	33.0	40.7	47.7	42.6	47.5
39.2	44.1	54.5	66.1	66.9	78.5	73.4	46.2	56.3	63.5	57.4	61.3
44.9	57.6	69.0	79.0	79.4	89.1	84.2	60.3	71.3	77.6	71.6	74.0
51.5	70.2	81.0	88.2	88.3	95.2	91.4	73.1	83.3	87.8	83.0	84.0
59.0	80.5	89.3	93.9	93.9	98.2	95.7	83.2	91.2	94.0	90.7	90.9
67.5	87.8	94.4	97.1	97.0	99.5	98.0	90.1	95.7	97.3	95.2	95.2
77.3	92.6	97.3	98.7	98.6	100.0	99.1	94.4	98.0	98.9	97.7	97.6
88.6	95.7	98.8	99.6	99.5	100.0	99.7	96.9	99.1	99.6	99.0	98.9
101.5	97.5	99.6	100.0	100.0	100.0	100.0	98.3	99.7	100.0	99.6	99.6
116.2	98.7	100.0	100.0	100.0	100.0	100.0	99.1	100.0	100.0	100.0	100.0
133.1	99.5	100.0	100.0	100.0	100.0	100.0	99.7	100.0	100.0	100.0	100.0
152.5	100.0	100.0	100.0	100.0	100.0	100.0	100.0	100.0	100.0	100.0	100.0
174.6	100.0	100.0	100.0	100.0	100.0	100.0	100.0	100.0	100.0	100.0	100.0
200.0	100.0	100.0	100.0	100.0	100.0	100.0	100.0	100.0	100.0	100.0	100.0
229.1	100.0	100.0	100.0	100.0	100.0	100.0	100.0	100.0	100.0	100.0	100.0
262.4	100.0	100.0	100.0	100.0	100.0	100.0	100.0	100.0	100.0	100.0	100.0
300.5	100.0	100.0	100.0	100.0	100.0	100.0	100.0	100.0	100.0	100.0	100.0

Sample #	L-6	M0	M1	M2	M3	M4	M-1	M-2	M-3	M-4
X Location	244.7	282.3	286.4	290.4	294.5	298.6	278.2	274.1	270.0	265.8
Y Location	77.7	90.9	88.0	85.1	82.2	79.4	93.7	96.6	99.5	102.3

Grain Size (μm)	%	%	%	%	%	%	%	%	%	%
	Finner									
1.0	0.0	0.0	0.0	0.0	0.0	0.0	0.0	0.0	0.0	0.0
1.2	0.1	0.1	0.2	0.1	0.1	0.2	0.1	0.1	0.1	0.1
1.3	0.4	0.3	0.4	0.3	0.3	0.4	0.4	0.3	0.3	0.4
1.5	0.7	0.6	0.7	0.6	0.6	0.8	0.7	0.7	0.6	0.7
1.7	1.0	1.1	1.1	0.9	0.9	1.2	1.1	1.1	1.0	1.1
2.0	1.5	1.6	1.4	1.3	1.4	1.8	1.7	1.6	1.4	1.5
2.3	1.9	2.1	1.8	1.8	1.8	2.2	2.2	2.1	1.9	2.0
2.6	2.4	2.7	2.2	2.2	2.2	2.7	2.7	2.6	2.3	2.5
3.0	2.8	3.2	2.5	2.6	2.6	3.0	3.1	3.1	2.8	2.9
3.4	3.2	3.6	2.8	3.0	2.9	3.3	3.5	3.5	3.2	3.2
3.9	3.5	4.0	3.0	3.3	3.1	3.5	3.8	3.9	3.5	3.5
4.5	3.8	4.3	3.2	3.5	3.3	3.7	4.0	4.2	3.7	3.8
5.1	4.0	4.5	3.4	3.7	3.4	3.7	4.2	4.5	4.0	3.9
5.9	4.2	4.7	3.5	3.9	3.6	3.7	4.3	4.7	4.1	4.1
6.7	4.4	4.8	3.7	4.0	3.6	3.7	4.4	4.9	4.3	4.2
7.7	4.6	5.0	3.8	4.1	3.6	3.7	4.5	5.1	4.4	4.4
8.8	4.8	5.1	3.9	4.3	3.6	3.7	4.6	5.3	4.6	4.5
10.1	5.2	5.3	4.1	4.4	3.7	3.7	4.8	5.5	4.8	4.7
11.6	5.6	5.5	4.4	4.7	3.8	3.8	5.0	5.8	5.1	5.0
13.2	6.3	5.9	4.7	5.0	4.1	4.0	5.3	6.3	5.5	5.4
15.2	7.4	6.5	5.2	5.5	4.5	4.4	5.8	7.0	6.1	6.2
17.4	9.3	7.5	6.1	6.4	5.3	5.3	6.9	8.1	7.2	7.5
19.9	12.3	9.6	7.6	8.0	6.7	7.4	8.9	10.0	9.1	10.0
22.8	17.2	13.5	10.2	10.9	9.4	12.2	13.1	13.2	12.4	14.4
26.1	24.4	20.5	14.3	15.7	14.4	21.7	20.7	18.5	18.1	21.9
29.9	34.2	31.9	20.6	23.5	22.6	37.7	33.3	26.4	26.8	33.3
34.3	46.0	47.8	29.5	34.5	34.6	58.7	50.4	37.3	38.9	48.1
39.2	58.6	65.7	40.7	48.0	49.6	78.7	68.8	50.4	53.3	64.1
44.9	70.4	81.6	53.3	62.4	65.2	91.9	84.1	64.0	67.9	78.3
51.5	80.1	92.1	65.7	75.1	78.5	97.8	93.6	76.0	80.2	88.6
59.0	87.3	97.4	76.6	84.9	87.9	99.6	98.0	85.3	89.1	94.8
67.5	92.2	99.4	85.2	91.3	93.6	100.0	99.5	91.6	94.6	98.0
77.3	95.4	100.0	91.2	95.2	96.7	100.0	100.0	95.5	97.5	99.4
88.6	97.3	100.0	95.1	97.3	98.3	100.0	100.0	97.7	99.0	100.0
101.5	98.5	100.0	97.4	98.5	99.2	100.0	100.0	98.9	99.7	100.0
116.2	99.2	100.0	98.8	99.2	99.7	100.0	100.0	99.6	100.0	100.0
133.1	99.7	100.0	99.5	99.7	100.0	100.0	100.0	100.0	100.0	100.0
152.5	100.0	100.0	100.0	100.0	100.0	100.0	100.0	100.0	100.0	100.0
174.6	100.0	100.0	100.0	100.0	100.0	100.0	100.0	100.0	100.0	100.0
200.0	100.0	100.0	100.0	100.0	100.0	100.0	100.0	100.0	100.0	100.0
229.1	100.0	100.0	100.0	100.0	100.0	100.0	100.0	100.0	100.0	100.0
262.4	100.0	100.0	100.0	100.0	100.0	100.0	100.0	100.0	100.0	100.0
300.5	100.0	100.0	100.0	100.0	100.0	100.0	100.0	100.0	100.0	100.0

Chapter 5

How sinuosity can affect the total length of submarine channels

Kyle M. Straub^a, David Mohrig^b, James Buttles^b, Brandon McElroy^b, & Carlos Pirmez^c

^aDepartment of Earth, Atmosphere, and Planetary Sciences, Massachusetts Institute of Technology, 77 Massachusetts Avenue, Building 54-824, Cambridge, MA 02139

^bDepartment of Geological Sciences, The University of Texas at Austin, Austin, TX 78712

^cShell International Exploration and Production, Inc., P.O. Box 481, Houston, TX 77001

ABSTRACT

Turbidity currents are responsible for crafting the morphology of continental margins (Bouma et al., 1985; Kostic et al., 2002; Parker et al., 1987; Pirmez et al., 2000) yet the processes that allow these currents to traverse great distances are incompletely known. Recent advances in the collection of bathymetric data reveal channels formed by turbidity currents have forms similar to rivers (Droz et al., 1996; Flood and Damuth, 1987; Imran et al., 1999; Kenyon et al., 1995; Komar, 1969; Pirmez and Imran, 2003; Schwenk et al., 2003) and that most channels in excess of 100 km in length are moderately to highly sinuous (Flood and Damuth, 1987; Kenyon et al., 1995; Schwenk et al., 2003). Here we present results from laboratory experiments that highlight the significance of channel bends in promoting the long runout of turbidity currents. We show that the flow through bends is accompanied by a mixing of suspended sediment back into the interiors of turbidity currents. This remixing counteracts the natural tendency for suspended-sediment concentration and grain size to stratify vertically, thereby reducing the rate at which sediment is lost from a current via deposition on the channel bed. Bend-induced mixing also helps maintain a relatively high suspended-sediment concentration at the interior of a current that provides the excess density structure necessary for driving the current further down slope. We hypothesize that a wholesale vertical mixing of suspended sediment within turbidity currents at channel bends is a necessary condition for the construction of submarine channels that are in excess of 100 km in length. These results are potentially useful for interpreting any channels that form on planetary surfaces with relatively dense ambient fluids.

5.1. INTRODUCTION

High resolution mapping of continental slopes has revealed the presence of ubiquitous channels (Clark et al., 1992; Demyttenaere et al., 2000; Droz et al., 1996; Flood and Damuth, 1987; Kenyon et al., 1995; Pirmez et al., 2000; Pratson et al., 1994; Schwenk et al., 2003), some extending in excess of 3000 km and into water depths exceeding 4000 m (Schwenk et al., 2003). These channels are primarily constructed by turbidity currents, mixtures of water and suspended sediment that move down continental margins as underflows. Turbidity currents dominate the transport of terrigenous sediment to deep-marine locations (Kneller and Buckee, 2000) and have built some of the largest sediment accumulations found on Earth (Bouma et al., 1985). These deposits host many of the largest producing petroleum reservoirs (Weimer and Link, 1991) in the world today. In spite of this, our knowledge of the system properties allowing for sediment in turbidity currents to be transported for great distances is incomplete. This deficiency is largely a consequence of difficulty in instrumenting natural flows due to the great water depth, infrequent occurrence, and high velocities associated with many turbidity currents. We argue here that furthering our understanding of the evolution of seascapes requires not only a refinement of internal, turbidity-current dynamics, but also a refinement in our knowledge of how interactions with seafloor topography mediates the transport properties of turbidity currents.

Submarine channels and rivers share many planform similarities (Imran et al., 1999; Pirmez and Imran, 2003), including comparable scaling relationships between channel widths and meander-bend wavelengths and amplitudes (Pirmez and Imran, 2003). In addition, the long profiles for channels in both environments are free to adjust their gradients in response to changes in sediment and liquid fluxes and tectonic activity (Pirmez et al., 2000). These similarities have led to the use of models for subaerial channelized flow as semi-quantitative guides for interpreting flow through sinuous submarine channels (Imran et al., 1999; Komar, 1969) even though significant differences exist between the two environments. In rivers, gravity acts on the water which in turn drags sediment downstream. In submarine channels, gravity acts on the excess density associated with sediment suspended within the turbidity current which in turn drives the down-slope flow.

In this work we analyze how the interaction of currents with channel bends increases the sediment transport efficiency in submarine channels.

A survey of published data on submarine channels reveals that most channels in excess of 100 km are moderately to highly sinuous (sinuosity > 1.2), including three of the four longest systems, the Bengal (Schwenk et al., 2003), Indus (Kenyon et al., 1995), and Amazon channels (Flood and Damuth, 1987) (Figure 5.1). Many channels less than 100 km in length are significantly less sinuous (Pratson et al., 1994). Is there a control of channel sinuosity on the length to which submarine channels grow? To address this question we performed two, reduced-scale laboratory experiments. The first experiment monitored current properties and depositional patterns associated with ten successive currents traversing a straight channel, while the second experiment monitored these same parameters in a moderately sinuous channel (1.32). Sediment transport phenomena associated with laterally confined turbidity currents have been frequently studied at laboratory scale, almost exclusively in horizontally uniform channels (Garcia, 1994; Hallworth et al., 1993; Keevil et al., 2006; Middleton, 1966; Mohrig and Buttle, 2007; Straub et al., submitted). Of particular relevance to our study is the work of Dade and Huppert (1994) who calibrated a scaling relationship for the run-out distance of turbidity currents using laboratory experiments performed in a straight channel. Dade and Huppert (1994) conclude that run-out distance, run-out time and characteristic deposit thickness all scale with initial volume of suspended sediment, initial total volume (sediment + liquid) of the current, and average settling velocity of the particles in suspension. We show here that run-out distance, run-out time and characteristic deposit thickness are also affected by the sinuosity of a channel.

5.2. RESULTS

Characteristic streamwise velocity profiles for turbidity currents in both the straight and sinuous channel are shown in Figure 5.2a. These profiles were used to calculate each current's vertically averaged, streamwise velocity, \bar{u} . Currents moving through the straight channel were 1.6 times faster than those in the sinuous channel. This gave currents moving through the straight channel a densimetric Froude (Fr) and Reynolds (Re) number of 0.80 and 15.8×10^3 , while currents moving through the sinuous channel had Fr and Re of

0.54 and 8.2×10^3 . Since all other current properties were held constant the velocity ratio for currents in straight versus sinuous channels can be recast to determine the change in form drag, C_f , for channels of differing sinuosity using:

$$F_d = C_f \rho \frac{1}{2} \bar{u}^2 HL \quad (1)$$

where F_d is the drag force applied to the channel bed by the current, ρ is current density, H is hydraulic radius for the channel, and L is channel length. Values for ρ , F_d , and H were purposely held constant between experiments in the straight and sinuous channel. Total channel length varied somewhat due to space limitations with L for the straight and sinuous channel equaling 3.5 and 4.2 m. Using (1) we calculate that C_f is 2.1 times greater for the sinuous channel compared to straight form. A similar increase in drag associated with the presence of channel bends has been observed in terrestrial rivers where the ratio of C_f between a moderately sinuous and a straight channel is found to range between 1.5 – 1.8 (Chow, 1959; Cowan, 1956).

In both experiments the bed topography was mapped following every current and differences between maps defined the average net accumulation of sediment along the centerlines of the straight and sinuous channels (Fig. 5.3). Both centerline profiles show an approximately similar initial deposit thickness that decreases linearly with distance from the source. Surprisingly, a greater amount of sediment deposition was measured in the straight channel versus the sinuous one, indicating that currents moving through the straight channel lost suspended sediment at higher rates.

Measurements of velocity and deposit thickness present an interesting paradox: why are the slower moving currents traveling down the sinuous channel more efficient at transporting sediment than the faster, straight-channel currents? This question has implications for determining the run-out distances of turbidity currents as well as the total lengths of submarine channel lengths since these forms are constructed as a result of sediment moved by the currents themselves. Sediment loss from currents via deposition and entrainment of ambient water at its upper interface are the two primary mechanisms for decreasing a current's excess density and limiting its run-out length (Hallworth et al., 1993; Parker et al., 1987). Velocity profiles measured at multiple downstream locations confirmed that water entrainment was negligible in both experiments. Sediment deposition

was therefore the dominant process controlling loss of excess density and current run-out lengths.

Profiles of suspended sediment concentration and its grain size were measured in both channels at 2.90 m downstream from the entrance point (Fig. 5.2b,c). The profiles show that currents moving through the straight channel are more stably stratified than currents moving through the sinuous channel. Near bed suspended sediment concentration, C_{nb} , and median grain size were both larger in the straight channel. We take these observations as evidence for large-scale vertical mixing within currents induced by flow through channel bends.

The vertical concentration and grain size profiles for currents in the sinuous versus straight channels provide an explanation for the observed differences in sediment deposition on the channel bed (Fig. 5.3). Deposition rate, $\Delta\eta$, is a function of (Parker et al., 1987):

$$\Delta\eta \sim C_{nb}W_s \quad (2)$$

where W_s is the settling velocity associated with the median grain size of the near bed suspended sediment. The remixing of coarser sediment into the interior of currents at channel bends acts to reduce C_{nb} and W_s , thereby reducing the deposition rates associated with the slower moving currents in the sinuous channel. Bend-induced remixing of suspended sediment is supported by recent laboratory measurements of Keevil et al. (2006) who report enhanced turbulence intensities for density currents at channel bends relative to channel crossings.

5.3. DISCUSSION

We propose that frequent remixing of the suspended sediment profile as a current moves through the many bends of a sinuous channel would act to significantly reduce rates of sediment loss via deposition (Fig. 5.4). The resulting maintenance of current density combined with a repositioning of the center of suspended sediment mass at some level higher off of the channel bed would promote greater run-out distances for a current, thereby providing the transporting flow necessary for extending long submarine channels. Use of a fully 3-D, non-conservative numerical model for density current flow down channels of arbitrary shape (Kassem and Imran, 2005) is necessary to test and refine our

understanding of the role of topographically induced mixing on turbidity current run out and channel construction. Even so, results presented here show that channelized run out is not simply a function of initial current properties (Dade and Huppert, 1994), but is also influenced by the plan form of the evolving channel itself. Moderate to highly sinuous channels promote the long-distance transport of sediment via turbidity currents into the deep marine environment.

5.4. METHODS

The two experiments were conducted in a basin 5 m long, 5 m wide and 1.2 m deep. Before filling the basin with water a channel was built on its floor using a 15:1 mixture of sand and cement mortar. The original channels were trapezoidal in cross-section with an initial depth of 0.11 m and basal and top widths of 0.20 m and 0.40 m, respectively and did not vary in the downstream direction. The moderately sinuous channel planform was generated using a sine-generated curve. The maximum angle at which the centerline deviates from the downstream direction is 55° and the centerline distance associated with one channel wavelength is 3.4 m. Currents entered the basin at one corner and moved through a momentum extraction box before entering the channel so that each flow was a sediment-laden plume driven by buoyancy alone. After traversing the study area the currents plunged into a moat where perforated pipes removed the current, preventing reflections.

Ten depositional turbidity currents were released in both the straight and sinuous channel. All turbidity currents had the same input values for current height, fluid discharge, and excess density, allowing us to isolate the influence of channel sinuosity on current behavior. The turbidity currents were composed of clear water, dissolved CaCl_2 and suspended sediment. Currents entered the channels with a 2.1 % excess density relative to the fresh water that filled the basin. Thirty-three percent of this excess density was due to suspended sediment and 67 % was from the dissolved salt. The sediment consisted of 60 % blown silica (ballotini) and 40 % crushed silica flour by weight with a cumulative size distribution where D_1 , D_5 , D_{16} , D_{25} , D_{50} , D_{75} , D_{84} , D_{95} , and D_{99} equaled nominal diameters of 1.7 μm , 3.1 μm , 18 μm , 23 μm , 31 μm , 41 μm , 46 μm , 60 μm , and 80 μm , respectively. Dissolved salt was used to simulate the finest portion of

suspended sediment within natural turbidity currents, a fraction that is transported to the distal end of a system without loss via deposition. Current thickness and discharge were constant for all flow events at values of 0.12 m and $4.7 \times 10^{-3} \text{ m}^3/\text{sec}$. The duration of each current was 5.3 ± 0.1 minutes.

Velocity profiles were collected using the downstream directed transducer on a Sontek Pulse-Coherent Acoustic-Doppler Profiler (PCADP). Use of the single transducer provided a suitably small footprint of about 30 mm in diameter for each profile. Suspended sediment profiles were collected using a system of stacked siphons. Three siphons were deployed at various heights above the channel bed during successive flow events to produce the two profiles shown in Figure 5.2. The siphons were positioned in the center of the channels and drew 600 mL of fluid through 5 mm plastic tubing into sample bottles located outside the basin. Clear fluid was drained from each sample using 1 μm filter paper. After drying, the sediment samples were analyzed for grain size with a Horiba LA-300 laser-particle-size analyzer (LPSA). The LPSA uses a diode laser to accurately measure a distribution of sizes ranging from 0.001 to 0.3 mm in nominal diameter.

The geometric scaling for our experiment was set at 1/1000 yielding maximum width and depth for both experiments that correspond to natural scales of 400 and 100 m, respectively. Three dimensionless parameters were used to compare model-current properties to natural or prototype systems: Fr , Re , and the ratio of particle fall velocity to shear velocity, w_s/u^* . An approximate dynamic similarity between currents of different scales is achieved by setting $Fr_{(model)} = Fr_{(prototype)}$ (Graf, 1971). This equality is satisfied by prototype values of u , H , and current duration of 2.5 m/s, 120 m, and 2.7 hr, respectively for currents in the sinuous channel. In addition, the characteristic Re for the straight and sinuous channel were 15,800 and 8,200, respectively. This value is sufficiently large to ensure approximate Reynolds similarity for fully turbulent gravity currents (Parsons and Garcia, 1998). Sediment transporting conditions were compared to natural systems by setting $w_s/u^*_{(model)} = w_s/u^*_{(prototype)}$, where $u^{*2} = C_d U_x^2$, C_d is a bed friction coefficient. Values of $C_{d(prototype)} = 2 \times 10^{-3}$ and $C_{d(model)} = 2 \times 10^{-2}$ were used as described in Mohrig and Buttle (2007). By satisfying this equality we found that D10, D50, and D90 correspond to 41 μm , 113 μm , and 207 μm for flows at natural scale. Further information about the experimental facility and setup can be found in Straub *et al.* (submitted).

ACKNOWLEDGMENTS

Support for our research was provided by Shell International Exploration and Production Inc. and the STC program of the National Science Foundation via the National Center for Earth-surface Dynamics under the agreement Number EAR- 0120914.

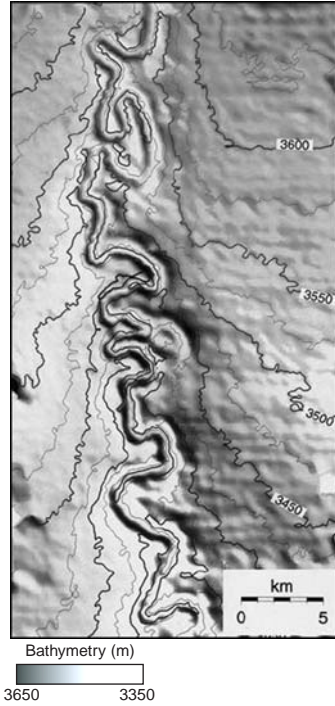


Figure 5.1. Bathymetric image of Amazon deepwater channel (illuminated from the east) showing segment of the channel between 3350 and 3650 m of water depth. Modified after Pirmez et al. (2000).

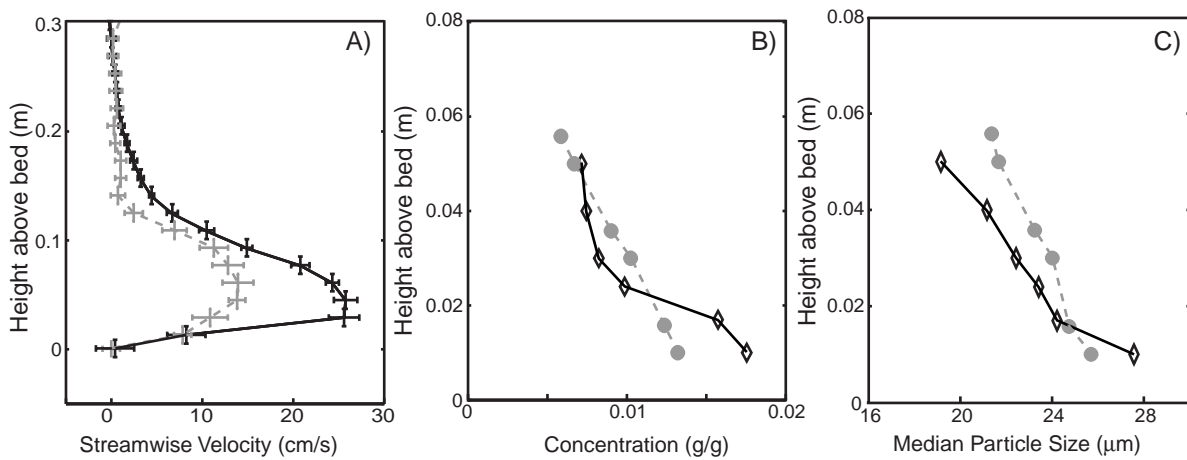


Figure 5.2. Profiles of streamwise velocity, suspended sediment concentration, and mean suspended particle size in the straight (black solid line) and sinuous (gray dashed line) channel measured at the channel centerline, 2.95 m downstream from the channel entrance. A) Profiles of mean streamwise velocity measured using a PCADP. Vertical error bars define the sampling volume for each bin. Horizontal error bars are +/- one standard deviation in velocity measured in each sampling volume. B) Profiles of suspended sediment concentration. Data points represent the local concentration drawn from 600 mL samples. C) Profiles of suspended sediment particle size. Data points represent the median grain size associated with the 600 mL samples.

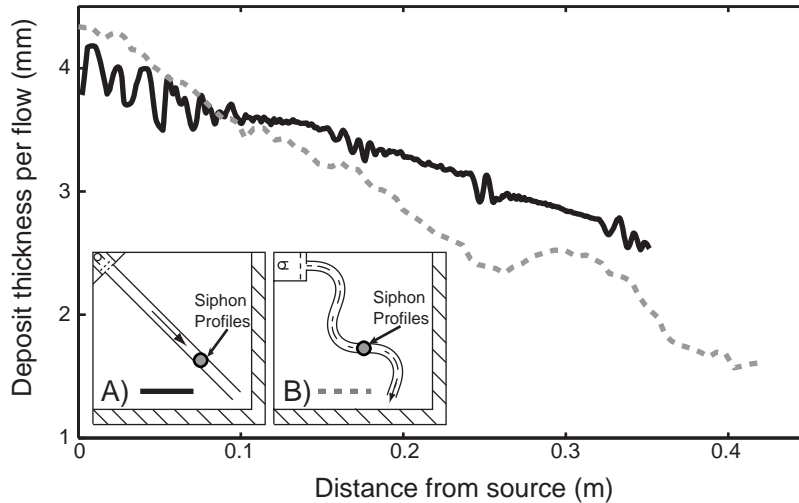


Figure 5.3. Deposit thickness per current along the centerline of the straight (black solid line) and sinuous (gray dashed line) channel. Straight channel profile is composed of 700 data points measured using a displacement laser at a spacing of 5 mm. Sinuous channel profile is composed of 92 data points measured with a 1 MHz ultrasonic transducer at a spacing of 40 mm. Inserts show the plan form configuration for the A) straight and B) sinuous channel. Hatched pattern defines location of the basin moat.

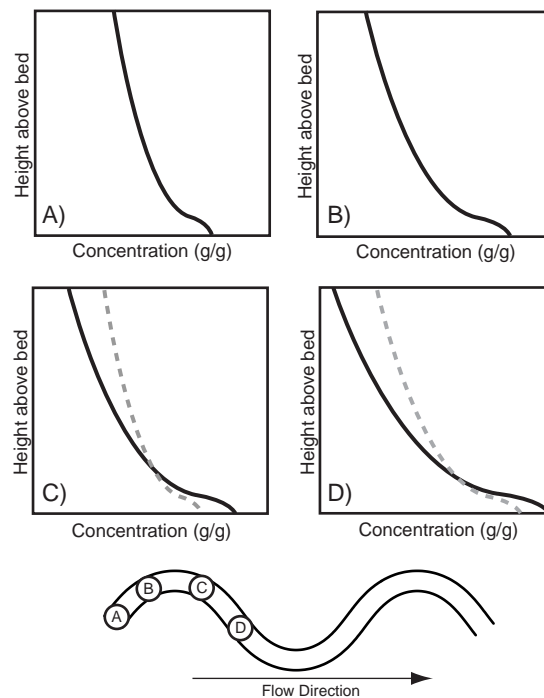


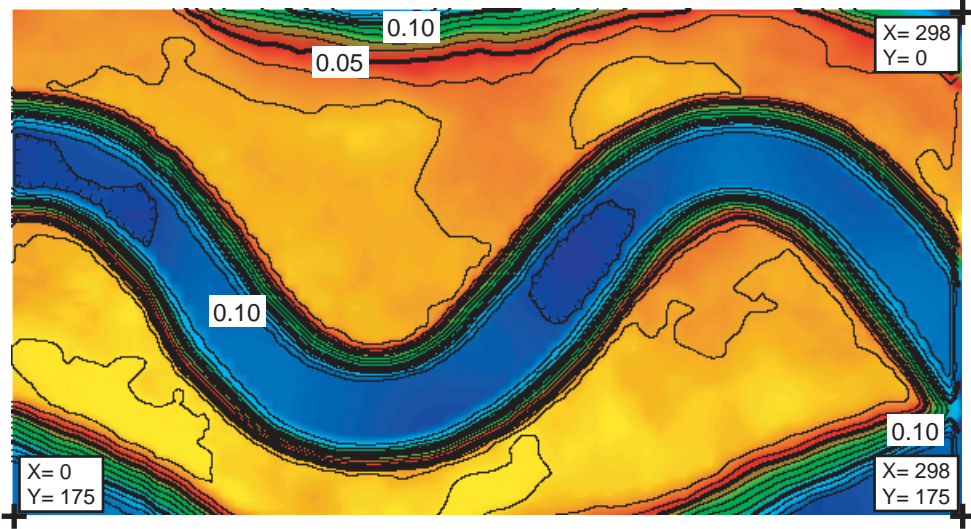
Figure 5.4. Schematic diagram illustrating consequence of channel bend induced mixing on suspended sediment concentration profiles in straight and sinuous channels. A) Well-mixed profile at channel entrance. B) Development of stably stratified profile prior to entering first channel bend. C) Vertical mixing in the channel bend reduces stratification and near bed, suspended sediment concentration (gray dashed) compared to a straight-channel current (black solid) at the same downstream position. D) Redevelopment of stably stratified profiles prior to encountering the next channel bend.

APPENDIXES

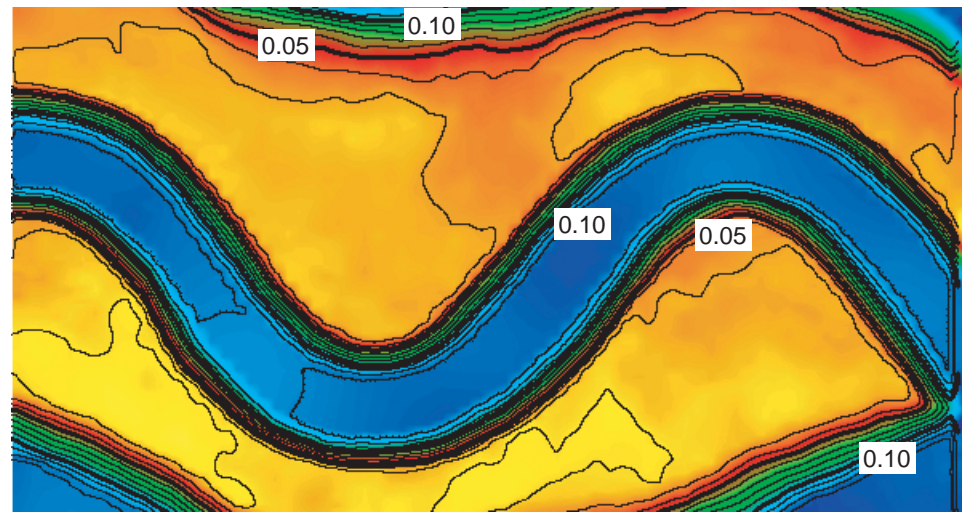
Appendix 1: Topographic maps from the 2 experimental channels. Channel flow was from the left to the right in each map. Topography is defined as a vertical distance between the bed and an overlying datum of constant elevation. Contour interval is 10 mm. Coordinate systems for 2 channels are defined by labeled X and Y locations of three map corners on Flow 1 map for each experimental channel.

Appendix 2: Tables defining particle size distributions for suspended sediment sampled with siphon system. X and Y locations defining horizontal position of siphon system correspond to coordinate system defined in Appendix 1.

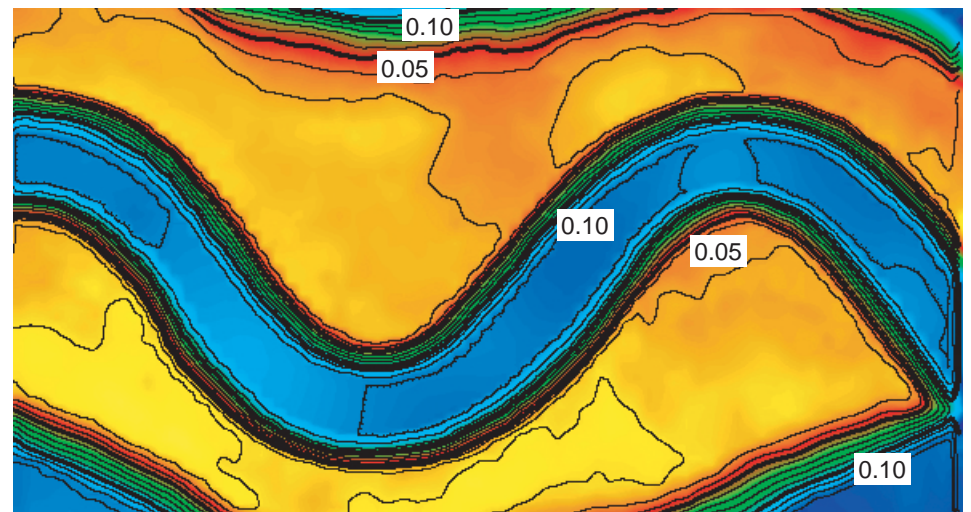
Sinuous Flow 1



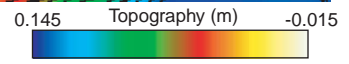
Sinuous Flow 2



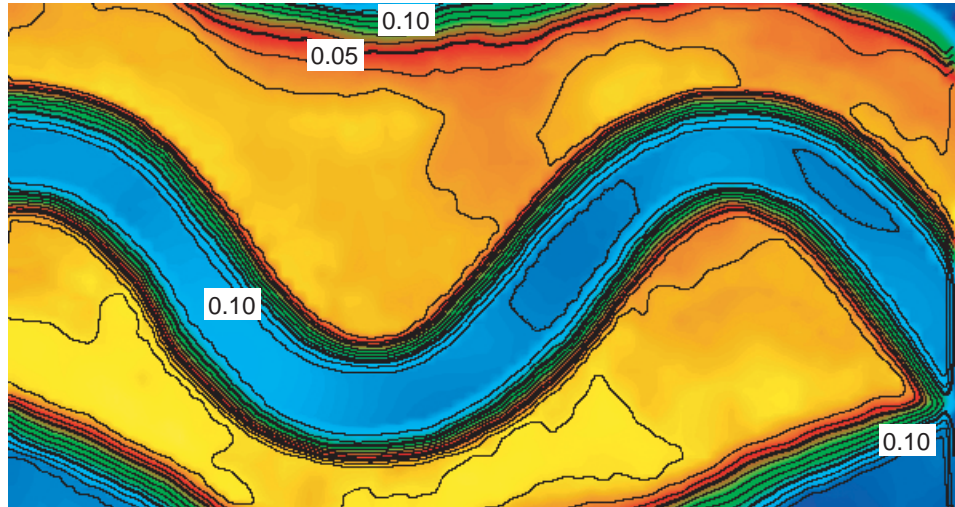
Sinuous Flow 3



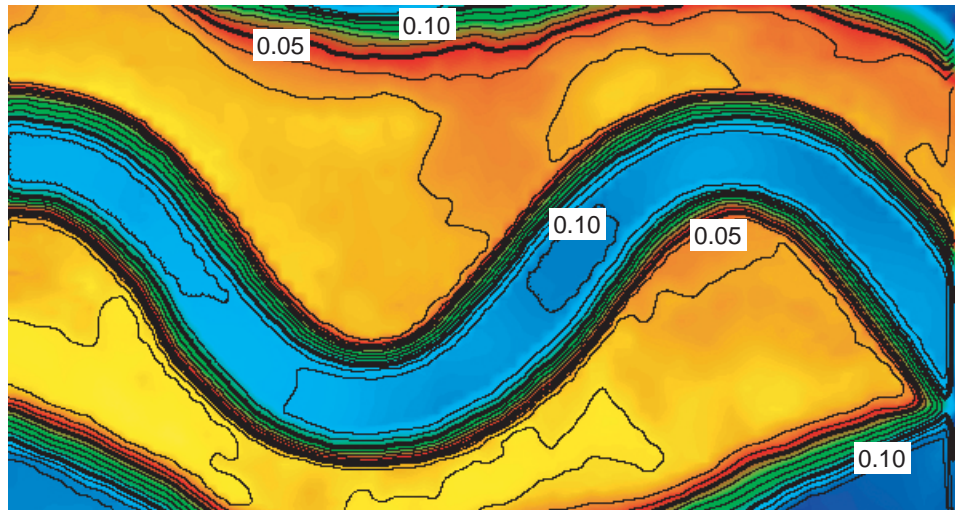
0.5 m



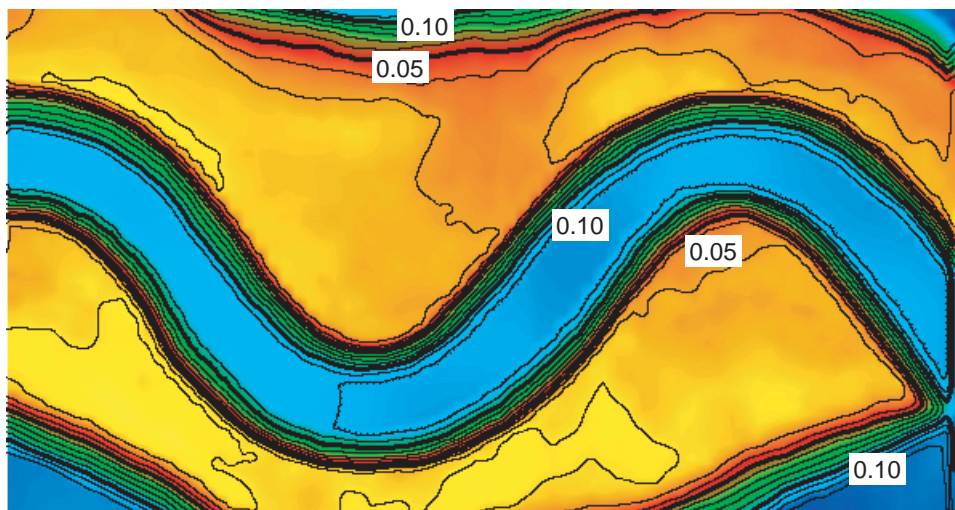
Sinuuous
Flow 4



Sinuuous
Flow 5



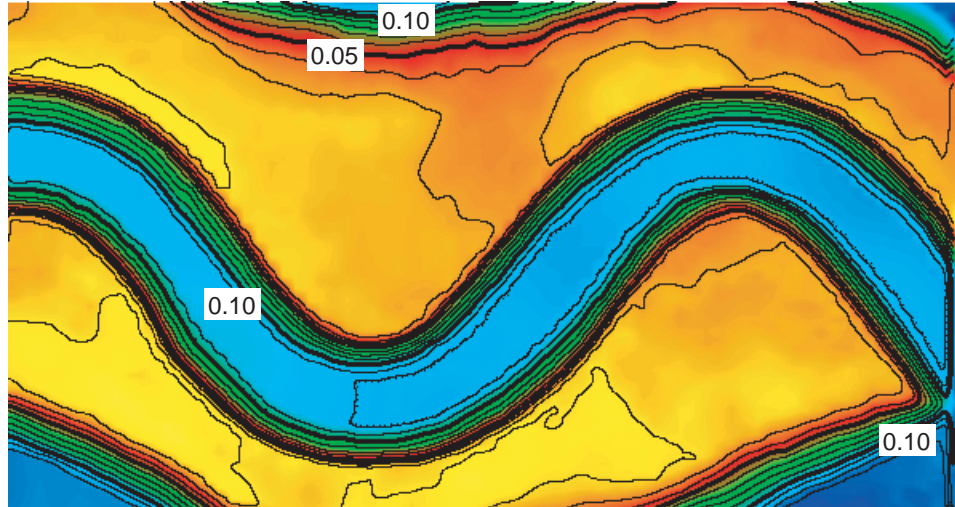
Sinuuous
Flow 6



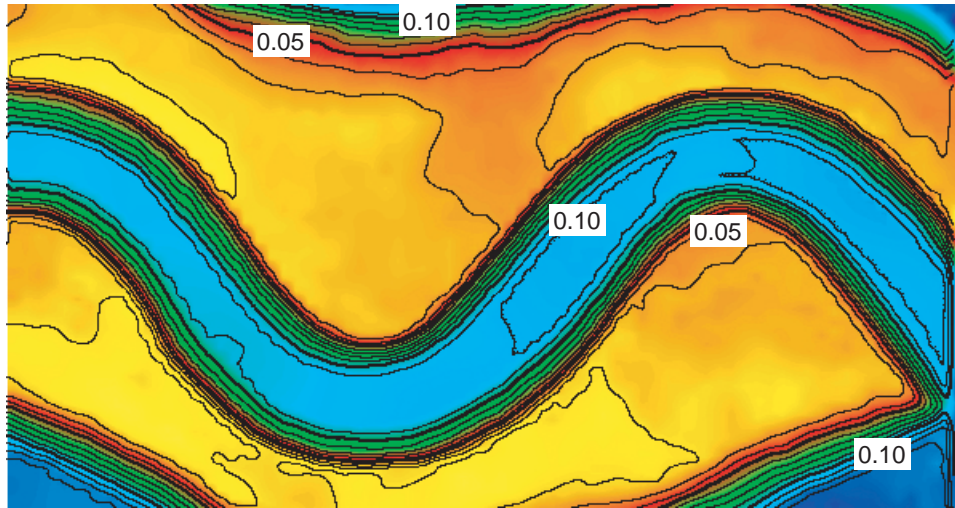
0.5 m

0.145 Topography (m) -0.015

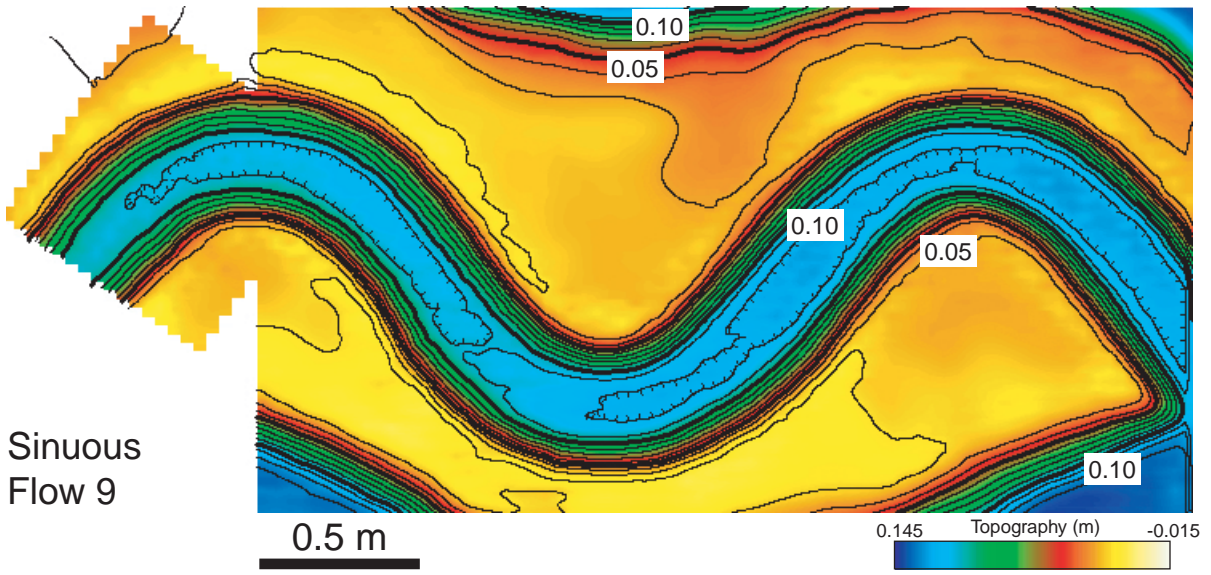
Sinuuous
Flow 7

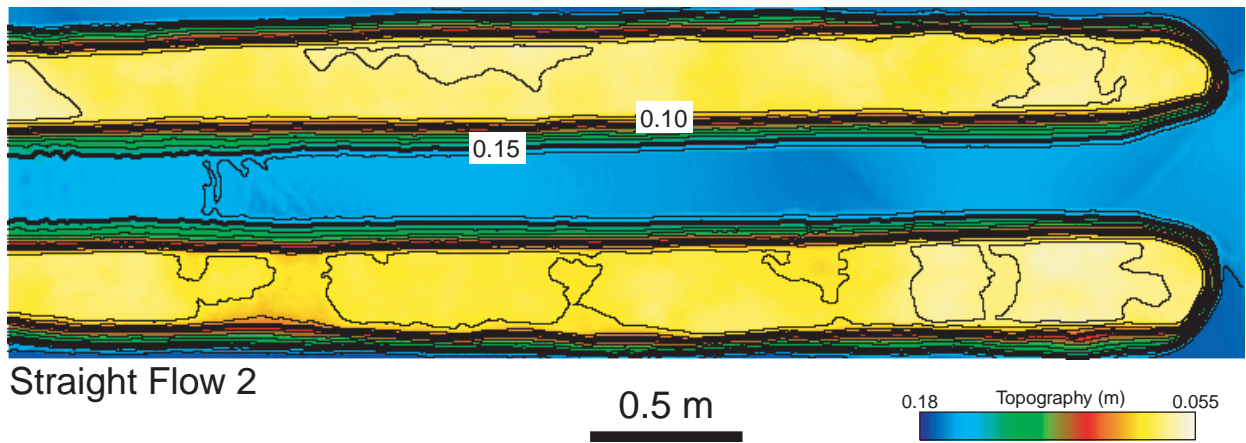
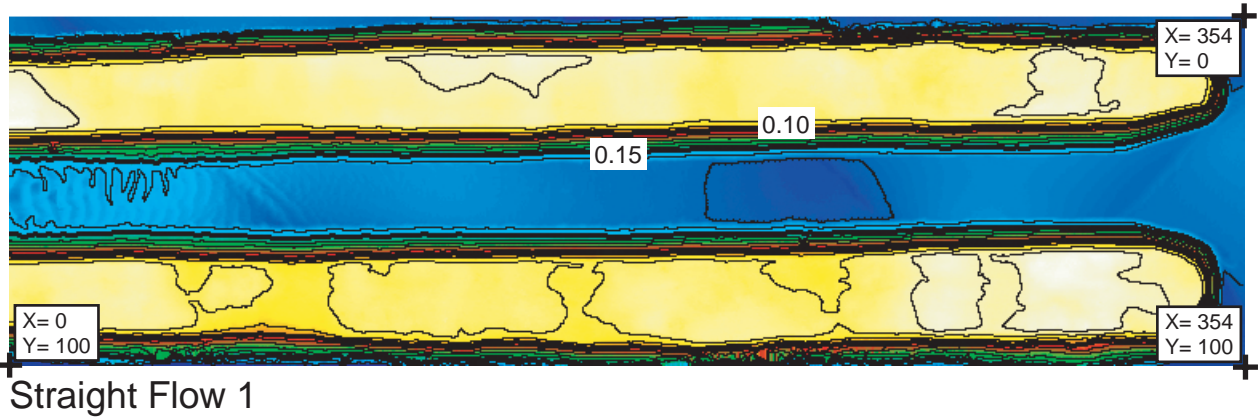
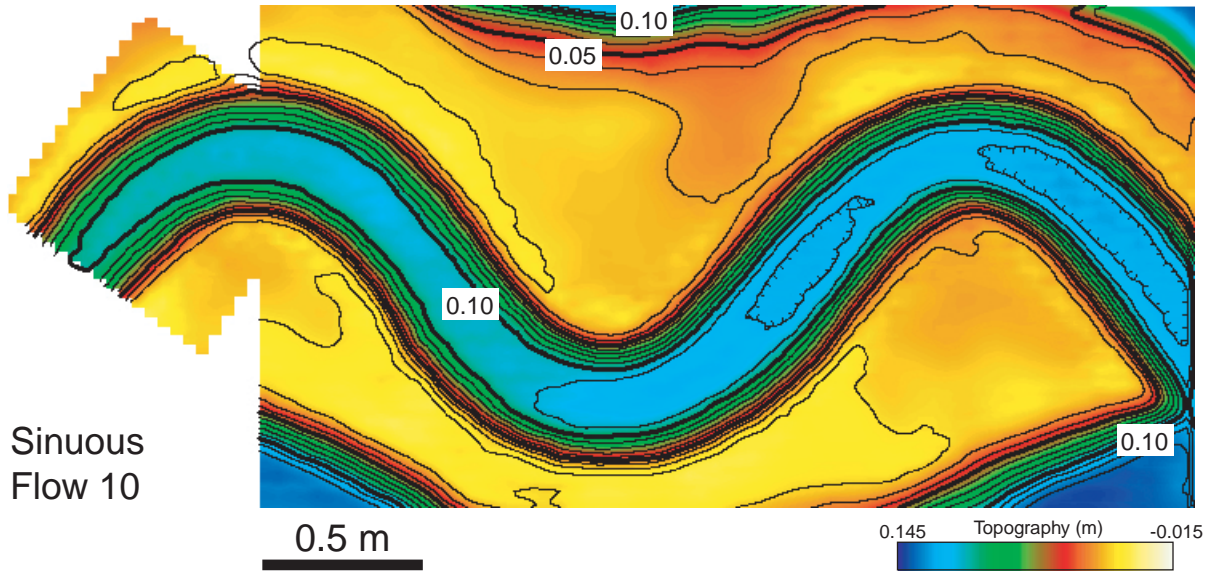


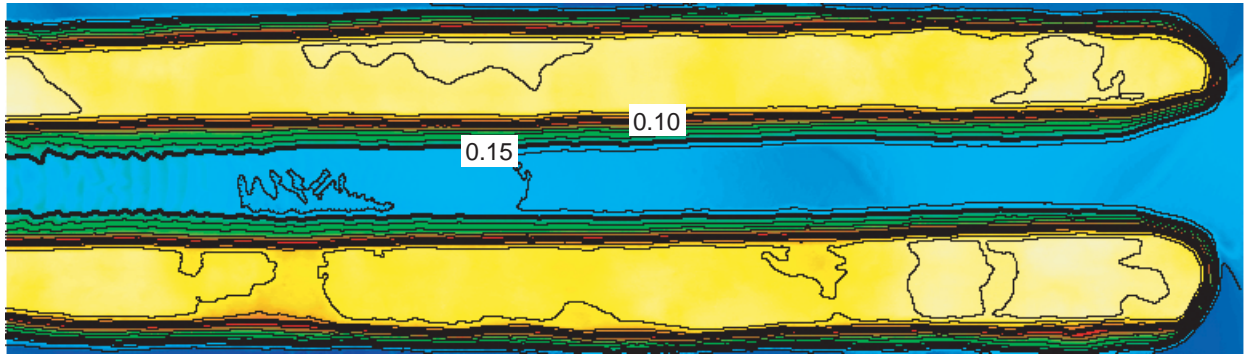
Sinuuous
Flow 8



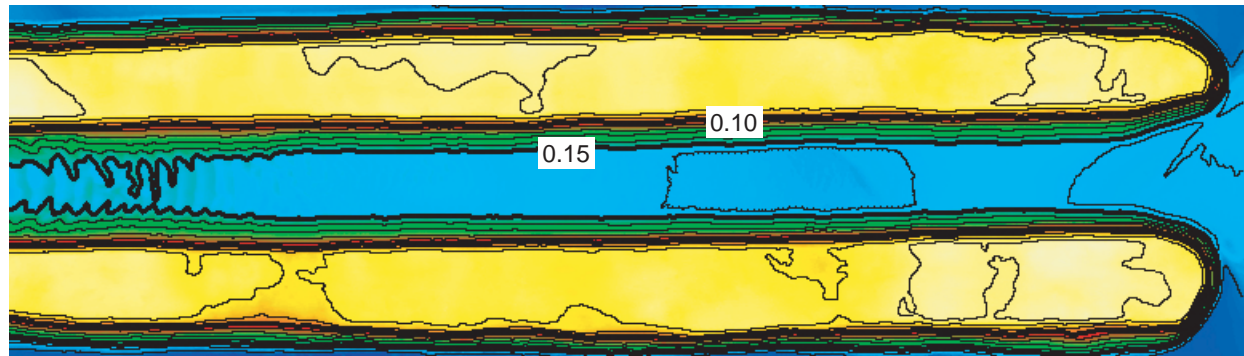
Sinuuous
Flow 9



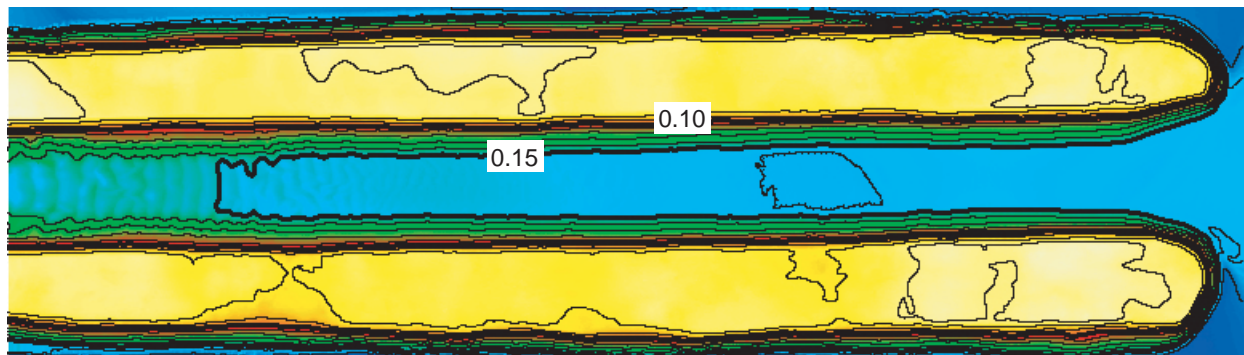




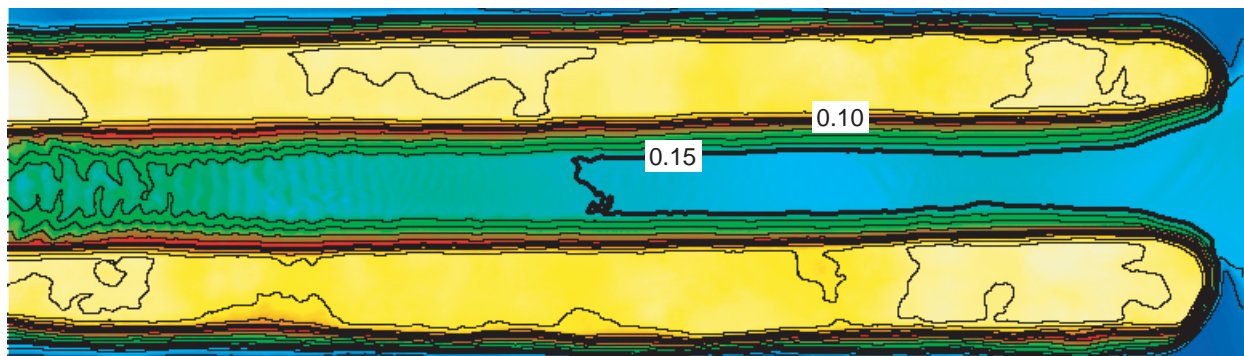
Straight Flow 3



Straight Flow 4



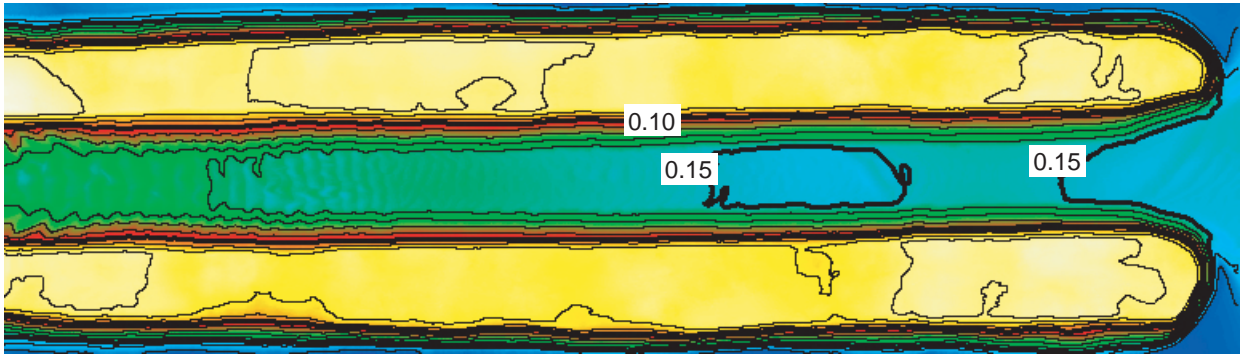
Straight Flow 5



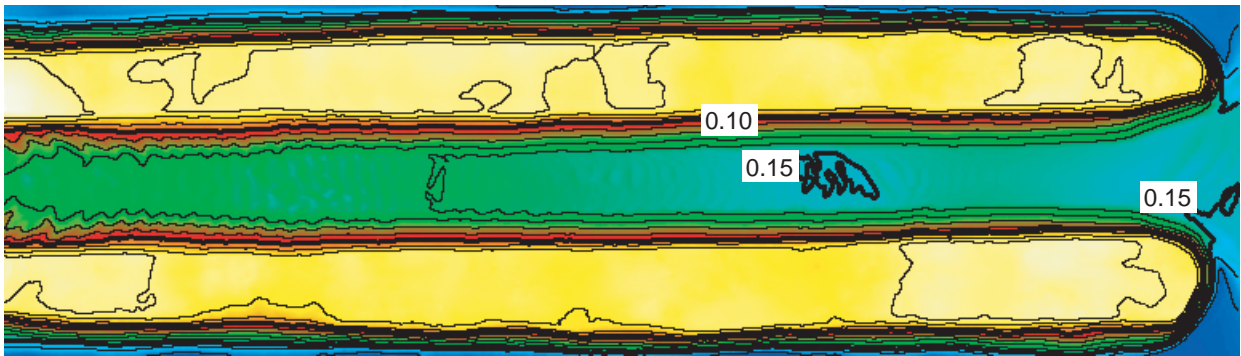
Straight Flow 7

0.5 m

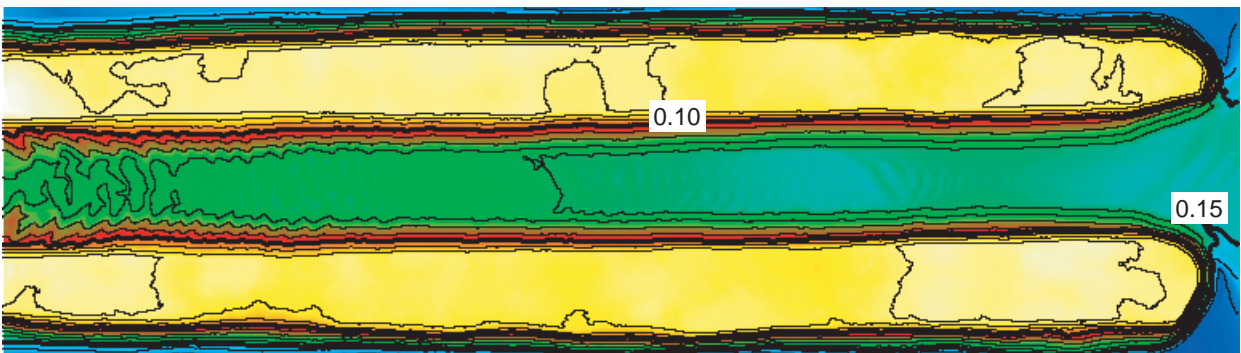
0.18 Topography (m) 0.055



Straight Flow 8



Straight Flow 9



Straight Flow 10



APPENDIX 2

	St	St	St	St	St	St	Sin	Sin	Sin	Sin	Sin	Sin
Z (m)	0.010	0.017	0.024	0.030	0.040	0.050	0.010	0.016	0.030	0.036	0.050	0.056
X Location	290.0	290.0	290.0	290.0	290.0	290.0	177.9	177.9	177.9	177.9	177.9	177.9
Y Location	50.0	50.0	50.0	50.0	50.0	50.0	84.7	84.7	84.7	84.7	84.7	84.7
Grain Size (μm)	% Finner											
1.0	0.0	0.0	0.1	0.2	0.2	0.2	0.0	0.1	0.0	0.0	0.1	0.0
1.2	0.2	0.2	0.3	0.4	0.5	0.5	0.2	0.3	0.2	0.2	0.3	0.2
1.3	0.5	0.4	0.6	0.9	1.0	0.9	0.5	0.6	0.5	0.5	0.7	0.6
1.5	1.0	0.8	1.0	1.6	1.8	1.5	1.0	1.1	1.0	1.1	1.3	1.1
1.7	1.7	1.3	1.6	2.5	3.0	2.4	1.8	1.6	1.8	1.8	2.1	2.0
2.0	2.7	1.9	2.2	3.6	4.5	3.5	2.7	2.3	2.8	2.8	3.1	3.1
2.3	3.8	2.5	2.9	4.9	6.3	4.7	3.8	2.9	3.9	4.0	4.3	4.4
2.6	4.9	3.1	3.5	6.1	8.2	5.9	4.9	3.6	5.1	5.2	5.7	5.7
3.0	6.1	3.8	4.2	7.4	10.3	7.3	6.1	4.3	6.4	6.4	7.1	7.1
3.4	7.1	4.4	4.8	8.6	12.3	8.6	7.3	4.8	7.7	7.6	8.5	8.5
3.9	8.1	5.0	5.3	9.7	14.2	9.9	8.4	5.3	8.9	8.6	9.8	9.7
4.5	8.9	5.5	5.8	10.7	15.9	11.2	9.4	5.8	10.1	9.5	11.0	10.9
5.1	9.6	6.0	6.3	11.7	17.5	12.4	10.4	6.2	11.1	10.4	12.2	11.9
5.9	10.2	6.4	6.8	12.5	18.9	13.6	11.3	6.6	12.1	11.1	13.4	12.8
6.7	10.8	6.9	7.3	13.5	20.3	15.0	12.2	7.1	13.1	11.9	14.5	13.8
7.7	11.4	7.4	8.0	14.5	21.8	16.5	13.2	7.6	14.2	12.7	15.8	14.8
8.8	12.0	8.1	8.9	15.7	23.3	18.4	14.3	8.2	15.5	13.6	17.4	16.0
10.1	12.9	9.0	10.2	17.3	25.2	20.9	15.6	9.2	17.0	14.9	19.3	17.6
11.6	14.0	10.3	12.2	19.6	27.4	24.2	17.4	10.7	19.0	16.6	21.8	19.8
13.2	15.7	12.3	15.3	22.7	30.3	28.7	19.7	13.2	21.7	19.2	25.3	23.0
15.2	18.2	15.7	20.0	27.2	34.2	34.6	22.9	17.0	25.4	23.0	29.9	27.6
17.4	22.0	21.3	26.9	33.4	39.3	42.3	27.4	22.9	30.5	28.9	36.1	34.3
19.9	27.6	30.2	36.1	41.5	46.0	52.4	33.4	31.4	37.3	37.3	44.0	43.4
22.8	35.6	43.0	47.4	51.2	54.4	61.6	41.2	42.4	45.9	48.2	53.4	54.7
26.1	45.7	58.9	59.6	61.9	63.9	71.7	50.7	55.0	56.1	60.8	63.7	67.1
29.9	57.3	75.1	71.4	72.2	73.8	80.7	61.3	67.8	66.8	73.4	73.9	78.8
34.3	68.8	88.0	81.3	81.2	82.8	87.9	71.7	79.0	77.0	84.0	82.7	88.0
39.2	79.0	95.6	88.7	88.1	89.8	93.1	81.0	87.5	85.4	91.5	89.5	94.1
44.9	86.8	98.8	93.7	93.0	94.6	96.4	88.3	93.2	91.5	96.1	94.2	97.5
51.5	92.2	99.8	96.7	96.1	97.4	98.4	93.4	96.7	95.4	98.4	97.1	99.1
59.0	95.6	100.0	98.5	98.0	98.9	99.4	96.6	98.5	97.8	99.5	98.7	99.8
67.5	97.7	100.0	99.5	99.0	99.7	100.0	98.5	99.5	99.0	100.0	99.5	100.0
77.3	98.9	100.0	100.0	99.6	100.0	100.0	99.5	100.0	99.7	100.0	100.0	100.0
88.6	99.6	100.0	100.0	100.0	100.0	100.0	100.0	100.0	100.0	100.0	100.0	100.0
101.5	100.0	100.0	100.0	100.0	100.0	100.0	100.0	100.0	100.0	100.0	100.0	100.0
116.2	100.0	100.0	100.0	100.0	100.0	100.0	100.0	100.0	100.0	100.0	100.0	100.0
133.1	100.0	100.0	100.0	100.0	100.0	100.0	100.0	100.0	100.0	100.0	100.0	100.0
152.5	100.0	100.0	100.0	100.0	100.0	100.0	100.0	100.0	100.0	100.0	100.0	100.0
174.6	100.0	100.0	100.0	100.0	100.0	100.0	100.0	100.0	100.0	100.0	100.0	100.0
200.0	100.0	100.0	100.0	100.0	100.0	100.0	100.0	100.0	100.0	100.0	100.0	100.0

Chapter 6

Constructional canyons built by sheet-like turbidity currents: Observations from offshore Brunei Darussalam

Kyle M. Straub^a and David Mohrig^b

^aDepartment of Earth, Atmosphere, and Planetary Sciences, Massachusetts Institute of Technology, 77 Massachusetts Avenue, Building 54-824, Cambridge, MA 02139

^bDepartment of Geological Sciences, The University of Texas at Austin, Austin, TX 78712

ABSTRACT

Submarine canyon formation and deepening are typically attributed to erosional processes. We present data from an industry-grade seismic volume located offshore Brunei Darussalam illustrating how topography typically associated with erosional processes can be produced under conditions of net sediment deposition. This data was generated via subsurface mapping in the vicinity of a shale-cored anticline on the Quaternary continental-slope. The shale ridge is located 20 km down slope from the present-day continental shelf-edge in ~900 m of water. Its crest line runs for 18 km and is oriented perpendicular to the regional slope. Three canyons traverse the structure at right-angles to the crest line with maximum canyon relief of 165 m. Subsurface mapping reveals that the structure is a site of net sediment deposition and defines a background sedimentation pattern that decreases gradually with distance from the shelf-edge. Profiles down canyon axes reveal local minima in deposit thickness over the anticline hinge that are associated with high downstream gradients. Deposition on ridges adjacent to canyons also displays local minima at the anticline hinge, but these minima are not correlated with gradient. A comparison of canyon axis and ridge deposition shows that somewhat higher rates of sedimentation on the ridges resulted in the preservation and growth of the submarine canyons with time. Laterally persistent seismic reflectors and depositional packages suggest that the canyon forming currents were sheet-like flows, extending for many kilometers in the strike direction. This interpretation is consistent with minima in ridge deposition being correlated with maximum canyon relief. The currents drained into

canyons as they approached the anticline hinge, leaving only a small supra-canyon fraction available to deposit sediment on the non-channelized zones. We use the cross-sectional area of the confined flow over the anticline crest to estimate a minimum thickness of 20 m for the sheet-like currents as they approached the anticline.

6.1. INTRODUCTION

The collection of high resolution bathymetric maps in the last two decades has revealed many previously unrecognized morphological features in the deep-marine environment (Piper and Normark, 1983; Pirmez and Flood, 1995; Pratson and Haxby, 1996; Pratson et al., 1994; Stelting et al., 1985). Advances in imaging of the seafloor are the result of advances in geophysical exploration technologies that include multibeam sonar systems and three-dimensional (3-D) seismic surveys. Many seafloor features have morphometric properties that are similar to better studied, terrestrial topography (Imran et al., 1999; Pirmez, 1994; Posamentier and Kolla, 2003). This similarity has motivated numerous investigations of continental-margin morphodynamics (Goff, 2001; Kneller and Buckee, 2000; Pirmez et al., 2000; Pratson et al., 1994) and many of these studies have employed quantitative process models developed for terrestrial systems to evaluate the evolution of submarine systems (Green et al., 2002; Komar, 1969; Mitchell, 2005, 2006; Pirmez and Imran, 2003). Channel and canyon systems on continental slopes have received the greatest attention (Fildani and Normark, 2004; Peakall et al., 2000; Pirmez and Imran, 2003; Skene et al., 2002). These conduits display a range of configurations shared by their terrestrial counterparts, including tributary and distributary channel networks (Cunningham et al., 2005; Garcia et al., 2005; Mitchell, 2005; Twitchell et al., 1995). Unfortunately, the great water depths at which many of these systems exist and the infrequent occurrence of flow in submarine channels and canyons has limited the number of direct observations defining the processes that evolve the submarine landscape (Best et al., 2005; Hay, 1987; Khripounoff et al., 2003; Xu et al., 2004). In several regions, maps of the present-day seafloor are the only data available with which to evaluate continental slope dynamics. In this work, we use an industry grade 3-D seismic survey to observe the growth of a canyon system as recorded in the deep-marine strata. We document the limitations to importing process models for canyon development in terrestrial systems to the deep-marine environment.

Submarine canyons are common features on continental margins and share many common attributes with terrestrial canyons (Canals et al., 2000; Green et al., 2002). These canyons are defined by high-relief, V-shaped valleys with steep sidewalls and an irregular floor. The heads of most submarine canyons are linked to the continental shelf-slope break, but many canyons begin tens of kilometers downslope from this point (Bertoni and Cartwright, 2005; Cunningham et al., 2005; Demyttenaere et al., 2000; Huyghe et al., 2004; Pirmez et al., 2000). The canyons typically initiate at regions where the continental slope gradient undergoes a rapid change (Demyttenaere et al., 2000; Goff, 2001; Huyghe et al., 2004), often associated structural deformation that includes faulting and folding by mobile substrate (Demyttenaere et al., 2000; Huyghe et al., 2004; Pirmez et al., 2000). All of these canyons are assumed to be areas of net erosion (Bertoni and Cartwright, 2005; Canals et al., 2000; Cunningham et al., 2005).

Direct observations (Burbank et al., 1999; Burbank et al., 1996; Formento-Trigilio et al., 2002; Snyder et al., 2000) and theoretical modeling (Burbank et al., 1996; Humphrey and Konrad, 2000; Tucker and Slingerland, 1996) of interactions between terrestrial channels and regions of local uplift have guided the study of submarine canyon evolution. In the terrestrial system, channels respond to regions of local uplift in one of three ways: 1) diversion around the region of uplift; 2) by depositing sufficient amounts of sediment both upstream and downstream of the uplift to suppress development of a structural high; or 3) incision through the region of uplift, creating a canyon (Burbank et al., 1996; Humphrey and Konrad, 2000). The pathway of river response to regions of local uplift depends on the stream power, the sediment load of the river, the rate of local uplift and erodibility of uplifted strata (Burbank et al., 1999; Snyder et al., 2000). To follow the incision path a channel must erode its bed at a rate equal to or greater than the rate of regional uplift, therefore all terrestrial canyons are the result of net erosional processes.

Turbidity currents differ from terrestrial channelized flows in several ways that substantially alter how they interact with topography. A critical difference between the two flow types is the density of the ambient fluid through which they flow. Ocean water is roughly 800 times denser than air. As a result of this difference in ambient fluid density, turbidity currents are less influenced by changes in topography than rivers (Kneller et al., 1991; Lamb et al., 2006; Straub et al., submitted). This difference in ambient fluid density

also allows the thickness of turbidity currents to be several times greater than the channels that guide them (Mohrig and Buttles, 2007), a situation that seldom if ever occurs in the terrestrial environment. Because of this difference rivers are always strongly channelized compared to submarine flows. Evidence from several studies suggests some turbidity currents that move down continental margins are poorly channelized (Field et al., 1999; Pickering et al., 1992; Spinnelli and Field, 2001; Wright et al., 1988). These currents are referred to as sheet-flow or sheet-like currents and are interpreted to have ratios of current width to thickness in excess of 1000 (Booth et al., 2000; Field et al., 1999; Twitchell et al., 2005; Violet et al., 2005). These sheet-flows have not been directly observed traveling down the continental slope, but outcrop and seismic studies suggest they contribute a substantial amount of the sediment to continental margins, aiding progradation of clinoforms (Pickering et al., 1992; Wright et al., 1988). Significant quantitative advances have been made in our understanding of the processes and morphodynamics of channelized submarine flow (Imran et al., 2004; Keevil et al., 2006; Pirmez and Imran, 2003; Straub et al., submitted). Little, however, is currently known about how sheet-flow currents interact with topography to evolve the seascape. We examine the construction of topography by apparent sheet-like turbidity currents on the northern continental margin of Borneo, offshore Brunei Darussalam.

6.2. CONTINENTAL MARGIN OFFSHORE BRUNEI DARUSSALAM

The morphology of the present-day continental slope offshore Brunei Darussalam is primarily influenced by the progradation of deltaic depocenters situated at its margin (Hutchison, 2004; Morley, 2007). Sediment is delivered to the margin primarily through three river systems, the Baram, Belait, and Tutong Rivers (Hiscott, 2001; Hutchison, 2004; Sandal, 1996). High sediment discharge from these river systems has resulted in the construction of a continental shelf that is 50-70 km wide and underlain by 8-10 km of siliclastic sediments since the Miocene (Hutchison, 2004). Of these three rivers, the Baram has the largest drainage basin area and water and sediment discharges, $0.0192 \times 10^6 \text{ km}^2$, $1445 \text{ m}^3/\text{s}$ and $12 \times 10^6 \text{ t/yr}$, respectively. The sediments are derived from erosion of uplifted rocks from the Rajang-Crocker ranges in central Borneo. Erosion rates measured in these ranges are amongst the highest in the world and have resulted in high

sedimentation rates in the South China Sea since the Eocene (Hutchison, 2004; Sandal, 1996).

Offshore Brunei Darussalam, the continental shelf-slope break occurs at a water-depth of ~200 m (Fig. 6.1). From that position the seabed descends steeply until reaching the floor of the Borneo Trough at a water depth of 2800 m. The upper slope is characterized by a relatively steep average gradient of 0.038 m/m (Demyttenaere et al., 2000). Its south-western margin is characterized by a pair of prominent shelf-edge parallel ridges with canyons traversing the ridges. These strike-parallel ridges are the product of diapirism by mobile overpressured shale that is rising into overlying sediments along faults (Demyttenaere et al., 2000; Ingram et al., 2004; Morley, 2007; van Rensbergen et al., 1999). Our study focuses on the second of these ridges and three canyons that traverse it.

6.2.1. Seismic data set parameters

To carry out this study we have taken advantage of access to a large, industry-grade 3-D seismic volume collected on the continental slope offshore Brunei Darussalam and covers an area of 4000 km² (40 x 100 km). This study focuses on a subset of the 3-D seismic survey, an area of 200 km² which encompasses the shelf-edge parallel anticlines shown in Figure 6.1. Present-day water depths increase from approximately 550 m to 1050 m moving from the proximal to distal end of the study region. We focus on the sedimentary section imaged by the first 0.3 seconds of two-way travel-time (TWT) beneath the seafloor. For this portion of the 3-D data volume, the frequency roll-off is near 80 Hz providing a vertical resolution in deposit thickness of approximately 3 m. The horizontal resolution is limited by 25 x 25 m spacing between lines of the seismic grid.

6.2.2. Shale diapirism

Two prominent ridges occur within the study area and both are oriented roughly parallel to the present-day shelf-slope break. The average bathymetric profile of the downslope surface topography for this region of the shelf and slope encompassing these ridges is presented in Figure 6.2A and its associated surface gradient is plotted as Figure 6.2B. This average profile is a swath profile calculated from a set of evenly spaced, parallel profiles that are oriented in the dominant downslope direction. Downslope gradient is calculated at

each node using the elevation difference between its upslope and downslope neighboring bins. The two shelf-edge parallel ridges create a stepped profile with low surface gradients upstream of the ridges and high surface gradients directly downslope of the ridge crests. These ridges are the product of shale diapirs (Demyttenaere et al., 2000; van Rensbergen et al., 1999). Mobile shale generally is derived from buried, laterally extensive depositional sequences that are in excess of a hundred meters thick, where a combination of high sedimentation rates and low permeability inhibit the flow of interstitial water and cause pore fluid pressures to rise above hydrostatic levels (van Rensbergen et al., 1999; Westbrook and Smith, 1983). Miocene to Pliocene loading of sediment associated with the Baram delta over a thick, shale-prone marine sequence of Oligo-Miocene age called the Setap Shale produced the conditions for mobile shales and diapirism in the study area (Sandal, 1996; van Rensbergen et al., 1999). Active diapir growth in this region occurred until the Late Pliocene or Early Pleistocene (Demyttenaere et al., 2000). In the seismic surveys the mobile shale is identified as low velocity, chaotic to reflection-free intervals not necessarily confined by stratigraphic units (Westbrook and Smith, 1983).

6.3. 3-D SEISMIC GEOMORPHOLOGY OF SHALE RIDGE

6.3.1. Map Trends

The present-day seafloor in our study area was picked on each in-line of the seismic volume (Fig. 6.3A). We also mapped four shallow regional surfaces named SR1, SR2, SR3, and SR4 in order of increasing depth below the present-day seafloor (Fig. 6.4). These sub-surface seismic horizons were selected for mapping because they had strong reflection amplitudes that could be tracked regionally over the full extent of the study region. Biostratigraphic dating provided from samples collected at petroleum exploration wells located near the study area suggest that our entire mapped interval is Quaternary in age (Hiscott, 2001). This interval overlies mobile shale that is characterized by zones of low reflectivity and chaotic reflectors in seismic cross-sections and time slices (Fig. 6.3B and Fig. 6.4). Maps of the four subsurface seismic horizons represent approximate realizations of four palaeo-seafloor configurations. When used in conjunction with the present-day

seafloor map, they allow us to evaluate how sediment deposition has evolved the seafloor through time.

Present-day water depths over the studied shale ridge range between 550 m and 1050 m (Fig. 6.3A). Three canyons traverse this ridge. Canyon relief is defined here as the difference in elevation between the canyon axis or thalweg and the average of the elevations for the overbank surfaces that bound each side of the feature (Figs. 6.3A and 6.5). The maximum relief for the three present-day canyons is 75 m, 140 m, and 161 m. This maximum relief for the canyon systems occurs close to the hinge line of the shale ridge (Fig. 6.3B). Upslope and down slope from the shale ridge the three canyon systems lose almost all of their relief and the seafloor can be characterized as unchannelized. A map of average local surface gradient was created using the present-day seafloor bathymetry (Fig. 6.3C). This surface gradient was calculated at every seismic bin by averaging the absolute gradient measured between the 8 neighboring bins. The highest surface gradients are associated with the side walls of canyons and the downslope limb of the shale ridge. The lowest surface gradients are located directly updip from the shale ridge in the unchannelized region.

The five mapped horizons have been converted from TWT to elevation below mean sea-level using a seismic velocity of 1460 m/s for seawater and 1700 m/sec for the shallow deposit. This seismic velocity for the first 300 m of sedimentary deposits beneath the seafloor was taken from a petroleum well control point located in our study region (van Rensbergen et al., 1999). The approximate palaeo-seafloor topography recorded in seismic horizons SR1-SR4 contain most of the features found on the present-day seafloor (Fig. 6.6). Topography associated with the shale ridge is observed in each map, with low surface gradients and high surface gradients located upslope and downslope of the shale ridge hinge-line, respectively. Several differences between the present-day seafloor and the palaeo-seafloors are noted. First, the relief of the channel-levee system located in the extreme south-western portion of the survey has decreased through time. Second, the maximum relief for all three canyons has increased through time.

Maps of deposit thickness were created by differencing seafloor and subsurface horizons (Fig. 6.7). These maps indicate that the study region is everywhere a site of net sediment accumulation. The first-order trend is a relatively systematic decrease in deposit

thickness with increasing down slope distance. Superimposed on this trend are relative lows in sediment deposition associated with the canyon thalwegs that traverse the shale ridge and a local maximum in deposit thickness is associated with the filling of the channel-levee system located in the south-western portion of the study region.

We use swath profiles to characterize how overall deposit thickness varies as a function of the downslope distance (Fig. 6.8). Average deposit thickness decreases as a function of distance from the shelf-edge. Figure 6.8B shows that excluding a local effect of the shale-cored anticline, overall deposit thickness decreases linearly at 9 m/km in the downslope direction. A local minimum in deposit thickness is associated with the hinge-line of the shale ridge. Interestingly, the increase in deposit thickness observed immediately downslope of the shale ridge hinge-line is spatially correlated with the largest measured surface gradients for the long profile of the system.

6.3.2. Comparison of Canyon Axis and Confining Overbank Surfaces

To separate the contributions of canyons and overbank surfaces to the average deposit thickness trend we analyze swath profiles from each of these regions independently. First we analyze properties of Canyon 1 (Fig. 6.1C) along a 0.5 km-wide transect labeled C1 on Figure 6.3A. The swath profiles of canyon bathymetry, downslope gradient and deposit thickness are calculated for this transect and are plotted in Figure 6.9A. Properties of the overbank to either side of the canyon are for the 0.5 km-wide transects labeled O1 and O2 in Figure 6.3A. The overbank profile locations are centered on the topographic highs adjacent to the canyon. Swath profiles for O1 and O2 are calculated and then averaged to produce the characteristic bathymetry, downslope gradient, and deposit thickness associated with the adjacent overbank surface (Fig. 6.9B). Present-day seafloor gradients also presented in Figure 6.9 are measured using a 150 m moving window centered on each analyzed bin.

Swath bathymetry shows a step-pool topography associated with the axis of Canyon 1 as it traverses the shale ridge (Fig. 6.9A-1). The two steps are characterized by extreme downslope gradients of 0.25 m/m and 0.09 m/m respectively. Swath profiles of deposit thickness along the canyon axis show local minimums centered over the shale

ridge hinge-line. The amplitude of this local minimum systematically increases as total sediment thickness increases between horizons SR4 and the present-day seafloor (SR0).

Mean bathymetry of the overbank surface that confines Canyon 1 smoothly increases at a gradient of 0.013 +/- 0.009 m/m updip from the shale ridge hinge-line and a average gradient of 0.073 +/- 0.002 m/m downslope of the hinge-line (Figs. 6.9B-1,-2). Local minimums in the swath profiles for overbank deposit thickness are centered on the shale ridge hinge-line (Fig. 6.9B-3). This thickness distribution is consistent to what is observed for the canyon axis profiles (Fig. 6.9A-3).

An identical set of measurements and calculations have been made for Canyon 2 (Fig. 6.1C) using transects C2, O2, and O3 (Fig. 6.3A). Results for Canyon 2 are presented in Figure 6.10. Similar to the Canyon 1 system, the highest sea-floor gradients along the canyon axis are measured where it traverses the shale ridge (Fig. 6.10-2) and the largest sea-floor gradients associated with the mean overbank surface are measured on the downslope side of the shale ridge. The shale ridge hinge-line is associated with local lows in deposit thicknesses for both the canyon axis and the confining overbank (Figs. 6.10A-3, B-3).

6.4. INTERPRETATION

6.4.1. Sheet-like Turbidity Currents

The subsurface horizons SR1-SR4 persist in the strike direction across the entire study region (Fig. 6.4). Upslope and downslope of the shale ridge hinge-line these horizons appear to drape pre-existing topography rather than onlap older horizons. These reflectors are only infrequently truncated by small channel features. This seismic facies suggests deposition via a laterally extensive process. A minimum deposition rate associated with this facies can be estimated using the duration of the Quaternary, 1.8 million years, as the time-span for deposition of the sedimentary package bounded by horizons SR4 and SR0. This minimum deposition rate is about 17 cm/ky, greater than most hemipelagic fallout rates and suggestive that these deposits are associated with turbidity currents (Reading, 1996). A turbidity current origin for the studied deposits is also supported by the depositional patterns observed in the vicinity of the shale ridge crest-line. Maximum

deposition rates on topographic highs and minimums within the canyons is a pattern that is difficult to explain if sedimentation is from a distributed fallout of fine-grained particles from the uppermost portion of the water column. On the other hand, this sedimentation pattern is consistent with deposition from bottom-hugging, laterally extensive turbidity currents, as will be described below.

6.4.2. Canyon Growth

Our five mapped horizons can be used to estimate how the relief of canyons 1 and 2 changed through time and these relief histories are presented in Figure 6.11. This data shows a progressive increase in the overall relief for each canyon. For example the maximum relief of Canyon 1 increased from about 74 m to about 159 m over the time window associated with horizons SR4 and SR0. Maximum relief for Canyon 2 increased from about 109 m to about 139 m during this same span of time. Growth in canyon relief is not axial symmetric. Increases in relief were skewed to the downslope limb of the shale-cored anticline for both canyons. This pattern of growth has caused the two canyons to lengthen downslope.

Unlike terrestrial systems the progressive deepening of these submarine canyons occurred during net depositional conditions. For canyon relief to increase in net depositional environments the magnitude of deposition along canyon axis must be less than the sedimentation on the confining topographic highs. We propose that the relatively low deposition rates within the canyons (Fig. 6.12 and 6.13) was the product of a change in flow properties as sheet-like currents funneled into the canyons from the unconfined surface positioned immediately updip. Associated with this funneling effect is a thickening of the currents. Observed sediment deposition on the topographic highs separating the canyons seems to indicate that flows in canyons exceeded 150 m in thickness. This increase in thickness and lateral confinement of the flows is hypothesized to have increased the re-entrainment rates for sediment as currents traversed the canyons. Sedimentation rates are lower within the confines of the canyons because a larger fraction of all suspended particles settling onto the bed there are immediately lifted back into the interior flow.

The measured patterns of sedimentation of the ridges separating the canyons (Fig. 6.12 and 6.13) are consistent with laterally extensive currents funneling into these conduits while traversing the shale-cored anticline (Figs. 6.9B-3, 6.10B-3). We interpret the reduction in sedimentation leading up to the position of the hinge line as an expression of collection of the current into the canyon. As canyon relief increases toward the hinge-line there is ever less supra-canyon current available to deposit sediment on the intervening highs. This trend reverses downslope of the hinge-line as canyon relief begins to decrease, transferring an ever increasing fraction of the total current onto the overbank surface where it contributes to increasing sediment deposition. We suggest that currents being collected and expelled from canyons is the dominant control on patterns of inter-canyon sedimentation. This proposal is supported by the unlikely spatial correlation between the largest downslope surface gradients (Figs. 6.9B-2, 6.10B-2) and the thickest inter-canyon sediment accumulations (Figs. 6.9B-3, 6.10B-3). Highest deposition rates on the steepest slopes are counterintuitive unless otherwise offset by an increasing volume of current becoming available to contribute to this sedimentation as the flows begin exiting the canyons.

Deepening of submarine canyons under net depositional conditions should asymptotically approach a steady-state canyon depth. Canyon deepening will continue until its cross-sectional area is sufficient to collect all of the current, starving the inter-canyon surface of current and its sediment supply. The maximum canyon depth in net depositional environments would therefore depend on the flow and sediment-transporting properties of the sheet-flows, including unconfined thickness, discharge and sizes of suspended particles. A schematic illustration of the proposed model for development of constructional submarine canyons is presented as Figure 6.14.

6.4.3. Turbidity current thickness

The cross-sectional area of the canyons traversing the shale-cored anticline (Fig. 6.4B) can be used to estimate a minimum thickness for sheet-like turbidity currents approaching the obstruction. Since deposition occurs on the bathymetric highs between canyons, the currents must be at least as thick as the maximum canyon relief while traversing the shale ridge. From Figure 6.4B we estimate the minimum cross-sectional area necessary the fill

up the canyons and inundate highest inter-canyon surface to be $4 \times 10^5 \text{ m}^2$. Evenly distributing this area across the unchannelized slope updip from the shale ridge yields a minimum thickness of 20 m for the laterally extensive, sheet-like current.

6.5. DISCUSSION

This study illustrates that topographic morphologies traditionally attributed to net erosional environments, can in fact develop under net depositional conditions in submarine settings. This observation has received recent attention due to the identification and characterization of submarine cyclic steps (Fildani et al., 2006; Sun and Parker, 2005). Cyclic steps are bedform-like features with upstream and downstream bounding hydraulic jumps (Sun and Parker, 2005). These features were assumed to be net erosional in character until recent studies by Winterwerp *et al.* (1992) and Taki and Parker (2005) observed their formation in net depositional settings. Depositional cyclic steps have recently been identified offshore Monterey Bay, CA associated with flow stripped from partially channelized turbidity currents rounding a submarine channel bend (Fildani et al., 2006).

We propose that the depositional, step-like topography identified in the axes of canyons 1 and 2 are also cyclic steps (Figs. 6.9A-1, 6.10A-1). Identification of net depositional features with seafloor characteristics frequently attributed to net erosional processes has been made possible through the mapping of subsurface stratigraphy in the 3-D seismic volume. This presents a potential problem for scientists studying regions where bathymetric maps are the only geological data available: how to infer dynamic processes from topographic data? Several recent studies have used purely erosional models of surface evolution to characterize seafloor topographic features where no subsurface data exists (Mitchell, 2005, 2006). Our work illustrates that simply identifying the sign (+/-) of surface topography evolution is potentially fraught with errors and highlights the need for additional study into submarine transport processes.

6.6. SUMMARY

Submarine canyons are often assumed to be sites of net erosion (Cunningham et al., 2005; Huyghe et al., 2004). This assumption is derived from surface evolution models constructed from observations of terrestrial canyons (Burbank et al., 1996; Burbank and

Pinter, 1999; Humphrey and Konrad, 2000). In this study, mapping of subsurface stratigraphy over a shale-cored anticline has revealed submarine canyons that deepened under conditions of net sediment deposition.

Canyons traversing a shale ridge in our study region grew in relief during the Quaternary as a result of higher deposition rates on inter-canyon topographic highs relative to canyon axes. Seismic horizons that extend in the strike direction for >18 km and deposits that thin with distance from the shelf-edge suggest that canyon forming currents were laterally extensive sheet-flows. Laterally persistent stratigraphy likely deposited by sheet-flows highlights critical differences in transport properties of terrestrial rivers and submarine turbidity currents. In the terrestrial environment the high density of the transporting fluid, water, relative to the ambient fluid, air, results in flows that are more strongly affected by and confined to local topography when compared against turbidity currents. As a result, terrestrial overbank environments, in regions of relative uplift and canyon formation, are seldom inundated by sediment depositing flows and increases in relief require focused erosion within canyons. In contrast, the low excess density of turbidity currents allows a significant quantity of a significantly large flow to traverse over inter-canyon highs without being funneled into canyons, thereby supplying overbank regions with sediment to counter deposition occurring within canyons (Fig. 6.15).

We propose that unchannelized sheet-like turbidity currents, responsible for the deepening of canyons in our study region, had a minimum thickness and width of 20 m and 18 km, respectively. The mechanism(s) responsible for initiating currents in excess of 20 m thick and 18 km wide is unknown for this region. Today a 50-70 km wide continental slope separates the major regional rivers from the continental shelf-edge, suggesting that a direct feed of sediment from rivers to the deep marine by hyperpycnal events is unlikely at times of relatively high sea level (Mulder et al., 2003). In addition, seismic cross-sections through the present-day continental shelf directly updip from the study area do not preserve a record of a direct fluvial link to the shelf-edge during Quaternary sea-level lowstands. This suggests that the sediment composing the large turbidity currents has a non-trivial residence time on the continental shelf prior to movement down the slope. Studies from the continental shelves offshore the Amazon River (Kineke et al., 1996; Trowbridge and Kineke, 1994) and Eel River (Traykovski et al., 2000) demonstrated the

ability of fine-grained sediment to be re-entrained as fluid muds by normal wave and current activity. Flow of fluid muds over the Borneo continental shelf-edge triggered by large storms or some other unknown mechanism is likely to be the source of sediment for the canyon constructing sheet-flows in our study region.

Submarine fans offshore large river systems such as the northern Borneo continental margin record the highest long-term deposition rates of any submarine feature (Bouma et al., 1985). Continental slopes incorporated in these fans possess many topographic elements that are morphologically similar to erosional terrestrial features (Green et al., 2002; Pirmez, 1994). This work demonstrates that submarine canyons, which might be interpreted as erosional features after analysis of only the present-day seafloor, can in some cases be net depositional features. The difficulties inherent in directly measuring the processes responsible for crafting continental slope morphologies increase the need for remotely sensed images of the subsurface. These seismic volumes allow the scientific community studying submarine environments to ground-truth interpretations of processes which craft these margins.

ACKNOWLEDGEMENTS

We thank Brunei Shell Petroleum for permission to publish seismic data from offshore Brunei Darussalam. Support for our research was provided by the STC Program of the National Science Foundation via the National Center for Earth-Surface Dynamics under Agreement Number EAR-0120914. Carlos Pirmez and the Shell Turbidite Research Group provided valuable help and stimulating discussions in the early stages of the project.

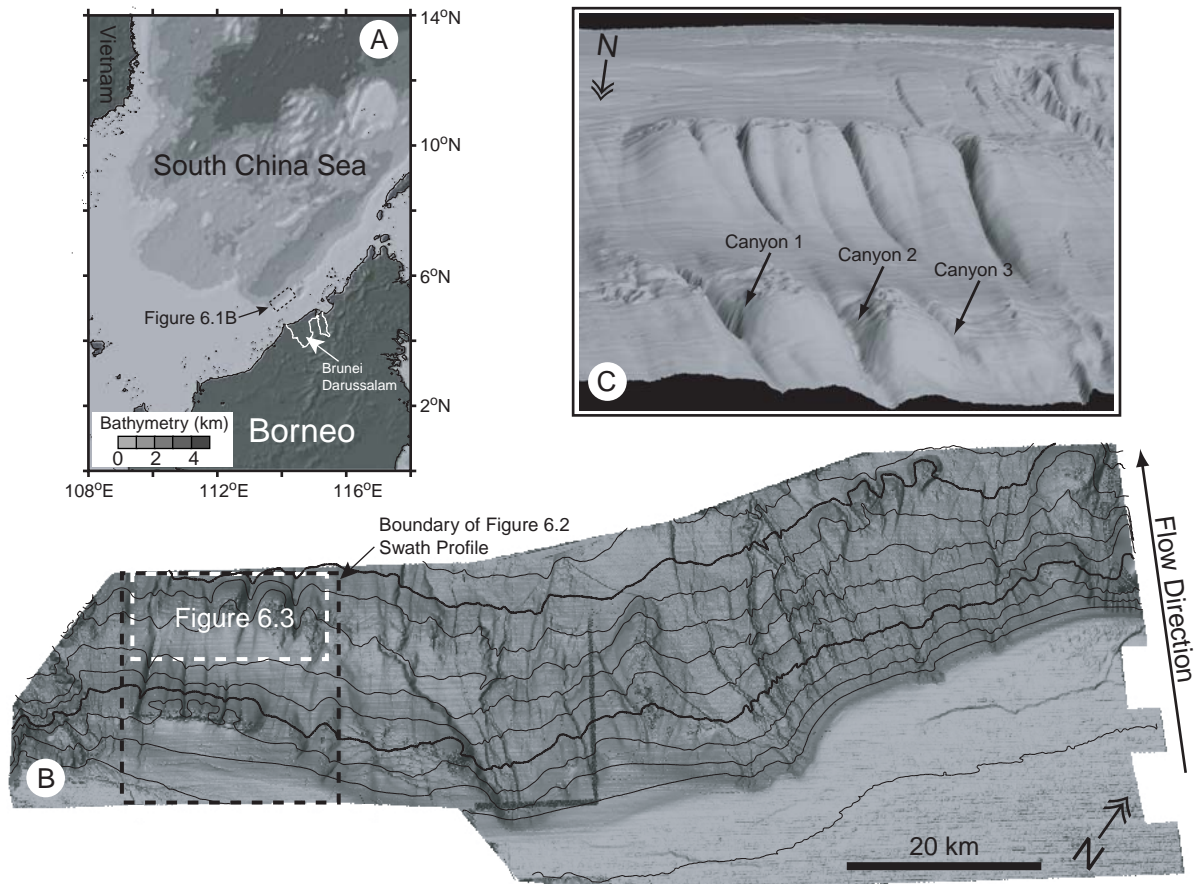


Figure 6.1. Location maps and 3-D perspective of study region. A) Bathymetric map of South China Sea with location of study region marked by dashed box. B) Slope map of continental shelf and slope, offshore Brunei Darussalam. Contour interval = 100 m water depth. Black dashed line defines area used to calculate swath profiles presented in Figure 6.2. White dashed line defines area studied using 3-D seismic volume. C) 3-D perspective view of study region with Canyons 1 and 2 labeled. Topography is vertically exaggerated.

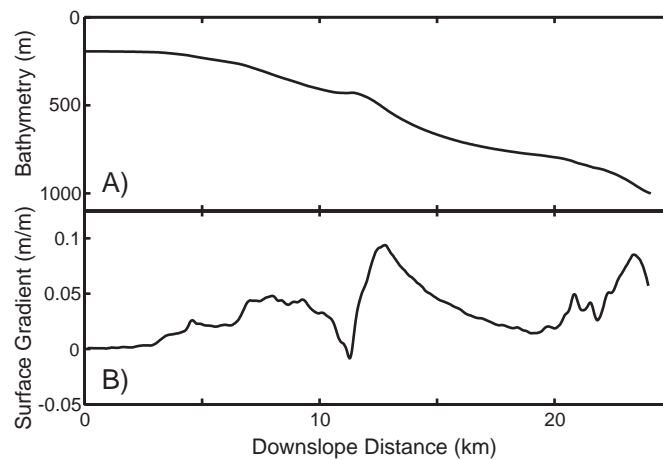
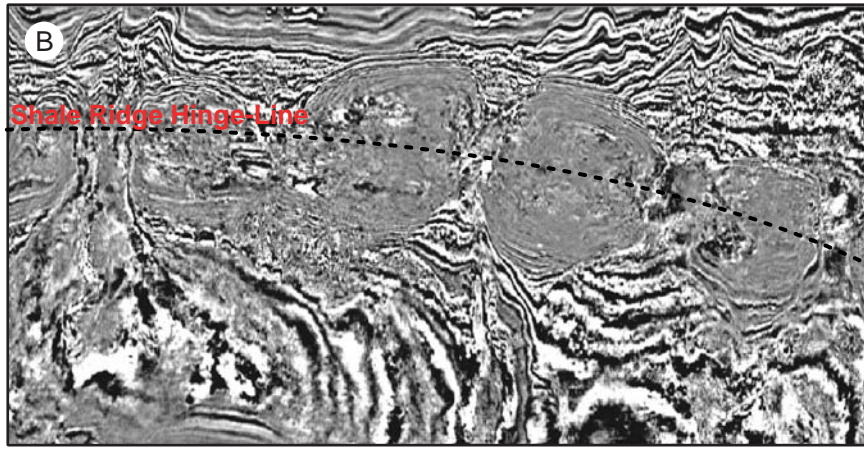
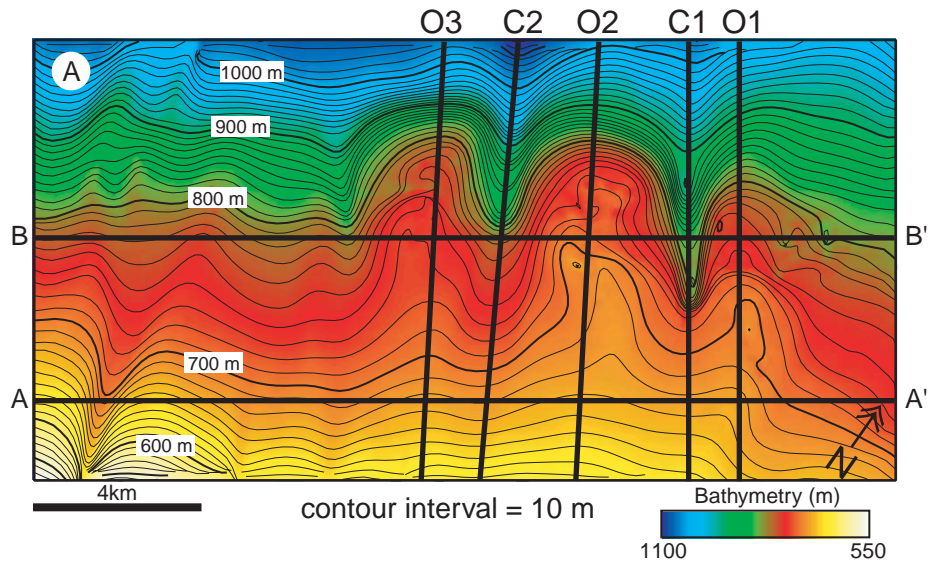


Figure 6.2. Bathymetry (A) and downslope surface gradient (B) for swath profile covering area marked on Figure 6.1B.



Time Slice at 1.65 sec TWT

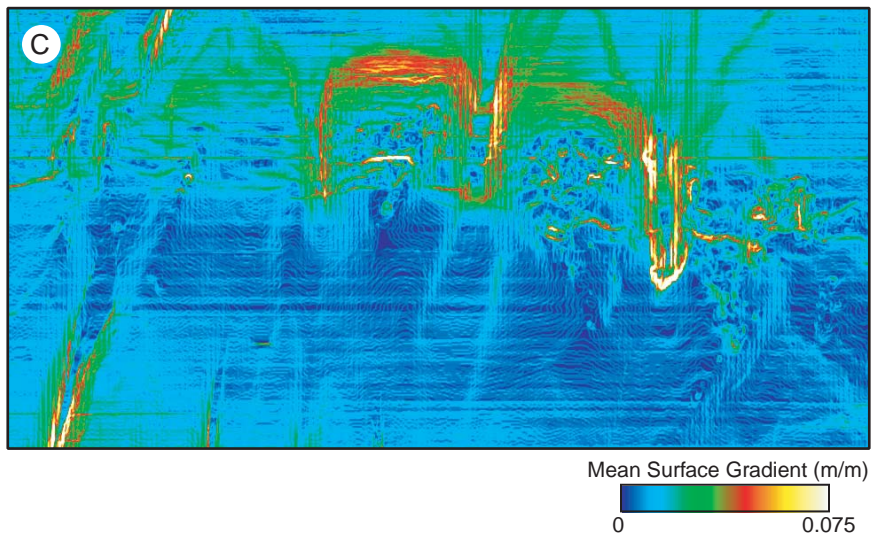


Figure 6.3. Area studied using 3-D seismic volume. Position of the 3-D seismic volume is marked on Figure 6.1B. A) Map of present-day seafloor with 10 m bathymetric contours. Strike cross-sections A-A' and B-B' define locations of seismic cross-sections displayed in Figure 6.4. Dip cross-sections C1, C2, O1, O2, and O3 define centerlines of 0.5 km wide swath profiles presented in figures 6.9 and 6.10. B) Time-slice of seismic volume at 1.65 sec of TWT. Dashed line marks the shale ridge hinge-line. C) Map of local mean surface gradient for the present-day seafloor.

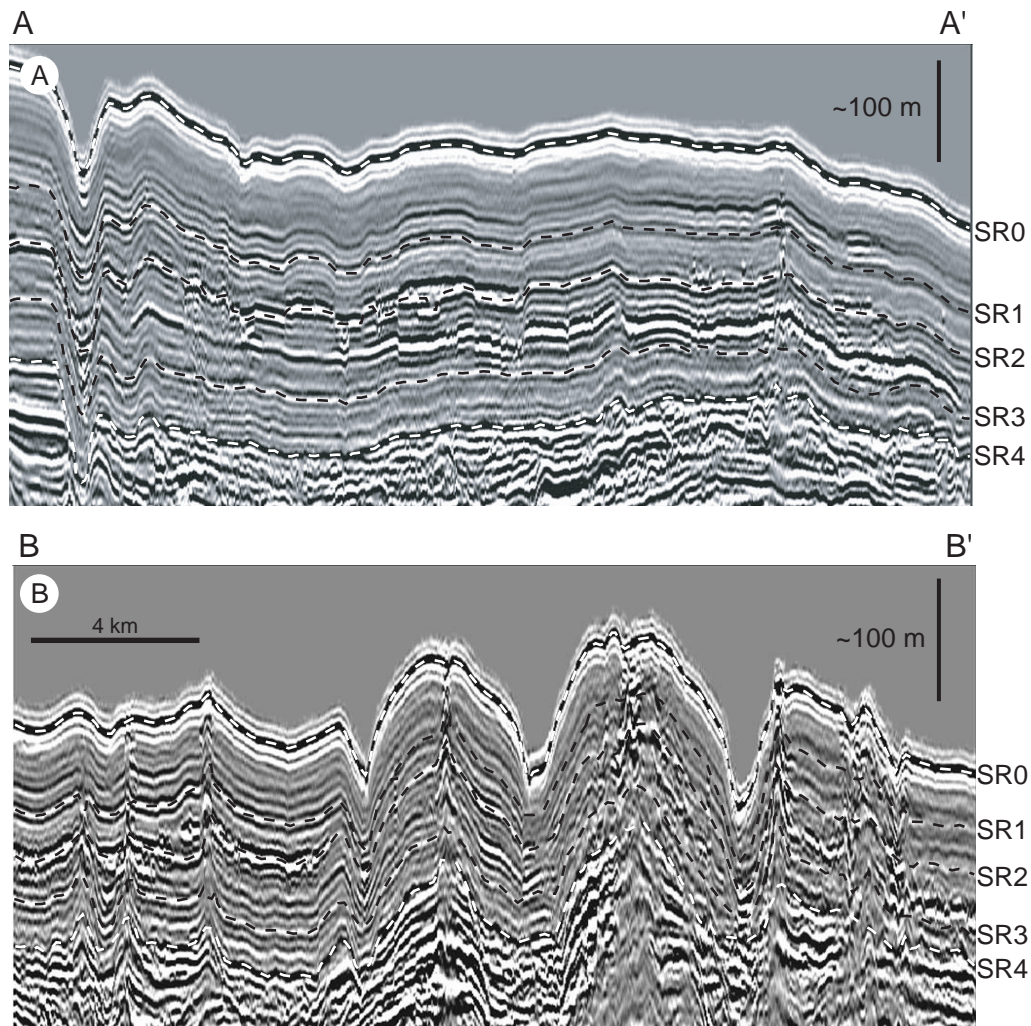


Figure 6.4. Characteristic strike-oriented seismic lines for study region. Dashed lines labeled SR0-SR4 follow mapped surface and subsurface seismic horizons used in this study. Locations for these two seismic cross-sections are marked in Figure 6.3A. A) Seismic cross-section located upslope of shale ridge. B) Seismic cross-section at shale ridge.

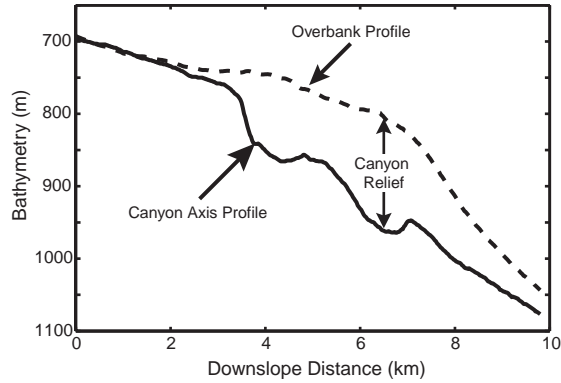


Figure 6.5. Long profile for axis of Canyon 1 (C1 of Figure 6.3A) and long profile of adjacent overbank surface (average value for O1 and O2 of Figure 6.3A). Vertical distance separating the two profiles is the local canyon relief.

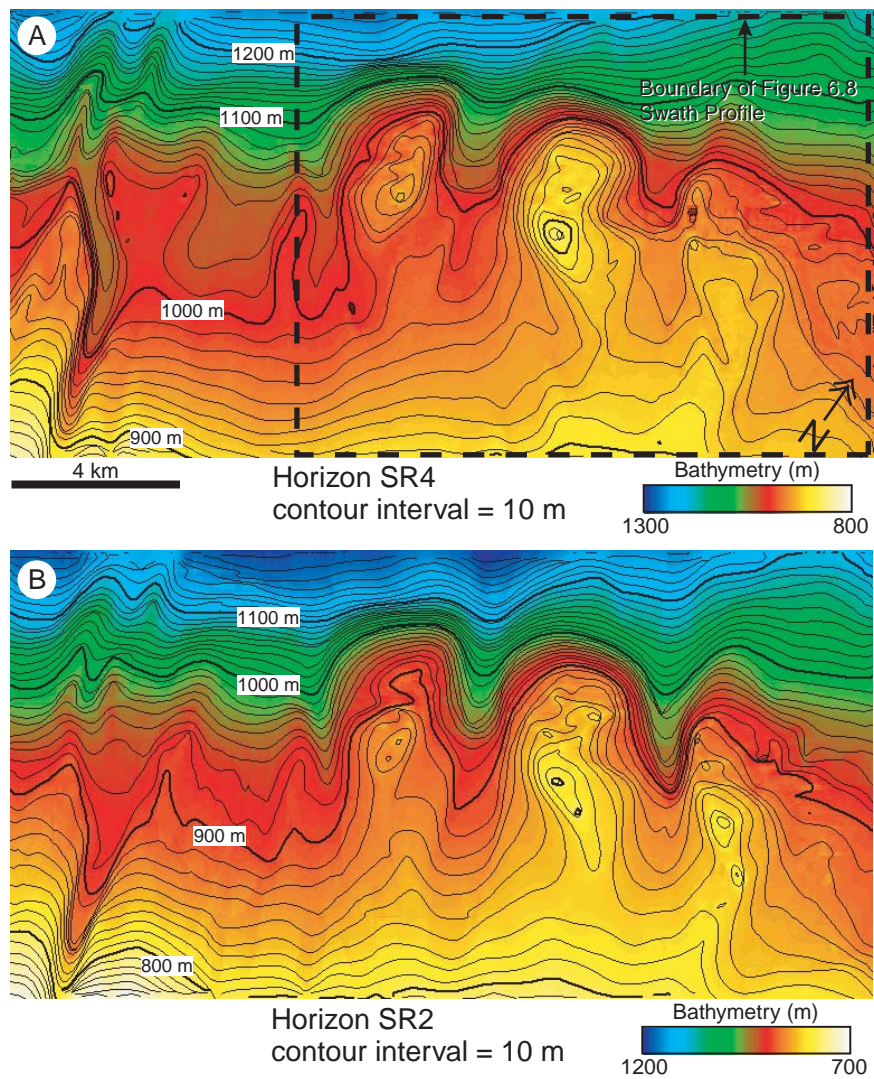


Figure 6.6. Structure maps for horizons SR4 and SR2. A) Structure map of horizon SR4 with 10 m contours. Black dashed line defines region used to calculate swath profiles presented in figure 6.8. B) Structure map of horizon SR2 with 10 m contours.

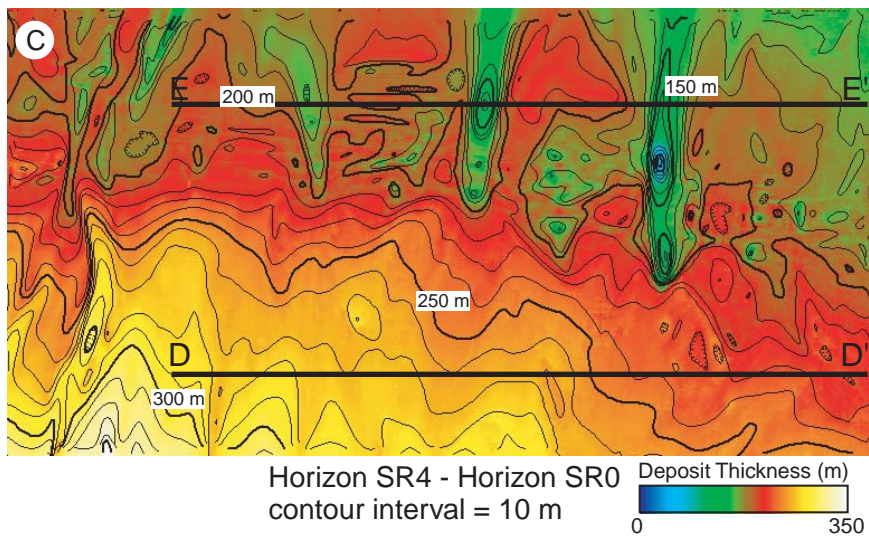
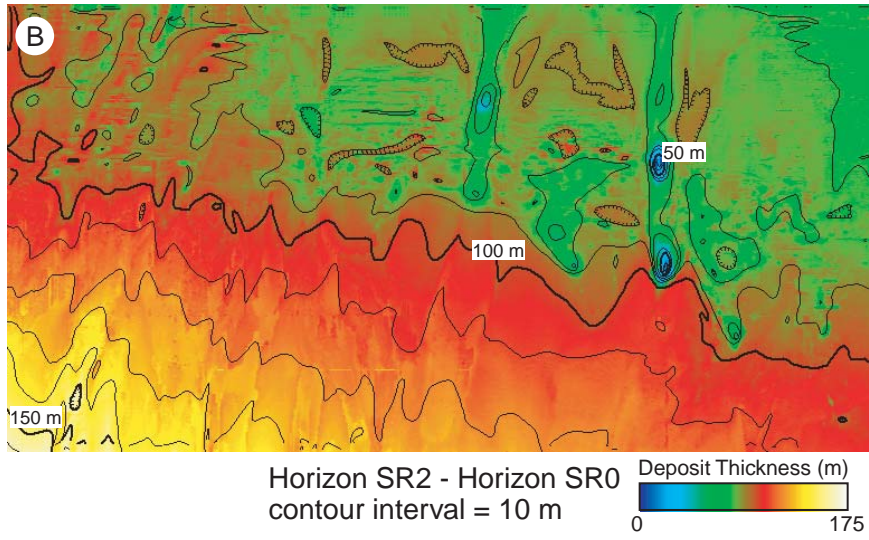
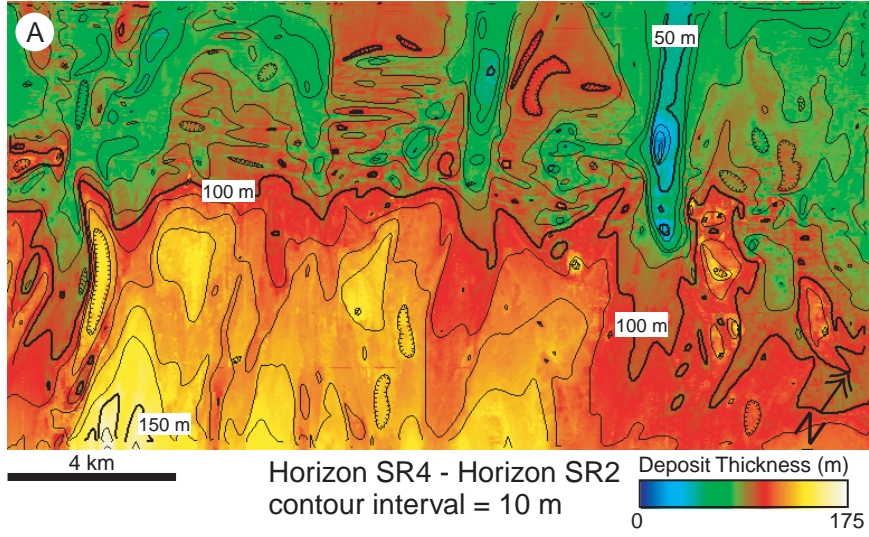


Figure 6.7. Maps of deposit thickness measured between regionally mapped seismic horizons. A) Deposit thickness of section between horizons SR4 and SR2 with 10 m contours. B) Thickness of deposit measured between horizons SR2 and SR0 (present-day seafloor) with 10 m contours. C) Thickness of sedimentary section bounded by horizons SR4 and SR0 with 10 m contours. Strike lines marked D-D' and E-E' define locations of deposit thickness profiles in Figure 6.13.

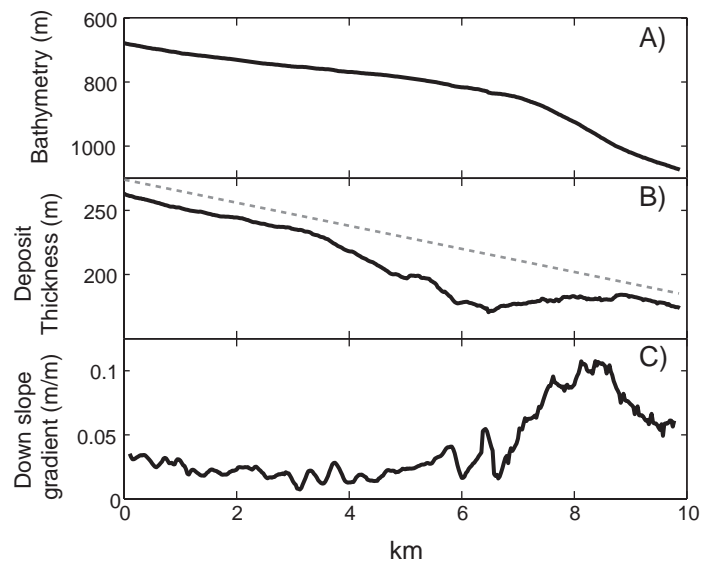


Figure 6.8. Average down-slope properties of study area marked in Figure 6.6A. A) Long profile of area. B) Thickness of sedimentary section between horizons SR0 and SR4. Gray dashed line defines a deposit taper of 9 m/km. C) Surface gradient of long profile in (A).

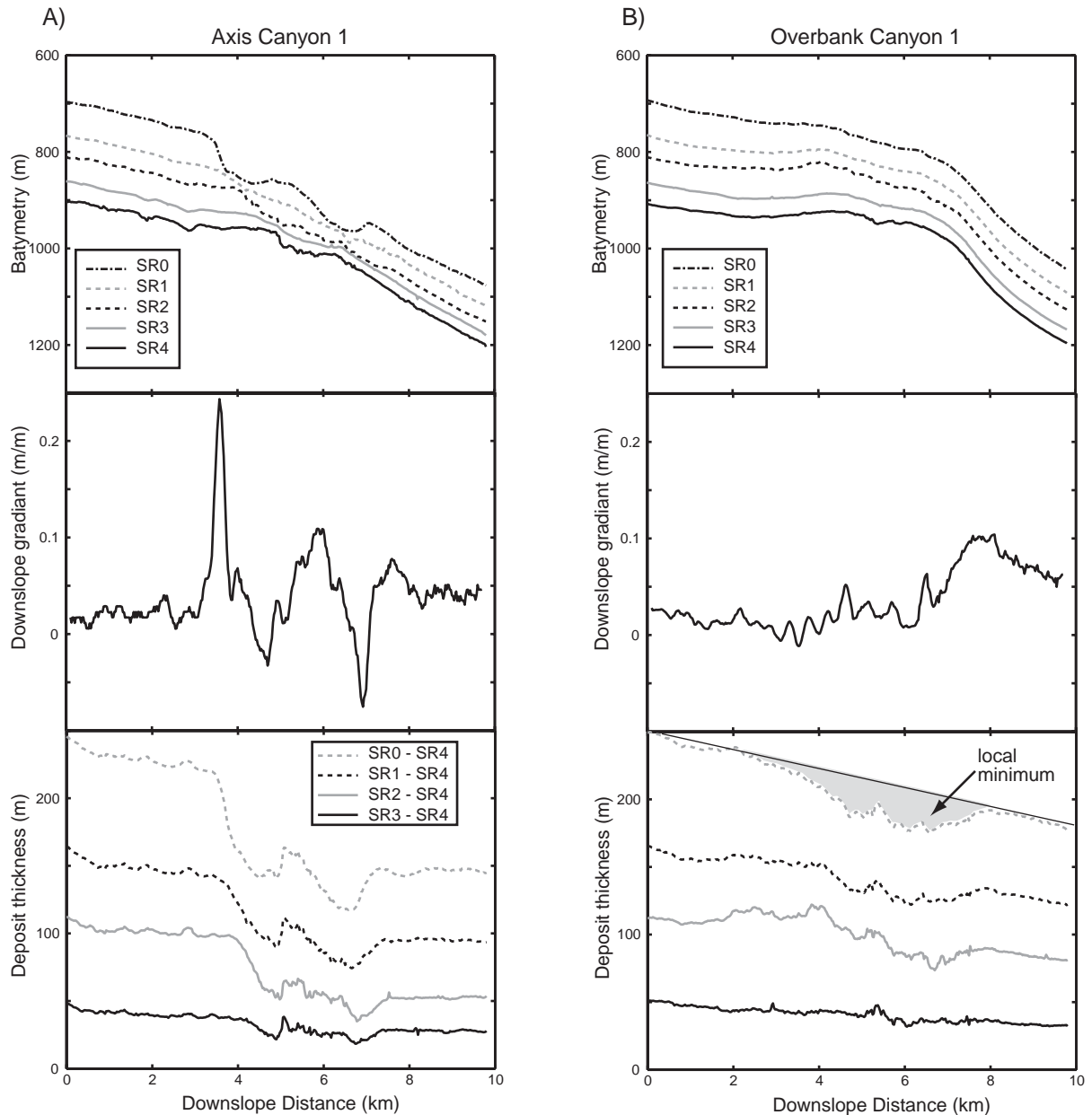


Figure 6.9. Comparison of properties for Canyon 1 and adjacent overbank at the shale ridge. A-1) Long profiles for seismic horizons SR4-SR0 following swath C1 (Fig. 6.3A) and the present-day axis of Canyon 1 (Fig. 6.1C). A-2) Surface gradient for long profile of horizon SR0, the present-day seafloor, following the axis of Canyon 1. A-3), Deposit thickness measured between horizons SR4-SR1 along swath C1, the axis of Canyon 1. B-1) Representative long profiles for the overbank surface laterally adjacent to Canyon 1. Each profile represents the average elevation for seismic horizons SR4-SR0 along transects O1 and O2 (Fig. 6.3A). B-2) Down-slope gradient of present-day seafloor associated with the average overbank profile in (B-1). B-3) Deposit thickness associated with successive long profiles in (B-1). Shaded region defines local minima in overbank sedimentation. See text for details.

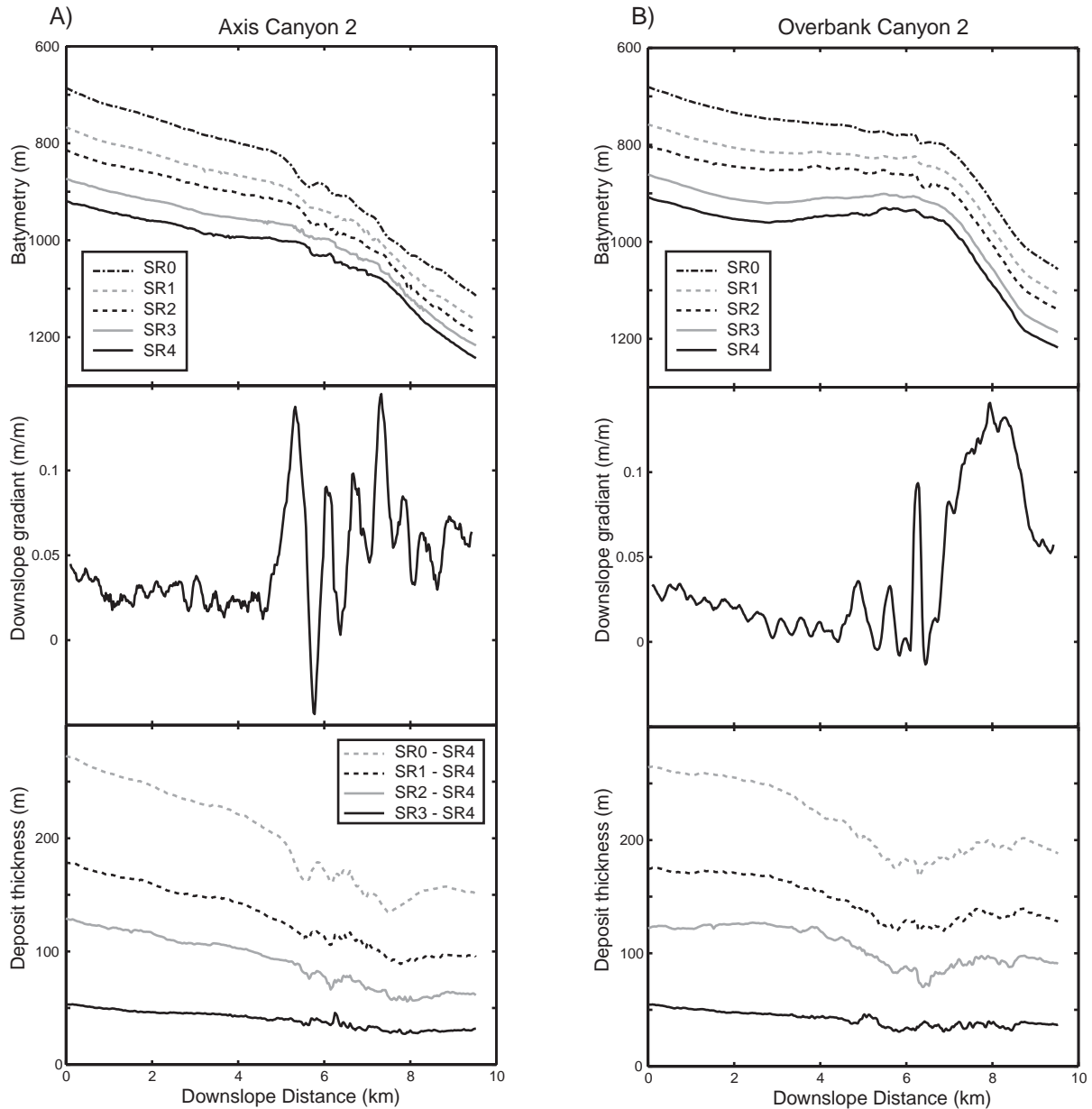


Figure 6.10. Comparison of properties for Canyon 2 and adjacent overbank at the shale ridge. A-1) Long profiles for seismic horizons SR4-SR0 following swath C2 (Fig. 6.3A) and the present-day axis of Canyon 2 (Fig. 6.1C). A-2) Surface gradient for long profile of horizon SR0, the present-day seafloor, following the axis of Canyon 2. A-3), Deposit thickness measured between horizons SR4-SR1 along swath C2, the axis of Canyon 2. B-1) Representative long profiles for the overbank surface laterally adjacent to Canyon 2. Each profile represents the average elevation for seismic horizons SR4-SR0 along transects O2 and O3 (Fig. 6.3A). B-2) Down-slope gradient of present-day seafloor associated with the average overbank profile in (B-1). B-3) Deposit thickness associated with successive long profiles in (B-1). Shaded region defines local minima in overbank sedimentation. See text for details.

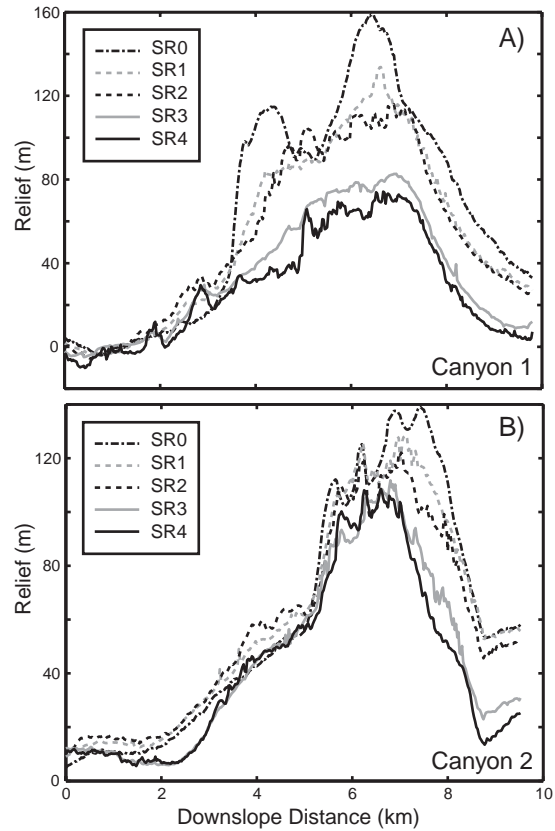


Figure 6.11. Plots defining down-canyon change in relief as a function of progressive sedimentation. Relief is defined as the difference in elevation of the average overbank surface and the canyon axis for seismic horizons SR4-SR0. A) Relief of Canyon 1 as a function of progressive sediment accumulation. Canyon axis and overbank surfaces defining relief are presented in figures 6.9A-1 and 6.9B-1. B) Relief of Canyon 2 with increasing sedimentation. Canyon axis and overbank surfaces defining relief are presented in figures 6.10A-1 and 6.10B-1.

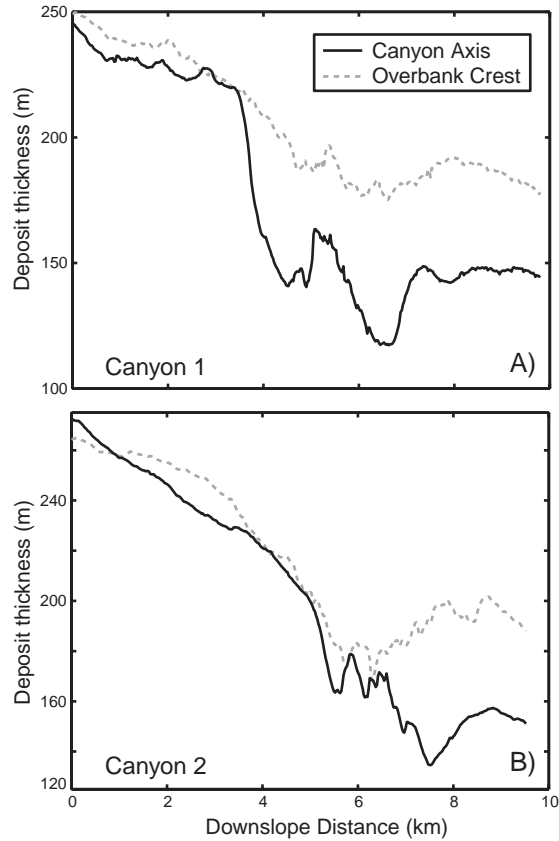


Figure 6.12. Comparison of deposit thickness for canyon axis and average overbank. Deposit thickness is measured between horizons SR4 and SR0. A) Canyon 1 profiles (see Figure 6.9 for details). B) Canyon 2 profiles (see Figure 6.10 for details).

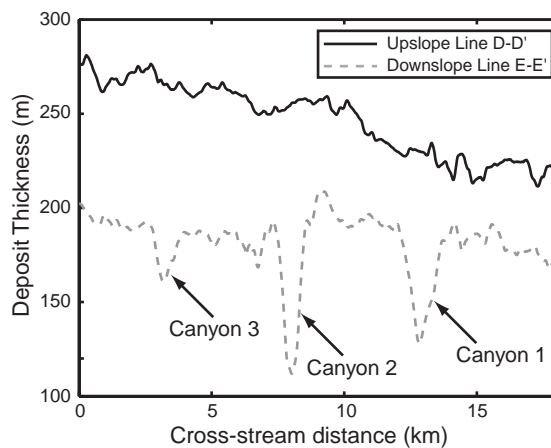


Figure 6.13. Strike profiles of deposit thickness measure upslope of shale ridge (line D-D' in Figure 6.7C) and at crest of shale ridge (line E-E' in Figure 6.7C). Deposit thickness is measured between horizons SR4 and SR0.

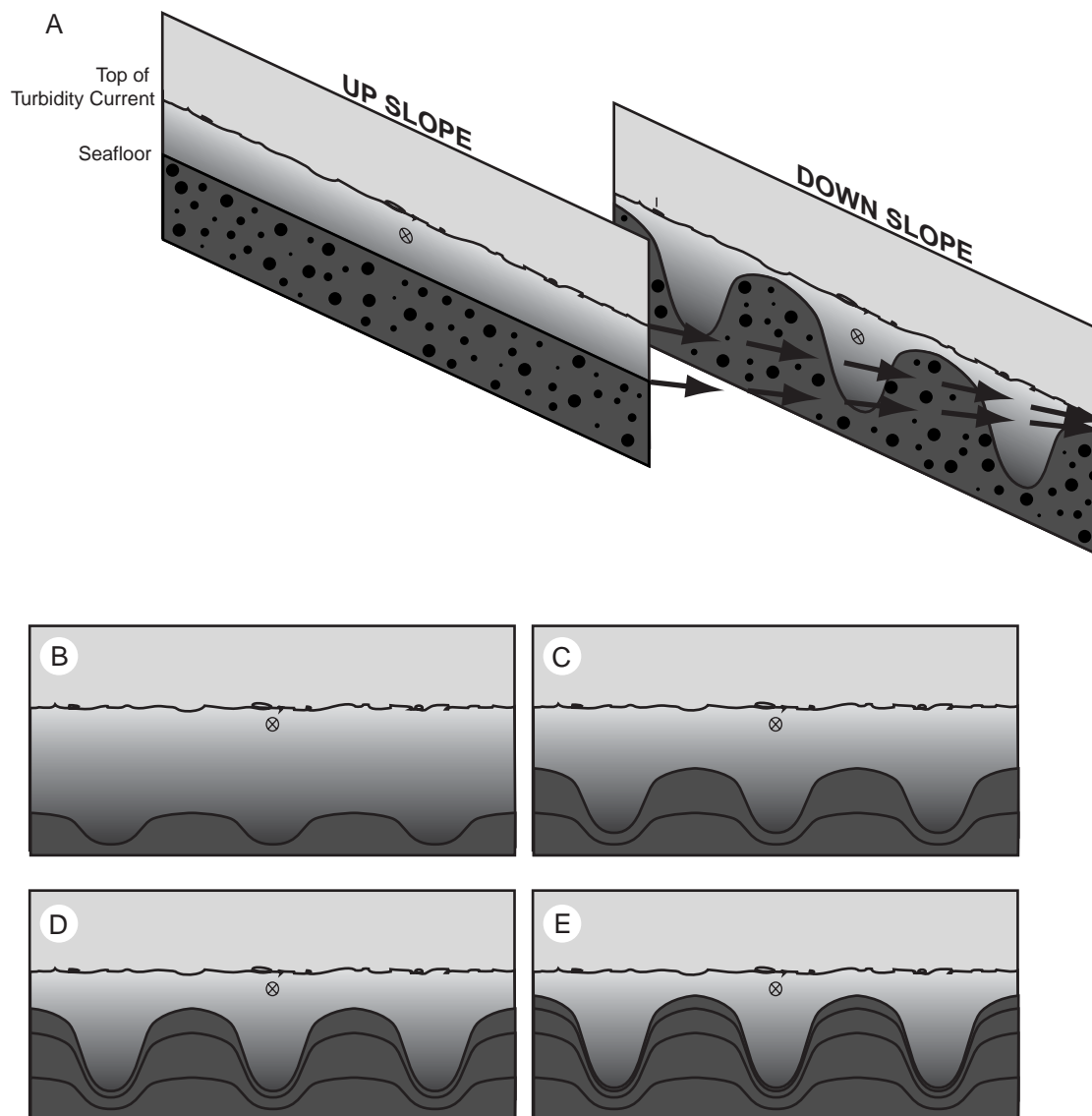


Figure 6.14. Conceptual illustrations of how sheet-like turbidity currents could interact with growing shale ridge to produce constructional canyons. A) Sheet-like current upslope of shale ridge and filling canyons at crest-line of shale ridge. Cross-sectional area of current is the same at both positions. B-E) Proposed evolution of shale ridge and canyon topography associated with net depositional, sheet-like turbidity currents. Canyon relief increases through time because sedimentation is always greatest on the unconfined surfaces separating the canyons from each other. As canyon relief increases, deposition decreases on these overbank surfaces. Sediment accumulation at the canyon axes also decreases with increasing canyon relief.

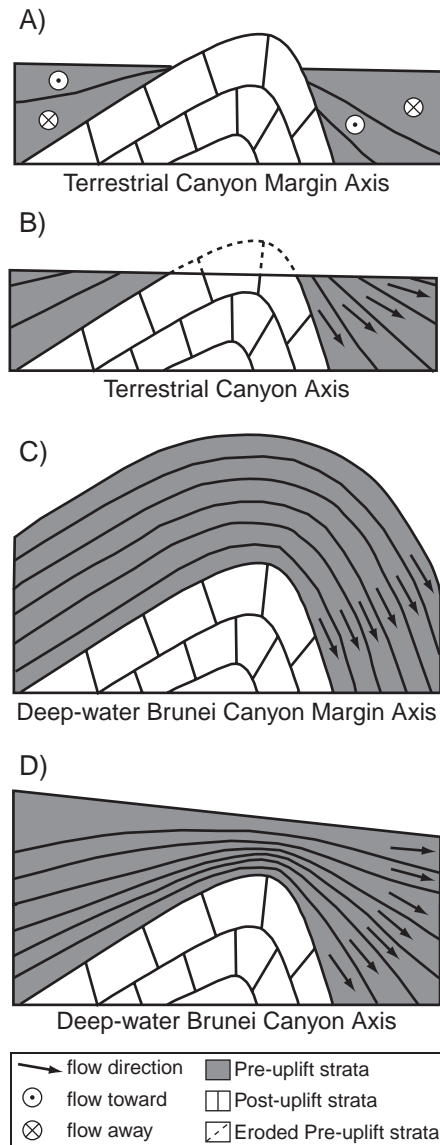


Figure 6.15. Stratigraphic characteristics related to rivers and submarine channels that are antecedent to a growing structure. A) Schematic stratigraphic cross-section following overbank profile of terrestrial canyon. Deposition by migrating channels keeps pace with erosion upslope and downslope of anticline hinge, but uplift rate surpasses deposition rate at anticline hinge. B) Cross-section following terrestrial canyon axis. Channel is depositional upslope and downslope of anticline hinge, but erosional over hinge axis. C) Cross-section following overbank profile of submarine canyon. Uplift of anticline does not significantly alter downslope deposition trends. D) Cross-section following submarine canyon axis. Uplift of anticline forces local minima in downslope deposition trends centered over position of maximum uplift.

Chapter 7

Conclusions

This thesis has addressed a series of questions at a range of scales. These questions center on turbidity current interactions with seafloor topography. At the largest scale I have characterized sheet-flow turbidity current deposits that resulted in the growth of constructional canyons on the Borneo continental slope. At the smallest scale I quantified turbidity current interactions with individual channel bends which influence both the amount of material lost to the regional overbank surface and influence the runout length of turbidity currents. While many recent studies have focused on the fluid dynamics associated with turbidity current interactions with topography, this work has focused on the deposits that result from these interactions. This choice allowed me to take advantage of the wealth of geometric data preserved in industry-grade 3-D seismic volumes and compare laboratory observations to these field-scale deposits.

Submarine channel systems are ubiquitous on continental margins. These channels are bounded over much of their length by prominent natural levees, built from the overflow and deposition of sediment contained in turbidity currents (Dennielou et al., 2006; Hay, 1987; Pirmez et al., 1997; Skene, 1998). Levees play a critical role in confining turbidity currents and therefore influence sediment transport capacity. In chapter 2 I used an industry-grade 3-D seismic volume to quantify levee deposit thickness trends and laboratory experiments to develop a quantitative sedimentation model describing levee growth. The field-scale observations centered on a tributary network of submarine channels located on the Borneo continental margin. I observed a roll-over in levee taper as a function of channel relief with a domain of rapid levee taper increase for low-relief channels, followed by a diminished rate of levee steepness increase for deeper channels. A link between the sediment transport field and levee morphodynamics was observed in laboratory experiments. These experiments suggest that the most important parameters controlling levee development include the degree of channel confinement and the structure of the suspended-sediment concentration profile.

In chapter 4, I used laboratory experiments to quantify the interactions between turbidity currents and aggrading sinuous submarine channels. A survey of submarine

channels reveals that most channels in excess of 100 km are moderately to highly sinuous. In spite of this, most laboratory studies of turbidity currents have been conducted in straight, approximately 2-D flumes (Amy et al., 2005; Garcia, 1994; Hallworth et al., 1993). Data presented in this chapter characterized channelized and overbank deposit trends resulting from low Froude number turbidity currents. Sedimentation caused the channel to aggrade with almost no change in channel planform, a pattern seen in many natural systems (Hackbarth and Shew, 1994; Pirmez et al., 1997). Thicker, coarser, steeper levees grew on the outer banks relative to the inner banks of bends. Outer banks of bends were sites of focused overbank flow, resulting from high current superelevation. This superelevation resulted from a combination of the balance between centrifugal and pressure-gradient forces and the runup of currents onto the outer banks of bends.

Turbidity current interactions with channel bends were also studied in chapter 5. In this chapter I found that bend-induced mixing of suspended sediment in turbidity currents helps to lower near-bed sediment concentration and mean particle size, thereby reducing deposition rates and aiding the long runout of turbidity currents. This contribution demonstrates that improvements to our understanding of sediment transport efficiency require models that quantify turbidity-current interactions with topography, in addition to models describing internal turbidity-current dynamics.

Finally, in chapter 6 I used a 3-D seismic survey to study the growth of submarine canyons traversing a shale-ridge. Unlike chapters 2-5, this chapter focuses on deposition from unconfined, sheet-flow currents. Regional maps of deposit thickness demonstrate that sedimentation decreases with distance from the shelf-edge. Local deposit minima centered over the shale-ridge hinge-line are observed. Sedimentation was lower along the axis of canyons compared to the inter-canyon topographic highs. This pattern of sediment accumulation has resulted in a deepening of the canyons under net depositional conditions. This canyon growth history is fundamentally different than the erosive deepening of canyons that is always associated with rivers (Burbank et al., 1996). The work illustrates how seascape interpretations based on terrestrial analogs can be prone to significant errors. These observations point to a challenge facing the submarine geology community: how best to interpret the evolution of seascapes in those cases where only seafloor topography is available.

The interactions between turbidity currents and seafloor topography characterized in this thesis also improve our general understanding of channelized landscapes. Landscape evolution models incorporating channels are governed by equations developed for rivers (Sun et al., 2002; Whipple and Tucker, 1999). In the introduction I noted that the ratio of current density to ambient fluid density was roughly 800 in the terrestrial environment and between 1.01 – 1.1 in the ocean. Chapters 2-6 illustrate that the low excess density of turbidity currents produces fundamental differences in current-channel interactions. These differences result in the construction of coarse, thick, and steep levees, high current superelevation in channel bends, and sheet-flow turbidity currents that are only marginally influenced by topography. An improved understanding of current-topography interactions for a large range of excess densities will aid our interpretation of terrestrial, marine, and extraterrestrial channelized environments using remotely sensed data.

Bibliography

- Adams, P.N., Slingerland, R.L., and Smith, N.D., 2004, Variations in natural levee morphology in anastomosed channel flood plain complexes: *Geomorphology*, v. 61, p. 127-142.
- Alexandar, J., and Mulder, T., 2002, Experimental quassi-steady density currents: *Marine Geology*, v. 186, p. 195-210.
- Altinakar, M.S., Graf, W.H., and Hopfinger, E.J., 1996, Flow structure in turbidity currents: *Journal of Hydraulic Research*, v. 34, p. 713-718.
- Amy, L.A., Peakall, J., and Talling, P.J., 2005, Density - and viscosity stratified gravity currents: Insight from laboratory experiments and implications for submarine flow deposits: *Sedimentary Geology*, v. 179, p. 5-29.
- Asselmann, N.E.M., and Middlekoop, H., 1995, Floodplain sedimentation: quantities, patterns and processes: *Earth Surface Processes and Landforms*, v. 20, p. 481-489.
- Bagnold, R.A., 1966, An approach to the sediment transport problem from general physics, U.S. Geological Survey Professional Paper, p. 37.
- Bertoni, C., and Cartwright, J., 2005, 3D seismic analysis of slope-confined canyons from the Plio-Pleistocene of the Ebro Continental Margin (Western Mediterranean): *Basin Research*.
- Best, J.L., Kostaschuk, R.A., Peakall, J., Villard, P.V., and Franklin, M., 2005, Whole flow field dynamics and velocity pulsing within natural sediment-laden underflows: *Geology*, v. 33, p. 765-768.
- Booth, J.R., DuVernay, A.E., Pfeiffer, D.S., and Styzen, M.J., 2000, Sequence stratigraphic framework, depositional models, and stacking patterns of ponded and slope fan systems in the Auger Basin: Central Gulf of Mexico Slope, GCSEPM Foundation 20th Annual Research Conference, Deep-water Reservoirs of the World, p. 82-103.
- Bouma, A., 2000, Fine-grained, mud-rich turbidite systems: model and comparison with coarse-grained, sand-rich systems, *in* Bouma, A.H., and Stone, G.G., eds., *Fine-grained turbidite systems*, Volume Special Publication 68, SEPM, p. 9-20.
- Bouma, A., Normark, W.R., and Barnes, N.E., 1985, *Submarine Fans and Related Turbidite Systems*: New York, Springer Verlag.
- Brierley, G.J., Ferguson, R.J., and Woolfe, K.J., 1997, What is a fluvial levee?: *Sedimentary Geology*, v. 114, p. 1-9.
- Brunt, R.L., McCaffrey, W.D., and Kneller, B., 2004, Experimental modeling of the spatial distribution of grain size development in a fill-and-spill mini-basin setting: *Journal of Sedimentary Research*, v. 74, p. 438-446.
- Buckee, C.M., Kneller, B.C., and Peakall, J., 2000, Turbulence structure in steady, solute-driven gravity currents, *in* Kneller, B.C., McCaffrey, W., Peakall, J., and Drutt, T., eds., *Sediment transport and deposition by particulate gravity currents*, Special Publication of the International Association of Sedimentologist.
- Burbank, D.W., McLean, J.K., Bullen, M., Abdрахmatov, K.Y., and Miller, M.M., 1999, Partitioning of intermontane basins by thrust-related folding, Tien Shan, Kyrgyzstan: *Basin Research*, v. 11, p. 75-92.
- Burbank, D.W., Meigs, A., and Brozovic, N., 1996, Interactions of growing folds and coeval depositional systems: *Basin Research*, v. 8, p. 199-223.

- Burbank, D.W., and Pinter, N., 1999, Landscape evolution: the interactions of tectonics and surface processes: *Basin Research*, v. 11, p. 1-6.
- Canals, M., Casamor, J.L., Urgeles, R., Lastras, G., Calafat, A.M., Masson, D.G., Berne, S., and Alonso, B., 2000, The Ebro Continental Margin, Western Mediterranean Sea: Interplay Between Canyon-Channel Systems and Mass Wasting Processes, GCSEPM Foundation 20th Annual Research Conference: Deep-Water Reservoirs of the World, p. 152-174.
- Cazanacli, D., and Smith, N.D., 1998, A study of morphology and texture of natural levee - Cumberland Marshes, Saskatchewan, Canada: *Geomorphology*, v. 25, p. 43-55.
- Choi, S.-U., and Garcia, M.H., 2001, Spreading of gravity plumes on an incline: *Coastal Engineering Journal*, v. 43, p. 221-237.
- Chow, V.T., 1959, *Open-channel hydraulics*: New York, McGraw-Hill, 680 p.
- Church, M., 2006, Bed material transport and the morphology of alluvial river channels: *Annual Reviews of Earth and Planetary Sciences*, v. 34, p. 325-354.
- Clark, J., Kenyon, N., and Pickering, K., 1992, Quantitative analysis of the geometry of submarine channels: Implications for the classification of submarine fans: *Geology*, v. 20, p. 633-636.
- Clark, J., and Pickering, K., 1996, Architectural elements and growth patterns of submarine channels: applications to hydrocarbon exploration: *American Association of Petroleum Geologist Bulletin*, v. 80, p. 194-221.
- Clemenceau, G.R., Colbert, J., and Eddens, J., 2000, Production results from levee-overbank turbidite sands at Ram/Powell field, Deepwater Gulf of Mexico, GCSEPM Foundation 20th Annual Research Conference, Deepwater Reservoirs of the World, p. 241-251.
- Corney, R.K.T., Peakall, J., Parsons, D.R., Elliott, L., Amos, K.J., Best, J.L., Keevil, G.M., and Ingram, D.B., 2006, The orientation of helical flow in curved channels: *Sedimentology*, v. 53, p. 249-257.
- Cowan, W.L., 1956, Estimating hydraulic roughness coefficients: *Agricultural Engineering*, v. 37, p. 473-475.
- Crosby, B.T., and Whipple, K.X., 2006, Knickpoint initiation and distribution within fluvial networks: 236 waterfalls in the Waipaoa River, North Island, New Zealand: *Geomorphology*, v. 82, p. 16-38.
- Cunningham, M.J., Hodgson, S., Masson, D.G., and Parson, L.M., 2005, An evaluation of along- and down-slope sediment transport processes between Goban Spur and Brenot Spur on the Celtic Margin of the Bay of Biscay: *Sedimentary Geology*, v. 179, p. 99-116.
- Dade, W.D., and Huppert, H.E., 1994, Predicting the geometry of channelized deep-sea turbidites: *Geology*, v. 22, p. 645-648.
- Damuth, J.E., Koola, V.E., Flood, R.D., Kawsmann, R.O., Monteiro, M.C., Palma, J.J.C., and Belderson, 1983, Distributary channel meandering and bifurcation patterns on Amazon Deep-Sea Fan as revealed by long-range side-scan sonar (GLORIA): *Geology*, v. 11, p. 94-98.
- Das, H., Imran, J., Pirmez, C., and Mohrig, D., 2004, Numerical modeling of flow and bed evolution in meandering submarine channels: *Journal of Geophysical Research*, v. 109, p. 1-17.

- Deitrich, W.E., 1982, Settling velocity of natural particles: *Water Resources Research*, v. 18, p. 1615-1626.
- Deitrich, W.E., and Whiting, P.J., 1989, Boundary shear stress and sediment transport in river meanders of sand and gravel, *in* Ikeda, S., and Parker, G., eds., *River Meandering*, American Geophysical Union Water Resources Monograph 12, p. 1-50.
- Demyttenaere, R., Tromp, J.P., Ibrahim, A., Allman-Ward, P., and Meckel, T., 2000, Brunei deep water exploration: From sea floor images and shallow seismic analogues to depositional models in a slope-turbidite setting, GCSEPM Foundation 20th Annual Research Conference, Deep-Water Reservoirs of the World, p. 304-317.
- Denniellou, B., Huchon, A., Beaudouin, C., and Berne, S., 2006, Vertical grain-size variability within a turbidite levee: Autocyclicity or allocyclicity? A case study from the Rhone neofan, Gulf of Lions, Western Mediterranean: *Marine Geology*, v. 234, p. 191-213.
- Deptuck, M.E., Steffens, G.S., Barton, M., and Pirmez, C., 2003, Architecture and evolution of upper fan channel-belts on the Niger Delta slope and in the Arabian Sea: *Marine and Petroleum Geology*, v. 20, p. 649-676.
- Droz, L., Rigaut, F., Cochonat, P., and Tofani, R., 1996, Morphology and recent evolution of the Zaire turbidite systems (Gulf of Guinea): *Geological Society of America Bulletin*, v. 108, p. 253-269.
- Engelund, F., 1974, Flow and bed topography in channel bends: *Journal of Hydraulic Engineering*, v. 100, p. 1631-1648.
- Felix, M., Sturton, S., and Peakall, J., 2005, Combined measurements of velocity and concentration in experimental turbidity currents: *Sedimentary Geology*, v. 179, p. 31-47.
- Ferguson, R.I., Parsons, D.R., Lane, S.N., and Hardy, R.J., 2003, Flow in meander bends with recirculation at the inner bank: *Water Resources Research*, v. 39, p. 1322.
- Field, M.E., Gardner, J.V., and Prior, D.B., 1999, Geometry and significance of stacked gullies on the northern California slope: *Marine Geology*, v. 154, p. 271-286.
- Fildani, A., and Normark, W.R., 2004, Late Quaternary evolution of channel and lobe complexes of Monterey Fan: *Marine Geology*, v. 206, p. 199-223.
- Fildani, A., Normark, W.R., Kostic, S., and Parker, G., 2006, Channel formation by flow stripping: large-scale scour features along the Monterey East Channel and their relation to sediment waves: *Sedimentology*.
- Filgueira-Rivera, M., Smith, N.D., and Slingerland, R.L., in press, Controls on natural levee development in the Columbia River, British Columbia, Canada: *Sedimentology*.
- Flood, R.D., and Damuth, J.E., 1987, Quantitative characteristics of sinuous distributary channels on the Amazon deep-sea fan: *Geological Society of America Bulletin*, v. 98, p. 728-738.
- Formento-Trigilio, M.L., Burbank, D.W., Nicol, A., Shulmeister, J., and Rieser, U., 2002, River response to an active fold-and-thrust belt in a convergent margin setting, North Island, New Zealand: *Geomorphology*, v. 49, p. 125-152.

- Garcia, M., Alonso, B., Ercilla, G., and Gracia, E., 2005, The tributary valley systems of the Almeria Canyon (Alboran Sea, SW Mediterranean): Sedimentary architecture: *Marine Geology*, v. 226, p. 207-223.
- Garcia, M.H., 1994, Depositional turbidity currents laden with poorly sorted sediment: *Journal of Hydraulic Engineering*, v. 120, p. 1240-1263.
- Garcia, M.H., and Parker, G., 1993, Experiments on the entrainment of sediment into suspension by a dense bottom current: *Journal of Geophysical Research*, v. 98, p. 4793-4807.
- Gardner, M.H., Borer, J.M., Melick, J.J., Mavilla, N., Dechesne, M., and Wagerle, R.N., 2003, Stratigraphic process-response model for submarine channels and related features from studies of Permian Brushy Canyon outcrops, West Texas: *Marine and Petroleum Geology*, v. 20, p. 757-787.
- Goff, J.A., 2001, Quantitative classification of canyon systems on continental slopes and a possible relationship to slope curvature: *Geophysical Research Letters*, v. 28, p. 4359-4362.
- Graf, W.H., 1971, *Hydraulics of sediment transport*: New York, McGraw-Hill, 513 p.
- Gray, T.E., Alexandar, J., and Leeder, M.R., 2005, Quantifying velocity and turbulence structure in depositing sustained turbidity currents across breaks in slope: *Sedimentology*, v. 52, p. 467-488.
- Greene, H.G., Maher, N.M., and Paull, C.K., 2002, Physiography of the Monterey Bay National Marine Sanctuary and implications about continental margin development: *Marine Geology*, v. 181, p. 55-82.
- Hackbarth, C.J., and Shew, R.D., 1994, Morphology and stratigraphy of a mid-Pleistocene turbidite leveed channel from seismic, core, and log data, northeastern Gulf of Mexico, GCSEPM Foundation 15th Annual Research Conference, *Submarine Fans and Turbidite Systems*, p. 127-140.
- Hallworth, M.A., Phillips, J.C., Huppert, H.E., and Sparks, R.S., 1993, Entrainment in turbulent gravity currents: *Nature*, v. 362, p. 829-831.
- Hauenstein, W., and Dracos, T., 1984, Investigations of plunging density currents generated by inflows in lakes: *Journal of Hydraulic Research*, v. 22, p. 157-179.
- Hay, A.E., 1987, Turbidity currents and submarine channel formation in Rupert Inlet, British Columbia. 2. The role of continuous and surge-type flow: *Journal of Geophysical Research*, v. 92, p. 2883-2900.
- Hay, A.E., Murray, J.W., and Burling, R.W., 1983, Submarine channels in Rupert Inlet, British Columbia: I, Morphology: *Sedimentary Geology*, v. 36, p. 289-315.
- Hiscott, R.N., 2001, Depositional sequences controlled by high rates of sediment supply, sea-level variations, and growth faulting: the Quaternary Baram Delta of northwestern Borneo: *Marine Geology*, v. 175, p. 67-102.
- Hiscott, R.N., Hall, F.R., and Pirmez, C., 1997, Turbidity current overspill from Amazon Channel: texture of the silt/sand load, paleoflow from anisotropy of magnetic susceptibility, and implications for flow processes, *in* Flood, R.D., Piper, D.J.W., Klaus, A., and Peterson, L.C., eds., *Proceedings of the Ocean Drilling Program, Scientific Results, Volume 155*: College Station, TX, Ocean Drilling Program, p. 53-78.
- Humphrey, N.F., and Konrad, S.K., 2000, River incision or diversion in response to bedrock uplift: *Geology*, v. 28, p. 43-46.

- Hungr, O., Morgan, G.C., and Kellerhals, R., 1984, Quantitative analysis of debris torrent hazards for design of remedial measures: *Canada Geotechnical Journal*, v. 7, p. 221-238.
- Hutchison, C.S., 2004, Marginal basin evolution: the southern South China Sea: *Marine and Petroleum Geology*, v. 21, p. 1129-1148.
- Huyghe, P., Foata, M., Deville, E., Mascle, G., and Group, C.W., 2004, Channel profiles through the active thrust front of the southern Barbados prism: *Geology*, v. 32, p. 429-432.
- Imran, J., Kassem, A., and Khan, S.M., 2004, Three-dimensional modeling of density current. I. Flow in straight confined and unconfined channels: *Journal of Hydraulic Engineering*, v. 42, p. 578-590.
- Imran, J., Parker, G., and Harff, P., 2002, Experiments on incipient channelization of submarine fans: *Journal of Hydraulic Research*, v. 40, p. 21-32.
- Imran, J., Parker, G., and Katopodes, N., 1998, A numerical model of channel inception on submarine fans: *Journal of Geophysical Research*, v. 103, p. 1219-1238.
- Imran, J., Parker, G., and Pirmez, C., 1999, A non-linear model of flow in meandering submarine and subaerial channels: *Journal of Fluid Mechanics*, v. 400, p. 295-331.
- Ingram, G.M., Chisholm, T.J., Grant, C.J., Hedlund, C.A., Stuart-Smith, P., and Teasdale, J., 2004, Deepwater North West Borneo: hydrocarbon accumulation in an active fold and thrust belt: *Marine and Petroleum Geology*.
- Izumi, N., 2004, The formation of submarine gullies by turbidity currents: *Journal of Geophysical Research*, v. 109, p. C03048.
- James, C.S., 1985, Sediment transfer to overbank sections: *Journal of Hydraulic Research*, v. 23, p. 435-452.
- Johannesson, H., and Parker, G., 1989, Secondary flow in mildly sinuous channel: *Journal of Hydraulic Engineering*, v. 115, p. 289-308.
- Kassem, A., and Imran, J., 2005, Three-dimensional modeling of density current. II. Flow in sinuous confined and unconfined channels: *Journal of Hydraulic Research*, v. 42, p. 591-602.
- Keevil, G.M., Peakall, J., Best, J.L., and Amos, K.J., 2006, Flow structure in sinuous submarine channels: Velocity and turbulence structure of an experimental submarine channel: *Marine Geology*, v. 229, p. 241-257.
- Kenyon, N., Amir, A., and Cramp, A., 1995, *in* Pickering, K., Hiscott, R.N., Kenyon, N., Ricci Lucchi, F., and Smith, R.D.A., eds., *Atlas of deep water environments; architectural style in turbidite systems*: London, Chapman and Hall, p. 89-93.
- Khripounoff, A., Vangriesheim, A., Babonneau, N., Crassous, P., Dennielou, B., and Savoye, B., 2003, Direct observations of intense turbidity current activity in the Zaire submarine valley at 4000 m water depth: *Marine Geology*, v. 194, p. 151-158.
- Kineke, G.C., Sternberg, R.W., Trowbridge, J.H., and Geyer, W.R., 1996, Fluid-mud processes on the Amazon continental shelf: *Continental Shelf Research*, v. 16, p. 667-696.
- Kirkgoz, M.S., 1983, Breaking and Run-Up of Long Waves, *in* Iida, K., and Iwasaki, T., eds., *Tsunamis - Their Science and Engineering*: Toyko, Terra Scientific, p. 467-478.

- Kneller, B., 2003, The influence of flow parameters on turbidite slope channel architecture: *Marine and Petroleum Geology*, v. 20, p. 901-910.
- Kneller, B., and Buckee, C.M., 2000, The structure and fluid mechanics of turbidity currents: a review of some recent studies and their geological implications: *Sedimentology*, v. 47, p. 62-94.
- Kneller, B., Edwards, D., McCaffrey, W., and Moore, R., 1991, Oblique reflection of turbidity currents: *Geology*, v. 19, p. 250-252.
- Komar, P.D., 1969, The channelized flow of turbidity currents with application to Monterey Deep-Sea Channel: *Journal of Geophysical Research*, v. 71, p. 4544-4558.
- Kostic, S., Parker, G., and Marr, J.G., 2002, Role of turbidity currents in setting the foreset slope of clinofolds prograding into standing fresh water: *Journal of Sedimentary Research*, v. 72, p. 353-362.
- Lamb, M.P., Toniolo, H., and Parker, G., 2006, Trapping of sustained turbidity currents by intraslope minibasins: *Sedimentology*, v. 53, p. 147-160.
- Langbein, W., and Leopold, L., 1966, River meanders and the theory of minimum variance, *in* Dury, G.H., ed., *Rivers and river terraces*, p. 238-263.
- Lee, S.E., Talling, P.J., Ernst, G.G., and Hogg, A.J., 2002, Occurrence and origin of submarine plunge pools at the base of the U.S. continental slope: *Marine Geology*, v. 185, p. 363-377.
- Leopold, L.B., and Wolman, M.G., 1960, River Meanders: *Geological Society of America Bulletin*, v. 71, p. 769-793.
- Lien, T., Walker, R.G., and Martinsen, O.J., 2003, Turbidities in the Upper Carboniferous Ross Formation, western Ireland: reconstructions of a channel and spillover system: *Sedimentology*, v. 50, p. 113-148.
- Luthi, S., 1981, Experiments on non-channelized turbidity currents: *Marine Geology*, v. 40, p. M59-M68.
- Middleton, G., 1966, Experiments on density and turbidity currents I. Motion of the head: *Canadian Journal of Earth Sciences*, v. 3, p. 523-546.
- , 1993, Sediment deposition from turbidity currents: *Annual Reviews of Earth Sciences*, v. 21, p. 89-114.
- Mitchell, N.C., 2005, Interpreting long-profiles of canyons in the USA Atlantic continental slope: *Marine Geology*, v. 214, p. 75-99.
- , 2006, Morphologies of knickpoints in submarine canyons: *Geological Society of America Bulletin*, v. 118, p. 589-605.
- Mohrig, D., and Buttles, J., 2007, Shallow channels constructed by deep turbidity currents: *Geology*, v. 35, p. 155-158.
- Mohrig, D., Heller, P.L., Paola, C., and Lyons, W.J., 2000, Interpreting avulsion process from ancient alluvial sequences: Guadalope-Matarranya (northern Spain) and Wasatch Formation (western Colorado): *GSA Bulletin*, v. 112, p. 1787-1803.
- Mohrig, D., Straub, K.M., Buttles, J., and Pirmez, C., 2005, Controls on geometry and composition of a levee built by turbidity currents in a straight laboratory channel, *in* Parker, G., and Garcia, M.H., eds., *River, Coastal, and Estuarine Morphodynamics: RCEM 2005*, Taylor and Francis Group, London, p. 579-584.
- Morley, C.K., 2007, Interaction between critical wedge geometry and sediment supply in a deep-water fold belt: *Geology*, v. 35, p. 139-142.

- Morris, W., and Busby-Spera, C., 1990, A submarine-fan valley-levee complex in the Upper Cretaceous Rosario Formation: Implication for turbidite facies models: *Geological Society of America Bulletin*, v. 102, p. 900-914.
- Mulder, T., Syvitski, J.P.M., Migeon, S., Faugeres, J., and Savoye, B., 2003, Marine hyperpycnal flows: initiation, behavior and related deposits. A review: *Marine and Petroleum Geology*, v. 20, p. 861-882.
- Nelson, J.M., and Smith, J.D., 1989, Flow meandering channels with natural topography, *in* Ikeda, S., and Parker, G., eds., *River Meandering: Water Resources Monography*, American Geophysical Union, #12, p. 69-101.
- Pantin, H.M., 2001, Experimental evidence for autosuspension, *in* McCaffrey, W.D., Kneller, B., and Peakall, J., eds., *Particulate Gravity Currents*: Oxford, Blackwell Science, p. 189-205.
- Parker, G., Garcia, M.H., Fukushima, Y., and Yu, W., 1987, Experiments on turbidity currents over an erodible bed: *Journal of Hydraulic Research*, v. 25, p. 123-147.
- Parsons, J.D., and Garcia, M.H., 1998, Similarity of gravity current fronts: *Physics of Fluids*, v. 10, p. 3209-3213.
- Parsons, J.D., Schweller, W.J., Stelting, C.W., Southard, J.B., Lyons, W.J., and Grotzinger, J.P., 2002, A preliminary experimental study of turbidite fan deposits: *Journal of Sedimentary Research*, v. 72, p. 619-628.
- Peakall, J., McCaffrey, B., and Kneller, B., 2000, A process model for the evolution, morphology, and architecture of sinuous submarine channels: *Journal of Sedimentary Research*, v. 70, p. 434-448.
- Pickering, K.T., Underwood, M.B., and Taira, A., 1992, Open-ocean to trench turbidity-current flow in the Nankai Trough: flow collapse and reflection: *Geology*, v. 20, p. 1099-1102.
- Piper, D.J.W., and Normark, W.R., 1983, Turbidite depositional patterns and flow characteristics, Navy submarine fan, California Borderland: *Sedimentology*, v. 30, p. 681-694.
- Pirmez, C., 1994, Growth of a submarine meandering channel-levee system on the Amazon Fan, Columbia University.
- Pirmez, C., Beaubouef, R.T., Friedmann, S.J., and Mohrig, D., 2000, Equilibrium profile and baselevel in submarine channels: examples from Late Pleistocene systems and implications for the architecture of deepwater reservoirs, GCSEPM Foundation 20th Annual Research Conference, Deep-Water Reservoirs of the World, p. 782-805.
- Pirmez, C., and Flood, R.D., 1995, Morphology and structure of Amazon channel, *in* Flood, R.D., Piper, D.J.W., Klaus, A., and Peterson, L.C., eds., *Proceedings of the Ocean Drilling Program, Initial Results, Volume 155*: College Station, TX, Ocean Drilling Program, p. 23-45.
- Pirmez, C., Flood, R.D., Baptiste, J., Yin, H., and Manley, P.L., 1997a, Clay content, porosity and velocity of Amazon Fan sediments determined from ODP Leg 155 cores and wireline logs: *Geophysical Research Letters*, v. 24, p. 317-320.
- Pirmez, C., Hiscott, R.N., and Kronen, J.D., 1997b, Sandy turbidite successions at the base of channel-levee systems of the Amazon fan revealed by FMS logs and cores: Unraveling the facies architecture of large submarine fans, *in* Flood, R.D., Piper, D.J.W., Klaus, A., and Peterson, L.C., eds., *Proceedings of the Ocean Drilling*

- Program, Scientific Results, Volume 155: College Station, TX, Ocean Drilling Program, p. 7-33.
- Pirmez, C., and Imran, J., 2003, Reconstruction of turbidity currents in Amazon Channel: *Marine and Petroleum Geology*, v. 20, p. 823-849.
- Pizzutto, J.E., 1987, Sediment diffusion during overbank flows: *Sedimentology*, v. 34, p. 301-317.
- Posamentier, H.W., 2003, Depositional elements associated with a basin floor channel-levee system: case study from the Gulf of Mexico: *Marine and Petroleum Geology*, v. 20, p. 677-690.
- Posamentier, H.W., and Kolla, V.E., 2003, Seismic geomorphology and stratigraphy of depositional elements in deep-water settings: *Journal of Sedimentary Research*, v. 73, p. 367-388.
- Posamentier, H.W., Meizarwin, P.S., Wisman, T., and Plawman, 2000, Deep Water Depositional Systems - Ultra Deep Makassar Strait, Indonesia, GCSEPM Foundation 20th Annual Research Conference, Deepwater Reservoirs of the World, p. 806-816.
- Prather, B.E., Booth, J.R., Steffens, G.S., and Craig, P.A., 1998, Classification, lithologic calibration and stratigraphic succession of seismic facies of intraslope basins, deep-water Gulf of Mexico: *AAPG Bulletin*, v. 92, p. 707-728.
- Pratson, L., and Haxby, W.F., 1996, What is the slope of the U.S. continental slope?: *Geology*, v. 24, p. 3-6.
- Pratson, L., Ryan, W.B.F., Mountain, G.S., and Twitchell, D.C., 1994, Submarine canyon initiation by downslope-eroding sediment flows: evidence in late Cenozoic strata on the New Jersey continental slope: *Geological Society of America Bulletin*, v. 106, p. 395-412.
- Prior, D.B., Bornhold, B.D., Wiseman, J.W.R., and Lowe, D.R., 1987, Turbidity current activity in a British Columbia fjord: *Science*, v. 237, p. 1330-1333.
- Puig, P., Ogston, A.S., Mullenbach, B.L., Nittrouer, C.A., and Sternberg, R.W., 2003, Shelf-to-canyon sediment-transport processes on the Eel continental margin (northern California): *Marine Geology*, v. 193, p. 129-149.
- Reading, H.G., 1996, *Sedimentary environments: Processes, facies and stratigraphy*: Oxford, Blackwell Science, 688 p.
- Rouse, H., 1939, Experiments on the mechanics of sediment transport, 5th International Congress of Applied Mechanics: Hoboken, NJ., John Wiley, p. 550-554.
- Rowland, J.C., Lepper, K., Deitrich, W.E., Wilson, C.J., and Sheldon, R., 2005, Tie channel sedimentation rates, oxbow formation age and channel migration rate from optically stimulated luminescences (OSL) analysis of floodplain deposits: *Earth Surface Processes and Landforms*, v. 30, p. 1161-1179.
- Rozovskii, I.L., 1961, Flow of water in bends of open channels: Washington, D.C., Office of Technical Service, US Department of Commerce, p. No. OTS 60-51133.
- Sandal, S.T., 1996, The geology and hydrocarbon resources of Negara Brunei Darussalam: Brunei Darussalam, Brunei Shell Petroleum Company Sendirian Berhad and Brunei Museum, 243 p.
- Schwenk, T., Speiss, V., Hubscher, C., and Breitzke, M., 2003, Frequent channel avulsions within the active channel-levee system of the middle Bengal Fan - an exceptional

- channel-levee development derived from Parasound and Hydrosweep data: Deep-Sea Research II, v. 50, p. 1023-1045.
- Shor, A.N., Piper, D.J.W., Clarke, J.E., and Mayer, L.A., 1990, Giant flute-like scour and other erosional features formed by the 1929 Grand-Banks turbidity current: Sedimentology, v. 37, p. 631-645.
- Simons, D.B., Richardson, E.V., and Nordin, C.F., 1965, Bedload equation for ripples and dunes: U.S. Geological Survey Professional Paper 462-H.
- Simpson, J.E., and Britter, R.E., 1979, The dynamics of the head of a gravity current advancing over a horizontal surface: Journal of Fluid Mechanics, v. 94, p. 477-495.
- Skene, K.I., 1998, Architecture of Submarine Channel Levees: Halifax, Nova Scotia, Canada, Dalhousie University.
- Skene, K.I., Piper, D.J.W., and Hill, P.S., 2002, Quantitative analysis of variations in depositional sequence thickness from submarine channel levees: Sedimentology, v. 49, p. 1411-1430.
- Smith, J.D., and McLean, S.R., 1984, A model for flow in meandering streams: Water Resources Research, v. 20, p. 1301-1315.
- Snyder, N.P., Whipple, K.X., Tucker, G.E., and Merritts, D.J., 2000, Landscape response to tectonic forcing: Digital elevation model analysis of stream profiles in the Mendocino triple junction region, northern California: Geological Society of America Bulletin, v. 112, p. 1250-1263.
- Spinnelli, G.A., and Field, M.E., 2001, Evolution of continental slope gullies on the northern California margin: Journal of Sedimentary Research, v. 71, p. 237-245.
- Starn, R.H., 1981, Light attenuation in natural waters: Gershun's law, Lambert-Beer law, and the mean light path: Applied Optics, v. 20, p. 2326-2338.
- Stelting, C.W., Pickering, K., Bouma, A., Coleman, J.M., Cremer, M., Droz, L., Meyer-Wright, A.A., Normark, W.R., O'Connell, S., Stow, D.A., and Scientist, D.L.S., 1985, Drilling results on the Middle Mississippi Fan, *in* Bouma, A., Barnes, N.E., and Normark, W.R., eds., Submarine Fans and Related Turbidite Sequences: New York, Springer-Verlag, p. 275-282.
- Straub, K.M., Mohrig, D., Buttles, J., McElroy, B., and Pirmez, C., submitted, Interactions between turbidity currents and topography in aggrading sinuous submarine channels: A laboratory study: Geological Society of America Bulletin.
- Sun, T., Paola, C., Parker, G., and Meakin, P., 2002, Fluvial fan deltas: Linking channel processes with large-scale morphodynamics: Water Resources Research, v. 38, p. 10.1029.
- Sun, T., and Parker, G., 2005, Transportational cyclic steps created by flow over an erodible bed. Part 2. Theory and numerical simulation: Journal of Hydraulic Research, v. 43, p. 502-514.
- Taki, K., and Parker, G., 2005, Transportational cyclic steps created by flow over an erodible bed. Part 1. Experiments: Journal of Hydraulic Research, v. 43, p. 488-501.
- Traykovski, P., Geyer, W.R., Irish, J.D., and Lynch, J.F., 2000, The role of wave-induced density-driven fluid mud flows for cross-shelf transport on the Eel River continental shelf: Continental Shelf Research, v. 20, p. 2113-2140.
- Trowbridge, J.H., and Kineke, G.C., 1994, Structure and dynamics of fluid muds on the Amazon continental shelf: Journal of Geophysical Research, v. 99, p. 865-874.

- Tucker, G.E., and Slingerland, R.L., 1996, Predicting sediment flux from fold and thrust belts: *Basin Research*, v. 8, p. 329-350.
- Twitchell, D.C., Cross, V.A., Hanson, A.D., Buck, B.J., Zybala, J.G., and Rudin, M.J., 2005, Seismic architecture and lithofacies of turbidites in Lake Mead (Arizona and Nevada, U.S.A.), an analogue for topographically complex basins: *Journal of Sedimentary Research*, v. 75, p. 134-148.
- Twitchell, D.C., Schwab, W.C., Nelson, C.H., and Kenyon, N., 1995, Geometry of sandy deposits at the distal edge of the Mississippi Fan, Gulf of Mexico, *in* Pickering, K., ed., *Atlas of Deep-Water Environments: Architectural style in turbidite systems*: London, Chapman and Hall, p. 282-286.
- van den Berg, J.H., van Gelder, A.V., and Mastbergen, D.R., 2002, The importance of breaching as a mechanism of subaqueous slope failure in fine sand: *Sedimentology*, v. 49, p. 81-95.
- van Rensbergen, P., Morley, C.K., Ang, D.W., Hoan, T.Q., and Lam, N.T., 1999, Structural evolution of shale diapirs from reactive rise to mud volcanism: 3D seismic data from the Baram delta, offshore Brunei, Darussalam: *Journal of the Geological Society of London*, v. 156, p. 633-650.
- Violet, J., Sheets, B., Pratson, L., Paola, C., Beaubouef, R.T., and Parker, G., 2005, Experiment on turbidity currents and their deposits in a model 3D subsiding minibasin: *Journal of Sedimentary Research*, v. 75, p. 820-843.
- Weimer, P., and Link, M.H., 1991, *in* Weimer, P., and Link, M.H., eds., *Seismic Facies and Sedimentary Process of Submarine Fans of Submarine Systems*: New York, Springer-Verlag, p. 9-67.
- Westbrook, G.K., and Smith, M.J., 1983, Long decollements and mud volcanoes: Evidence from the Barbados Ridge Complex for the role of high pore-fluid pressure in the development of an accretionary complex: *Geology*, v. 11, p. 279-283.
- Whipple, K.X., and Tucker, G.E., 1999, Dynamics of the stream-power river incision model: Implications for height limits of mountain ranges, landscape response timescales, and research needs: *Journal of Geophysical Research*, v. 104, p. 17661-17674.
- Winterwerp, J.C., Bakker, W.T., Mastbergen, D.R., and van Rossum, H., 1992, Hyperconcentrated sand-water mixture flows over erodible bed: *Journal of Hydraulic Engineering*, v. 119, p. 1508-1525.
- Wright, L.D., Wiseman, W.J.J., Bornhold, B.D., Prior, D.B., Suhayda, J.N., Keller, G.H., Yang, L.S., and Fan, Y.B., 1988, Marine dispersal and deposition of Yellow River silts by gravity-driven underflows: *Nature*, p. 629-632.
- Xu, J.P., Nobel, M.A., and Rosenfeld, L.K., 2004, In-situ measurements of velocity structure within turbidity currents: *Geophysical Research Letters*, v. 31, p. doi:10.1029/2004GL019718.
- Yen, C., and Yen, B.C., 1971, Water surface configuration in channel bends: *Journal of Hydraulic Engineering*, v. 97, p. 303-321.
- Yu, B., Cantelli, A., Marr, J.G., Pirmez, C., O'Byrne, C., and Parker, G., 2006, Experiments on self-channelized subaqueous fans emplaced by turbidity currents and dilute mudflows: *Journal of Sedimentary Research*, v. 76, p. 889-902.